

ANALYSIS AND DESIGN OF ELECTRIC MACHINES USING 2D METHOD OF
MOMENTS

A Dissertation

Submitted to the Faculty

of

Purdue University

by

Daniel C. Horvath

In Partial Fulfillment of the

Requirements for the Degree

of

Doctor of Philosophy

August 2019

Purdue University

West Lafayette, Indiana

THE PURDUE UNIVERSITY GRADUATE SCHOOL
STATEMENT OF DISSERTATION APPROVAL

Prof. Steven Pekarek, Chair

School of Electrical and Computer Engineering

Prof. Scott Sudhoff

School of Electrical and Computer Engineering

Prof. Dionysios Aliprantis

School of Electrical and Computer Engineering

Prof. Dan Jiao

School of Electrical and Computer Engineering

Approved by:

Dr. Dimitrios Peroulis

Head of Electrical and Computer Engineering

ACKNOWLEDGMENTS

I would like to thank my major advisor, Professor Steven Pekarek, with the utmost sincerity. I would not have entered nor come this far in my graduate studies were it not for his support, guidance and patience. I would also like to thank Professors Sudhoff, Aliprantis, Jiao and Wasynczuk, as they were all contributors to my education in the power and energy field. Next, I would like to acknowledge the many friendly coworkers in the Purdue Power Engineering research group. This group is among the greatest assets of Purdue ECE. I would also like to thank my parents, for their love and for their support of my intellectual pursuits. Finally, I would like to thank my wife, Sally for her love, support and patience during my graduate studies.

TABLE OF CONTENTS

	Page
LIST OF TABLES	vii
LIST OF FIGURES	viii
ABSTRACT	xii
1 INTRODUCTION	1
1.1 Introduction to the Method of Moments	2
1.2 Literature Review	4
2 BACKGROUND	9
2.1 System of Equations	9
2.2 MoM Matrix Elements	12
2.2.1 Point-Matching MoM	13
2.2.2 Galerkin MoM	15
2.3 Nonlinear Materials	18
2.4 Electromagnetic Force	22
2.4.1 Force Exerted on Line Elements by Line Sources	22
2.4.2 Force Exerted on Point(Line) Elements by Line(Point) Sources .	24
2.4.3 Force Exerted on Point Element by Point Source	25
2.5 Calculation of Inductance	25
2.5.1 Definition of Partial Inductance	25
2.5.2 Definition of Free Space Inductance	27
2.5.3 Partial Inductance Expressions	28
3 EXTENDING MOM TO THE ANALYSIS OF ELECTRIC MACHINERY .	32
3.1 Closed-Form Magnetic Field Integral Expressions	32
3.1.1 Calculating \bar{B}_x and \bar{B}_y	33
3.1.2 Calculating \bar{B}_{normal}	37

	Page
3.2 Permanent Magnet Sources	48
3.2.1 Equivalent Free Current Source Method	50
3.2.2 Fixed Magnetization Method	52
3.3 Computing Torque	53
3.3.1 Maxwell Stress Tensor Method	54
3.3.2 Lorentz Torque - Midpoint Approximation Method	55
3.3.3 Lorentz Torque - Analytical Integration Method	55
3.3.4 Comparison of Torque Calculation Methods	58
3.4 Inductance of Distributed Windings	62
3.4.1 Partial Inductance Expressions	63
3.4.2 Distributed Winding Inductance: Example Calculation	65
3.5 Eliminating Redundancy in Material Boundaries	70
3.6 Exploitation of Geometric Periodicity	73
3.6.1 DBOR Reduction for Galerkin Formulations	74
3.6.2 DBOR Reduction for Linear Point Matching Formulations	80
3.6.3 DBOR Reduction for Nonlinear Point Matching Formulations	84
4 DESIGN OF PERMANENT MAGNET SYNCHRONOUS MACHINES	87
4.1 Description of Design Problem	87
4.2 Observation Locations for Machine Design	94
4.3 Optimization Results	96
4.4 Time Comparison with FEA-based model	104
5 HYBRID NONLINEAR MODEL FOR V-SHAPE INTERIOR PMSM	111
5.1 Motivating Nonlinear Analysis	112
5.2 Hybrid Method Description	117
5.2.1 Mesh and Nonlinear Characteristic	117
5.2.2 Matrix Equation	118
5.2.3 Modified Newton-Raphson Algorithm	119
5.3 Comparison of Hybrid Models	121

	Page
5.3.1 All Steel Nonlinear: Model A	123
5.3.2 Nonlinear Rotor Bridges and Full Stator: Model B	129
5.3.3 Nonlinear Rotor Bridges and Stator Teeth: Model C	133
5.3.4 Nonlinear Rotor Bridges Only: Model D	138
5.4 Comparing Computation with FEA	142
5.5 Discussion	142
6 SUMMARY AND CONCLUSIONS	145
6.1 Suggested Future Work	145
REFERENCES	148
A ANALYTICAL EVALUATION OF TORQUE INTEGRAL	152
A.1 Third Integral Term	153
A.2 Fourth Integral Term	164
A.3 Combining Integral Terms	169
B MESH GENERATION	180
VITA	182

LIST OF TABLES

Table	Page
4.1 Design Specifications	89
4.2 Degrees of freedom in design	90
4.3 Design Constraints	92
4.4 Design 50 Parameters	102
4.5 Design 50 Conductor Density	103
4.6 CPU Time Breakdown of MoM Field Analysis	104
4.7 CPU Time Breakdown of MATLAB-based FEA	109
5.1 Comparison Conditions “OP 1” and Parameters for “Design 284” [49] . .	124
5.2 Computational Performance Comparison - All Steel Nonlinear	128
5.3 Computational Performance Comparison - Rotor Bridges and Stator Non-linear	132
5.4 Computational Performance Comparison - Rotor Bridges and Stator Teeth Nonlinear	137
5.5 Computational Performance Comparison - Only Rotor Bridges Nonlinear	141
5.6 CPU Time Breakdown of MATLAB-based FEA of IPM Machine	144

LIST OF FIGURES

Figure	Page
2.1 Example of mesh requirements in representative inductor.	10
2.2 Geometry used to establish \mathbf{f}_{BI} entries in the Point Matching formulation.	14
2.3 Geometry used to establish \mathbf{f}_{BI_f} entries in Galerkin formulation.	15
2.4 Geometry used to establish \mathbf{f}_{BI} entries in the Galerkin formulation.	17
2.5 Geometry used to establish \mathbf{f}_{BI} entries in the Point Matching formulation.	18
2.6 Force/torque (a) on \mathbf{p}_2 by \mathbf{l}_1 and (b) on \mathbf{l}_2 by \mathbf{p}_1	24
2.7 Current loops divided into segments.	26
2.8 Simple bar electromagnet.	28
2.9 Reference frame of sheet partial inductance calculation.	29
3.1 Geometry used to establish magnetic field integrals.	33
3.2 Coincident elements case for \bar{B}_\perp	42
3.3 Source intersecting with observation, split at intersection point.	44
3.4 Hysteretic relationship between B and H in permanent magnet materials.	49
3.5 Torque waveforms over one slot pitch at high mesh resolution.	60
3.6 Percent error in average torque calculation, compared with converged FEA solution.	61
3.7 Percent error in peak-peak torque calculation, compared with converged FEA solution.	61
3.8 Distributed windings in stator.	62
3.9 Sheet and point in original global reference frame (a) and reference frame of $L_{pm, }$ (b).	63
3.10 as winding self inductance vs rotor position.	68
3.11 $as-bs$ mutual inductance vs rotor position.	69
3.12 Inductances L_d and L_q vs rotor position.	69
3.13 Material boundary with redundant elements.	71

Figure	Page
3.14 Example geometry of boundary between magnetizeable materials.	71
4.1 Machine parameter definitions.	91
4.2 Magnetic field observation locations within machine cross section.	95
4.3 Pareto-optimal front of Design Study 1.	97
4.4 Cross section of Design 50.	98
4.5 Flux density waveforms in teeth and backiron, zero stator current - PM flux only.	98
4.6 Flux density waveforms in teeth and backiron, rated stator current.	99
4.7 Flux density waveforms in teeth and backiron, saturating conditions.	99
4.8 Torque waveform over two slot pitches in Design 50.	100
4.9 Comparison of Pareto-optimal Fronts, Torque Ripple Constrained.	101
4.10 MATLAB FEA of SPM machine: mesh (a) and zoomed mesh, with flux lines (b).	107
4.11 MATLAB FEA: Tooth and Yoke flux density waveforms.	107
4.12 MATLAB FEA: Torque waveforms.	108
5.1 Diagram of rotor geometry in IPM machine.	112
5.2 Linear MoM model of IPM machine: Single pole mesh of IPM machine; 8414 elements per pole.	114
5.3 Linear MoM model of IPM machine: Flux density vs rotor position com- parison in (a) tooth 1 and (b) yoke 1.	114
5.4 Linear MoM model of IPM machine: Airgap flux density comparison at $\theta_{rm} = 0$ of (a) ρ component and (b) ϕ component.	115
5.5 Linear MoM model of IPM machine: Torque vs rotor position.	115
5.6 Linear MoM model of IPM machine: Convergence of torque calculations at $\theta_{rm} = 0.0654$ rad.	116
5.7 Hybrid MoM mesh: linear/nonlinear elements occupying separate domains (a) and in superposition(b).	117
5.8 Flow chart for selective relax N-R process.	122
5.9 Hybrid MoM model of IPM machine: low (a) and high (b) mesh resolution cases - all steel nonlinear NL.	125

Figure	Page
5.10 Hybrid MoM model of IPM machine: low (a) and high (b) mesh resolution cases - all steel nonlinear (zoomed view of bridge/teeth).	126
5.11 Hybrid MoM model of IPM machine: Magnetic field vs rotor position in stator tooth 1 in low (a) and high (b) mesh resolution cases - all steel nonlinear.	126
5.12 Hybrid MoM model of IPM machine: Magnetic field vs rotor position in stator yoke 1 in low (a) and high (b) mesh resolution cases - all steel nonlinear.	127
5.13 Hybrid MoM model of IPM machine: Torque vs rotor position in stator tooth 1 in low (a) and high (b) mesh resolution cases - all steel nonlinear.	127
5.14 Hybrid MoM model of IPM machine: low (a) and high (b) mesh resolution cases - rotor bridges and stator NL.	130
5.15 Hybrid MoM model of IPM machine: low (a) and high (b) mesh resolution cases - rotor bridges and stator NL (zoomed view of bridge/teeth). . . .	130
5.16 Hybrid MoM model of IPM machine: Magnetic field vs rotor position in stator tooth 1 in low (a) and high (b) mesh resolution cases - rotor bridges and stator NL.	131
5.17 Hybrid MoM model of IPM machine: Magnetic field vs rotor position in stator yoke 1 in low (a) and high (b) mesh resolution cases - rotor bridges and stator NL.	131
5.18 Hybrid MoM model of IPM machine: Torque vs rotor position in stator tooth 1 in low (a) and high (b) mesh resolution cases - rotor bridges and stator NL.	132
5.19 Hybrid MoM model of IPM machine: low (a) and high (b) mesh resolution cases - only rotor bridges and stator teeth NL.	134
5.20 Hybrid MoM model of IPM machine: low (a) and high (b) mesh resolution cases - only rotor bridges and stator teeth NL (zoomed view of bridge/teeth).	134
5.21 Hybrid MoM model of IPM machine: Magnetic field vs rotor position in stator tooth 1 in low (a) and high (b) mesh resolution cases - only rotor bridges and stator teeth NL.	135
5.22 Hybrid MoM model of IPM machine: Magnetic field vs rotor position in stator yoke 1 in low (a) and high (b) mesh resolution cases - only rotor bridges and stator teeth NL.	135

Figure	Page
5.23 Hybrid MoM model of IPM machine: Torque vs rotor position in stator tooth 1 in low (a) and high (b) mesh resolution cases - only rotor bridges and stator teeth NL.	136
5.24 Hybrid MoM model of IPM machine: low (a) and high (b) mesh resolution cases - only rotor bridges NL.	139
5.25 Hybrid MoM model of IPM machine: low (a) and high (b) mesh resolution cases - only rotor bridges NL (zoomed view of bridge/teeth).	139
5.26 Hybrid MoM model of IPM machine: Magnetic field vs rotor position in stator tooth 1 in low (a) and high (b) mesh resolution cases - only rotor bridges NL.	140
5.27 Hybrid MoM model of IPM machine: Magnetic field vs rotor position in stator yoke 1 in low (a) and high (b) mesh resolution cases - only rotor bridges NL.	140
5.28 Hybrid MoM model of IPM machine: Torque vs rotor position in stator tooth 1 in low (a) and high (b) mesh resolution cases - only rotor bridges NL.	141
5.29 MATLAB FEA of IPM machine: zoomed in mesh with flux lines.	143
5.30 MATLAB FEA of IPM: Torque waveforms.	143
5.31 MATLAB FEA of IPM machine: flux waveform density in teeth (a) and backiron (b).	144
B.1 Mesh element orientation.	180
B.2 Example of linearly- and logarithmically- spaced nodes.	181

ABSTRACT

Horvath, Daniel C. Ph.D., Purdue University, August 2019. Analysis and Design of Electric Machines Using 2D Method of Moments. Major Professor: Steven D. Pekarek.

Recently, researchers have pointed their attention toward Method of Moments (MoM)-based approaches to model low frequency magnetic devices (i.e. transformers and inductors). This has been prompted by the use of population-based design (PBD) methods wherein the performance of large numbers (on the order of millions) of candidate designs must be evaluated. MoM is attractive for such problems due to the fact that only the magnetic material is discretized. In addition, for the case in which the magnetic material is linear, only a surface mesh is required. In this research, point-matching and Galerkin-based MoM formulations are utilized for the design of electric machinery. In the formulations considered, the model inputs are the free currents of machine windings and the bound currents of permanent magnets. The unknowns are the magnetizations within the magnetic material which are used to compute winding inductance, electromagnetic torque, and core loss.

The proposed Galerkin formulation has been utilized in the PBD of a surface-mount permanent magnet machine with favorable results. Specifically, it is shown that a machine's performance can be evaluated on a time scale expected of a practical design tool. This is achieved in part through judicious exploitation of the periodic structure and excitation of machines to reduce the size of the system matrix. It is shown how the exploitation of periodic structure may be extended to the point-matching formulation for use in nonlinear analyses. Finally, alternative hybrid approaches that combine surface and volume meshing are explored for the analysis of

an internal permanent magnet machine. It is shown that such a combination holds promise as a tool for rapid evaluation of machine performance.

1. INTRODUCTION

Modeling tools available to the electric machine designer typically exhibit a tradeoff between accuracy and computational expense. On one end of the spectrum, lumped parameter models offer rapid prediction of a machine's performance. However, many assumptions/approximations are made in their derivation, potentially compromising their accuracy. On the other end, methods such as finite element analysis (FEA) provide a numerical solution to the differential equations governing the system. The underlying physics used to derive a finite element model is uncompromised until a relatively simple field variation is assumed (linear field variation for example) within each element of the solution domain. Although accurate, the relatively large element count in this method yields a large system of equations (commonly on the order of 10,000 unknowns for 2D FEA) which is computationally more expensive to form and solve than analytical models.

The Method of Moments (MoM) is an alternative numerical method for solving electromagnetic fields. In contrast to FEA, which is based upon solving differential equations, MoM is based upon solving integral equations. A further distinction between the two methods is that FEA solves for the field *distribution* in the meshed domain whereas MoM solves for the *sources* which create the fields. In the case of linear magnetic materials, these sources reside on the boundary of the magnetic material. In the case of nonlinear magnetic materials, the sources may reside within the active magnetic material. Since no sources may reside in vacuum/air regions, MoM has an advantage that only the active material is meshed. As a result, the number of unknowns can be greatly reduced compared to FEA. Additional advantages include that any combination of polygons can be used to establish the mesh, and the nodes are not required to be coincident. Thus for machine design one can use pre-meshed building blocks and readily assemble them to generate candidate designs.

Furthermore, only a surface mesh is required when the materials are magnetically linear.

MoM has traditionally been utilized in the field of high-frequency computational electromagnetic [1–3], while it has perhaps been under-utilized in low frequency magnetics. The lack of utilization of MoM is likely due to the complexity of integral evaluations needed to populate the MoM system matrix. The integrals have traditionally been evaluated using numerical techniques, leading to significant computational cost especially since MoM system matrices are dense (not sparse) in nature. However, recently in [4] closed form expressions are derived for all integrals required in a Galerkin formulation of 2D magnetostatics problems, which enhances the attractiveness of the method. Herein, a focus is on the MoM, including the foundation of its derivation and a review of the existing state of its use in low frequency magnetics.

1.1 Introduction to the Method of Moments

The Method of Weighted Residuals (MWR) may be used to derive the MoM. A general integro-differential equation may be represented as

$$\mathcal{L}\varphi = f \tag{1.1}$$

where f is a known forcing function, \mathcal{L} represents a linear operator (e.g. a differentiation or integration) and φ is the unknown. Since only the simplest problems can be solved analytically, we resort to numerical methods for problems of practical interest wherein we introduce approximations. The unknown function φ can be represented approximately by $\bar{\varphi}$ using a set of N basis functions scaled by constants:

$$\bar{\varphi} = \sum_{j=1}^N c_j v_j \tag{1.2}$$

where v_j are small support basis functions and c_j are constants which now take on the role of the unknowns in the solution procedure. If using the approximate solution,

some amount of error is expected. This error is termed the “residual” and is defined as

$$\mathcal{R} \triangleq \mathcal{L}\bar{\varphi} - f \quad (1.3)$$

In the MWR, \mathcal{R} is minimized indirectly by weighting it and setting the weighted residual to zero. That is, with the inner product defined as

$$\langle \xi, w \rangle \triangleq \int_{\Omega_0} \xi w d\Omega \quad (1.4)$$

the residual is *weighted* (or *tested*) and set to zero:

$$\langle \mathcal{R}, w \rangle = \int_{\Omega_0} (\mathcal{L}\bar{\varphi} - f) w d\Omega = 0 \quad (1.5)$$

Substituting (1.2) and evaluating (1.5) over the entire solutions domain Ω ,

$$\sum_{n=1}^N c_n \int_{\Omega} w_m \mathcal{L}(v_n) d\Omega = \int_{\Omega} w_m f d\Omega \quad (1.6)$$

Hence, evaluating (1.6) for $m = 1, 2, \dots, N$, yields an equation system.

The choice of different test and basis functions are often utilized to delineate numerical formulations within the literature of computational electromagnetics. There are several options. When test and basis functions are the same, the MWR is called Galerkin’s method.

The MWR may be used to numerically solve differential or integral equations, but in the latter case \mathcal{L} is an integral operator. A MWR in which the weighted residuals are set to zero and which involves an integral operator may be called a “Method of Moments” [2]. According to Harrington [5], the name “Method of Moments” originates from taking the n^{th} moment of continuous function F as

$$\int x^n F(x) dx. \quad (1.7)$$

however this terminology has been kept to describe the case where x^n is replaced with a general weighting function w_n . A final note on the method naming: it is suggested in [6] that the name Method of Moments came about to describe the cases of the MWR in which the test and basis functions are not the same, and the inconsistent usage of the terms MWR and MoM is elaborated further therein.

1.2 Literature Review

Various integral equation methods appear throughout the literature for the quasi-static study of magnetic devices, differing in many aspects. The methods differ in their choice of: method name, integral equation, unknown and testing/basis functions. The use of closed-form expressions to evaluate integrals as opposed to numerically integrating them to populate system matrices is yet another way to categorize the methods. The literature review in [4] extensively discusses many of the integral equation methods employed in modeling low-frequency electromagnetic devices in general, categorized by the choice of unknown in the formulation. That literature review will not be repeated in its entirety herein, however the notable sources that are most similar to the formulations used herein are highlighted.

In chronological order, MoM formulations using magnetization as the unknown are found in [7–10]. The program GFUN is documented in [7] wherein 2D and 3D fields are computed using analytical expressions to populate system matrices, assuming constant magnetization within polygon (2D) elements and triangular or rectangular prisms (3D). The calculations correspond to the field calculation at an observation point. Hence, pulse (delta) basis (testing) functions are used. In [8,9], the program RADIA is described, born out of the need to compute 3D magnetic fields and their integrals in particle accelerators. The 3D magnetostatic field solution is found by solving the unknown magnetizations in discretized iron regions and the influence matrix is populated using analytical expressions. The magnetic field is computed at the center of observation elements due to a polyhedron region with constant magnetization. Hence this amounts again to a point matching scheme using delta test and pulse basis functions. The field prediction matches closely to measurements. The magnetostatic MoM is reviewed in [10]. The magnetic fields in 3D space are computed at the element center due to regions of constant magnetization. Numerical integration is used to populate the system matrices.

A formulation similar to those utilizing magnetization as the unknown is the surface current method (SCM) found in [11]. A compact notation is introduced which represents the x - and y - components together using complex numbers, which also reduces the sizes of system matrices. A closed-form Galerkin expression for pulse bases is presented. An adaptive meshing procedure is presented. Two methods for nonlinear analysis are discussed. The first involves a volume mesh while the second involves sampled points within the active material. The methods are applied in the analysis of two electric machines. Reasonable agreement with FEA is obtained.

The application of various MoM formulations specifically in the analysis of electric machinery is found in [12]. In [12], researchers extend the 2D form of the method first described in [7], a point-matching formulation, to use the auxiliary field as the unknown and develop the method in terms of polar coordinates which aids in the volume mesh generated therein, consisting of radial and tangential lines. The method was used to solve the nonlinear fields in a wound rotor synchronous machine using a modified Newton-Raphson method, converging in 10 or fewer iterations under heavy saturation. Computation times of 20-30 minutes are given, but this must be considered in the context of the computing power available at the time of publication (1988).

The boundary element method (BEM) is an integral equation method related to MoM which has been investigated by several researchers for use in the analysis of low-frequency electromagnetic devices. A review of the use of the BEM to analyze low-frequency electromagnetic devices is provided in [13]. The BEM transforms a differential equation into its equivalent integral equation form through use of Green's functions/integral theorems. Some authors claim the BEM and MoM are equivalent [14] or are so only in certain contexts [15], yet others distinguish one from the other [16, 17]. Indeed, BEM and MoM are both integral equation numerical methods and share the property of having full system matrices but they differ largely in their derivations. In the 2D magnetostatic BEM, the unknown vector is comprised of the vector potential and its normal derivative, thus the system matrix is a tableau

that couples the effects of the two types of unknowns. In contrast, MoM utilizes a single unknown vector in its formulation, thus clearly defining the role of the system matrix – a mapping of currents to field values, affecting a summation of the individual contributions.

In [14] BEM formulations are discussed for 2D magnetostatic and eddy current problems as well as for 3D eddy current problems. In the 2D formulations, the magnetic vector potential is the unknown. The formulations are established via appropriate selection of Green’s function for first the Poisson and then the diffusion equation for static and eddy current problems respectively. A 3D eddy current formulation is described that is formulated in terms of the direct field quantities \mathbf{E} and \mathbf{H} where the unknowns are surface electric and magnetic currents. Only linear magnetic materials are considered, therefore time-harmonic forms are utilized in the eddy current forms of both 2D and 3D. Linear base/testing functions are used in the 2D formulations but the matrix entries are populated using numerically-evaluated integrals. The 2D form is used to evaluate a C-I core actuator and both methods are used to model a simple inductor. Run times are discussed for the 3D formulation only, but are prohibitive to utilization within an optimization loop, as even using the coarsest mesh of a C-I actuator, the solution takes approximately 940 s for a single design.

In [16], BEM formulations are discussed for 2D magnetostatic problems. Therein analytical solutions are derived for all integrals required in the assembly of the system matrix in Galerkin’s method for delta, pulse and linear base/test functions. The dual reciprocity method is evaluated as a means to model nonlinear behaviour in a quasi-meshless fashion. Results match FEA in lightly saturated conditions. A similar result is reported when the method is used for analysis of a wound-rotor synchronous machine in [18].

Since a focus of this research is to explore the feasibility of utilizing MoM within population-based design/optimization, research that documents the use of FEA to evaluate designs within optimizations is of interest in order to make comparisons with total computation times. In [19] researchers set forth two optimizations to maximize

average torque while minimizing pulsating torque in switched reluctance machines. The overall rotor and stator tooth face shapes are degrees of freedom in the optimizations. One of the optimizations is GA-based, evaluating 6400 candidate designs using FEA, meshing the stator and rotor only once for each design and remeshing only the airgap at each rotor position. Torque is computed at 15 rotor positions in each design where parallel processing is utilized to divide the workload. The researchers report a total computation time of 20 hours for magnetically linear materials and approximately 40 hours for magnetically nonlinear materials using programs written in MATLAB.

In [20] researchers detail the so-called “computationally efficient FEA” (CE-FEA) in which the goal is to obtain accurate machine performance information with a minimum number of magnetostatic FEA evaluations, as opposed to using the computationally expensive time stepping FEA. Using the FEA solutions at several rotor positions, flux linkages in the windings and flux densities in each mesh element are computed. Periodicity arguments are invoked allowing the construction of pertinent waveforms over one electrical cycle. A Fourier decomposition of the waveforms is then computed. Subsequently, torque is computed analytically based on expressions utilizing the flux linkage Fourier coefficients as opposed to a numerical torque evaluation such as the Maxwell Stress Tensor (MST) [21], presumably in order to save computation time. Core loss is evaluated using expressions mapping the square of flux density harmonics and its Fourier coefficients to loss densities in each mesh element. In one design study of a fractional-slot concentrated-winding machine, response surfaces are generated over three design parameters. The researchers report that 100 designs may be evaluated in 20 minutes using the program MagNet and the aforementioned Fourier-based post-processing schemes. Each design evaluation required magnetostatic FEA solutions at 5 rotor positions. Comparisons with time-stepping FEA agree well and the researchers report that using time-stepping FEA to produce the same results would require a computation time of approximately 40 hours. Researchers in [22] use CE-FEA to perform an optimization for synchronous reluc-

tance machines with and without permanent magnets. The optimization is performed using differential evolution (DE), an optimization method similar to a genetic algorithm (GA). The researchers report that 10,000 candidate designs were evaluated in “hours.”

2. BACKGROUND

The 2D MoM presented in [4] is briefly summarized to set the stage for the research herein. The derivation in [4] does not start with the statement of the governing differential- or integral-equations; rather it is established based on elementary physics that relates line current to flux density in free space. The method builds on this relationship to accommodate the influence that a magnetic material has on flux density. From these relationships, a system of equations is formed in which unknowns are the magnetization in the elements and the inputs are free current. The modeling of magnetically nonlinear materials is also summarized.

Following the solution of the equation system, the resultant magnetic field and bound/free current distribution may be used to determine other quantities of interest, which is commonly referred to as post-processing. The post-processing steps to compute force and inductance derived in [4] are summarized in this chapter in order to establish the basis for developments in the following chapter.

Keeping with most modern texts [23], [24], the field \mathbf{B} will be referred to as the “magnetic field,” (or sometimes “flux density”) throughout this research and the field \mathbf{H} as the “auxiliary field.” Terms such as “magnetic induction” for \mathbf{B} and “field intensity” for \mathbf{H} are avoided.

2.1 System of Equations

In a MoM formulation in which the system is characterized with linear materials, the material boundary is discretized into edge elements (i.e. a surface mesh). If the relationship between magnetic field and auxiliary field is nonlinear, the material is volume-meshed. An example of the respective discretizations are shown in Figs. 2.1a and 2.1b for a representative inductor. As shown in Figure 2.1, inert regions, including

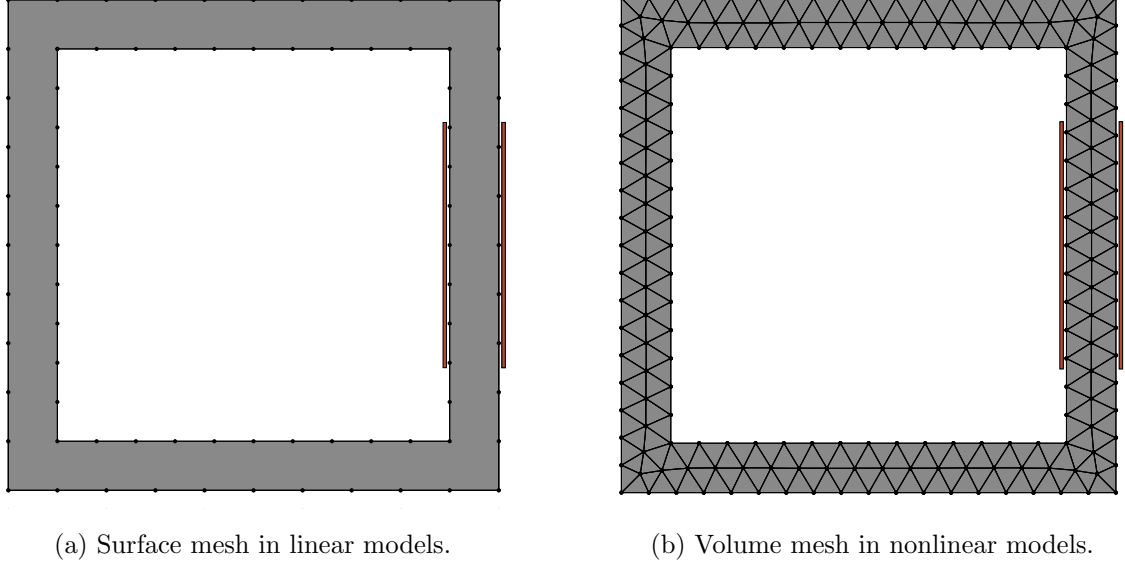


Fig. 2.1.: Example of mesh requirements in representative inductor.

the region inside and surrounding the inductor, are not meshed in the MoM, as there are no sources in inactive regions. In [4], the formulation was derived for static fields where free current is known and the element magnetization is the unknown. A key observation that the formulation [4] hinges on is that the total magnetic field, \mathbf{B}_{tot} , at an arbitrary observation point is the summation of the magnetic field contributions from all sources; namely, free currents I_f and bound currents I_b present in the system. Bound currents exist at the boundary of linear magnetic materials and are found by taking the curl of the magnetization field \mathbf{M} [23]:

$$\nabla \times \mathbf{M} = \mathbf{J}_b \quad (2.1)$$

$$\mathbf{M} \times \hat{n} = \mathbf{K}_b \quad (2.2)$$

where \mathbf{J}_b and \mathbf{K}_b are bound volume and surface current density, respectively and \hat{n} is the outward normal unit vector at the edge of the magnetized region. Only the component of magnetization tangent to the edge element contributes to the bound

current, therefore the unknown in the linear formulation is \mathbf{M}_{tan} . The total magnetic field within an element j can be expressed as

$$\mathbf{B}_{\text{tan,tot}}(j) = \sum_{i=1}^N \mathbf{f}_{BM}(j, i) \mathbf{M}_{\text{tan}}(i) + \sum_{k=1}^{N_f} \mathbf{f}_{BI_f}(j, k) \mathbf{I}_f(k) \quad (2.3)$$

where N is the number of unknown element magnetizations and N_f is the number of free current sources. Within element j the constitutive relation $\mathbf{M}_j = \chi_j \mathbf{H}_j$ is used to algebraically eliminate \mathbf{H} yielding an alternative expression for the total magnetic field:

$$\begin{aligned} \mathbf{B}_{\text{tan,tot}}(j) &= \mu_0(\mathbf{H}_{\text{tan}}(j) + \mathbf{M}_{\text{tan}}(j)) \\ &= \mu_0 \left(\frac{\chi_j + 1}{\chi_j} \right) \mathbf{M}_{\text{tan}}(j) \\ &= \frac{\mu_0 \mu_{r,j}}{\mu_{r,j} - 1} \mathbf{M}_{\text{tan}}(j) \end{aligned} \quad (2.4)$$

where $\mu_{r,j} = \chi_j + 1$. Enforcing equality between (2.3) and (2.4) yields

$$\frac{\mu_0 \mu_{r,j}}{\mu_{r,j} - 1} \mathbf{M}_{\text{tan}}(j) = \sum_{i=1}^N \mathbf{f}_{BM}(j, i) \mathbf{M}_{\text{tan}}(i) + \sum_{k=1}^{N_f} \mathbf{f}_{BI_f}(j, k) \mathbf{I}_f(k) \quad (2.5)$$

Evaluating (2.5) for each element (i.e. for $j = 1 \dots N$) yields a system of equations, written symbolically in matrix form as

$$\mathbf{f}_{B_{\text{tot}}M} \mathbf{M}_{\text{tan}} = \mathbf{f}_{BM} \mathbf{M}_{\text{tan}} + \mathbf{f}_{BI_f} \mathbf{I}_f \quad (2.6)$$

that can be expressed in a form:

$$[\mathbf{f}_{B_{\text{tot}}M} - \mathbf{f}_{BM}] \mathbf{M}_{\text{tan}} = \mathbf{f}_{BI_f} \mathbf{I}_f \quad (2.7)$$

It is noted that in this research, MATLAB's backslash operator (otherwise known as "mldivide") is used to solve the linear system of equations, although specialized solvers have been developed for integral equation methods which yield improved computational complexity over generic linear matrix equations solvers [3]. It is also noted that the matrix notation used herein indicates the type of mapping that occurs within

the subscripts. For instance, the matrix $\mathbf{f}_{B_{\text{tot}}}M$ is the matrix which maps the unknown element magnetization M to the total magnetic field B_{tot} .

The system of equations (2.6) is representative of formulations in which any basis and weighting functions are chosen. The following two sections summarize matrix entries for all matrices appearing in (2.6), wherein each subsection utilizes a different basis/testing function choice.

2.2 MoM Matrix Elements

The two formulations utilized herein both assume constant magnetization in the element. Categorizing the two formulations in terms of basis and testing functions, this corresponds to the use of a pulse basis function. By observing the magnetic field at a single point within an element, for example the center point of an element, corresponds to using Dirac delta functions as test functions, referred to as “point matching” [1]. Delta test functions are a common choice due to the relative simplicity encountered when computing their integrals. In contrast, the calculation of the average magnetic field at an observation element corresponds to the use of a pulse test function. Since the test and basis functions are equivalent we refer to this method as a “Galerkin” MoM.

Prior to deriving the expressions used to populate the system matrices, it is helpful to review the expression for the magnetic field resulting from a filamentary current source. A filamentary current source extending infinitely in the \hat{z} direction with magnitude I produces a magnetic field in the x - y plane that is independent of z , at a distance $\mathbf{r} = \langle r_x, r_y \rangle$ away from the current source. The magnetic field is expressed as [23]

$$\mathbf{B}(\mathbf{r}) = \frac{\mu_0 I}{2\pi \|\mathbf{r}\|^2} (-r_y \hat{x} + r_x \hat{y}) \quad (2.8)$$

2.2.1 Point-Matching MoM

The population of all matrices appearing in (2.6), in order of increasing complexity, begins with $\mathbf{f}_{B_{\text{tot}}M}$, which, by the characterization of the magnetic material as in (2.4), is simply a diagonal matrix with dimensions $N \times N$. Entries of $\mathbf{f}_{B_{\text{tot}}M}$ are given by

$$\mathbf{f}_{B_{\text{tot}}M}(i, i) = \frac{\mu_0 \mu_{r,i}}{\mu_{r,i} - 1} M_{\text{tan},i} \quad (2.9)$$

Entries of the $N \times N_f$ matrix \mathbf{f}_{BI_f} require no integration and are found by taking the component of the magnetic field due to an infinite line current tangent to element j :

$$\mathbf{f}_{BI_f}(j, i) = \frac{\mu_0}{2\pi} \left[\frac{-\frac{(y_{j,\text{obs}} - y_{I_f,i})}{(x_{j,\text{cen}} - x_{I_f,i})^2 + (y_{j,\text{obs}} - y_{I_f,i})^2}}{\frac{x_{j,\text{obs}} - x_{I_f,i}}{(x_{j,\text{cen}} - x_{I_f,i})^2 + (y_{j,\text{obs}} - y_{I_f,i})^2}} \right]^T \begin{bmatrix} l_{x,j} \\ l_{y,j} \end{bmatrix} \frac{1}{\|\mathbf{l}_j\|} \quad (2.10)$$

The matrix \mathbf{f}_{BM} is populated by first separating it into the matrix product $\mathbf{f}_{BM} = \mathbf{f}_{BI} \mathbf{f}_{IM}$, where the diagonal matrix \mathbf{f}_{IM} relates the element magnetization vector \mathbf{M}_{tan} to element bound current \mathbf{I}_b . Since the magnitude of bound current density is the ratio of element current and element length:

$$\|\mathbf{K}_{b,i}\| = \frac{I_{b,i}}{l_i} \quad (2.11)$$

then by (2.2),

$$\mathbf{K}_{b,i} = \mathbf{M}_{\text{tan},i} \times \hat{n}_i = -\|\mathbf{M}_{\text{tan},i}\| = -\hat{z} \frac{I_{b,i}}{l_i} \quad (2.12)$$

and therefore $\mathbf{I}_b = \mathbf{f}_{IM} \mathbf{M}_{\text{tan}}$ where the $N \times N$ diagonal matrix entries $\mathbf{f}_{IM}(i, i) = -l_i$. Entries in the $N \times N$ matrix \mathbf{f}_{BI} are found by integrating the magnetic field at the observation location j , denoted $(x_{j,\text{obs}}, y_{j,\text{obs}})$ due to a finite sheet current in source element i . The components of (2.8) are integrated along the length of the observation element

$$\mathbf{B}'_{j,i} = \left\langle B'_{j,i,x}, B'_{j,i,y} \right\rangle = \int_0^{x'_{i,2}} \mathbf{B}'_i(\mathbf{r}'(t)) dt \quad (2.13)$$

The integration setup is illustrated in Figure 2.2. The primed quantities indicate a reference frame in which the source element i is collinear with the x' -axis and its first

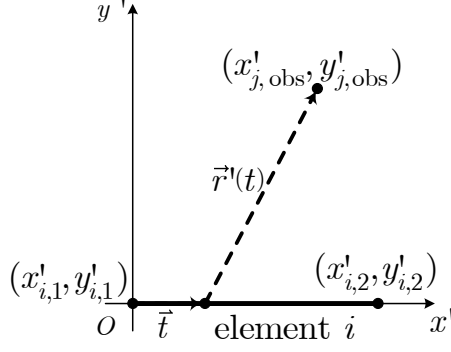


Fig. 2.2.: Geometry used to establish \mathbf{f}_{BI} entries in the Point Matching formulation.

point coincident with the origin as shown in Figure 2.2. In this reference frame, the x and y components of the magnetic field are

$$\begin{aligned} B'_{j,i,x} &= f'_{j,i,x} \mathbf{I}_b(i) \\ &= -\frac{\mu_0}{2\pi x'_{i,2}} \left(\arctan \left(\frac{x'_{i,2} - x'_{j,obs}}{y'_{j,obs}} \right) - \arctan \left(\frac{-x'_{j,obs}}{y'_{j,obs}} \right) \right) \mathbf{I}_b(i) \end{aligned} \quad (2.14)$$

$$\begin{aligned} B'_{j,i,y} &= f'_{j,i,y} \mathbf{I}_b(i) \\ &= -\frac{\mu_0}{4\pi x'_{i,2}} \ln \left(\frac{(x'_{i,2} - x'_{j,obs})^2 + y'^2_{j,obs}}{x'^2_{j,obs} + y'^2_{j,obs}} \right) \mathbf{I}_b(i) \end{aligned} \quad (2.15)$$

Rotating to the global system of coordinates yields the matrix entries

$$\begin{bmatrix} f_{j,i,x} \\ f_{j,i,y} \end{bmatrix} = \begin{bmatrix} \cos(\phi_i) & -\sin(\phi_i) \\ \sin(\phi_i) & \cos(\phi_i) \end{bmatrix} \begin{bmatrix} f'_{j,i,x} \\ f'_{j,i,y} \end{bmatrix} \quad (2.16)$$

where ϕ_i is the angle initially used to perform the integration in the reference frame of the source element i . Taking the component tangent to the observation element yields:

$$\mathbf{f}_{BI_b}(j, i) = \begin{bmatrix} f_{j,i,x} & f_{j,i,y} \end{bmatrix} \begin{bmatrix} l_{x,j} \\ l_{y,j} \end{bmatrix} \frac{1}{\|\mathbf{l}_j\|} \quad (2.17)$$

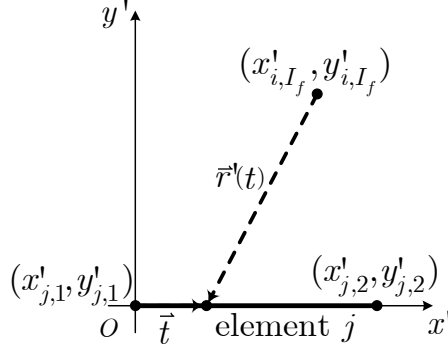


Fig. 2.3.: Geometry used to establish \mathbf{f}_{BI_f} entries in Galerkin formulation.

This subsection highlighted the point-matching formulation derived in [4], wherein it was shown that inaccuracy is encountered when using materials with high magnetic permeability with geometries whose magnetic circuit include a large airgap. Another such linear point matching formulation in [4] utilized a volume mesh in the interior of the active material wherein the observation location is the centroid of each triangular mesh element. This formulation has similar accuracy to a Galerkin formulation, presented in the next subsection, but requires a greater unknown count due to the volume mesh. Since the derivation in this section is readily applied to a volume mesh, it will be utilized for analysis of nonlinear analysis in the following section.

2.2.2 Galerkin MoM

This section describes the matrix entries in the case in which both the basis and weighting functions of unknown elements are pulse bases, which is termed a Galerkin formulation. As discussed earlier in this Chapter, the Galerkin solution has improved accuracy over the point-matching formulation. The terms in $\mathbf{f}_{B_{\text{tot}}M}$ remain unchanged from (2.9). In the case that the free current $I_f(i)$ is a filament, the corresponding

column of the $N \times N_f$ matrix \mathbf{f}_{BI_f} has entries determined by integrating the magnetic field tangent to the observation element j due to filament source i :

$$\bar{B}'_{j,i} = \frac{1}{x'_{j,2}} \int_0^{x'_{i,2}} \mathbf{B}'_{\tan,i}(\mathbf{r}'(t)) dt \quad (2.18)$$

The integration is performed in the reference frame of the observation element [4], which is indicated using the prime symbol. In this reference frame, the first node of the observation element is coincident with the origin and the observation element lies along the x -axis, as shown in Figure 2.3. Within Figure 2.3 the filamentary current with magnitude $I_f(i)$ is located at point (x'_{i,I_f}, y'_{i,I_f}) in a direction out of the page. The closed form solution to (2.18) is [25]:

$$\begin{aligned} \bar{B}'_{j,i} &= \mathbf{f}_{BI_f}(j,i) \mathbf{I}_f(i) \\ &= \frac{\mu_0}{2\pi l_j} \left(\tan^{-1} \left(\frac{x'_{2,j} - x'_{I_f,i}}{y'_{I_f,i}} \right) - \tan^{-1} \left(-\frac{x'_{I_f,i}}{y'_{I_f,i}} \right) \right) \mathbf{I}_f(i) \end{aligned} \quad (2.19)$$

In the case in which free current $I_f(i)$ is a sheet current, an alternative expression is required to populate the corresponding column, a description of which is provided next.

The matrix \mathbf{f}_{BM} is populated by first expressing it in terms of its components $\mathbf{f}_{BM} = \mathbf{f}_{BI} \mathbf{f}_{IM}$. The diagonal matrix \mathbf{f}_{IM} relates the element magnetization vector \mathbf{M}_{\tan} to element bound current, i.e. $\mathbf{I}_b = \mathbf{f}_{IM} \mathbf{M}_{\tan}$. Then, identical to the point matching formulation, $\mathbf{f}_{IM}(i,i) = -l_i$. The matrix \mathbf{f}_{BI} then relates the bound currents I_b to the magnetic fields they produce at the locations of all other bound current elements. Since both source and observation bound current elements are finite sheet currents in the Galerkin formulation, the bound current density in the source element is uniform along its length. Such a source/observation pair ($\mathbf{l}_1/\mathbf{l}_2$) is depicted in Figure 2.4. Likewise, we are now interested in observing the magnetic field due to the sheet current source (itself the result of an integration) not at a single point, but along the entire observation element, in the average sense. Therefore it is necessary to integrate the magnetic field a second time - this time along the observation element.

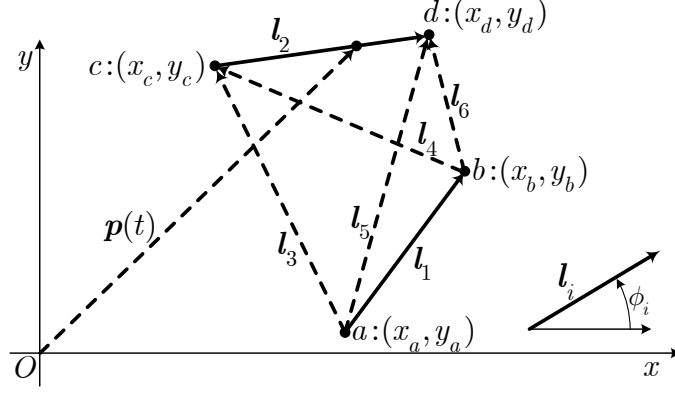


Fig. 2.4.: Geometry used to establish \mathbf{f}_{BI} entries in the Galerkin formulation.

The following is a summary of analytical solutions to this double integral, derived in [4].

$$\mathbf{f}_{BI}(j, i) = -\frac{\mu_0}{2\pi l_2 l_1^2} \begin{pmatrix} \mathbf{l}_1 \cdot \mathbf{l}_2 \text{atan2}^*(\mathbf{l}_5 \times_2 \mathbf{l}_6, \mathbf{l}_5 \cdot \mathbf{l}_6) \\ +\mathbf{l}_1 \cdot \mathbf{l}_3 \text{atan2}^*(\mathbf{l}_5 \times_2 \mathbf{l}_3, \mathbf{l}_5 \cdot \mathbf{l}_3) \\ +\mathbf{l}_1 \cdot \mathbf{l}_4 \text{atan2}^*(\mathbf{l}_4 \times_2 \mathbf{l}_6, \mathbf{l}_4 \cdot \mathbf{l}_6) \\ +\mathbf{l}_1 \times_2 \mathbf{l}_2 \ln^*(l_6/l_5) \\ +\mathbf{l}_1 \times_2 \mathbf{l}_3 \ln^*(l_3/l_5) \\ +\mathbf{l}_1 \times_2 \mathbf{l}_4 \ln^*(l_6/l_4) \end{pmatrix} \quad (2.20)$$

where

$$\text{atan2}^*(\alpha, \beta) = \begin{cases} \frac{\pi}{2} & \alpha = \beta = 0 \\ \text{atan2}(\alpha, \beta) & \text{else} \end{cases} \quad (2.21)$$

$$\ln^*(\alpha) = \begin{cases} 0 & \alpha = 0, \alpha \rightarrow \infty \\ \ln^*(\alpha) & \text{else} \end{cases} \quad (2.22)$$

Several notes are in order regarding (2.20) - (2.22). In (2.20) the operator \times_2 is the scalar form of the cross product for vector arguments both in the same 2D plane. Source element i corresponds to the vector \mathbf{l}_1 while observation element j corresponds

to the vector \mathbf{l}_2 . From \mathbf{l}_1 and \mathbf{l}_2 , the vectors $\mathbf{l}_3 - \mathbf{l}_6$ are defined as shown in Figure 2.4, which define the relative positioning of the respective endpoints of \mathbf{l}_1 and \mathbf{l}_2 . Singularities arise in certain cases, such as when elements are adjacent or coincident, and require special attention and analysis of each of the cases [25]. In the coincident element case, $j = i$, or more generally $(\mathbf{l}_3 \rightarrow 0) \wedge (\mathbf{l}_6 \rightarrow 0)$, and the limit of the integral goes to $\mathbf{f}_{BI}(j, i) = -\mu_0/(2/l_2)$. Adjacency occurs when $(\mathbf{l}_3 \rightarrow 0) \oplus (\mathbf{l}_4 \rightarrow 0) \oplus (\mathbf{l}_5 \rightarrow 0) \oplus (\mathbf{l}_6 \rightarrow 0)$, where \oplus is the exclusive-or logical operation. With the functions atan2^* and \ln^* , the form in (2.20), as is, handles element adjacency singularities effectively when $(\mathbf{l}_3 \rightarrow 0) \oplus (\mathbf{l}_4 \rightarrow 0)$. However when $(\mathbf{l}_5 \rightarrow 0) \oplus (\mathbf{l}_6 \rightarrow 0)$, \mathbf{l}_1 is replaced by $\mathbf{l}_{1,\text{ex}} = -\mathbf{l}_1$ and \mathbf{l}_2 is replaced by $\mathbf{l}_{2,\text{ex}} = -\mathbf{l}_2$. Subsequently $\mathbf{l}_3 - \mathbf{l}_6$ are recomputed using the exchanged endpoints and the negation of (2.20) is used for $\mathbf{f}_{BI}(j, i)$. The expression (2.20) may also be used to populate the column of \mathbf{f}_{BI_f} when free current $I_f(i)$ is a sheet current.

2.3 Nonlinear Materials

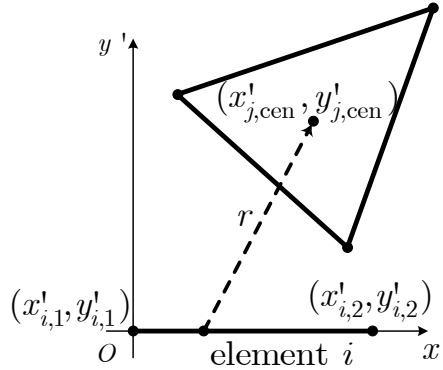


Fig. 2.5.: Geometry used to establish \mathbf{f}_{BI} entries in the Point Matching formulation.

In the case in which a material is characterized by a nonlinear relationship between \mathbf{B} and \mathbf{H} , the MoM formulation described above is altered in two ways. First, the material volume (as opposed to the material edge) must be meshed. Second, the

magnetization within each volume has two vector components (as opposed to simply M_{tan}). In the present example, triangles form the volume mesh, although any polygon, or combination of polygons can be applied. Indeed, 4-sided polygons are utilized in the volume mesh in Chapter 5. Furthermore, the nodes defining the triangle (polygon) vertices do not need to be coincident.

The unknown magnetization vector becomes

$$\mathbf{M}(2i - 1) = M_{x,i} \quad (2.23)$$

$$\mathbf{M}(2i) = M_{y,i} \quad (2.24)$$

Nonlinearity is introduced through $\mathbf{f}_{B_{\text{tot}}M}$, which becomes a function of \mathbf{M} due to the dependence of permeability on magnetization. The system of equations in the nonlinear formulation becomes

$$\mathbf{f}_{B_{\text{tot}}M}(\mathbf{M}) = \mathbf{f}_{BM}\mathbf{M} + \mathbf{f}_{BI_f}I_f \quad (2.25)$$

Hence, entries of $\mathbf{f}_{B_{\text{tot}}M}$ are given by

$$\begin{aligned} \mathbf{f}_{B_{\text{tot}}M}(2i - 1, 2i - 1) &= f_{B_{\text{tot}}M}(\|M_i\|) \frac{M_{x,i}}{\|M_i\|} \\ \mathbf{f}_{B_{\text{tot}}M}(2i, 2i) &= f_{B_{\text{tot}}M}(\|M_i\|) \frac{M_{y,i}}{\|M_i\|} \end{aligned}$$

where the function $f_{B_{\text{tot}}M}(\|M_i\|)$ maps $\|M_i\|$ to $\|B_{\text{tot},i}\|$ using a lookup table with linear interpolation and $\|M_i\| = \sqrt{M_{x,i}^2 + M_{y,i}^2}$.

The matrix \mathbf{f}_{BM} is populated by first separating it into its components $\mathbf{f}_{BM} = \mathbf{f}_{BI_f}\mathbf{f}_{IM}$, where the diagonal matrix \mathbf{f}_{IM} relates the element magnetization vector \mathbf{M} to element bound current \mathbf{I}_b . Since the bound current density is the ratio of side bound current and element length:

$$\mathbf{K}_{b,i,k} = \frac{I_{b,i}(k)}{\|\mathbf{l}_{i,k}\|}, \quad (2.26)$$

then by (2.2)

$$I_{b,i}(k) = \|\mathbf{l}_{i,k}\| \langle M_{x,i}, M_{y,i} \rangle \times \frac{1}{\|\mathbf{l}_{i,k}\|} \langle y_{i,k+1} - y_{i,k}, -(x_{i,k+1} - x_{i,k}) \rangle. \quad (2.27)$$

where $\|\mathbf{l}_{i,k}\|$ is the length of side k of polygon i and is given by

$$\|\mathbf{l}_{i,k}\| = \sqrt{(y_{i,k+1} - y_{i,k})^2 + (x_{i,k+1} - x_{i,k})^2}. \quad (2.28)$$

Utilizing this relationship for each $k \in [1 \dots S_i]$,

$$\mathbf{I}_{b,i}(1 : S_i) = \begin{bmatrix} (x_{i,2} - x_{i,1}) & (y_{i,2} - y_{i,1}) \\ \vdots & \vdots \\ (x_{i,1} - x_{i,S_i}) & (y_{i,1} - y_{i,S_i}) \end{bmatrix} \begin{bmatrix} M_{x,i} \\ M_{y,i} \end{bmatrix} = f_{IM,i} \begin{bmatrix} M_{x,i} \\ M_{y,i} \end{bmatrix} \quad (2.29)$$

Hence \mathbf{f}_{IM} is a $S_i N \times 2N$ block diagonal matrix whose diagonal blocks are $f_{IM,i}$ where S_i is the number of sides of the polygon. The nonlinear solution is found by first arranging the system of equations into the nonlinear residual form (not to be confused with the residual associated with the MWR):

$$\mathbf{g}(\mathbf{M}) = \mathbf{f}_{BM}\mathbf{M} + \mathbf{f}_{BI_f}\mathbf{I}_f - \mathbf{f}_{B_{\text{tot}}M}(\mathbf{M}). \quad (2.30)$$

Subsequently, any one of a number of nonlinear solvers can be applied. In this research, a Newton-Raphson (N-R) procedure has been applied in which the goal is to determine a magnetization vector \mathbf{M}^* such that $\mathbf{g}(\mathbf{M}^*) = \mathbf{0}$. The N-R procedure iterates on the solution according to the rule

$$\mathbf{x}^{k+1} = \mathbf{x}^k - \mathbf{J}(\mathbf{x}^k)^{-1} \mathbf{g}(\mathbf{x}^k) \quad (2.31)$$

where $\mathbf{x} = \mathbf{M}$ and the Jacobian matrix $\mathbf{J}(\mathbf{x})$ is given by

$$\mathbf{J} = \frac{\partial \mathbf{g}}{\partial \mathbf{x}} \quad (2.32)$$

$$= \begin{bmatrix} \frac{\partial g_1}{\partial x_1} & \frac{\partial g_1}{\partial x_2} & \cdots & \frac{\partial g_1}{\partial x_N} \\ \frac{\partial g_2}{\partial x_1} & \frac{\partial g_2}{\partial x_2} & \cdots & \frac{\partial g_2}{\partial x_N} \\ \vdots & \vdots & \ddots & \vdots \\ \frac{\partial g_N}{\partial x_1} & \frac{\partial g_N}{\partial x_2} & \cdots & \frac{\partial g_N}{\partial x_N} \end{bmatrix} \quad (2.33)$$

The Jacobian matrix entries are found by differentiating (2.30):

$$\frac{\partial}{\partial \mathbf{x}} \mathbf{g}(\mathbf{x}) = \frac{\partial}{\partial \mathbf{M}} \mathbf{g}(\mathbf{M}) = \mathbf{f}_{BM} - \frac{\partial}{\partial \mathbf{M}} \mathbf{f}_{B_{\text{tot}}M}(\mathbf{M}) \quad (2.34)$$

Substituting (2.26) into (2.34), the entries in the last term of (2.34) are

$$\begin{aligned}
\frac{\partial}{\partial \mathbf{M}} \mathbf{f}_{B_{\text{tot}} M}(\mathbf{M})(2i-1, 2i-1) &= \frac{d}{dM_{x,i}} f_{B_{\text{tot}} M}(\|M_i\|) \frac{M_{x,i}}{\|M_i\|} \\
\frac{\partial}{\partial \mathbf{M}} \mathbf{f}_{B_{\text{tot}} M}(\mathbf{M})(2i-1, 2i) &= \frac{d}{dM_{y,i}} f_{B_{\text{tot}} M}(\|M_i\|) \frac{M_{x,i}}{\|M_i\|} \\
\frac{\partial}{\partial \mathbf{M}} \mathbf{f}_{B_{\text{tot}} M}(\mathbf{M})(2i, 2i-1) &= \frac{d}{dM_{x,i}} f_{B_{\text{tot}} M}(\|M_i\|) \frac{M_{y,i}}{\|M_i\|} \\
\frac{\partial}{\partial \mathbf{M}} \mathbf{f}_{B_{\text{tot}} M}(\mathbf{M})(2i, 2i) &= \frac{d}{dM_{y,i}} f_{B_{\text{tot}} M}(\|M_i\|) \frac{M_{y,i}}{\|M_i\|} \\
\frac{\partial}{\partial \mathbf{M}} \mathbf{f}_{B_{\text{tot}} M}(\mathbf{M})(\text{else}) &= 0
\end{aligned} \tag{2.35}$$

Evaluating the derivatives in (2.35) yields

$$\begin{aligned}
\frac{d}{dM_{x,i}} f_{B_{\text{tot}} M}(\|M_i\|) \frac{M_{x,i}}{\|M_i\|} &= \frac{M_{x,i}^2}{\|M_i\|^2} f'_{B_{\text{tot}} M}(\|M_i\|) + \frac{M_{y,i}^2}{\|M_i\|^3} f_{B_{\text{tot}} M}(\|M_i\|) \\
\frac{d}{dM_{y,i}} f_{B_{\text{tot}} M}(\|M_i\|) \frac{M_{x,i}}{\|M_i\|} &= \frac{M_{x,i} M_{y,i}}{\|M_i\|^2} f'_{B_{\text{tot}} M}(\|M_i\|) - \frac{M_{x,i} M_{y,i}}{\|M_i\|^3} f_{B_{\text{tot}} M}(\|M_i\|) \\
\frac{d}{dM_{x,i}} f_{B_{\text{tot}} M}(\|M_i\|) \frac{M_{y,i}}{\|M_i\|} &= \frac{d}{dM_{y,i}} f_{B_{\text{tot}} M}(\|M_i\|) \frac{M_{x,i}}{\|M_i\|} \\
\frac{d}{dM_{y,i}} f_{B_{\text{tot}} M}(\|M_i\|) \frac{M_{y,i}}{\|M_i\|} &= \frac{M_{y,i}^2}{\|M_i\|^2} f'_{B_{\text{tot}} M}(\|M_i\|) + \frac{M_{x,i}^2}{\|M_i\|^3} f_{B_{\text{tot}} M}(\|M_i\|)
\end{aligned} \tag{2.36}$$

Lookup tables for $f_{B_{\text{tot}} M}(\|M_i\|)$ and $f'_{B_{\text{tot}} M}(\|M_i\|)$ terms in (2.36) are required in order to implement the N-R process. The lookup table for $f_{B_{\text{tot}} M}(\|M_i\|)$ is formed by first sampling the continuous function \mathbf{r}_{BM} which represents the ratio between magnetic field (in T) and magnetization (in T) [26]. The sampled M and B are then related by

$$M_{\text{sample}} = \frac{B_{\text{sample}}}{\mu_0 \mathbf{r}_{BM}(B_{\text{sample}})} \tag{2.37}$$

where M_{sample} and B_{sample} are respectively the input and output data of the lookup table. Subsequently the lookup table for $f'_{B_{\text{tot}} M}(\|M_i\|)$ is formed by numerically computing the derivative of the lookup table for $f_{B_{\text{tot}} M}(\|M_i\|)$, i.e. the first order finite difference.

2.4 Electromagnetic Force

Following the solution of (2.6) or (2.30), the free and bound current distributions are fully known, which in turn enables the evaluation of the magnetic field at any point in space. Knowledge of the magnetic field and current enables the calculation of the Lorentz force

$$\mathbf{F} = \mathbf{I} \times \mathbf{B}. \quad (2.38)$$

In the MoM formulation considered herein, currents may either be filaments or sheets, whose 2D cross sections are respectively points and lines. Therefore it is desired to be able to compute the force on: line elements by line sources, line elements by point sources, point elements by line sources and point elements by point sources. One need only to consider the force on each current of the movable member, or the rotor in the case of electric machines, by sources on the stationary member, i.e. the stator. This is true since by Newton's first law, a rigid body can not exert a force on itself.

2.4.1 Force Exerted on Line Elements by Line Sources

The force on observation element \mathbf{l}_2 by source element \mathbf{l}_1 is evaluated by integrating the force on the point $\mathbf{p}(t)$, shown in Fig. 2.4, where t is a variable parameterizing the line segment \mathbf{l}_2 . Source element \mathbf{l}_1 carries current I_1 , distributed uniformly along its length, which creates the magnetic field $\mathbf{B}_1(\mathbf{p})$ at point \mathbf{p} . Observation element \mathbf{l}_2 carries a current I_2 distributed uniformly along its length. In the 2D formulation considered herein, the currents exist only in the \hat{z} direction and hence the magnetic fields exist only in the x - y plane. With I_2 and $\mathbf{B}_1(\mathbf{p})$, the Lorentz force integral is expressed mathematically from (2.38) as

$$\begin{aligned} \mathbf{F}_{||} &= \frac{I_2}{l_2} \int_{\mathbf{l}_2} \hat{z} \times \mathbf{B}_1(\mathbf{p}) d\mathbf{p} \\ &= \frac{I_2}{l_2} \int_0^1 \hat{z} \times \mathbf{B}_1(\mathbf{p}) \left\| \frac{d\mathbf{p}(t)}{dt} \right\| dt \\ &= I_2 \int_0^1 \hat{z} \times \mathbf{B}_1(\mathbf{p}) dt \end{aligned} \quad (2.39)$$

Closed form solutions to this integral were derived in [4] for the x - and y - components of force:

$$F_{x,||} = \frac{\mu_0 I_1 I_2}{2\pi l_1^2 l_2^2} \begin{pmatrix} -l_1 l_2 l_2 \sin(\phi_2 - \phi_2 - \phi_1) \text{atan2}(\mathbf{l}_5 \times_2 \mathbf{l}_6, \mathbf{l}_5 \cdot \mathbf{l}_6) \\ -l_1 l_2 l_3 \sin(\phi_3 - \phi_2 - \phi_1) \text{atan2}(\mathbf{l}_5 \times_2 \mathbf{l}_3, \mathbf{l}_5 \cdot \mathbf{l}_3) \\ -l_1 l_2 l_4 \sin(\phi_4 - \phi_2 - \phi_1) \text{atan2}(\mathbf{l}_4 \times_2 \mathbf{l}_6, \mathbf{l}_4 \cdot \mathbf{l}_6) \\ +l_1 l_2 l_2 \cos(\phi_2 - \phi_2 - \phi_1) \ln(l_6/l_5) \\ +l_1 l_2 l_3 \cos(\phi_3 - \phi_2 - \phi_1) \ln(l_3/l_5) \\ +l_1 l_2 l_4 \cos(\phi_4 - \phi_2 - \phi_1) \ln(l_6/l_4) \end{pmatrix} \quad (2.40)$$

$$F_{y,||} = -\frac{\mu_0 I_1 I_2}{2\pi l_1^2 l_2^2} \begin{pmatrix} l_1 l_2 l_2 \cos(\phi_2 - \phi_2 - \phi_1) \text{atan2}(\mathbf{l}_5 \times_2 \mathbf{l}_6, \mathbf{l}_5 \cdot \mathbf{l}_6) \\ +l_1 l_2 l_3 \cos(\phi_3 - \phi_2 - \phi_1) \text{atan2}(\mathbf{l}_5 \times_2 \mathbf{l}_3, \mathbf{l}_5 \cdot \mathbf{l}_3) \\ +l_1 l_2 l_4 \cos(\phi_4 - \phi_2 - \phi_1) \text{atan2}(\mathbf{l}_4 \times_2 \mathbf{l}_6, \mathbf{l}_4 \cdot \mathbf{l}_6) \\ +l_1 l_2 l_2 \sin(\phi_2 - \phi_2 - \phi_1) \ln(l_6/l_5) \\ +l_1 l_2 l_3 \sin(\phi_3 - \phi_2 - \phi_1) \ln(l_3/l_5) \\ +l_1 l_2 l_4 \sin(\phi_4 - \phi_2 - \phi_1) \ln(l_6/l_4) \end{pmatrix} \quad (2.41)$$

It is noted that the difference $\phi_2 - \phi_2$ appears in several terms of (2.40) and (2.41). Although equal to zero, expressing the difference is useful since one can then generalize the calculation of all the angle difference cosine and sine terms found in (2.40) and (2.41). Specifically, one can show that for a set of vectors given in Cartesian and polar coordinates by:

$$\begin{aligned} \mathbf{l}_\alpha &= \langle x_\alpha, y_\alpha \rangle = \langle l_\alpha \cos \phi_\alpha, l_\alpha \sin \phi_\alpha \rangle \\ \mathbf{l}_\beta &= \langle x_\beta, y_\beta \rangle = \langle l_\beta \cos \phi_\beta, l_\beta \sin \phi_\beta \rangle \\ \mathbf{l}_\gamma &= \langle x_\gamma, y_\gamma \rangle = \langle l_\gamma \cos \phi_\gamma, l_\gamma \sin \phi_\gamma \rangle \end{aligned} \quad (2.42)$$

where each angle ϕ_i and respective vector \mathbf{l}_i is shown in Fig. 2.4, the cosine and sine terms can be solved directly using:

$$\begin{aligned} l_\alpha l_\beta l_\gamma \cos(\phi_\gamma - \phi_\beta - \phi_\alpha) &= \mathbf{l}_\alpha \cdot \langle \mathbf{l}_\beta \cdot \mathbf{l}_\gamma, \mathbf{l}_\beta \times_2 \mathbf{l}_\gamma \rangle \\ &= \begin{pmatrix} x_\alpha x_\beta x_\gamma + x_\alpha y_\beta y_\gamma \\ + y_\alpha x_\beta y_\gamma - y_\alpha y_\beta x_\gamma \end{pmatrix} \end{aligned} \quad (2.43)$$

$$\begin{aligned} l_\alpha l_\beta l_\gamma \sin(\phi_\gamma - \phi_\beta - \phi_\alpha) &= \mathbf{l}_\alpha \times_2 \langle \mathbf{l}_\beta \cdot \mathbf{l}_\gamma, \mathbf{l}_\beta \times_2 \mathbf{l}_\gamma \rangle \\ &= \begin{pmatrix} x_\alpha x_\beta y_\gamma - x_\alpha y_\beta x_\gamma \\ - y_\alpha x_\beta x_\gamma - y_\alpha y_\beta y_\gamma \end{pmatrix}. \end{aligned} \quad (2.44)$$

2.4.2 Force Exerted on Point(Line) Elements by Line(Point) Sources

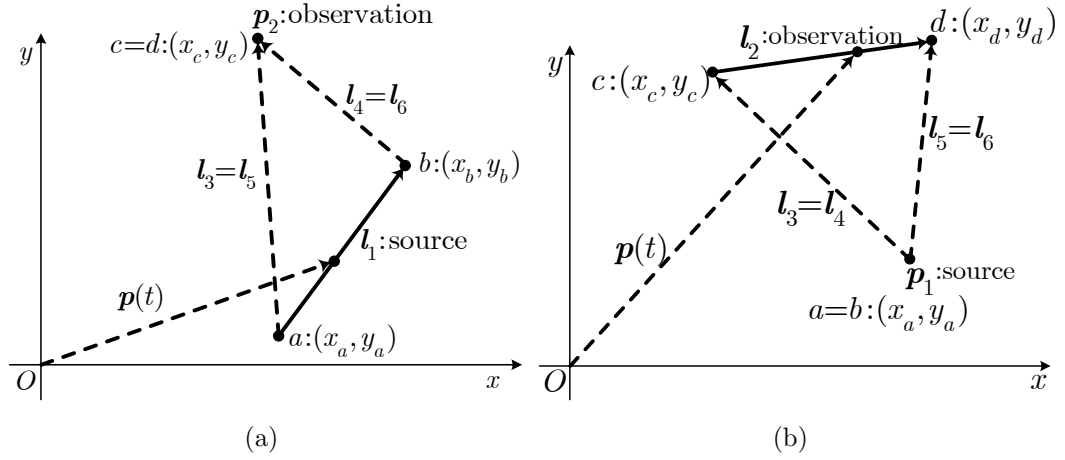


Fig. 2.6.: Force/torque (a) on \mathbf{p}_2 by \mathbf{l}_1 and (b) on \mathbf{l}_2 by \mathbf{p}_1 .

The force exerted on point observation element \mathbf{p}_2 by line source \mathbf{l}_1 , as shown in Fig. 2.6a, is determined using the expressions

$$F_{x,|} = \frac{\mu_0 I_1 I_2}{2\pi l_1} \begin{pmatrix} \sin(\phi_1) \text{atan2}(\mathbf{l}_5 \times_2 \mathbf{l}_6, \mathbf{l}_5 \cdot \mathbf{l}_6) \\ + \cos(\phi_1) \log\left(\frac{l_6}{l_5}\right) \end{pmatrix} \quad (2.45)$$

$$F_{y,|} = -\frac{\mu_0 I_1 I_2}{2\pi l_1} \begin{pmatrix} \cos(\phi_1) \text{atan2}(\mathbf{l}_5 \times_2 \mathbf{l}_6, \mathbf{l}_5 \cdot \mathbf{l}_6) \\ -\sin(\phi_1) \log\left(\frac{l_6}{l_5}\right) \end{pmatrix} \quad (2.46)$$

The force exerted on observation line element \mathbf{l}_2 by point source \mathbf{p}_1 , as shown in Fig. 2.6b, is determined using the expressions

$$F_{x,|} = -\frac{\mu_0 I_1 I_2}{2\pi l_2} \begin{pmatrix} \sin(\phi_2) \text{atan2}(\mathbf{l}_4 \times_2 \mathbf{l}_6, \mathbf{l}_4 \cdot \mathbf{l}_6) \\ +\cos(\phi_2) \log\left(\frac{l_6}{l_4}\right) \end{pmatrix} \quad (2.47)$$

$$F_{y,|} = \frac{\mu_0 I_1 I_2}{2\pi l_2} \begin{pmatrix} \cos(\phi_2) \text{atan2}(\mathbf{l}_4 \times_2 \mathbf{l}_6, \mathbf{l}_4 \cdot \mathbf{l}_6) \\ -\sin(\phi_2) \log\left(\frac{l_6}{l_4}\right) \end{pmatrix} \quad (2.48)$$

where the integration and simplification steps are included in Appendix A.

2.4.3 Force Exerted on Point Element by Point Source

In the case where both source and observation elements are points, the force exerted on point element $\mathbf{p}_2 = (x_c, y_c)$ by point element $\mathbf{p}_1 = (x_a, y_a)$ is determined using

$$F_{x,..} = \frac{\mu_0 I_1 I_2}{2\pi((x_c - x_a)^2 + (y_c - y_a)^2)} (x_a - x_c) \quad (2.49)$$

$$F_{y,..} = \frac{\mu_0 I_1 I_2}{2\pi((x_c - x_a)^2 + (y_c - y_a)^2)} (y_a - y_c) \quad (2.50)$$

2.5 Calculation of Inductance

2.5.1 Definition of Partial Inductance

Before discussing the method for computing inductance detailed in [4], the term partial inductance is described, adapted from the discussion in [27]. Two circuits, each divided into individual segments ①-④, are shown in Figure 2.7. Current i_n in circuit n produces the magnetic field \mathbf{B}_n . Integrating \mathbf{B}_n over the open surface

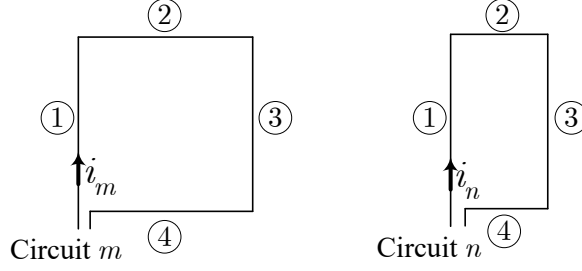


Fig. 2.7.: Current loops divided into segments.

bounded by circuit m allows the mutual inductance between the two circuits to be expressed as

$$L_{mn} = \frac{\int_{S_m} \mathbf{B}_n \cdot d\mathbf{S}_m}{i_n} \quad (2.51)$$

Since $\mathbf{B} = \nabla \times \mathbf{A}$, and using Stoke's theorem, the mutual inductance may be expressed as

$$L_{mn} = \frac{\int_{S_m} (\nabla \times \mathbf{A}_n) \cdot d\mathbf{S}_m}{i_n} \quad (2.52)$$

$$= \frac{\oint_{C_m} \mathbf{A}_n \cdot d\mathbf{l}_m}{i_n} \quad (2.53)$$

To account for each segment's contribution, the integration is separated into integrals for the individual contours C_1 - C_4 for the respective segments ①-④ of circuit m

$$L_{mn} = \frac{1}{i_n} \left[\int_{C_{m1}} \mathbf{A}_n \cdot d\mathbf{l}_{m1} + \int_{C_{m2}} \mathbf{A}_n \cdot d\mathbf{l}_{m2} + \int_{C_{m3}} \mathbf{A}_n \cdot d\mathbf{l}_{m3} + \int_{C_{m4}} \mathbf{A}_n \cdot d\mathbf{l}_{m4} \right] \quad (2.54)$$

Further dividing the problem, the vector potential \mathbf{A}_n may be separated into components due to each segment of circuit n . For example, the first term in (2.54) may be expanded as

$$\frac{1}{i_n} \int_{C_{m1}} \mathbf{A}_n \cdot d\mathbf{l}_{m1} = \frac{1}{i_n} \int_{C_{m1}} (\mathbf{A}_{n1} + \mathbf{A}_{n2} + \mathbf{A}_{n3} + \mathbf{A}_{n4}) \cdot d\mathbf{l}_{m1} \quad (2.55)$$

Each term in (2.55) corresponds to a partial inductance, expressed as the ratio

$$L_{p,i,j} = \frac{\int_{C_{mi}} \mathbf{A}_{nj} \cdot d\mathbf{l}_{mi}}{i_{nj}} \quad (2.56)$$

Designations such as “self” and “mutual” also serve to describe the partial inductance expressions. Self partial inductances describe the contribution to the vector potential integral (2.56) when the source and path are coincident, or when $m = n$ and $i = j$. Mutual partial inductances describe the contribution to the vector potential integral (2.56) when the source and path are distinct, or when $m \neq n$ or when $m = n$ and $i \neq j$.

2.5.2 Definition of Free Space Inductance

The method for computing inductance detailed in [4] is now presented. Therein, partial inductances were utilized to quantify the contributions to the total magnetic flux that links conductors carrying free currents produced by each of the bound currents. The mutual inductance (2.51) between circuits m and n may be rewritten as

$$L_{mn} = \frac{\lambda_{mn}}{i_n} \quad (2.57)$$

In order to quantify the flux in circuit m due only to circuit n , all other current sources present in the system must be unexcited. Yet, bound currents that establish themselves in a magnetic material in response to the sole excitation source i_n are also contributors to the flux and must be accounted for. To this end, the distinction is made that all other free current sources (i.e. all except i_n) must be unexcited while the fields of bound currents must be included in the linked flux. This can be expressed mathematically as

$$\lambda_{mn} = L_{mn}^{fs} i_n + \sum_{i=1}^N \mathbf{L}_{mi}^{fs} \mathbf{I}_b(i) \quad (2.58)$$

where \mathbf{I}_b is the vector of bound currents in the edge elements and the superscript “ fs ” stands for “free space.” Each of the free space inductances \mathbf{L}_{mi}^{fs} separately maps the flux linking circuit n due to bound current $\mathbf{I}_b(i)$ as if there were only the bound current and circuit n in free space. The free space inductance must be found with all other currents (free *and* bound) set to zero. In (2.58), the term L_{mn}^{fs} is the mutual (or self when $m = n$) inductance of the conductor carrying free current by itself in

free space. As an example, consider the simple bar magnet shown in Figure 2.8. The flux linking the winding defined by free current carrying conductors m and m' may be expressed as

$$\lambda_{mm} = L_{mm}^{fs} i_m + \sum_{i=1}^N L_{mi}^{fs} \mathbf{I}_b(i) \quad (2.59)$$

Using partial inductances, L_{mm}^{fs} , the free space inductance of the winding m and m'

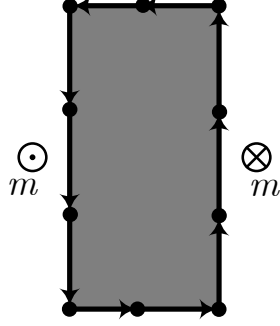


Fig. 2.8.: Simple bar electromagnet.

may be expressed as

$$L_{mm}^{fs} = L_{p,m,m} + L_{p,m,m'} + L_{p,m',m} + L_{p,m',m'} \quad (2.60)$$

The remaining flux linking the winding, i.e. that attributable to the bound currents, is found by determining L_{mi}^{fs} for each bound current indexed by i :

$$L_{mi}^{fs} = L_{p,m,i} + L_{p,m',i} \quad (2.61)$$

It is noted that terms $L_{p,m,m}$ and $L_{p,m',m'}$ are both self partial inductances and $L_{p,m',m}$ and $L_{p,m,m'}$ are both mutual partial inductances.

2.5.3 Partial Inductance Expressions

Considering again the simple bar magnet of Fig. 2.8, and the path integral (2.56), since the direction is the same for the current and integration path in the case of $L_{p,m,m}$

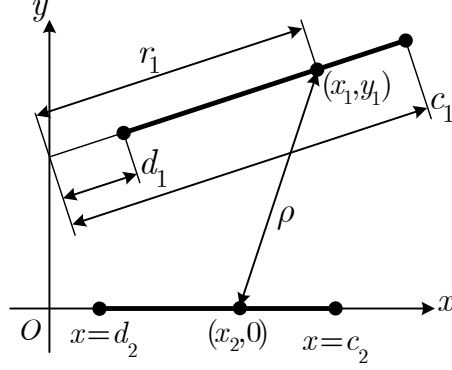


Fig. 2.9.: Reference frame of sheet partial inductance calculation.

and $L_{p,m',m'}$, the dot product in (2.56) has positive sign. Similarly, since the direction is opposite for the current and integration path in the case of $L_{p,m',m}$ and $L_{p,m,m'}$, the dot product in (2.56) has negative sign. In [4], the vector potential produced by a filamentary current, which has negative sign in the expression, is integrated as in (2.56). With the sign convention just considered, the resultant partial inductance between filaments may be expressed as

$$L_{p,i,j,\text{fil}} = \begin{cases} -\frac{\mu_0}{2\pi} \ln \left(\frac{\rho}{\rho_0} \right), & \text{current / path same direction} \\ \frac{\mu_0}{2\pi} \ln \left(\frac{\rho}{\rho_0} \right), & \text{current / path opposite direction} \end{cases} \quad (2.62)$$

where ρ is the distance between the filamentary currents i and j . The constant ρ_0 results from eliminating a diverging term from the integration and it is used to further select an offset that conveniently cancels other offsets in the integral evaluations that follow. This is permissible since the vector potential may have a chosen offset without affecting the magnetic field \mathbf{B} (since $\nabla \times \rho_0 = 0$). Furthermore, it is noted that any constant offset present in a partial inductance expression will always be cancelled in the final inductance result. The partial inductance between two sheets currents is found by integrating the elementary partial inductance expressions along lines

forming the sheet cross sections. The lines are first translated into a reference frame convenient for integration, shown in Fig. 2.9. Subsequently, performing the integral

$$L_{p,i,j} = \frac{1}{w_1 w_2} \int_{d_1}^{c_1} \int_{d_2}^{c_2} L_{i,j,\text{fl}} dx_2 dr_1 \quad (2.63)$$

$$= \frac{1}{w_1 w_2} \int_{d_1}^{c_1} \int_{d_2}^{c_2} \ln \left(\frac{\rho}{\rho_0} \right) dx_2 dr_1 \quad (2.64)$$

$$= \frac{1}{w_1 w_2} \int_{d_1}^{c_1} \int_{d_2}^{c_2} \ln \left((x_2 - c_s r_1)^2 + (s_n r_1 + b_1)^2 \right) dx_2 dr_1, \quad (2.65)$$

where from Fig. 2.9

$$\rho = \sqrt{(x_2 - x_1)^2 + (0 - y_1)^2}, \quad (2.66)$$

yields the following expression for the partial inductance:

$$L_{p,i,j} = -\frac{\mu_0}{4\pi w_1 w_2} \begin{bmatrix} 1 \\ -1 \\ 1 \\ -1 \end{bmatrix}^T \begin{bmatrix} X_1 \cdot (s_n X_1 + 2b_1) \\ \cdot \tan^{-1} \left(\frac{(X_2 - c_s X_1)}{\cdot / (s_n X_1 + b_1)} \right) \\ + (2b_1 c_s X_2 + s_n (X_2 \cdot^2 - b_1^2)) \\ \cdot \tan^{-1} \left(\frac{(X_1 + b_1 s_n - c_s X_2)}{\cdot / (s_n X_2 + b_1 c_s)} \right) \\ + \left(\frac{c_s}{2} (b_1^2 - X_1 \cdot^2 - X_2 \cdot^2) + X_2 \cdot (X_1 + b_1 s_n) \right) \\ \cdot \ln((X_2 - c_s X_1) \cdot^2 + (s_n X_1 + b_1) \cdot^2) \end{bmatrix} \quad (2.67)$$

where the operations using periods mimic the notation used in MATLAB to perform element-wise operations. Before translating into the reference frame of Fig. 2.9, the endpoints of sheet i were $(x_{i,1}, y_{i,1})$ and $(x_{i,2}, y_{i,2})$, and the endpoints of sheet j were $(x_{j,1}, y_{j,1})$ and $(x_{j,2}, y_{j,2})$. The following equation set summarizes the procedure to

translate the sheets into the reference frame and determine the remaining quantities needed to evaluate (2.67):

$$\begin{aligned}
\phi &= \text{atan2}(y_{j2} - y_{j1}, x_{j2} - x_{j1}) \\
\text{temp}_x &= \begin{pmatrix} (x_{i2} - x_{j1}) \cos(-\phi) - (y_{i2} - y_{j1}) \sin(-\phi) \\ -(x_{i1} - x_{j1}) \cos(-\phi) + (y_{i1} - y_{j1}) \sin(-\phi) \end{pmatrix} \\
\text{temp}_y &= \begin{pmatrix} (x_{i2} - x_{j1}) \sin(-\phi) + (y_{i2} - y_{j1}) \cos(-\phi) \\ -(x_{i2} - x_{j1}) \sin(-\phi) - (y_{i2} - y_{j1}) \cos(-\phi) \end{pmatrix} \\
c_1 &= \sqrt{\text{temp}_x^2 + \text{temp}_y^2} \\
d_1 &= 0 \\
c_2 &= \begin{pmatrix} (x_{i2} - x_{j1}) \cos(-\phi) - (y_{i2} - y_{j1}) \sin(-\phi) \\ -(x_{i1} - x_{j1}) \cos(-\phi) + (y_{i1} - y_{j1}) \sin(-\phi) \end{pmatrix} \\
d_2 &= -(x_{i1} - x_{j1}) \cos(-\phi) + (y_{i1} - y_{j1}) \sin(-\phi) \\
w_1 &= c_1 - d_1 \\
w_2 &= c_2 - d_2 \\
b_1 &= (x_{i1} - x_{j1}) \sin(-\phi) + (y_{i1} - y_{j1}) \cos(-\phi) \\
c_s &= \frac{\text{temp}_x}{c_1} \\
s_n &= \frac{\text{temp}_y}{c_1} \\
X_1 &= \begin{bmatrix} c_1 & c_1 & d_1 & d_1 \end{bmatrix}^T \\
X_2 &= \begin{bmatrix} c_2 & d_2 & d_2 & c_2 \end{bmatrix}^T .
\end{aligned} \tag{2.68}$$

3. EXTENDING MOM TO THE ANALYSIS OF ELECTRIC MACHINERY

The preceding chapter forms the basis of the MoM formulations considered herein based on the work of Howard [4], [25], [28]. Extensions from the magnetostatic modeling of general electromagnetic devices to the modeling of electric machinery are derived in this chapter. These include the derivation of closed-form magnetic field integral expressions supplementing those already described, modeling of permanent magnet materials, the calculation of electromagnetic torque, and accounting for the distributed nature of conductors that are placed within stator and rotor slots in the inductance calculation.

In a single PBD run, the MoM-based magnetic field analysis will be conducted many times, potentially millions. Therefore it is important to minimize the computational cost of each instance of the magnetic field analysis - a savings which will compound throughout an optimization run. This chapter also details two techniques which may be used to reduce the number of unknowns in the equation system. One such technique eliminates the redundancy in the boundary mesh between two neighboring magnetic materials by combining into a single meshed boundary. The other technique exploits the periodic nature inherent in the geometry of electric machinery to significantly reduce the size of the system matrix.

3.1 Closed-Form Magnetic Field Integral Expressions

Equation (2.20) in Chapter 2 represents the average tangential magnetic field as a simplified closed form expression. That expression is key to the Galerkin MoM formulation's solution using pulse bases, offering computational performance gains over the numerically computed integral. Similar closed form expressions for the average

x , average y and average normal magnetic field components are useful throughout the machine design process. For example, the additional expressions are needed for determining the average normal magnetic field at observation locations which are not part of the original solution domain such as in, for example, a tooth or backiron cross section. This section establishes such closed-form integral expressions using similar parameterization, integration and simplification steps as detailed in [4].

3.1.1 Calculating \bar{B}_x and \bar{B}_y

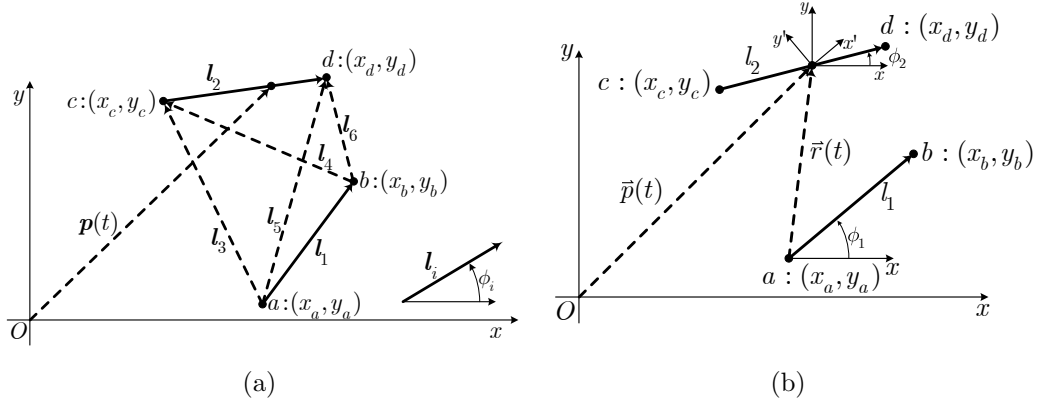


Fig. 3.1.: Geometry used to establish magnetic field integrals.

As shown in Figure 2.4, the magnetic field at point $\mathbf{p}(t)$ on observation element l_2 due to the sheet current in source element l_1 was established by Howard [4] to be

$$\begin{bmatrix} B_{x,s}(\mathbf{p}(t)) \\ B_{y,s}(\mathbf{p}(t)) \end{bmatrix} = \begin{bmatrix} \cos \phi_1 & -\sin \phi_1 \\ \sin \phi_1 & \cos \phi_1 \end{bmatrix} \begin{bmatrix} B'_{x,s}(\mathbf{r}'(t)) \\ B'_{y,s}(\mathbf{r}'(t)) \end{bmatrix} \quad (3.1)$$

where

$$\mathbf{r}(t) = \begin{bmatrix} r_x \\ r_y \end{bmatrix} = \mathbf{p}(t) - \begin{bmatrix} x_a \\ y_a \end{bmatrix} \quad (3.2)$$

$$\begin{aligned}
r'_x(t) &= \cos \phi_1 r_x(t) + \sin \phi_1 r_y(t) \\
&= \cos \phi_1 ((x_d - x_c)t + (x_c - x_a)) + \sin \phi_1 ((y_d - y_c)t + (y_c - y_a))
\end{aligned} \tag{3.3}$$

$$\begin{aligned}
r'_y(t) &= -\sin \phi_1 r_x(t) + \cos \phi_1 r_y(t) \\
&= -\sin \phi_1 ((x_d - x_c)t + (x_c - x_a)) + \cos \phi_1 ((y_d - y_c)t + (y_c - y_a))
\end{aligned} \tag{3.4}$$

$$B'_{x,s}(\mathbf{r}') = \frac{-\mu_0 I_1}{2\pi l_1} \left(\tan^{-1} \left(\frac{l_1 - r'_x}{r'_y} \right) - \tan^{-1} \left(\frac{-r'_x}{r'_y} \right) \right) \tag{3.5}$$

$$B'_{y,s}(\mathbf{r}') = \frac{-\mu_0 I_1}{4\pi l_1} \ln \left(\frac{(l_1 - r'_x)^2 + r'^2_y}{r'^2_x + r'^2_y} \right) \tag{3.6}$$

where the subscript “s” indicates that the field is due to the source, which in this case is the current I_1 distributed uniformly along the length of element \mathbf{l}_1 . Equations (3.5) and (3.6) are established through integration, performed in the reference frame of the source element as indicated by the prime symbol. The source/observation pair is transformed into this reference frame by first translating the pair such that the first endpoint of the source element is coincident with the origin. The source/observation pair is then rotated such that the x' axis is collinear with the the source element.

The average value of the magnetic field is obtained by integrating the magnetic field at $\mathbf{p}(t)$ over observation line element \mathbf{l}_2 and subsequently dividing by its length, l_2 . Performing this integration procedure on the x -component of the magnetic field in (3.1) yields

$$\begin{aligned}
\bar{B}_{x,s} &= \frac{1}{l_2} \int_{l_2} B_{x,s}(\mathbf{p}) dp \\
&= \frac{1}{l_2} \int_0^1 B_{x,s}(\mathbf{p}(t)) \left\| \frac{d}{dt} \mathbf{p}(t) \right\| dt \\
&= \int_0^1 \left(\cos(\phi_1) B'_{x,s}(\mathbf{r}'(t)) - \sin(\phi_1) B'_{y,s}(\mathbf{r}'(t)) \right) dt
\end{aligned} \tag{3.7}$$

where since the domain of \mathbf{l}_2 is described parametrically with the variable $t \in [0, 1]$,

$$\mathbf{p}(t) = \begin{bmatrix} x_d - x_c \\ y_d - y_c \end{bmatrix} t + \begin{bmatrix} x_c \\ y_c \end{bmatrix}, \quad t \in [0, 1], \tag{3.8}$$

then

$$\begin{aligned}
\left\| \frac{d}{dt} \mathbf{p}(t) \right\| &= \left\| \begin{bmatrix} x_d - x_c \\ y_d - y_c \end{bmatrix} \right\| \\
&= \sqrt{(x_d - x_c)^2 + (y_d - y_c)^2} \\
&= l_2.
\end{aligned} \tag{3.9}$$

Closed-form solutions to the integrals in (3.7) were derived in Howard [4] as (H.A.47):

$$\begin{aligned}
\int_0^1 B'_{x,s}(\mathbf{r}') dt &= \frac{-\mu_0 I_1}{2\pi l_1} \int_0^1 \tan^{-1} \left(\frac{l_1 - r'_x(t)}{r'_y(t)} \right) - \tan^{-1} \left(\frac{-r'_x(t)}{r'_y(t)} \right) dt \\
&= \frac{-\mu_0 I_1}{2\pi l_1} \left(\begin{aligned} &\text{atan2}(\mathbf{l}_5 \times_2 \mathbf{l}_6, \mathbf{l}_5 \cdot \mathbf{l}_6) \\ &+ \frac{l_4 \cos(\phi_4 - \phi_2)}{l_2} \text{atan2}(\mathbf{l}_4 \times_2 \mathbf{l}_6, \mathbf{l}_4 \cdot \mathbf{l}_6) \\ &- \frac{l_3 \cos(\phi_3 - \phi_2)}{l_2} \text{atan2}(\mathbf{l}_3 \times_2 \mathbf{l}_5, \mathbf{l}_3 \cdot \mathbf{l}_5) \\ &+ \frac{l_4 \sin(\phi_4 - \phi_2)}{2l_2} \ln \left(\frac{l_6^2}{l_4^2} \right) \\ &- \frac{l_3 \sin(\phi_3 - \phi_2)}{2l_2} \ln \left(\frac{l_5^2}{l_3^2} \right) \end{aligned} \right)
\end{aligned} \tag{3.10}$$

and (H.A.78):

$$\begin{aligned}
\int_0^1 B'_{y,s}(\mathbf{r}') dt &= \frac{-\mu_0 I_1}{4\pi l_1} \int_0^1 \ln \left(\frac{(l_1 - r'_x)^2 + r_y'^2}{r_x'^2 + r_y'^2} \right) dt \\
&= \frac{-\mu_0 I_1}{4\pi l_1} \left(\begin{aligned} &- \frac{2l_4 \sin(\phi_4 - \phi_2)}{l_2} \text{atan2}(\mathbf{l}_4 \times_2 \mathbf{l}_6, \mathbf{l}_4 \cdot \mathbf{l}_6) \\ &+ \frac{2l_3 \sin(\phi_3 - \phi_2)}{l_2} \text{atan2}(\mathbf{l}_3 \times_2 \mathbf{l}_5, \mathbf{l}_3 \cdot \mathbf{l}_5) \\ &+ \frac{l_4 \cos(\phi_4 - \phi_2)}{l_2} \ln \left(\frac{l_6^2}{l_4^2} \right) \\ &- \frac{l_3 \cos(\phi_3 - \phi_2)}{l_2} \ln \left(\frac{l_5^2}{l_3^2} \right) \\ &+ \ln \left(\frac{l_6^2}{l_5^2} \right) \end{aligned} \right)
\end{aligned} \tag{3.11}$$

Substituting (3.10) and (3.11) into (3.7) and collecting terms,

$$\bar{B}_{x,s} = \frac{-\mu_0 I_1}{2\pi l_1 l_2} \left(\begin{aligned} & l_2 \begin{pmatrix} \cos(\phi_1) \cos(\phi_2 - \phi_2) \\ + \sin(\phi_1) \sin(\phi_2 - \phi_2) \end{pmatrix} \text{atan2}(\mathbf{l}_5 \times_2 \mathbf{l}_6, \mathbf{l}_5 \cdot \mathbf{l}_6) \\ & + l_3 \begin{pmatrix} \cos(\phi_1) \cos(\phi_3 - \phi_2) \\ + \sin(\phi_1) \sin(\phi_3 - \phi_2) \end{pmatrix} \text{atan2}(\mathbf{l}_5 \times_2 \mathbf{l}_3, \mathbf{l}_5 \cdot \mathbf{l}_3) \\ & + l_4 \begin{pmatrix} \cos(\phi_1) \cos(\phi_4 - \phi_2) \\ + \sin(\phi_1) \sin(\phi_4 - \phi_2) \end{pmatrix} \text{atan2}(\mathbf{l}_4 \times_2 \mathbf{l}_6, \mathbf{l}_4 \cdot \mathbf{l}_6) \\ & + l_2 \begin{pmatrix} \cos(\phi_1) \sin(\phi_2 - \phi_2) \\ - \sin(\phi_1) \cos(\phi_2 - \phi_2) \end{pmatrix} \ln \left(\frac{l_6}{l_5} \right) \\ & + l_3 \begin{pmatrix} \cos(\phi_1) \sin(\phi_3 - \phi_2) \\ - \sin(\phi_1) \cos(\phi_3 - \phi_2) \end{pmatrix} \ln \left(\frac{l_3}{l_5} \right) \\ & + l_4 \begin{pmatrix} \cos(\phi_1) \sin(\phi_4 - \phi_2) \\ - \sin(\phi_1) \cos(\phi_4 - \phi_2) \end{pmatrix} \ln \left(\frac{l_6}{l_4} \right) \end{aligned} \right) \quad (3.12)$$

where the expressions $\cos(\phi_2 - \phi_2) = 1$ and $\sin(\phi_2 - \phi_2) = 0$ are used in the first and fourth terms in order to have coefficients which follow a pattern. The angle difference formulae are used to simplify the coefficients in (3.12):

$$\bar{B}_{x,s} = \frac{-\mu_0 I_1}{2\pi l_1 l_2} \left(\begin{aligned} & l_2 \cos(\phi_2 - \phi_2 - \phi_1) \text{atan2}(\mathbf{l}_5 \times_2 \mathbf{l}_6, \mathbf{l}_5 \cdot \mathbf{l}_6) \\ & + l_3 \cos(\phi_3 - \phi_2 - \phi_1) \text{atan2}(\mathbf{l}_5 \times_2 \mathbf{l}_3, \mathbf{l}_5 \cdot \mathbf{l}_3) \\ & + l_4 \cos(\phi_4 - \phi_2 - \phi_1) \text{atan2}(\mathbf{l}_4 \times_2 \mathbf{l}_6, \mathbf{l}_4 \cdot \mathbf{l}_6) \\ & + l_2 \sin(\phi_2 - \phi_2 - \phi_1) \ln (l_6/l_5) \\ & + l_3 \sin(\phi_3 - \phi_2 - \phi_1) \ln (l_3/l_5) \\ & + l_4 \sin(\phi_4 - \phi_2 - \phi_1) \ln (l_6/l_4) \end{aligned} \right) \quad (3.13)$$

Multiplying each coefficient in (3.12) by $l_1 l_2$ while factoring $l_1 l_2$ into the denominator:

$$\bar{B}_{x,s} = \frac{-\mu_0 I_1}{2\pi l_1^2 l_2^2} \begin{pmatrix} l_1 l_2 l_2 \cos(\phi_2 - \phi_2 - \phi_1) \text{atan2}(\mathbf{l}_5 \times_2 \mathbf{l}_6, \mathbf{l}_5 \cdot \mathbf{l}_6) \\ + l_1 l_2 l_3 \cos(\phi_3 - \phi_2 - \phi_1) \text{atan2}(\mathbf{l}_5 \times_2 \mathbf{l}_3, \mathbf{l}_5 \cdot \mathbf{l}_3) \\ + l_1 l_2 l_4 \cos(\phi_4 - \phi_2 - \phi_1) \text{atan2}(\mathbf{l}_4 \times_2 \mathbf{l}_6, \mathbf{l}_4 \cdot \mathbf{l}_6) \\ + l_1 l_2 l_2 \sin(\phi_2 - \phi_2 - \phi_1) \ln(l_6/l_5) \\ + l_1 l_2 l_3 \sin(\phi_3 - \phi_2 - \phi_1) \ln(l_3/l_5) \\ + l_1 l_2 l_4 \sin(\phi_4 - \phi_2 - \phi_1) \ln(l_6/l_4) \end{pmatrix} \quad (3.14)$$

A similar procedure is applied to obtain the y -component, yielding

$$\bar{B}_{y,s} = \frac{-\mu_0 I_1}{2\pi l_1^2 l_2^2} \begin{pmatrix} -l_1 l_2 l_2 \sin(\phi_2 - \phi_2 - \phi_1) \text{atan2}(\mathbf{l}_5 \times_2 \mathbf{l}_6, \mathbf{l}_5 \cdot \mathbf{l}_6) \\ -l_1 l_2 l_3 \sin(\phi_3 - \phi_2 - \phi_1) \text{atan2}(\mathbf{l}_5 \times_2 \mathbf{l}_3, \mathbf{l}_5 \cdot \mathbf{l}_3) \\ -l_1 l_2 l_4 \sin(\phi_4 - \phi_2 - \phi_1) \text{atan2}(\mathbf{l}_4 \times_2 \mathbf{l}_6, \mathbf{l}_4 \cdot \mathbf{l}_6) \\ + l_1 l_2 l_2 \cos(\phi_2 - \phi_2 - \phi_1) \ln(l_6/l_5) \\ + l_1 l_2 l_3 \cos(\phi_3 - \phi_2 - \phi_1) \ln(l_3/l_5) \\ + l_1 l_2 l_4 \cos(\phi_4 - \phi_2 - \phi_1) \ln(l_6/l_4) \end{pmatrix} \quad (3.15)$$

the coefficients of (3.14) and (3.15) may be evaluated using dot and cross products relationships (2.43) and (2.44) from the force calculation in 2.4. As an aside, expressions (3.14) and (3.15) appear in the force expressions for $F_{x,\parallel}$ and $F_{y,\parallel}$, and these forces may be interpreted as the average magnetic field multiplied by the current in the observation element.

3.1.2 Calculating \bar{B}_{normal}

Regular Case

In [4] it was shown that the component of the magnetic field at point $\mathbf{p}(t)$ tangent to the observation element is

$$B_{\text{tan},s}(\mathbf{p}(t)) = B_{x,s}(\mathbf{p}(t)) \cos(\phi_2) + B_{y,s}(\mathbf{p}(t)) \sin(\phi_2) \quad (3.16)$$

Therein, the Galerkin MoM matrix entry (2.20) was obtained by integrating (3.16). In a similar fashion, the component of the magnetic field at point $\mathbf{p}(t)$ *normal* to the observation element can be expressed as

$$B_{\perp,s}(\mathbf{p}(t)) = -B_{x,s}(\mathbf{p}(t)) \sin(\phi_2) + B_{y,s}(\mathbf{p}(t)) \cos(\phi_2) \quad (3.17)$$

where the subscript “ \perp ” indicates the normal component and the angles ϕ_1 and ϕ_2 are defined in Figure 3.1b. There are two choices for the normal direction. The direction chosen herein is 90 degrees counter clockwise from \mathbf{l}_2 , corresponding with (3.17). The average normal magnetic field over element \mathbf{l}_2 is then

$$\bar{B}_{\perp,s} = \frac{1}{l_2} \int_{\mathbf{l}_2} B_{\perp,s}(\mathbf{p}) d\mathbf{p} \quad (3.18)$$

This integral is performed by first parameterizing the vector \mathbf{p} in terms of a new variable t which ranges from 0 to 1. Referring to coordinates in Figure 2.4, the integration path can then be described in terms of \mathbf{p} and t as

$$\mathbf{p}(t) = \begin{bmatrix} x_p \\ y_p \end{bmatrix} = \begin{bmatrix} x_d - x_c \\ y_d - y_c \end{bmatrix} t + \begin{bmatrix} x_c \\ y_c \end{bmatrix}, \quad t \in [0, 1] \quad (3.19)$$

The integration can then be expressed as [29]

$$\bar{B}_{\perp,s} = \frac{1}{l_2} \int_0^1 B_{\perp,s}(\mathbf{p}) \left\| \frac{d}{dt} \mathbf{p}(t) \right\| dt \quad (3.20)$$

Since

$$\left\| \frac{d}{dt} \mathbf{p}(t) \right\| = \left\| \begin{bmatrix} x_d - x_c \\ y_d - y_c \end{bmatrix} \right\| = \sqrt{(x_d - x_c)^2 + (y_d - y_c)^2} = l_2 \quad (3.21)$$

the coefficient in front of the integral in (3.20) is cancelled. Now substituting (3.17) and (3.1) into (3.20), we have

$$\bar{B}_{\perp,s} = \int_0^1 \left(- \left(\cos \phi_1 B'_{x,s}(\mathbf{r}'(t)) - \sin \phi_1 B'_{y,s}(\mathbf{r}'(t)) \right) \sin \phi_2 \right. \\ \left. + \left(\sin \phi_1 B'_{x,s}(\mathbf{r}'(t)) + \cos \phi_1 B'_{y,s}(\mathbf{r}'(t)) \right) \cos \phi_2 \right) dt \quad (3.22)$$

The trigonometric coefficients do not depend on t , so they are factored out. Collecting terms, we have

$$\bar{B}_{\perp,s} = \begin{pmatrix} (\sin \phi_1 \cos \phi_2 - \cos \phi_1 \sin \phi_2) \int_0^1 B'_{x,s}(\mathbf{r}'(t)) dt \\ + (\sin \phi_1 \sin \phi_2 + \cos \phi_1 \cos \phi_2) \int_0^1 B'_{y,s}(\mathbf{r}'(t)) dt \end{pmatrix} \quad (3.23)$$

Applying the angle difference formulae,

$$\bar{B}_{\perp,s} = \sin(\phi_1 - \phi_2) \int_0^1 B'_{x,s}(\mathbf{r}'(t)) dt + \cos(\phi_1 - \phi_2) \int_0^1 B'_{y,s}(\mathbf{r}'(t)) dt \quad (3.24)$$

Substituting (3.10) and (3.11),

$$\bar{B}_{\perp,s} = \frac{-\mu_0 I_1}{2\pi l_1} \sin(\phi_1 - \phi_2) \begin{pmatrix} \text{atan2}(\mathbf{l}_5 \times_2 \mathbf{l}_6, \mathbf{l}_5 \cdot \mathbf{l}_6) \\ + \frac{l_4 \sin(\phi_4 - \phi_2)}{2l_2} \ln \left(\frac{l_6^2}{l_4^2} \right) \\ - \frac{l_3 \sin(\phi_3 - \phi_2)}{2l_2} \ln \left(\frac{l_5^2}{l_3^2} \right) \\ + \frac{l_4 \cos(\phi_4 - \phi_2)}{l_2} \text{atan2}(\mathbf{l}_4 \times_2 \mathbf{l}_6, \mathbf{l}_4 \cdot \mathbf{l}_6) \\ - \frac{l_3 \cos(\phi_3 - \phi_2)}{l_2} \text{atan2}(\mathbf{l}_3 \times_2 \mathbf{l}_5, \mathbf{l}_3 \cdot \mathbf{l}_5) \end{pmatrix} \quad (3.25)$$

$$+ \frac{-\mu_0 I_1}{4\pi l_1} \cos(\phi_1 - \phi_2) \begin{pmatrix} -\frac{2l_4 \sin(\phi_4 - \phi_2)}{l_2} \text{atan2}(\mathbf{l}_4 \times_2 \mathbf{l}_6, \mathbf{l}_4 \cdot \mathbf{l}_6) \\ + \frac{2l_3 \sin(\phi_3 - \phi_2)}{l_2} \text{atan2}(\mathbf{l}_3 \times_2 \mathbf{l}_5, \mathbf{l}_3 \cdot \mathbf{l}_5) \\ + \frac{l_4 \cos(\phi_4 - \phi_2)}{l_2} \ln \left(\frac{l_6^2}{l_4^2} \right) \\ - \frac{l_3 \cos(\phi_3 - \phi_2)}{l_2} \ln \left(\frac{l_5^2}{l_3^2} \right) \\ + \ln \left(\frac{l_6^2}{l_5^2} \right) \end{pmatrix} \quad (3.26)$$

Factoring out the exponent from natural logarithm terms, rearranging the order of terms within atan2 and ln functions to obtain favorable sign flips, simplifying and collecting terms, this becomes

$$\bar{B}_{\perp,s} = \frac{-\mu_0 I_1}{2\pi l_1 l_2} \left(\begin{aligned} & l_2 \sin(\phi_1 - \phi_2) \text{atan2}(\mathbf{l}_5 \times_2 \mathbf{l}_6, \mathbf{l}_5 \cdot \mathbf{l}_6) \\ & + l_3 \left(\begin{aligned} & \sin(\phi_1 - \phi_2) \cos(\phi_3 - \phi_2) \\ & - \cos(\phi_1 - \phi_2) \sin(\phi_3 - \phi_2) \end{aligned} \right) \text{atan2}(\mathbf{l}_5 \times_2 \mathbf{l}_3, \mathbf{l}_5 \cdot \mathbf{l}_3) \\ & + l_4 \left(\begin{aligned} & \sin(\phi_1 - \phi_2) \cos(\phi_4 - \phi_2) \\ & - \cos(\phi_1 - \phi_2) \sin(\phi_4 - \phi_2) \end{aligned} \right) \text{atan2}(\mathbf{l}_4 \times_2 \mathbf{l}_6, \mathbf{l}_4 \cdot \mathbf{l}_6) \\ & + l_2 \cos(\phi_1 - \phi_2) \ln \left(\frac{l_6}{l_5} \right) \\ & + l_3 \left(\begin{aligned} & \sin(\phi_1 - \phi_2) \sin(\phi_3 - \phi_2) \\ & + \cos(\phi_1 - \phi_2) \cos(\phi_3 - \phi_2) \end{aligned} \right) \ln \left(\frac{l_3}{l_5} \right) \\ & + l_4 \left(\begin{aligned} & \sin(\phi_1 - \phi_2) \sin(\phi_4 - \phi_2) \\ & + \cos(\phi_1 - \phi_2) \cos(\phi_4 - \phi_2) \end{aligned} \right) \ln \left(\frac{l_6}{l_4} \right) \end{aligned} \right) \quad (3.27)$$

Applying angle difference formulae, the coefficients of atan2 and ln terms can be simplified, yielding

$$\bar{B}_{\perp,s} = \frac{-\mu_0 I_1}{2\pi l_1 l_2} \left(\begin{aligned} & -l_2 \sin(\phi_2 - \phi_1) \text{atan2}(\mathbf{l}_5 \times_2 \mathbf{l}_6, \mathbf{l}_5 \cdot \mathbf{l}_6) \\ & -l_3 \sin(\phi_3 - \phi_1) \text{atan2}(\mathbf{l}_4 \times_2 \mathbf{l}_3, \mathbf{l}_5 \cdot \mathbf{l}_3) \\ & -l_4 \sin(\phi_4 - \phi_1) \text{atan2}(\mathbf{l}_4 \times_2 \mathbf{l}_6, \mathbf{l}_4 \cdot \mathbf{l}_6) \\ & + l_2 \cos(\phi_2 - \phi_1) \ln \left(\frac{l_6}{l_5} \right) \\ & + l_3 \cos(\phi_3 - \phi_1) \ln \left(\frac{l_3}{l_5} \right) \\ & + l_4 \cos(\phi_4 - \phi_1) \ln \left(\frac{l_6}{l_4} \right) \end{aligned} \right) \quad (3.28)$$

The following relationships are useful in the further simplification of the normal magnetic field integral expression:

$$\mathbf{l}_\alpha \cdot \mathbf{l}_\beta = l_\alpha l_\beta \cos(\phi_\alpha - \phi_\beta) \quad (3.29)$$

$$\mathbf{l}_\alpha \times_2 \mathbf{l}_\beta = l_\alpha l_\beta \sin(\phi_\beta - \phi_\alpha) \quad (3.30)$$

Multiplying (3.28) by l_1/l_1 and distributing into the terms inside parentheses of (3.28), (3.29) and (3.30) may be applied yielding

$$\bar{B}_{\perp,s} = \frac{-\mu_0 I_1}{2\pi l_1^2 l_2} \begin{pmatrix} -\mathbf{l}_1 \times_2 \mathbf{l}_2 \text{atan2}(\mathbf{l}_5 \times_2 \mathbf{l}_6, \mathbf{l}_5 \cdot \mathbf{l}_6) \\ -\mathbf{l}_1 \times_2 \mathbf{l}_3 \text{atan2}(\mathbf{l}_5 \times_2 \mathbf{l}_3, \mathbf{l}_5 \cdot \mathbf{l}_3) \\ -\mathbf{l}_1 \times_2 \mathbf{l}_4 \text{atan2}(\mathbf{l}_4 \times_2 \mathbf{l}_6, \mathbf{l}_4 \cdot \mathbf{l}_6) \\ +\mathbf{l}_1 \cdot \mathbf{l}_2 \ln\left(\frac{l_6}{l_5}\right) \\ +\mathbf{l}_1 \cdot \mathbf{l}_3 \ln\left(\frac{l_3}{l_5}\right) \\ +\mathbf{l}_1 \cdot \mathbf{l}_4 \ln\left(\frac{l_6}{l_4}\right) \end{pmatrix}. \quad (3.31)$$

Note that the pattern of inputs to the \cdot and \times_2 operations in the coefficients of terms in (3.31) is different from the Galerkin tangent flux density integral (2.20) - the pattern is flipped and/or negated. The pattern of inputs to the atan2 and \ln functions is the same as (2.20).

Coincident and Adjacent Singular Cases

As was the case for the average tangent integral (2.20), it is possible that in using the expression (3.31), singularities may be encountered depending on the relative orientation of \mathbf{l}_1 and \mathbf{l}_2 . Handling singularities arising in (3.31) is similar to their handling in (2.20), but there are some differences. First, coincidence is considered. Recalling two useful identities from [25]:

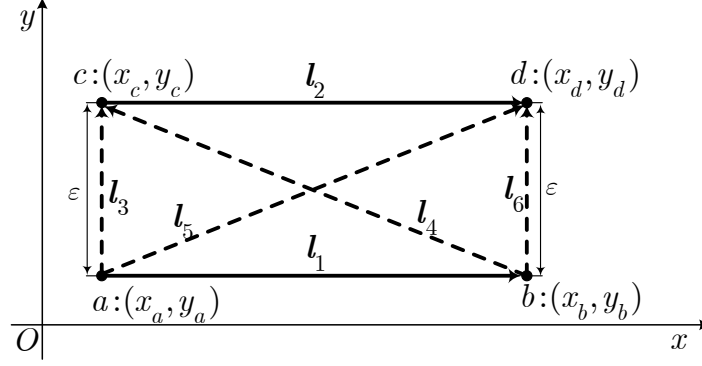
$$\lim_{\alpha \rightarrow 0} \alpha \ln(\alpha^2) = 2\alpha \ln(\alpha) = 0 \quad (3.32)$$

$$\lim_{\alpha, f(\alpha), g(\alpha) \rightarrow 0} \alpha \text{atan2}(f(\alpha), g(\alpha)) = 0 \quad (3.33)$$

One additional identity becomes useful:

$$\lim_{\alpha \rightarrow 0} \alpha \ln(1/\alpha) = -\alpha \ln(\alpha) = 0 \quad (3.34)$$

Considering the coincident case, the source and observation are separated a distance ϵ from each other, referring to Fig. 3.2, and the limit of (3.31) is evaluated as $\epsilon \rightarrow 0$.

Fig. 3.2.: Coincident elements case for \bar{B}_\perp

Equivalently, $\mathbf{l}_3, \mathbf{l}_6 \rightarrow 0$ and $\mathbf{l}_4 \rightarrow -\mathbf{l}_1$ and $\mathbf{l}_5 \rightarrow -\mathbf{l}_2$. In this case, the limit evaluates to

$$\bar{B}_{\perp,s} = \lim_{\epsilon \rightarrow 0} \frac{-\mu_0 I_1}{2\pi l_1^2 l_2} \left(\begin{aligned} & - \underbrace{\mathbf{l}_1 \times \mathbf{l}_2}_{=0} \underbrace{\text{atan2}(\mathbf{l}_5 \times \mathbf{l}_6, \mathbf{l}_5 \cdot \mathbf{l}_6)}_{\pi/2} = 0 \\ & - \underbrace{\mathbf{l}_1 \times \mathbf{l}_3}_{\rightarrow 0} \underbrace{\text{atan2}(\mathbf{l}_5 \times \mathbf{l}_3, \mathbf{l}_5 \cdot \mathbf{l}_3)}_{\pi/2} \rightarrow 0 \\ & - \underbrace{\mathbf{l}_1 \times \mathbf{l}_4}_{\rightarrow 0} \underbrace{\text{atan2}(\mathbf{l}_4 \times \mathbf{l}_6, \mathbf{l}_4 \cdot \mathbf{l}_6)}_{-\pi/2} \rightarrow 0 \\ & + \underbrace{\mathbf{l}_1 \cdot \mathbf{l}_2}_{=l_1 l_2} \ln \left(\frac{l_6}{l_5} \right) \xrightarrow{-\infty} -\infty \\ & + \underbrace{\mathbf{l}_1 \cdot \mathbf{l}_3}_{=0} \ln \left(\frac{l_3}{l_5} \right) \xrightarrow{0} 0 \\ & + \underbrace{\mathbf{l}_1 \cdot \mathbf{l}_4}_{\rightarrow -l_1 l_2} \ln \left(\frac{l_6}{l_4} \right) \xrightarrow{-\infty} \infty \end{aligned} \right). \quad (3.35)$$

Conveniently, the two diverging terms cancel and we are left with

$$\bar{B}_{\perp,s}(i, i) = 0 \quad (3.36)$$

This matches our intuition since a sheet current has only fields tangential to the surface near the surface of the current.

The case of element adjacency, i.e. when $(\mathbf{l}_3 \rightarrow 0) \oplus (\mathbf{l}_4 \rightarrow 0) \oplus (\mathbf{l}_5 \rightarrow 0) \oplus (\mathbf{l}_6 \rightarrow 0)$, is handled in the same way as in (2.20). Recall that the starred versions of the atan2

and \ln functions given by (2.21) and (2.22) may be used to exactly determine the limit of (3.31) in the two cases $(\mathbf{l}_3 \rightarrow 0) \oplus (\mathbf{l}_4 \rightarrow 0)$. Therefore the following expression represents the final form used for $\bar{B}_{\perp,s}$:

$$\bar{B}_{\perp,s} = -\frac{\mu_0 I_1}{2\pi l_1^2 l_2} \begin{pmatrix} -\mathbf{l}_1 \times_2 \mathbf{l}_2 \text{atan2}^*(\mathbf{l}_5 \times_2 \mathbf{l}_6, \mathbf{l}_5 \cdot \mathbf{l}_6) \\ -\mathbf{l}_1 \times_2 \mathbf{l}_3 \text{atan2}^*(\mathbf{l}_5 \times_2 \mathbf{l}_3, \mathbf{l}_5 \cdot \mathbf{l}_3) \\ -\mathbf{l}_1 \times_2 \mathbf{l}_4 \text{atan2}^*(\mathbf{l}_4 \times_2 \mathbf{l}_6, \mathbf{l}_4 \cdot \mathbf{l}_6) \\ +\mathbf{l}_1 \cdot \mathbf{l}_2 \ln^*\left(\frac{l_6}{l_5}\right) \\ +\mathbf{l}_1 \cdot \mathbf{l}_3 \ln^*\left(\frac{l_3}{l_5}\right) \\ +\mathbf{l}_1 \cdot \mathbf{l}_4 \ln^*\left(\frac{l_6}{l_4}\right) \end{pmatrix} \quad (3.37)$$

In the two cases that $(\mathbf{l}_5 \rightarrow 0) \oplus (\mathbf{l}_6 \rightarrow 0)$, the endpoints of \mathbf{l}_1 and \mathbf{l}_2 are exchanged (\mathbf{l}_1 becomes $\mathbf{l}_{1,\text{ex}} = -\mathbf{l}_1$ and \mathbf{l}_2 becomes $\mathbf{l}_{2,\text{ex}} = -\mathbf{l}_2$), $\mathbf{l}_3 - \mathbf{l}_6$ are recomputed using the new endpoints and then (3.37) is evaluated again and the result is negated.

Intersection Special Case

In the course of using (3.37) to determine the average flux density in critical machine locations (for example, in a stator tooth cross section), when volume meshing is used it was found that when a source mesh element \mathbf{l}_1 intersects the observation element \mathbf{l}_2 , the form (3.37) does not produce the correct average normal magnetic field, even with the special cases identified thus far. In particular, the intersection region must be excluded from the integration domain, as $r \rightarrow 0$ there. The value of the integral in the intersection case is finite - i.e. a singularity does not exist there - but the integral result is incorrect. This was discovered by comparing the result with a numerically-averaged normal field, computing the magnetic field at many finite points along the line and averaging the normal component of these field vectors.

Consider a source \mathbf{l}_1 which intersects an observation element \mathbf{l}_2 . The source is split at the intersection point into lower and upper parts, $\mathbf{l}_{1,l}$ and $\mathbf{l}_{1,u}$ respectively, which are each separated a distance ϵ from the observation line along the line of the source. This case is depicted in Fig. 3.3. As we let ϵ approach 0, we expect/desire

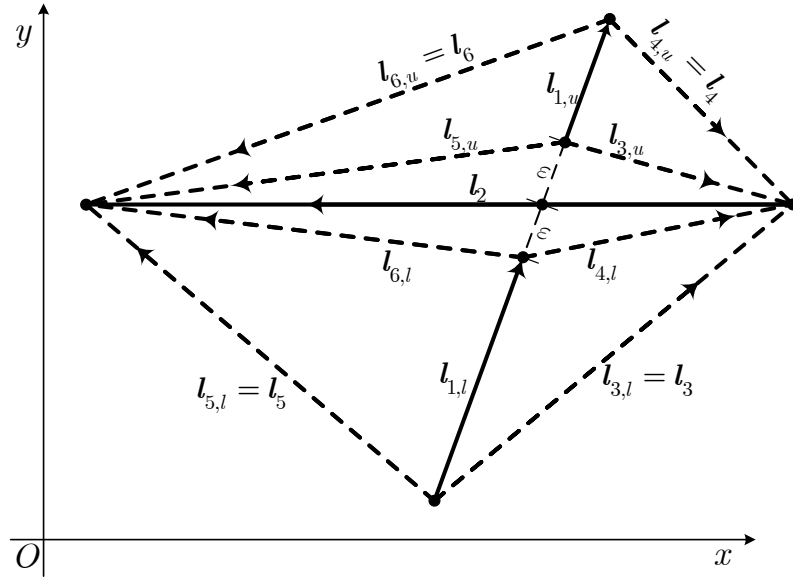


Fig. 3.3.: Source intersecting with observation, split at intersection point.

the lower and upper parts of the split source to contribute together the same total magnetic field as the whole source. The lower and upper parts of the split source now

carry respective currents $(l_{1,l}/l_1)I_1$ and $(l_{1,u}/l_1)I_1$. Adding together the effects of the split sources, the average normal magnetic field in the observation element is

$$\bar{B}_{\perp,s} = -\frac{\mu_0}{2\pi l_2} \left(\frac{1}{l_{1,l}^2} \left(\frac{l_{1,l}}{l_1} I_1 \right) \begin{pmatrix} -\mathbf{l}_{1,l} \times_2 \mathbf{l}_2 \text{atan2}^*(\mathbf{l}_{5,l} \times_2 \mathbf{l}_{6,l}, \mathbf{l}_{5,l} \cdot \mathbf{l}_{6,l}) \\ -\mathbf{l}_{1,l} \times_2 \mathbf{l}_3 \text{atan2}^*(\mathbf{l}_{5,l} \times_2 \mathbf{l}_{3,l}, \mathbf{l}_{5,l} \cdot \mathbf{l}_{3,l}) \\ -\mathbf{l}_{1,l} \times_2 \mathbf{l}_4 \text{atan2}^*(\mathbf{l}_{4,l} \times_2 \mathbf{l}_{6,l}, \mathbf{l}_{4,l} \cdot \mathbf{l}_{6,l}) \\ +\mathbf{l}_{1,l} \cdot \mathbf{l}_2 \ln^* \left(\frac{l_{6,l}}{l_{5,l}} \right) \\ +\mathbf{l}_{1,l} \cdot \mathbf{l}_3 \ln^* \left(\frac{l_{3,l}}{l_{5,l}} \right) \\ +\mathbf{l}_{1,l} \cdot \mathbf{l}_4 \ln^* \left(\frac{l_{6,l}}{l_{4,l}} \right) \end{pmatrix} + \right. \\ \left. \frac{1}{l_{1,u}^2} \left(\frac{l_{1,u}}{l_1} I_1 \right) \begin{pmatrix} -\mathbf{l}_{1,u} \times_2 \mathbf{l}_2 \text{atan2}^*(\mathbf{l}_{5,u} \times_2 \mathbf{l}_{6,u}, \mathbf{l}_{5,u} \cdot \mathbf{l}_{6,u}) \\ -\mathbf{l}_{1,u} \times_2 \mathbf{l}_3 \text{atan2}^*(\mathbf{l}_{5,u} \times_2 \mathbf{l}_{3,u}, \mathbf{l}_{5,u} \cdot \mathbf{l}_{3,u}) \\ -\mathbf{l}_{1,u} \times_2 \mathbf{l}_4 \text{atan2}^*(\mathbf{l}_{4,u} \times_2 \mathbf{l}_{6,u}, \mathbf{l}_{4,u} \cdot \mathbf{l}_{6,u}) \\ +\mathbf{l}_{1,u} \cdot \mathbf{l}_2 \ln^* \left(\frac{l_{6,u}}{l_{5,u}} \right) \\ +\mathbf{l}_{1,u} \cdot \mathbf{l}_3 \ln^* \left(\frac{l_{3,u}}{l_{5,u}} \right) \\ +\mathbf{l}_{1,u} \cdot \mathbf{l}_4 \ln^* \left(\frac{l_{6,u}}{l_{4,u}} \right) \end{pmatrix} \right) \quad (3.38)$$

Multiplying (3.38) by l_1/l_1 and utilizing the following relationships

$$l_1 \frac{l_{1,l}}{l_{1,l}} = l_1 \hat{l}_{1,l} = \mathbf{l}_1 \quad (3.39)$$

$$l_1 \frac{l_{1,u}}{l_{1,u}} = l_1 \hat{l}_{1,u} = \mathbf{l}_1, \quad (3.40)$$

each $\mathbf{l}_{1,l}$ and $\mathbf{l}_{1,u}$ in operations \times_2 and \cdot in the atan2^* and \ln^* coefficients is converted to \mathbf{l}_1 . Realizing that the vectors on the outer perimeter of the split system are equivalent to the original system where \mathbf{l}_1 is not split:

$$\begin{aligned} \mathbf{l}_{3,l} &= \mathbf{l}_3 \\ \mathbf{l}_{4,u} &= \mathbf{l}_4 \\ \mathbf{l}_{5,l} &= \mathbf{l}_5 \\ \mathbf{l}_{6,u} &= \mathbf{l}_6 \end{aligned} \quad (3.41)$$

the expression (3.38) may be manipulated to obtain

$$\bar{B}_{\perp,s} = -\frac{\mu_0 I_1}{2\pi l_1^2 l_2} \left(\left(\begin{aligned} & -\mathbf{l}_1 \times_2 \mathbf{l}_2 \text{atan2}^*(\mathbf{l}_5 \times_2 \mathbf{l}_{6,l}, \mathbf{l}_5 \cdot \mathbf{l}_{6,l}) \\ & -\mathbf{l}_1 \times_2 \mathbf{l}_3 \text{atan2}^*(\mathbf{l}_5 \times_2 \mathbf{l}_{3,l}, \mathbf{l}_5 \cdot \mathbf{l}_{3,l}) \\ & -\mathbf{l}_1 \times_2 \mathbf{l}_{4,l} \text{atan2}^*(\mathbf{l}_{4,l} \times_2 \mathbf{l}_{6,l}, \mathbf{l}_{4,l} \cdot \mathbf{l}_{6,l}) \\ & +\mathbf{l}_1 \cdot \mathbf{l}_2 \ln^* \left(\frac{l_{6,l}}{l_5} \right) \\ & +\mathbf{l}_1 \cdot \mathbf{l}_3 \ln^* \left(\frac{l_{3,l}}{l_5} \right) \\ & +\mathbf{l}_1 \cdot \mathbf{l}_{4,l} \ln^* \left(\frac{l_{6,l}}{l_{4,l}} \right) \end{aligned} \right) + \left(\begin{aligned} & -\mathbf{l}_1 \times_2 \mathbf{l}_2 \text{atan2}^*(\mathbf{l}_{5,u} \times_2 \mathbf{l}_6, \mathbf{l}_{5,u} \cdot \mathbf{l}_6) \\ & -\mathbf{l}_1 \times_2 \mathbf{l}_{3,u} \text{atan2}^*(\mathbf{l}_{5,u} \times_2 \mathbf{l}_{3,u}, \mathbf{l}_{5,u} \cdot \mathbf{l}_{3,u}) \\ & -\mathbf{l}_1 \times_2 \mathbf{l}_4 \text{atan2}^*(\mathbf{l}_4 \times_2 \mathbf{l}_6, \mathbf{l}_4 \cdot \mathbf{l}_6) \\ & +\mathbf{l}_1 \cdot \mathbf{l}_2 \ln^* \left(\frac{l_6}{l_{5,u}} \right) \\ & +\mathbf{l}_1 \cdot \mathbf{l}_{3,u} \ln^* \left(\frac{l_{3,u}}{l_{5,u}} \right) \\ & +\mathbf{l}_1 \cdot \mathbf{l}_4 \ln^* \left(\frac{l_6}{l_4} \right) \end{aligned} \right) \right). \quad (3.42)$$

Since [4]

$$\begin{aligned} \phi_\beta - \phi_\alpha &= \text{atan2}(\sin(\phi_\beta - \phi_\alpha), \cos(\phi_\beta - \phi_\alpha)) \\ &= \text{atan2}(\mathbf{l}_\alpha \times_2 \mathbf{l}_\beta, \mathbf{l}_\alpha \cdot \mathbf{l}_\beta) \end{aligned}, \quad (3.43)$$

then each of the $\text{atan2}^*(\cdot)$ terms may be expanded, where the like coefficients of all terms are regrouped (likewise for the \ln^* terms) so that the original expression (3.37)

is recovered along with six correction terms which represent the effect of excluding the intersection region:

$$\bar{B}_{\perp,s} = -\frac{\mu_0 I_1}{2\pi l_1^2 l_2} \left(\begin{array}{l} \left(\begin{array}{l} -\mathbf{l}_1 \times_2 \mathbf{l}_2 \text{atan2}^*(\mathbf{l}_5 \times_2 \mathbf{l}_6, \mathbf{l}_5 \cdot \mathbf{l}_6) \\ -\mathbf{l}_1 \times_2 \mathbf{l}_3 \text{atan2}^*(\mathbf{l}_5 \times_2 \mathbf{l}_3, \mathbf{l}_5 \cdot \mathbf{l}_3) \\ -\mathbf{l}_1 \times_2 \mathbf{l}_4 \text{atan2}^*(\mathbf{l}_4 \times_2 \mathbf{l}_6, \mathbf{l}_4 \cdot \mathbf{l}_6) \\ +\mathbf{l}_1 \cdot \mathbf{l}_2 \ln^*\left(\frac{l_6}{l_5}\right) \\ +\mathbf{l}_1 \cdot \mathbf{l}_3 \ln^*\left(\frac{l_3}{l_5}\right) \\ +\mathbf{l}_1 \cdot \mathbf{l}_4 \ln^*\left(\frac{l_6}{l_4}\right) \end{array} \right) + \\ \left(\begin{array}{l} -\mathbf{l}_1 \times_2 \mathbf{l}_2 \text{atan2}^*(\mathbf{l}_{5,u} \times_2 \mathbf{l}_{6,l}, \mathbf{l}_{5,u} \cdot \mathbf{l}_{6,l}) \\ -\mathbf{l}_1 \times_2 \mathbf{l}_{3,u} \text{atan2}^*(\mathbf{l}_{5,u} \times_2 \mathbf{l}_{3,u}, \mathbf{l}_{5,u} \cdot \mathbf{l}_{3,u}) \\ -\mathbf{l}_1 \times_2 \mathbf{l}_{4,l} \text{atan2}^*(\mathbf{l}_{4,l} \times_2 \mathbf{l}_{6,l}, \mathbf{l}_{4,l} \cdot \mathbf{l}_{6,l}) \\ +\mathbf{l}_1 \cdot \mathbf{l}_2 \ln^*\left(\frac{l_{6,l}}{l_{5,u}}\right) \\ +\mathbf{l}_1 \cdot \mathbf{l}_{3,u} \ln^*\left(\frac{l_{3,u}}{l_{5,u}}\right) \\ +\mathbf{l}_1 \cdot \mathbf{l}_{4,l} \ln^*\left(\frac{l_{6,l}}{l_{4,l}}\right) \end{array} \right) \end{array} \right) \quad (3.44)$$

Viewing Fig. 3.3, it is apparent that as $\epsilon \rightarrow 0$, the differences in angles

$$\phi_{6,l} - \phi_{5,u} = \text{atan2}^*(\mathbf{l}_{5,u} \times_2 \mathbf{l}_{6,l}, \mathbf{l}_{5,u} \cdot \mathbf{l}_{6,l}) \rightarrow 0 \quad (3.45)$$

but the difference in angles

$$\phi_{3,u} - \phi_{5,u} = \text{atan2}^*(\mathbf{l}_{5,u} \times_2 \mathbf{l}_{3,u}, \mathbf{l}_{5,u} \cdot \mathbf{l}_{3,u}) \rightarrow \pi \quad (3.46)$$

$$\phi_{6,l} - \phi_{4,l} = \text{atan2}^*(\mathbf{l}_{4,l} \times_2 \mathbf{l}_{6,l}, \mathbf{l}_{4,l} \cdot \mathbf{l}_{6,l}) \rightarrow \pi. \quad (3.47)$$

However, when $\epsilon = 0$ exactly, the angles $\phi_{3,u} - \phi_{5,u}$ and $\phi_{6,l} - \phi_{4,l}$ are ambiguously-defined to be $\pm\pi$. The numerical manifestation of this subtlety is a discontinuity

which occurs at this argument combination, i.e. $\pm\pi = \text{atan2}(\pm 0, -1)$, since the cross and dot products are computed on anti-parallel lines. With this subtlety in mind, as $\epsilon \rightarrow 0$

$$\mathbf{l}_{5,u} \rightarrow \mathbf{l}_{6,l} \quad (3.48)$$

$$\mathbf{l}_{3,u} \rightarrow \mathbf{l}_{4,l}. \quad (3.49)$$

With (3.45)-(3.47), (3.48) and (3.49), the correction terms of (3.44) may be manipulated to show that

$$\lim_{\epsilon \rightarrow 0} \left(\begin{array}{l} -\mathbf{l}_1 \times_2 \mathbf{l}_2 \text{atan2}^*(\mathbf{l}_{5,u} \times_2 \mathbf{l}_{6,l}, \mathbf{l}_{5,u} \cdot \mathbf{l}_{6,l}) \rightarrow 0 \\ -\mathbf{l}_1 \times_2 \mathbf{l}_{3,u} \text{atan2}^*(\mathbf{l}_{5,u} \times_2 \mathbf{l}_{3,u}, \mathbf{l}_{5,u} \cdot \mathbf{l}_{3,u}) \\ -\mathbf{l}_1 \times_2 \mathbf{l}_{4,l} \text{atan2}^*(\mathbf{l}_{4,l} \times_2 \mathbf{l}_{6,l}, \mathbf{l}_{4,l} \cdot \mathbf{l}_{6,l}) \end{array} \right\} \rightarrow |\mathbf{l}_1 \times_2 \mathbf{l}_{4,l}| 2\pi$$

$$\lim_{\epsilon \rightarrow 0} \left(\begin{array}{l} +\mathbf{l}_1 \cdot \mathbf{l}_2 \ln^* \left(\frac{l_{6,l}}{l_{5,u}} \right) \\ +\mathbf{l}_1 \cdot \mathbf{l}_{3,u} \ln^* \left(\frac{l_{3,u}}{l_{5,u}} \right) \\ +\mathbf{l}_1 \cdot \mathbf{l}_{4,l} \ln^* \left(\frac{l_{6,l}}{l_{4,l}} \right) \end{array} \right\} \Sigma \rightarrow 0$$

$$= |\mathbf{l}_1 \times_2 \mathbf{l}_{4,l}| 2\pi. \quad (3.50)$$

where the absolute value is used as a result of considering all possible cases of the relative orientation between \mathbf{l}_1 and \mathbf{l}_2 .

In practice, a check is made to find any intersection of the line segments of source \mathbf{l}_1 and observation \mathbf{l}_2 . If an intersection exists, the intersection point enables the calculation of $\mathbf{l}_{4,l}$ and the correction term $|\mathbf{l}_1 \times_2 \mathbf{l}_{4,l}| 2\pi$ is added to the six original terms in (3.37) inside the parenthesis.

3.2 Permanent Magnet Sources

It is widely-known that permanent magnet materials exhibit a hysteretic relationship between B and H , an example of which is shown in Fig. 3.4. In a properly-designed machine, the magnet will operate in the second quadrant of the hysteresis

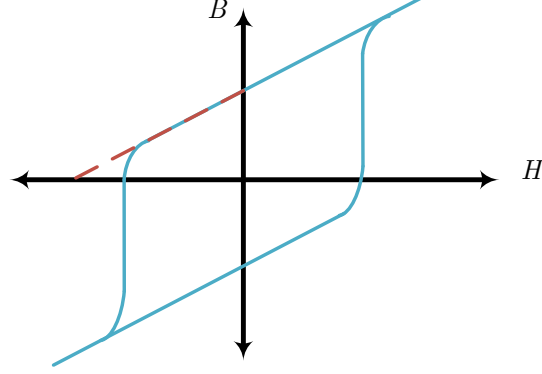


Fig. 3.4.: Hysteretic relationship between B and H in permanent magnet materials.

curve, again referring to Fig. 3.4, where a linear approximation is often valid. In permanent magnet materials, the equation $\mathbf{B} = \mu_0(\mathbf{H} + \mathbf{M})$ holds true, as with all magnetic materials. However, in the linearly-approximated region of PM materials, \mathbf{M} can be separated into two components, where a portion of the magnetic dipoles are induced in response to magnetic fields while the other remains fixed:

$$\mathbf{M} = \mathbf{M}_{\text{ind}} + \mathbf{M}_{\text{fixed}} \quad (3.51)$$

According to the constitutive relationship of the PM material, $\mathbf{M}_{\text{ind}} = \chi_{PM}\mathbf{H}$. The magnetic field in the PM material can then be expressed as

$$\begin{aligned} \mathbf{B} &= \mu_0(\mathbf{H} + \mathbf{M}_{\text{ind}} + \mathbf{M}_{\text{fixed}}) \\ \mathbf{B} &= \mu_0(1 + \chi_{r,PM})\mathbf{H} + \mu_0\mathbf{M}_{\text{fixed}} \end{aligned} \quad (3.52)$$

$$\mathbf{B} = \mu_0\mu_{r,PM}\mathbf{H} + \mu_0\mathbf{M}_{\text{fixed}} \quad (3.53)$$

where $\mu_{r,PM}$ is the relative permeability of the PM material, often referred to as the relative “recoil permeability.” Hence, the B - H line does not pass through the origin but is instead affine, typically operating in the second quadrant. This is known as the “straight line” relationship [21] (red line in Fig. 3.4). The respective x - and y -

intercepts of the straight line relationship are the points $(H_c, 0)$ and $(0, B_r)$. H_c is termed the “coercive force,” given by setting \mathbf{B} to zero in (3.53):

$$\mathbf{H}_c = -\frac{\mathbf{B}_r}{\mu_0\mu_{rec}} \quad (3.54)$$

where B_r is termed the “residual flux density,” given by

$$B_r = \mu_0 M_{\text{fixed}}. \quad (3.55)$$

The straight line relationship to the hysteresis curve is valid provided the PM does not de-magnetize. De-magnetization occurs when the auxiliary field becomes more negative than the limit, typically near the value H_c . Once the auxiliary field surpasses the limit, the fixed magnetization term is no longer constant.

Representation of PMs in the MoM can be accomplished by either of two methods. In one method, the PM flux source is represented by an equivalent fixed free current source, amounting to an additional source in the equation system inputs. In the second method, an additional source term is required in the equation system inputs, similar to the first method, while a further addition to represent the fixed magnetic field component B_r in the PM material is also required. In either method, the PM material responds to the fields present from all sources present in the system, according to the constitutive relation of the PM material. Hence, as for any magnetizable material in the MoM, the boundary of the PM material is meshed, creating additional unknown magnetizations.

3.2.1 Equivalent Free Current Source Method

In this method, the fixed magnetization (3.55) is replaced with a fixed free current source, effectively contributing an additional magnetic field source in the inputs of the system of equations (2.6). Therefore the system of equations becomes

$$[\mathbf{f}_{B_{tot}M} - \mathbf{f}_{BM}]\mathbf{M}_{\text{tan}} = \mathbf{f}_{BI_f}\mathbf{I}_f + \mathbf{f}_{BI_{PM}}\mathbf{I}_{PM} \quad (3.56)$$

It remains to assign the proper value of free current to the term \mathbf{I}_{PM} . Viewing (3.53), it is tempting to attribute the equivalent free current source magnitude I_{PM} to the term

$B_r = \mu_0 \mathbf{M}_{fixed}$ alone such that $\|\mathbf{K}_b\| = \|\mathbf{M}_{fixed} \times \hat{n}\| = I_{PM}/l_{PM}$ and subsequently $I_{PM} = B_r l_{PM}/\mu_0$. However, this leads to slightly incorrect results as a weaker free current source is required to achieve the correct operating characteristic. To see why, consider the material/equivalent free current source placed in a test fixture, the core of which is assumed to have infinite permeability. Invoking Ampere's law in a closed path around the test fixture, the H field in the infinitely permeable material vanishes. With the airgap in the test fixture set to zero, in the language of magnetic equivalent circuits (MECs) this is considered a “short-circuited” condition. Under these conditions, H is only nonzero in the PM material:

$$H_{PM} l_{PM} = I_{f,enclosed}. \quad (3.57)$$

In the equivalent source the B - H characteristic is $B = \mu_0 \mu_{r,PM} H_{PM}$. Substituting this into (3.57), we have that

$$\frac{B}{\mu_0 \mu_{r,PM}} l_{PM} = I_{f,enclosed}. \quad (3.58)$$

Hence, the magnitude of free current required to source a magnetic field of $B = B_r$ in this short-circuited condition is

$$\|\mathbf{I}_{PM}\| = I_{f,enclosed} = \frac{B_r}{\mu_0 \mu_{r,PM}} l_{PM}. \quad (3.59)$$

Since in the equivalent source the B - H characteristic is $B = \mu_0 \mu_{r,PM} H_{PM}$, the B - H characteristic is not affine, as a PM material truly is, but is effectively shifted into the first quadrant. However, if one wishes to calculate the actual \mathbf{H} field in the PM material, for example to compare against demagnetizing limits, the flux density in the PM material solved using (3.56) is input into (3.52) from which \mathbf{H} can be solved. There is an alternative PM representation presented in the next subsection in which the PM B - H characteristic correctly operates in the second quadrant.

3.2.2 Fixed Magnetization Method

Similar to the formation of the $\mathbf{f}_{B_{tot}M}$ matrix, the auxiliary field can be algebraically eliminated from the B - H characteristic of PM material (3.53)

$$\begin{aligned}
 \mathbf{B} &= \mu_0(\mathbf{H} + \mathbf{M}_{\text{ind}} + \mathbf{M}_{\text{fixed}}) \\
 &= \mu_0 \left(\frac{1 + \chi_{r,PM}}{\chi_{r,PM}} \right) \mathbf{M}_{\text{ind}} + \mu_0 \mathbf{M}_{\text{fixed}} \\
 &= \frac{\mu_0 \mu_{r,PM}}{\mu_{r,PM} - 1} \mathbf{M}_{\text{ind}} + \mu_0 \mathbf{M}_{\text{fixed}} \\
 \mathbf{B} = \mathbf{B}_{\text{tot}} &= f_{B_{tot}M} \mathbf{M}_{\text{ind}} + \mu_0 \mathbf{M}_{\text{fixed}} \\
 &= f_{B_{tot}M} \mathbf{M}_{\text{ind}} + \mathbf{B}_r
 \end{aligned} \tag{3.60}$$

Using this result, the system of equations can be modified to be

$$\begin{aligned}
 \mathbf{f}_{B_{tot}M} \mathbf{M}_{\text{tan}} + \mathbf{B}_r &= \mathbf{f}_{BM} \mathbf{M}_{\text{tan}} + \mathbf{f}_{BI_f} \mathbf{I}_f + \mathbf{f}_{BI_{PM}} \mathbf{I}_{PM} \\
 [\mathbf{f}_{B_{tot}M} - \mathbf{f}_{BM}] \mathbf{M}_{\text{tan}} &= \mathbf{f}_{BI_f} \mathbf{I}_f + \mathbf{f}_{BI_{PM}} \mathbf{I}_{PM} - \mathbf{B}_r
 \end{aligned} \tag{3.61}$$

where the entries in \mathbf{B}_r are only nonzero for PM elements oriented along the direction of $\mathbf{M}_{\text{fixed}}$. Hence for all other elements the equation system is unchanged from the first method.

In contrast to the equivalent free current source of the previous method, the bound current source I_{PM} in this method is of greater magnitude. To see why, again consider the PM material in a test fixture in the short-circuit condition. Invoking Ampere's law around the same path, the current source is bound, not free, hence $H_{PM} l_{PM} = I_{f,\text{enclosed}} = 0$ and therefore $H_{PM} = 0$. This means that in the short-circuit condition, the induced dipoles are not making contributions to the flux density in this case. Substituting $H_{PM} = 0$ into (3.60), we have that $B = \mu_0 \mathbf{M}_{\text{fixed}} = B_r$. Hence, the fixed magnetization alone is sourcing the magnetic field. The corresponding bound current source magnitude is given by

$$\|\mathbf{K}_b\| = \|\mathbf{M}_{\text{fixed}} \times \hat{n}\| = \frac{I_{PM}}{l_{PM}} \tag{3.62}$$

$$\|\mathbf{I}_{PM}(i)\| = \frac{B_r}{\mu_0} l_{PM} \tag{3.63}$$

Recall that in the previous method, since the auxiliary field is nonzero in the short-circuit condition, induced magnetic dipoles in addition to a weaker free current source are acting together to source the total magnetic field. Since in this method the current source is a bound current due to the fixed magnetization component, the offset in the B - H relationship remains and it is therefore affine. Hence, modeling permanent magnets using this second method properly attains second quadrant operation.

Although the discussion herein focused on the simple case of a rectangular magnet with magnetization parallel to its sides, the methods discussed are applicable for arbitrary magnetization direction, PMs within electric machinery are often radially-magnetized. Under this condition, the PM source sheets are placed along the radial lines forming the magnet sides. Furthermore, researchers have determined current distributions which model commonly-used permanent magnet shapes and more complicated magnetization patterns [30]. These methods could be used within the MoM by placing the bound current sources where the curl of magnetization is nonzero, even within the interior of the PM material if necessary. This may be accomplished without the need for additional mesh elements so that the original surface mesh of the PM material is still utilized.

3.3 Computing Torque

The electromagnetic torque is often a quantity of interest in the design of electromechanical devices. Several methods exist to facilitate this calculation. Herein methods involving direct field quantities are considered, leaving untouched any energy-based approaches such as the Virtual Work and Global Co-energy. Although there is no known restriction preventing the investigation of such energy-based approaches, in the MoM, since there is no airgap mesh which may be virtually distorted by taking an analytical derivative, we are left with taking the finite difference-based derivative of co-energy, which has been long considered unattractive due to potential numerical

error. The two torque approaches considered herein based on direct field quantities are the Maxwell Stress Tensor (MST) method and the Lorentz torque method.

3.3.1 Maxwell Stress Tensor Method

A common post-processing approach to calculating electromagnetic force/torque acting on the rotor of an electric machine is the Maxwell Stress Tensor (MST) method [21]. Therein the dot product of the MST and surface normal is integrated over a surface enclosing the movable member. The surface integral becomes a line integral in the 2D case, yielding the normal and tangential components of force per unit length as

$$\mathbf{F} = \frac{1}{\mu_0} \oint \left(\frac{1}{2}(B_n^2 - B_t^2)\hat{n} + B_n B_t \hat{t} \right) d\mathbf{l} \quad (3.64)$$

and the electromagnetic torque per unit length is

$$\mathbf{T} = \frac{1}{\mu_0} \oint \left(\langle \mathbf{r}_n, \mathbf{r}_t \rangle \times \left(\frac{1}{2}(B_n^2 - B_t^2)\hat{n} + B_n B_t \hat{t} \right) \right) d\mathbf{l} \quad (3.65)$$

where \hat{n} and \hat{t} are respectively the unit vectors normal and tangent to the differential integration path $d\mathbf{l}$. Utilizing the solution of (2.6), one can compute the total fields B_n and B_t by summing the individual contributions of all free and bound currents, using (3.31) and (2.20) respectively, to observation elements placed along an airgap surface that encloses the rotor.

The integration is performed numerically using a mesh that is iteratively refined until further resolution yields negligible change in computed torque. For each iteration, the computation required is proportional to $\mathcal{O}((N_b + N_f)N_{ag})$ where N_{ag} represents the mesh resolution of the airgap line. Disadvantages of using the MST within MoM include the need to introduce a mesh into a previously unmeshed region (airgap) and the need to numerically integrate and iterate. An attractive alternative that eliminates these shortcomings is a Lorentz force approach.

3.3.2 Lorentz Torque - Midpoint Approximation Method

Using the appropriate expressions for force described in 2.4, the torque can be computed using the cross product

$$\mathbf{T}_{\text{mid}} = \mathbf{r}_{\text{mid}} \times \mathbf{F}_{\text{mid}} \quad (3.66)$$

wherein it is assumed that the force \mathbf{F}_{mid} is concentrated at the element midpoint and the radius \mathbf{r}_{mid} is the vector from the origin (rotational axis of machine) to element midpoint.

This method is quite simple and produces torque values which are reasonably accurate. However, the assumption that the radius and force vary little over the element is reasonable provided the elements are small or far from the origin. In the case of the bound current sheets constituting the fixed excitation of permanent magnet materials, this assumption is poor. As will be shown in the following section, for little additional computational expense, the torque may be integrated along the observation line, taking into account the varying radius.

3.3.3 Lorentz Torque - Analytical Integration Method

Similar to Section 2.4, we may wish to compute the torque on: line elements by line sources, line elements by point sources, point elements by line sources, and point elements by point sources. The closed-form expressions required to evaluate these torques are provided in this subsection.

Torque Exerted on Line Elements by Line Sources

The torque exerted on observation element \mathbf{l}_2 by source element \mathbf{l}_1 is evaluated by integrating the torque on point \mathbf{p} as shown in Fig. 2.4. Source element \mathbf{l}_1 carries a current I_1 , distributed uniformly along its length, which creates the magnetic field $\mathbf{B}_1(\mathbf{p})$ at point \mathbf{p} . Observation element \mathbf{l}_2 carries a current I_2 distributed uniformly along its length. In the 2D formulation considered herein, the current exists only in

the \hat{z} direction and hence the magnetic fields exist only in the x - y plane. With I_2 and $\mathbf{B}_1(\mathbf{p})$ the Lorentz torque integral is expressed mathematically from (3.66) as

$$\begin{aligned}
\mathbf{T}_{||} &= \frac{I_2}{l_2} \int_{l_2} \mathbf{p} \times \hat{z} \times \mathbf{B}_1(\mathbf{p}) dp \\
&= \frac{I_2}{l_2} \int_0^1 \mathbf{p}(t) \times \hat{z} \times \mathbf{B}_1(\mathbf{p}(t)) \left\| \frac{d}{dt} \mathbf{p}(t) \right\| dt \\
&= I_2 \int_0^1 \langle p_x, p_y \rangle \times \hat{z} \times \langle B_{x,1}(\mathbf{p}), B_{y,1}(\mathbf{p}), \rangle dt
\end{aligned} \tag{3.67}$$

The full derivation of the integral evaluation and simplification steps is provided in Appendix A. The final expression for the torque $T_{||}$ is

$$\begin{aligned}
T_{||} = & -\frac{\mu_0 I_1 I_2}{4\pi l_1^2 l_2^2} \left(\begin{aligned} & \left(\begin{aligned} & l_1 l_2 l_2 l_c \cos(\phi_1 + \phi_2 - \phi_2 - \phi_c) \\ & + l_1 l_2 l_2 l_d \cos(\phi_1 + \phi_2 - \phi_2 - \phi_d) \end{aligned} \right) \text{atan2}(\mathbf{l}_5 \times_2 \mathbf{l}_6, \mathbf{l}_5 \cdot \mathbf{l}_6) \\ & + \left(\begin{aligned} & l_1 l_2 l_3 l_c \cos(\phi_1 + \phi_2 - \phi_3 - \phi_c) \\ & + l_1 l_2 l_3 l_a \cos(\phi_1 + \phi_2 - \phi_3 - \phi_a) \end{aligned} \right) \text{atan2}(\mathbf{l}_5 \times_2 \mathbf{l}_3, \mathbf{l}_5 \cdot \mathbf{l}_3) \\ & + \left(\begin{aligned} & l_1 l_2 l_4 l_c \cos(\phi_1 + \phi_2 - \phi_4 - \phi_c) \\ & + l_1 l_2 l_4 l_b \cos(\phi_1 + \phi_2 - \phi_4 - \phi_b) \end{aligned} \right) \text{atan2}(\mathbf{l}_4 \times_2 \mathbf{l}_6, \mathbf{l}_4 \cdot \mathbf{l}_6) \\ & - \left(\begin{aligned} & l_1 l_2 l_2 l_c \sin(\phi_1 + \phi_2 - \phi_2 - \phi_c) \\ & + l_1 l_2 l_2 l_d \sin(\phi_1 + \phi_2 - \phi_2 - \phi_d) \end{aligned} \right) \log\left(\frac{l_6}{l_5}\right) \\ & - \left(\begin{aligned} & l_1 l_2 l_3 l_c \sin(\phi_1 + \phi_2 - \phi_3 - \phi_c) \\ & + l_1 l_2 l_3 l_a \sin(\phi_1 + \phi_2 - \phi_3 - \phi_a) \end{aligned} \right) \log\left(\frac{l_3}{l_5}\right) \\ & - \left(\begin{aligned} & l_1 l_2 l_4 l_c \sin(\phi_1 + \phi_2 - \phi_4 - \phi_c) \\ & + l_1 l_2 l_4 l_b \sin(\phi_1 + \phi_2 - \phi_4 - \phi_b) \end{aligned} \right) \log\left(\frac{l_6}{l_4}\right) \end{aligned} \right) \end{aligned} \tag{3.68}$$

Again the zero-valued quantity $\phi_2 - \phi_2$ appears in several of the coefficients in (3.68) as in Section 2.4. Expressing the difference is useful since one can then generalize the calculation of all the angle difference cosine and sine terms found in (3.68). Specif-

ically, one can show that the cosine and sine terms can be solved directly using: (3.68):

$$\begin{aligned}
& l_\alpha l_\beta l_\gamma l_\delta \cos(\phi_\alpha + \phi_\beta - \phi_\gamma - \phi_\delta) \\
&= (\mathbf{l}_\alpha \cdot \mathbf{l}_\delta)(\mathbf{l}_\beta \cdot \mathbf{l}_\gamma) \\
&= -(\mathbf{l}_\alpha \times_2 \mathbf{l}_\delta)(\mathbf{l}_\beta \times_2 \mathbf{l}_\gamma) \\
&= \begin{pmatrix} x_\alpha x_\beta x_\gamma x_\delta + y_\alpha x_\beta x_\gamma y_\delta + x_\alpha y_\beta y_\gamma x_\delta + y_\alpha y_\beta y_\gamma y_\delta \\ +x_\alpha y_\beta x_\gamma y_\delta - y_\alpha y_\beta x_\gamma x_\delta - x_\alpha x_\beta y_\gamma y_\delta + y_\alpha x_\beta y_\gamma x_\delta \end{pmatrix} \quad (3.69)
\end{aligned}$$

$$\begin{aligned}
& l_\alpha l_\beta l_\gamma l_\delta \sin(\phi_\alpha + \phi_\beta - \phi_\gamma - \phi_\delta) \\
&= -(\mathbf{l}_\beta \cdot \mathbf{l}_\gamma)(\mathbf{l}_\alpha \times_2 \mathbf{l}_\delta) \\
&= -(\mathbf{l}_\beta \times_2 \mathbf{l}_\gamma)(\mathbf{l}_\alpha \cdot \mathbf{l}_\delta) \\
&= \begin{pmatrix} -x_\alpha x_\beta x_\gamma y_\delta - x_\alpha y_\beta y_\gamma y_\delta + y_\alpha x_\beta x_\gamma x_\delta + y_\alpha y_\beta y_\gamma x_\delta \\ -x_\alpha x_\beta y_\gamma x_\delta + x_\alpha y_\beta x_\gamma x_\delta - y_\alpha x_\beta y_\gamma y_\delta + y_\alpha y_\beta x_\gamma y_\delta \end{pmatrix} \quad (3.70)
\end{aligned}$$

At first glance, the expression (3.68) may appear tedious to implement in a computer program. However, the sequence of inputs to (3.69) and (3.70) $\gamma = (2; 2) \rightarrow (3; 3) \rightarrow (4; 4)$ and $\delta = (c; d) \rightarrow (c; a) \rightarrow (c; b)$ may be used to compute the respective atan2 coefficients in (3.68), where $\alpha = 1$ and $\beta = 2$. The same sequence may be used to compute the log coefficients. Compared with the midpoint approximation method, the number of operations in the analytical integration of torque is roughly the same. Each coefficient of the atan2 and ln functions in (3.68) has twice as many terms as each coefficient in (2.40) and (2.41), but the combined effort of evaluating $F_{x,||}$ and $F_{y,||}$ using (2.40) and (2.41) and subsequently taking the cross product renders the midpoint approximate and analytical integral torque methods equal from the perspective of computational burden. However, the atan2 and ln functions are evaluated only once each in (3.68). In fact, the computation times are observed to be slightly lower for the analytical integration method, and as expected, improved accu-

racy is achieved over the midpoint approximation method, as shown in the following subsection.

Torque Exerted on Point(Line) Elements by Line(Point) Sources

Referring to Figs. 2.6a and 2.6b, the torque exerted on observation point element $\mathbf{p}_2 = (x_c, y_c)$ by line source \mathbf{l}_1 is determined using the expression

$$T_{\cdot|} = -\frac{\mu_0 I_1 I_2}{2\pi l_1} \begin{pmatrix} \begin{pmatrix} x_c \cos(\phi_1) \\ +y_c \sin(\phi_1) \end{pmatrix} \text{atan2} \begin{pmatrix} \mathbf{l}_5 \times_2 \mathbf{l}_6, \\ \mathbf{l}_5 \cdot \mathbf{l}_6 \end{pmatrix} \\ \begin{pmatrix} -x_c \sin(\phi_1) \\ +y_c \cos(\phi_1) \end{pmatrix} \log \left(\frac{l_6}{l_5} \right) \end{pmatrix} \quad (3.71)$$

and the torque on observation line element \mathbf{l}_2 by point source $\mathbf{p}_1 = (x_a, y_a)$ is determined using the expression

$$T_{|\cdot} = \frac{\mu_0 I_1 I_2}{2\pi l_2} \begin{pmatrix} \begin{pmatrix} x_a \cos(\phi_2) \\ +y_a \sin(\phi_2) \end{pmatrix} \text{atan2} \begin{pmatrix} \mathbf{l}_4 \times_2 \mathbf{l}_6, \\ \mathbf{l}_4 \cdot \mathbf{l}_6 \end{pmatrix} \\ \begin{pmatrix} -x_a \sin(\phi_2) \\ +y_a \cos(\phi_2) \end{pmatrix} \log \left(\frac{l_6}{l_4} \right) \end{pmatrix}. \quad (3.72)$$

Torque Exerted on Point Elements by Point Sources

In the case where both source and observation elements are points, the torque exerted on point element $\mathbf{p}_2 = (x_c, y_c)$ by point element $\mathbf{p}_1 = (x_a, y_a)$ is given by

$$T_{..} = \frac{\mu_0 I_1 I_2}{2\pi((x_c - x_a)^2 + (y_c - y_a)^2)} (x_c y_a - x_a y_c) \quad (3.73)$$

3.3.4 Comparison of Torque Calculation Methods

Using either the midpoint approximation or the closed-form integral expression, computing the torque between each rotor element and each stator element and sum-

ming yields the total torque. Under the condition that the mesh elements are located in a rotationally-periodic fashion, the periodicity of the machine geometry can be exploited by computing only the torque on elements of a single rotor pole by the stator elements of all poles and subsequently multiplying by the pole count.

To validate the expressions for force and torque, an MoM-based model of an SPMSM “Design 50” was utilized. Design 50 was taken from the Pareto optimal front of a PBD study detailed in Chapter 4. Its design/geometric parameters and excitation are provided in Table 4.4 and its conductor density is listed in Table 4.5. The results are compared to those obtained using a commercial Finite Element Analysis (FEA) package COMSOL [31]. The mesh of the FEA model was adaptively refined so that calculated quantities could serve as the reference solution. Within the MoM, remanant radial magnetization in the PMs is modeled using a pair of sheet currents along the edges of each magnet—with current magnitude set to $I_{PM} = d_m B_r / (\mu_0 \mu_m)$. The total ampere-turns of stator current in each slot is modeled as a free current point source located at the center of each respective slot. The torque was also computed using the MST method where the numerical integration was performed using MATLAB’s built-in `quadgk` function.

The x - and y -components of force were calculated using (2.45)-(2.46) and (2.49)-(2.50) in Chapter 2 and the torque acting at the midpoint of each element using (3.66). The net torque calculated directly using the force expressions is listed as the “MoM Midpoint” torque within Figures 3.5 - 3.7.

The torque obtained as a function of rotor position is shown in Fig. 3.5. The MoM mesh for this comparison utilized 6,330 elements per pole and the FEA was set to adaptively refine its mesh, eventually reaching 388,644 elements per pole. Visually inspecting the waveforms in Fig. 3.5, it is apparent that the MoM torque integral agrees well with FEA whereas some error is present in the midpoint torque waveform.

Not shown in Fig. 3.5 are data representing the MST-based torque waveform. This is because the MoM Lorentz and MST methods matched nearly exactly in all cases. The average percent error was $1.8 \times 10^{-11}\%$ between MST and Lorentz over the

32 rotor positions in computing the torque waveform in Fig. 3.5. This should come as no surprise since the starting point for deriving the MST is the Lorentz force [23].

The error in the average torque as a function of MoM element count is shown in Fig.3.6. It is interesting that the error in average torque is relatively small even with few elements in either the integrated or the midpoint torque calculations, yet the integrated torque outperforms the midpoint torque method save for one point. The error in the peak-peak torque is shown with respect to element count in Fig. 3.7. At low element counts, the peak-peak error is rather large for both MoM torque predictions, and the midpoint torque gets no lower than 2% at high element counts. Note that the MoM mesh is refined on all surfaces except for the permanent magnet source sheets since these are best represented as a single sheet with uniform sheet current density. This is the source of the steady state error in the midpoint method. Hence, the MoM Midpoint torque provides a means to gauge the error resulting from neglecting the force/radius variation across an element.

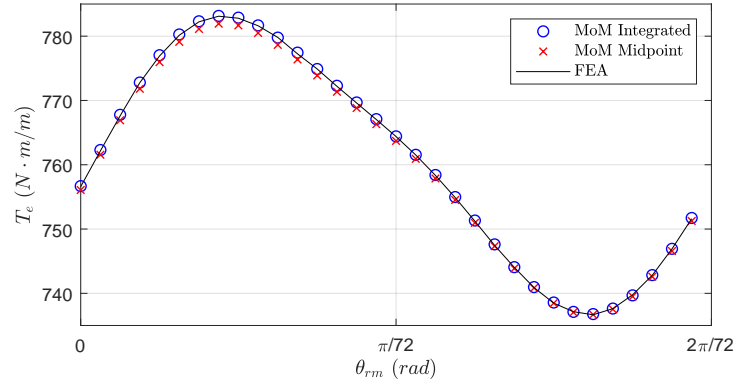


Fig. 3.5.: Torque waveforms over one slot pitch at high mesh resolution.

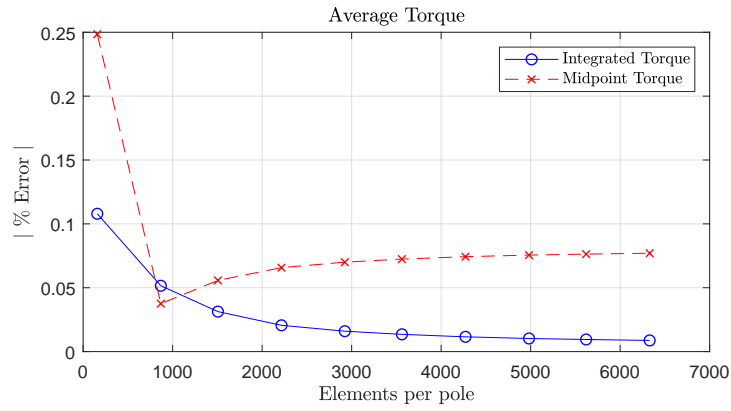


Fig. 3.6.: Percent error in average torque calculation, compared with converged FEA solution.

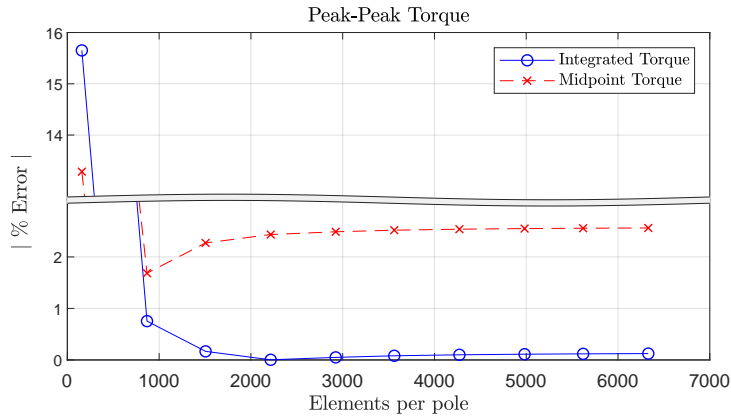


Fig. 3.7.: Percent error in peak-peak torque calculation, compared with converged FEA solution.

3.4 Inductance of Distributed Windings

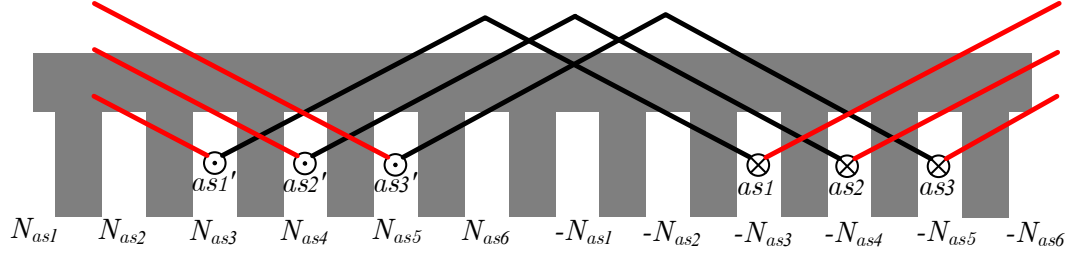


Fig. 3.8.: Distributed windings in stator.

In the design process, it is often desired to evaluate the inductances associated with distributed windings of electric machinery. One may use the inductances within a lumped parameter model such as a qd model of an electric machine [32] to evaluate its performance. In this research, inductances are used in the calculation of required line-line voltage for a given stator current, applied within the optimization study in Chapter 4. In this section, the inductance calculation method from [4], as summarized in Section 2.5, can be extended to the case in which the conductors in a winding are spatially-distributed within stator slots, as shown in Fig. 3.8.

Aside from the distributed nature of the conductors, electric machinery are typically wound with round stator conductors, hence it is desired to represent the conductors as filaments, rather than sheets as was the focus in Section 2.5. Furthermore, stator conductors are not truly filaments but have a finite radius that must also be accounted for. The partial inductance expression (2.67), denoted $L_{p||}$ in this section, quantifies the flux linking a sheet conductor where the flux produced is via a bound sheet current. For electric machinery, a partial inductance expression denoted $L_{p\cdot|}$ is derived in this section which quantifies the flux linking a filamentary stator conductor due to a bound current sheet (subscript denotes mutual partial, sheet to filament). Additionally, two expressions denoted $L_{ps\cdot}$ and $L_{pm\cdot}$ are derived in this section, which respectively quantify the flux linking a filamentary stator conductor due to that fila-

mentary stator conductor itself (subscript denotes self partial of filament) and due to other filamentary stator conductors making up the winding (subscript denotes mutual partial, filament to filament).

3.4.1 Partial Inductance Expressions

Expression (2.67) for $L_{p||}$ was derived by integrating the filament-filament partial inductance expression (2.62) over the lines representing the source and observation sheet cross sections, which amounts to a double integral. We may stop short of integrating the second sheet in (2.63) to obtain the sheet to filament mutual partial inductance as

$$L_{pm.} = -\frac{\mu_0}{4\pi w_2} \begin{pmatrix} (x_{22}^L - x_1^L) \ln((x_{22}^L - x_1^L)^2 + (y_1^L)^2) \\ + 2y_1^L \tan^{-1} \left(\frac{x_{22}^L - x_1^L}{y_1^L} \right) \\ -(x_{21}^L - x_1^L) \ln((x_{21}^L - x_1^L)^2 + (y_1^L)^2) \\ - 2y_1^L \tan^{-1} \left(\frac{x_{21}^L - x_1^L}{y_1^L} \right) \end{pmatrix} \quad (3.74)$$

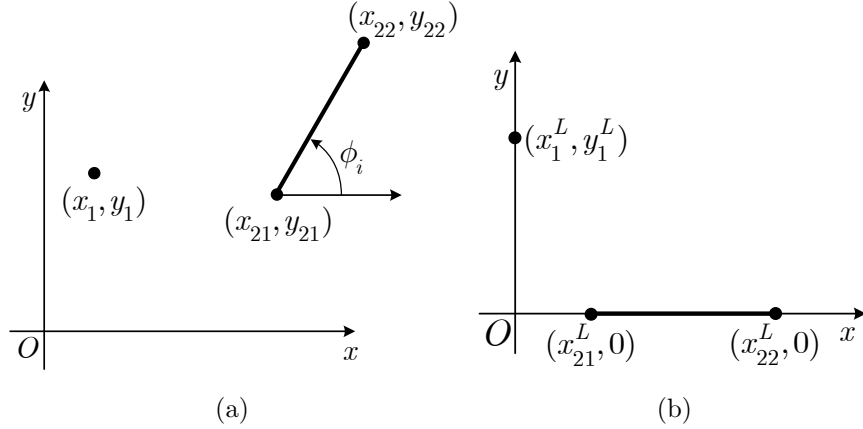


Fig. 3.9.: Sheet and point in original global reference frame (a) and reference frame of $L_{pm.}$ (b).

where x_1^L , y_1^L , x_{21}^L and x_{22}^L are variables which are transformed from the global reference frame, shown in Fig. 3.9a, into a particular reference frame convenient for

evaluating the integration, shown in Fig. 3.9b, using shift and rotation operations. The transformed coordinates are given by

$$(x_1^L, y_1^L) = \begin{pmatrix} -\sin(\phi_i)(x_1 - x_{21}) \\ 0, +\cos(\phi_i)(y_1 - y_{21}) \end{pmatrix} \quad (3.75)$$

$$(x_{21}^L, y_{21}^L) = \begin{pmatrix} -\cos(\phi_i)(x_1 - x_{21}) \\ +\sin(\phi_i)(y_1 - y_{21}), 0 \end{pmatrix} \quad (3.76)$$

$$(x_{22}^L, y_{22}^L) = \begin{pmatrix} l_i - \cos(\phi_i)(x_1 - x_{21}) \\ +\sin(\phi_i)(y_1 - y_{21}), 0 \end{pmatrix} \quad (3.77)$$

where the superscript “ L ” indicates that the quantities have been transformed into the reference frame as shown in Fig. 3.9b. Expression $L_{p||}$ has no self or mutual designation because it can represent either case, depending on the coordinates of the sheets. In contrast, although it is possible to allow the filament path to lie along the sheet cross section, i.e. the filament coincides with one point along the sheet cross section, this lacks meaning. Hence, this inductance expression is designated strictly as a mutual partial inductance since the sheet source and filament path will never spatially coincide, and therefore the subscript “pm” is given.

To determine the self partial inductance of a filament, setting $\rho = 0$ in $L_{p,i,j,\text{fil}}$ of (2.62) isn’t feasible since the result goes to infinity. Paul [33] takes the integral of the vector potential evaluated at the conductor radius r_w using an expression for the vector potential which is dependent on the length of the wire. We may apply this approach instead using $L_{p,i,j,\text{fil}}$ to obtain

$$L_{\text{ps.}} = -\frac{\mu_0}{2\pi} \ln \left(\frac{r_w}{\rho_0} \right) \quad (3.78)$$

where it remains to select ρ_0 . Since this is an arbitrary choice, herein it is selected to be $\rho_0 = 1$. To include the effect of the flux linked within the conductor itself, Paul suggests using the concept of internal inductance, which for round wires is given per-unit-length by

$$L_{\text{internal}} = \frac{\mu_0}{8\pi} \quad (3.79)$$

(which is, interestingly, independent of the wire radius), so that the final expression for L_{ps} is

$$L_{\text{ps}} = \frac{\mu_0}{8\pi} - \frac{\mu_0}{2\pi} \ln(r_w) \quad (3.80)$$

The concept of internal inductance has also been used in the modeling of power system transmission lines such as in [34].

The mutual partial inductance for filaments is determined by setting $\rho = d$ with $\rho_0 = 1$ in (2.62), where d is the between filaments, so that

$$L_{\text{pm}} = -\frac{\mu_0}{2\pi} \ln(d). \quad (3.81)$$

3.4.2 Distributed Winding Inductance: Example Calculation

The following example demonstrates an inductance calculation of the SPMSM “Design 50.” Design 50 was taken from the Pareto optimal front of a PBD study detailed in Chapter 4. Its design/geometric parameters and excitation are provided in Table 4.4 and its conductor density is listed in Table 4.5. The relative permeability of the permanent magnet material was altered to be $\mu_{rm} = 2.0$ so that an enhanced saliency would be present. In the inductance calculation example herein, it has been assumed that the ampere-turns in each slot are segregated by phase, but within each phase group are assumed concentrated at a single point distinct from the other phases in the slot. The remaining parameters and setup are unchanged from that presented in Chapter 4.

The a -phase winding is excited with 1 A and phases b and c are left unexcited. Consider coil $as1$ having $N_{as}(3)$ turns, whose coil sides are represented by $\odot as1'$ and $\otimes as1$ in Fig. 3.8. Note that the prime superscript in this section denotes the coil side with current direction out of the page, as is common in electric machinery notation [32], not a quantity which has been transformed to the reference frame of some element, as is used throughout the rest of this dissertation. The total flux linking coil $as1$ has several contributors. They are: all bound currents in the system, conductors in phase a in pole 1, conductors in phase a in poles $2 - P$, and conductors

from other phases b and c in all poles. To capture the flux linking coil $a1$ due to all bound currents in the system, the sheet to filament mutual partial inductance expression (3.74) is utilized to find the free space inductance

$$\mathbf{L}_{as}^{fs}(i) = \mathbf{L}_{\text{pm}|.}(x_{21}^{L_1}, x_{22}^{L_1}, x_1^{L_1}, y_1^{L_1}) - \mathbf{L}_{\text{pm}|.}(x_{21}^{L_2}, x_{22}^{L_2}, x_1^{L_2}, y_1^{L_2}) \quad (3.82)$$

for each bound sheet current $i = 1 \dots N_b$ in the system, where the super script “ L_1 ” refers to the reference frame of bound current sheet i and the $as1'$ coil side and the superscript “ L_2 ” refers to the reference frame of bound current sheet i and the $as1$ coil side. Each of the coordinate sets in the global reference frame are transformed to the aforementioned respective reference frames using (3.75)-(3.77).

To capture the flux linking coil $a1$ due to all free currents in the system, the filament to filament mutual partial inductance expression (3.81) is used to find the free space inductance of the coil

$$L_{as1,f}^{fs}(j) = \begin{cases} L_{\text{pm}\cdot\cdot}(d_{as1'}) - L_{\text{pm}\cdot\cdot}(d_{as1}) & , \quad \forall j \neq j_{as1'}, j_{as1} \\ L_{\text{ps}\cdot}(r_w) - L_{\text{pm}\cdot\cdot}(d_{as1'}) & , \quad j = j_{as1'} \\ L_{\text{pm}\cdot\cdot}(d_{as1}) - L_{\text{ps}\cdot}(r_w) & , \quad j = j_{as1} \end{cases} \quad (3.83)$$

for each free current $j = 1 \dots N_f$, where $d_{as1'}$ and d_{as1} are the distance between the free current and the respective coil sides $as1'$ and $as1$. The special cases for $j = j_{as1'}$ and $j = j_{as1}$ account for flux linking the winding due to the winding itself, hence the self partial filament expression is used in place of the mutual partial filament expression. In the case that we are determining the flux linking an unexcited coil, such as $bs1$ when calculating L_{bsas} , the special cases are not needed since the winding that creates flux is not the winding from which we are measuring flux. The total flux linking the coil $as1$ is calculated using

$$\lambda_{as1} = N_{as}(3) \left(\left[\mathbf{L}_{as1,b}^{fs} \right]^T \mathbf{I}_b + \left[\mathbf{L}_{as1,f}^{fs} \right]^T \mathbf{I}_f \right). \quad (3.84)$$

It is important to note that the vector of free current \mathbf{I}_f is that used in the MoM equation system (2.6) and therefore it is not populated with the phase currents but

the ampere turns NI of stator excitation. The prior calculation is repeated for the remaining coils $as2-as3$ using the respective turns counts $N_{as}(4)$ and $N_{as}(5)$ and the total flux linkage in pole 1 is their sum:

$$\lambda_{as,p=1} = \lambda_{as1} + \lambda_{as2} + \lambda_{as3}. \quad (3.85)$$

A P pole machine has $P/2$ sets of coils for the whole machine in such a consequent pole winding arrangement, therefore the total flux linkage is multiplied by $P/2$:

$$\lambda_{as} = \frac{P}{2} \lambda_{as,p=1}. \quad (3.86)$$

With L_{asas} and L_{bsas} , it is assumed that the remaining terms of the surface PMSM machine's inductance matrix may be populated by applying appropriate phase shifts, as in an inductive lumped parameter machine model. Such relationships are best illustrated by listing the inductance matrix of a synchronous machine [32]:

$$\begin{aligned} \mathbf{L}_s &= \begin{bmatrix} L_{asas} & L_{asbs} & L_{ascs} \\ L_{bsas} & L_{bsbs} & L_{bscs} \\ L_{csas} & L_{csbs} & L_{cscs} \end{bmatrix} \\ &= L_{ls} \begin{bmatrix} 1 & 0 & 0 \\ 0 & 1 & 0 \\ 0 & 0 & 1 \end{bmatrix} + L_A \begin{bmatrix} 1 & -\frac{1}{2} & -\frac{1}{2} \\ -\frac{1}{2} & 1 & -\frac{1}{2} \\ -\frac{1}{2} & -\frac{1}{2} & 1 \end{bmatrix} \\ &\quad - L_B \begin{bmatrix} \cos(2\theta_r) & \cos 2\left(\theta_r - \frac{\pi}{3}\right) & \cos 2\left(\theta_r + \frac{\pi}{3}\right) \\ \cos 2\left(\theta_r - \frac{\pi}{3}\right) & \cos 2\left(\theta_r - \frac{2\pi}{3}\right) & \cos 2(\theta_r + \pi) \\ \cos 2\left(\theta_r + \frac{\pi}{3}\right) & \cos 2(\theta_r + \pi) & \cos 2\left(\theta_r + \frac{2\pi}{3}\right) \end{bmatrix}. \end{aligned} \quad (3.87)$$

Next, using the reference frame transformation to the rotor [32]

$$\mathbf{K}_s^r = \frac{2}{3} \begin{bmatrix} \cos \theta_r & \cos\left(\theta_r - \frac{2\pi}{3}\right) & \cos\left(\theta_r + \frac{2\pi}{3}\right) \\ \sin \theta_r & \sin\left(\theta_r - \frac{2\pi}{3}\right) & \sin\left(\theta_r + \frac{2\pi}{3}\right) \\ \frac{1}{2} & \frac{1}{2} & \frac{1}{2} \end{bmatrix} \quad (3.88)$$

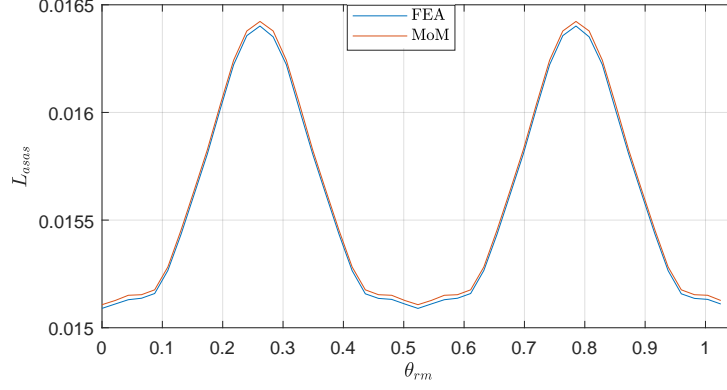


Fig. 3.10.: as winding self inductance vs rotor position.

and its inverse

$$[\mathbf{K}_s^r]^{-1} = \begin{bmatrix} \cos \theta_r & \sin \theta_r & 1 \\ \cos \left(\theta_r - \frac{2\pi}{3} \right) & \sin \left(\theta_r - \frac{2\pi}{3} \right) & 1 \\ \cos \left(\theta_r + \frac{2\pi}{3} \right) & \sin \left(\theta_r + \frac{2\pi}{3} \right) & 1 \end{bmatrix} \quad (3.89)$$

the q - and d -axis inductances are then given by

$$\begin{bmatrix} L_q & 0 & 0 \\ 0 & L_d & 0 \\ 0 & 0 & L_{ls} \end{bmatrix} = \mathbf{K}_s^r \mathbf{L}_s [\mathbf{K}_s^r]^{-1}. \quad (3.90)$$

The inductance calculation procedure previously described was applied to the modified Design 50 machine. The MoM mesh utilized 1014 elements per pole. The rotor was swept across an angular span corresponding to two pole pitches divided into 48 positions where the inductance calculation procedure was applied at each rotor position. The MoM-predicted self inductance of the stator a -phase winding, L_{asas} , is shown in Fig. 3.10 and is compared against the FEA prediction of the same inductance. The MoM-predicted mutual inductance between the stator a -phase and b -phase, L_{bsas} , is shown in Fig. 3.11 and is compared against the FEA prediction of the same inductance. The MoM-predicted q - and d -axis inductances are shown in Fig. 3.12. The same transformation is applied to the FEA-predicted inductances, and they are compared with the MoM inductance. The waveforms are in good agreement.

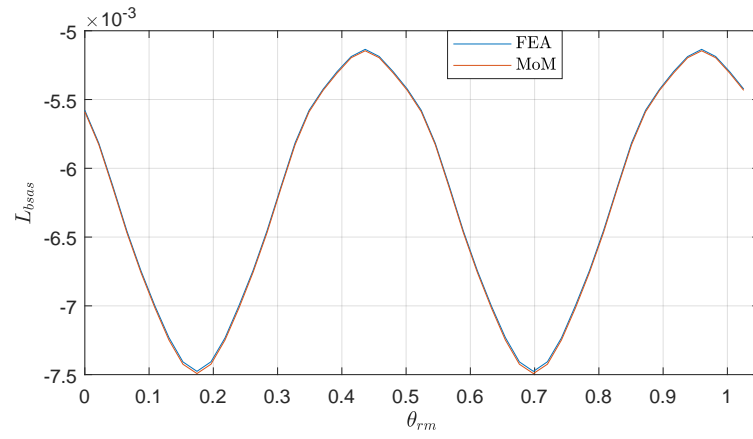


Fig. 3.11.: as - bs mutual inductance vs rotor position.

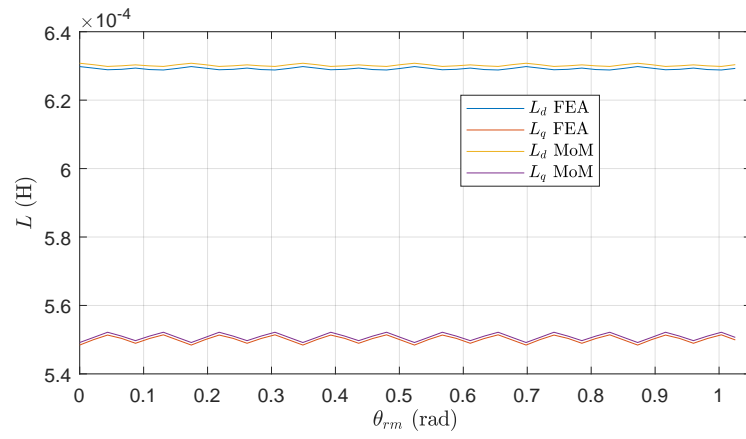


Fig. 3.12.: Inductances L_d and L_q vs rotor position.

As noted above, in the inductance calculation example herein, it has been assumed that the ampere-turns in each slot are segregated by phase, but within each phase group are assumed concentrated at a single point distinct from the other phases in the slot. This assumption minimizes the sizes of influence matrices associated with stator conductors and mesh elements. This assumption does not introduce significant error and for the purpose of exploration of a large design space with many degrees of freedom, some compromise is necessary between accuracy and computational burden. In the case that a higher fidelity model is desired, such as near the end of the design phase, the MoM may be used to analyze windings with multi-conductor coils in the slot where each turn is represented by a distinct filament. In order to avoid the computational burden of computing all partial inductances associated with each distinct filament comprising a winding, one may find the concept of geometric mean radius (GMR) and geometric mean distance (GMD) to be useful – concepts used in transmission line modeling in terrestrial power systems [34] – so that only the aggregate effect of the inductance between bundles of conductors is considered.

3.5 Eliminating Redundancy in Material Boundaries

Based on the MoM formulations presented in Chapter 2, one might choose to mesh a shared boundary dividing two magnetizeable materials twice, where the mesh encircles the volume of each material. An example of two materials with different permeabilities is shown in the inductive ring structure in Figure 3.13. Therein, two materials of different permeabilities constitute the inductive core where the winding is represented as a red dot/cross pair. Shown in Figure 3.13a is the approach using a dual mesh layer, where the mesh elements are anti-coincident, but are shown with separation to better illustrate the arrangement. This double layer of mesh elements is redundant, and can be reduced to a single layer as will be demonstrated. Shown in Figure 3.13b is the same inductive ring using only a single layer of mesh elements.

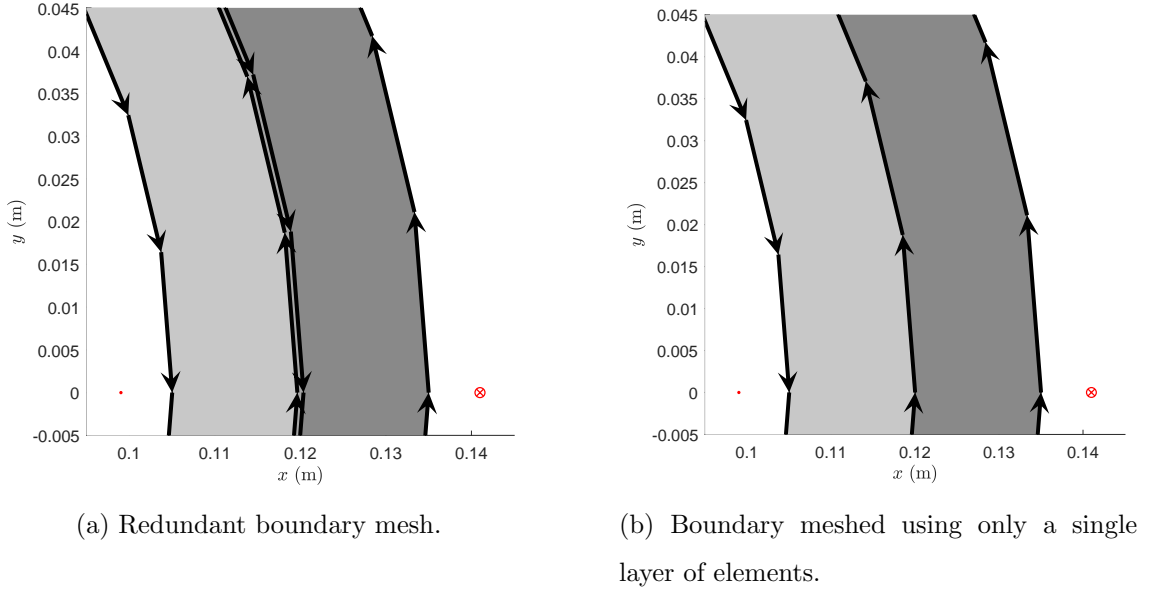


Fig. 3.13.: Material boundary with redundant elements.

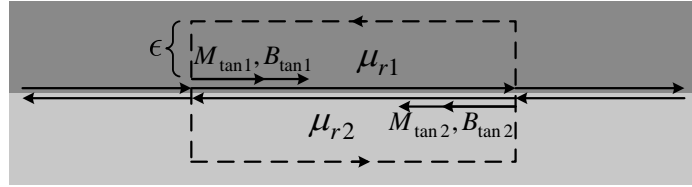


Fig. 3.14.: Example geometry of boundary between magnetizeable materials.

Similar to Ampere's law, the closed-path integral of magnetization gives the enclosed bound current:

$$\oint \vec{M} \cdot d\vec{l} = I_{b,enclosed} \quad (3.91)$$

The closed path taken in integral (3.91) is shown in Figure 3.14 around the two anti-coincident elements. Evaluating the closed path integral as the height $\epsilon \rightarrow 0$, the following relationship is established:

$$-M_{\tan 1}l_1 - M_{\tan 2}l_2 = I_{b1} + I_{b2} \quad (3.92)$$

With $l_1 = l_2 = l$, and noting from Chapter 2 that $\mathbf{B}_{\tan tot} = \mathbf{f}_{B_{tot}M} \mathbf{M}_{\tan}$, (3.92) can be expressed as

$$\frac{B_{\tan 1}}{\frac{\mu_0 \mu_{r1}}{\mu_{r1}-1}} + \frac{B_{\tan 2}}{\frac{\mu_0 \mu_{r2}}{\mu_{r2}-1}} = -\frac{I_{b1} + I_{b2}}{l} \quad (3.93)$$

A similar Amperian loop to that shown in Figure 3.14 can be traversed for the auxiliary field, yielding the enclosed free current [23]:

$$\oint \vec{H} \cdot d\vec{l} = I_{f,enclosed} \quad (3.94)$$

Taking the closed path integral (3.94) around the redundant elements as the height $\epsilon \rightarrow 0$, the following relationship is established:

$$-H_{\tan 1} l_1 - H_{\tan 2} l_2 = I_{f,enclosed} = 0 \quad (3.95)$$

Substituting the relationship $B = \mu H$ for the respective materials, with $l_1 = l_2 = l$:

$$\frac{B_{\tan 1}}{\mu_0 \mu_{r1}} = -\frac{B_{\tan 2}}{\mu_0 \mu_{r2}} \quad (3.96)$$

Rearranging (3.96) and substituting into (3.93),

$$-\frac{\mu_{r1}}{\mu_{r2}} \frac{B_{\tan 2}}{\frac{\mu_0 \mu_{r1}}{\mu_{r1}-1}} + \frac{B_{\tan 2}}{\frac{\mu_0 \mu_{r2}}{\mu_{r2}-1}} = -\frac{I_{b1} + I_{b2}}{l} \quad (3.97)$$

Rearranging, solving for $B_{\tan 2}$ and simplifying,

$$B_{\tan 2} = \left(\frac{\mu_0 \mu_{r1} \mu_{r2}}{\mu_{r1} \mu_{r2} - \mu_{r1}^2} \right) \left(-\frac{I_{b1} + I_{b2}}{l} \right) \quad (3.98)$$

$$= \left(\frac{\mu_0 \frac{\mu_{r2}}{\mu_{r1}}}{\frac{\mu_{r2}}{\mu_{r1}} - 1} \right) \left(-\frac{I_{b1} + I_{b2}}{l} \right) \quad (3.99)$$

If instead of separately modeling the anti-coincident bound currents, we model their combination as a single current I_c , then $I_c = I_{b1} + I_{b2}$, $M_{\tan c} = -I_c/l$ and in terms of the combined current,

$$B_{\tan 2} = \left(\frac{\mu_0 \frac{\mu_{r2}}{\mu_{r1}}}{\frac{\mu_{r2}}{\mu_{r1}} - 1} \right) \left(-\frac{I_c}{l} \right) = \left(\frac{\mu_0 \mu_{rc}}{\mu_{rc} - 1} \right) M_{\tan c} \quad (3.100)$$

where the combined relative permeability μ_{rc} is defined as

$$\mu_{rc} = \frac{\mu_{r2}}{\mu_{r1}} \quad (3.101)$$

In summary, the mesh representing a boundary between two magnetizeable materials can be transformed from one which has two anti-coincident layers to one having only a single layer of mesh elements. The elements in the single mesh layer have a relative permeability which models the combined effect of both materials. Finally, for the single layer of mesh elements, the relationship $\mathbf{f}_{B_{tot}M}$ becomes

$$\mathbf{f}_{B_{tot}M}(i, i) = \frac{\mu_0 \mu_{rc}}{\mu_{rc} - 1} \quad (3.102)$$

This element reduction technique has been utilized to model the boundary between the permanent magnets and the outer rotor steel diameter.

Although this analysis has only considered elements and their corresponding nodes which are anti-coincident, it is possible to generate a mesh along such a boundary in which the two mesh layers are not coincident in any fashion. Such a mesh may lead to elements which intersect. Such a situation is problematic, as it has no physical interpretation. Interestingly, no singularities have been encountered when populating matrix entries in \mathbf{f}_{BM} corresponding to two intersecting elements. Nonetheless, the element reduction technique described herein avoids the need to consider intersecting elements on shared material boundaries.

3.6 Exploitation of Geometric Periodicity

The geometry of electric machinery exhibits angular periodicity about the machine axis. Such a structure is referred to as a discrete body-of-revolution (DBOR). For example, a machine with integer slot/pole/phase has a geometric period of one pole because the geometry repeats itself once every pole. It is the goal of this section to demonstrate how to take advantage of this periodicity in order to decrease the computation time. Such techniques are utilized in the analysis of electromagnetic scattering problems [2, 35–37] in addition to BEM-based acoustics problems [38]. In contrast, within FEA-based electric machine models, the concept of exploiting the geometric periodicity is achieved through the use of so-called periodic boundary conditions [21]. By exploiting periodicity within FEA, a volume mesh of only a single pole is required,

hence reducing the largest component of the FEA solution considerably, roughly by a factor of $1/P$. The only additional computational cost is “the expense of a somewhat larger bandwidth” [21], that is that the system matrix is altered slightly, although the sparseness is affected little. The DBOR reduction procedure will be derived in the following subsection for the linear Galerkin formulation. In the subsequent subsection, the DBOR reduction for the Galerkin formulation is extended to the case of the point-matching formulation. Lastly, it is shown how the DBOR reduction of the point-matching formulation may be applied to model nonlinear materials/equation systems.

3.6.1 DBOR Reduction for Galerkin Formulations

The $N \times N$ system of equations to be solved in the MoM procedure is represented as $\mathbf{A}\mathbf{x} = \mathbf{b}$. In the equation system, $\mathbf{A} = (\mathbf{f}_{B_{tot}} - \mathbf{f}_{BM})$, $\mathbf{x} = \mathbf{M}_{tan}$ and $\mathbf{b} = \mathbf{f}_{BI_f}\mathbf{I}_f + \mathbf{f}_{BM_{PM}}\mathbf{M}_{PM}$. By organizing the N unknowns within the equation system so that they are grouped by pole then it is apparent that the system influence matrix happens to be block-circulant, and can be written in terms of sub-matrices $[\mathbf{A}]_1 - [\mathbf{A}]_P$ as

$$\begin{bmatrix} [\mathbf{A}]_1 & [\mathbf{A}]_2 & [\mathbf{A}]_3 & \cdots & [\mathbf{A}]_P \\ [\mathbf{A}]_P & [\mathbf{A}]_1 & [\mathbf{A}]_2 & \cdots & [\mathbf{A}]_{P-1} \\ [\mathbf{A}]_{P-1} & [\mathbf{A}]_P & [\mathbf{A}]_1 & \cdots & [\mathbf{A}]_{P-2} \\ \vdots & \vdots & \vdots & \ddots & \vdots \\ [\mathbf{A}]_2 & [\mathbf{A}]_3 & [\mathbf{A}]_4 & \cdots & [\mathbf{A}]_1 \end{bmatrix} \begin{Bmatrix} \{\mathbf{x}\}_1 \\ \{\mathbf{x}\}_2 \\ \{\mathbf{x}\}_3 \\ \vdots \\ \{\mathbf{x}\}_P \end{Bmatrix} = \begin{Bmatrix} \{\mathbf{b}\}_1 \\ \{\mathbf{b}\}_2 \\ \{\mathbf{b}\}_3 \\ \vdots \\ \{\mathbf{b}\}_P \end{Bmatrix} \quad (3.103)$$

for a machine with P poles where each pole is meshed into N_P elements. Such an organization of the unknowns is consistent with the notion of meshing only one pole and subsequently applying rotation operations to form the mesh of the remaining poles. In fact it is a requirement that the mesh have the property of being rotationally periodic to apply the DBOR reduction process. Also note that the ordering of the elements within each respective pole must be the same. Further note that each sub-

matrix $[\mathbf{A}]$ has dimensions $N_P \times N_P$, each sub-vector $\{\mathbf{x}\}$ and $\{\mathbf{b}\}$ have dimensions $N_P \times 1$ where $N_P = N/P$. All the unique information is contained within sub-matrices $[\mathbf{A}]_1 - [\mathbf{A}]_P$, and so it is desired to avoid repeating this information by assembling the entire system matrix. Simply computing the elements of the entire system matrix and storing them in computer memory is often the most time-consuming component of the MoM procedure, regardless of having closed form expressions to populate each matrix entry given in [4]. The dense or full nature of system matrices in integral equation methods is mostly to blame for these long computation times.

It is well-known that a generic $n \times n$ circulant matrix \mathbf{C} is diagonalized by the discrete Fourier transform (DFT) matrix [39]:

$$\mathbf{C} = \begin{bmatrix} c_1 & c_2 & \dots & c_n \\ c_n & c_1 & \dots & c_{n-1} \\ \vdots & \vdots & \ddots & \vdots \\ c_2 & c_3 & \dots & c_1 \end{bmatrix} = \mathbf{F} \mathbf{\Lambda} \mathbf{F}^{-1} \quad (3.104)$$

where $\mathbf{F}(j, k) = e^{-i\frac{2\pi}{n}(j-1)(k-1)}$ is the $n \times n$ DFT matrix, $j = 1 \dots n$, $k = 1 \dots n$ and $i = \sqrt{-1}$. In (3.104) the matrix $\mathbf{\Lambda}$ has only diagonal elements which are the eigenvalues of \mathbf{C} , given by

$$\begin{bmatrix} \lambda_1 \\ \lambda_2 \\ \vdots \\ \lambda_n \end{bmatrix} = \mathbf{F} \begin{bmatrix} c_1 \\ c_2 \\ \vdots \\ c_n \end{bmatrix} \quad (3.105)$$

In the case of block-circulant matrices, the Kronecker product can leverage the DFT matrix to act on the sub-matrices. The Kronecker product, symbolized by \otimes , is defined as follows:

$$\mathbf{D} \otimes \mathbf{E} = \begin{bmatrix} d_{11}\mathbf{E} & d_{12}\mathbf{E} & \dots & d_{1n}\mathbf{E} \\ d_{21}\mathbf{E} & d_{22}\mathbf{E} & \dots & d_{2n}\mathbf{E} \\ \vdots & \vdots & \ddots & \vdots \\ d_{m1}\mathbf{E} & d_{m2}\mathbf{E} & \dots & d_{mn}\mathbf{E} \end{bmatrix} \quad (3.106)$$

for the $m \times n$ matrix \mathbf{D} and the $p \times q$ matrix \mathbf{E} . The Kronecker product $\mathbf{D} \otimes \mathbf{E}$ is a block matrix with dimensions $mp \times nq$. Using this tool, the entire system matrix \mathbf{A} can be block-diagonalized:

$$\mathbf{A} = (\mathbf{F} \otimes \mathbf{I}_{N_P}) \begin{bmatrix} [\tilde{\mathbf{A}}]_1 & \mathbf{0} & \dots & \mathbf{0} \\ \mathbf{0} & [\tilde{\mathbf{A}}]_2 & \dots & \mathbf{0} \\ \vdots & \vdots & \ddots & \vdots \\ \mathbf{0} & \mathbf{0} & \dots & [\tilde{\mathbf{A}}]_P \end{bmatrix} (\mathbf{F}^{-1} \otimes \mathbf{I}_{N_P}) \quad (3.107)$$

where \mathbf{I}_{N_P} is the identity matrix of dimensions $N_P \times N_P$, N_P is the number of unknowns per pole, and \mathbf{F} is now the $P \times P$ DFT matrix with entries $\mathbf{F}(j, k) = e^{-i\frac{2\pi}{P}(j-1)(k-1)}$. By utilizing the Kronecker product in this way, the block equation system may be treated in a more general way whereby sub-matrices and sub-vectors are treated as individual elements in a larger matrix (as in the case where the identity matrix $\mathbf{I}_{N_P} = 1$).

By substituting (3.107) into (3.103), only P independent systems need to be solved:

$$\begin{bmatrix} [\tilde{\mathbf{A}}]_1 & \mathbf{0} & \dots & \mathbf{0} \\ \mathbf{0} & [\tilde{\mathbf{A}}]_2 & \dots & \mathbf{0} \\ \vdots & \vdots & \ddots & \vdots \\ \mathbf{0} & \mathbf{0} & \dots & [\tilde{\mathbf{A}}]_P \end{bmatrix} \begin{bmatrix} \{\tilde{\mathbf{x}}\}_1 \\ \{\tilde{\mathbf{x}}\}_2 \\ \vdots \\ \{\tilde{\mathbf{x}}\}_P \end{bmatrix} = \begin{bmatrix} \{\tilde{\mathbf{b}}\}_1 \\ \{\tilde{\mathbf{b}}\}_2 \\ \vdots \\ \{\tilde{\mathbf{b}}\}_P \end{bmatrix} \quad (3.108)$$

where

$$\begin{bmatrix} \{\tilde{\mathbf{x}}\}_1 \\ \{\tilde{\mathbf{x}}\}_2 \\ \vdots \\ \{\tilde{\mathbf{x}}\}_P \end{bmatrix} = (\mathbf{F}^{-1} \otimes \mathbf{I}_{N_P}) \begin{bmatrix} \{\mathbf{x}\}_1 \\ \{\mathbf{x}\}_2 \\ \vdots \\ \{\mathbf{x}\}_P \end{bmatrix} \quad (3.109)$$

and

$$\begin{bmatrix} \{\tilde{\mathbf{b}}\}_1 \\ \{\tilde{\mathbf{b}}\}_2 \\ \vdots \\ \{\tilde{\mathbf{b}}\}_P \end{bmatrix} = (\mathbf{F}^{-1} \otimes \mathbf{I}_{N_P}) \begin{bmatrix} \{\mathbf{b}\}_1 \\ \{\mathbf{b}\}_2 \\ \vdots \\ \{\mathbf{b}\}_P \end{bmatrix} \quad (3.110)$$

and analogous to (3.105), $[\tilde{\mathbf{A}}]_1 - [\tilde{\mathbf{A}}]_P$ are given by

$$\begin{bmatrix} [\tilde{\mathbf{A}}]_1 \\ [\tilde{\mathbf{A}}]_2 \\ \vdots \\ [\tilde{\mathbf{A}}]_P \end{bmatrix} = (\mathbf{F} \otimes \mathbf{I}_{N_P}) \begin{bmatrix} [\mathbf{A}]_1 \\ [\mathbf{A}]_2 \\ \vdots \\ [\mathbf{A}]_P \end{bmatrix} \quad (3.111)$$

which requires fewer computer operations than by directly block-diagonalizing using $(\mathbf{F}^{-1} \otimes \mathbf{I}_{N_P})\mathbf{A}(\mathbf{F} \otimes \mathbf{I}_{N_P})$. More importantly, directly block-diagonalizing \mathbf{A} would require the assembly of the entire system matrix, which we have set out to avoid doing in the first place.

A procedure to solve the entire system of equations $\mathbf{A}\mathbf{x} = \mathbf{b}$, without assembly of the entire influence matrix \mathbf{A} , is as follows:

1. Compute $\{\tilde{\mathbf{b}}\}_1 - \{\tilde{\mathbf{b}}\}_P$ using (3.110).
2. Compute $[\tilde{\mathbf{A}}]_1 - [\tilde{\mathbf{A}}]_P$ using (3.111).
3. Solve the P individual sub-systems for $\{\tilde{\mathbf{x}}\}_1 - \{\tilde{\mathbf{x}}\}_P$ as in (3.108).
4. The solution to the entire system of equations $\mathbf{A}\mathbf{x} = \mathbf{b}$ is given by transforming $\{\tilde{\mathbf{x}}\}_1 - \{\tilde{\mathbf{x}}\}_P$ back to $\{\mathbf{x}\}_1 - \{\mathbf{x}\}_P$ using the relationship in (3.109). It should be noted that due to the properties of the Kronecker product, the inverse relationship of (3.109) is given readily by $(\mathbf{F}^{-1} \otimes \mathbf{I}_{N_P})^{-1} = ((\mathbf{F}^{-1})^{-1}) \otimes \mathbf{I}_{N_P}^{-1} = \mathbf{F} \otimes \mathbf{I}_{N_P}$. Moreover, the inverse of the $P \times P$ DFT matrix is $\mathbf{F}^{-1} = \frac{1}{P}\mathbf{F}^*$.

A note on the implementation of the preceding procedure: although the quantities $(\mathbf{F} \otimes \mathbf{I}_{N_P})$ and $(\mathbf{F}^{-1} \otimes \mathbf{I}_{N_P})$ help to demonstrate the block-diagonalization procedure, there is a better way to perform these “block transforms” from the perspective of computation. In particular, MATLAB has built-in Fast Fourier Transform (FFT) functions which perform the DFT with $\mathcal{O}(n \log n)$ operations, rather than the $\mathcal{O}(n^2)$ operations of the matrix-vector product approach in (3.110)-(3.109). For example, in MATLAB the command `b_tilde_mtx = ifft(b_mtx,[],2)` will take the

inverse DFT of each row of $\mathbf{b_mtx}$, where $\mathbf{b_mtx}$ is a matrix with columns $\{\mathbf{b}\}_1 - \{\mathbf{b}\}_P$. Then the output $\mathbf{b_tilde_mtx}$ is a matrix with columns $\{\tilde{\mathbf{b}}\}_1 - \{\tilde{\mathbf{b}}\}_P$.

One further simplification can be made to the DBOR reduction process, accompanied with further reduction in computation time. The angular period of the machine geometry is a single pole, and under normal electric machinery operating conditions the excitation is periodic in nature, with angular period of two poles. In particular, the input vector \mathbf{b} can be written in terms of only $\{\mathbf{b}\}_1$, alternating in sign:

$$\mathbf{b} = \begin{bmatrix} \{\mathbf{b}\}_1 \\ -\{\mathbf{b}\}_1 \\ \{\mathbf{b}\}_1 \\ -\{\mathbf{b}\}_1 \\ \vdots \\ \{\mathbf{b}\}_1 \\ -\{\mathbf{b}\}_1 \end{bmatrix} \quad (3.112)$$

In which case, when multiplied together with $(\mathbf{F}^{-1} \otimes \mathbf{I}_{N_P})$, only one block-row is nonzero:

$$(\mathbf{F}^{-1} \otimes \mathbf{I}_{N_P}) \begin{bmatrix} \{\mathbf{b}\}_1 \\ -\{\mathbf{b}\}_1 \\ \{\mathbf{b}\}_1 \\ -\{\mathbf{b}\}_1 \\ \vdots \\ \{\mathbf{b}\}_1 \\ -\{\mathbf{b}\}_1 \end{bmatrix} = \begin{bmatrix} \mathbf{0} \\ \vdots \\ \mathbf{0} \\ \{\tilde{\mathbf{b}}\}_{P/2+1} \\ \mathbf{0} \\ \vdots \\ \mathbf{0} \end{bmatrix} = \begin{bmatrix} \mathbf{0} \\ \vdots \\ \mathbf{0} \\ \{\mathbf{b}\}_1 \\ \mathbf{0} \\ \vdots \\ \mathbf{0} \end{bmatrix} \quad (3.113)$$

This result is evident if one considers the input vector to be a cosine wave, sampled only at its extrema, with amplitude $\{\mathbf{b}\}_1$, i.e. $\mathbf{b} = \{\mathbf{b}\}_1 \cos(\pi k)$ for $k = 1 \dots P$; the DFT of which is the discrete impulse function $\delta[n - (P/2 + 1)]$ scaled by $\{\mathbf{b}\}_1$. Since only $\{\tilde{\mathbf{b}}\}_{P/2+1}$ is nonzero, only the solution of sub-system $P/2 + 1$ is nonzero, and therefore of $\{\tilde{\mathbf{x}}\}_1 - \{\tilde{\mathbf{x}}\}_P$ only $\{\tilde{\mathbf{x}}\}_{P/2+1}$ is nonzero. Restated for emphasis, only the

subsystem of index $P/2 + 1$ need be solved. Consequently, the solution of the entire system is given by

$$(\mathbf{F} \otimes \mathbf{I}_{N_P}) \begin{bmatrix} \mathbf{0} \\ \vdots \\ \mathbf{0} \\ \{\tilde{\mathbf{x}}\}_{P/2+1} \\ \mathbf{0} \\ \vdots \\ \mathbf{0} \end{bmatrix} = \begin{bmatrix} \{\tilde{\mathbf{x}}\}_{P/2+1} \\ -\{\tilde{\mathbf{x}}\}_{P/2+1} \\ \{\tilde{\mathbf{x}}\}_{P/2+1} \\ -\{\tilde{\mathbf{x}}\}_{P/2+1} \\ \vdots \\ \{\tilde{\mathbf{x}}\}_{P/2+1} \\ -\{\tilde{\mathbf{x}}\}_{P/2+1} \end{bmatrix} \quad (3.114)$$

In summary, with periodic excitation, the solution procedure can be simplified to the following:

1. Perform only one block-row of the transform in (3.111), yielding $[\tilde{\mathbf{A}}]_{P/2+1}$. Or equivalently, $[\tilde{\mathbf{A}}]_{P/2+1} = \sum_{k=1}^P (-1)^{(k-1)} [\mathbf{A}]_k$. Note that a complete DFT need not be performed since it is known *a priori* that only one block-row of the DFT is non-zero.
2. Solve the single system $[\tilde{\mathbf{A}}]_{P/2+1} \{\tilde{\mathbf{x}}\}_{P/2+1} = \{\mathbf{b}\}_1$.
3. The solution to the entire system of equations is a vector composed of $\{\tilde{\mathbf{x}}\}_{P/2+1}$, alternating in sign, as in (3.114).

Using Fourier analysis combined with the Kronecker product, we have shown that this block circulant system will yield a periodic bound current solution provided that the input is also periodic. Using this “20/20” hindsight, in the simple example of a 4-pole machine, substituting the periodic excitation and solution, the entire system of equations can be represented as

$$\begin{bmatrix} [\mathbf{A}]_1 & [\mathbf{A}]_2 & [\mathbf{A}]_3 & [\mathbf{A}]_4 \\ [\mathbf{A}]_4 & [\mathbf{A}]_1 & [\mathbf{A}]_2 & [\mathbf{A}]_3 \\ [\mathbf{A}]_3 & [\mathbf{A}]_4 & [\mathbf{A}]_1 & [\mathbf{A}]_2 \\ [\mathbf{A}]_2 & [\mathbf{A}]_3 & [\mathbf{A}]_4 & [\mathbf{A}]_1 \end{bmatrix} \begin{pmatrix} \{\mathbf{x}\}_1 \\ -\{\mathbf{x}\}_1 \\ \{\mathbf{x}\}_1 \\ -\{\mathbf{x}\}_1 \end{pmatrix} = \begin{pmatrix} \{\mathbf{b}\}_1 \\ -\{\mathbf{b}\}_1 \\ \{\mathbf{b}\}_1 \\ -\{\mathbf{b}\}_1 \end{pmatrix} \quad (3.115)$$

Expanding, each block-row of (3.115) comes out to be

$$([\mathbf{A}]_1 - [\mathbf{A}]_2 + [\mathbf{A}]_3 - [\mathbf{A}]_4)\{\mathbf{x}\}_1 = \{\mathbf{b}\}_1 \quad (3.116)$$

therefore only one sub-system must be solved to find $\{\mathbf{x}\}_1$. Equation (3.116) succinctly represents the simplified DBOR reduction procedure given above.

Some computation time comparisons are now given for the DBOR solver. An example 12 pole machine, meshed with $N_P = 194$ elements per pole, requires 1.879 s to assemble the required matrices in MATLAB for the case of the entire system and 0.234 s for the DBOR solver. This is an 8-fold decrease in computation time. It should be noted that the improvement is expected to be proportional to the pole count, since this is the proportion of the entire system matrix that must be populated in order to apply the DBOR reduction.

3.6.2 DBOR Reduction for Linear Point Matching Formulations

The unknown quantity in the Galerkin MoM formulations used herein is the tangential magnetization vector, \mathbf{M}_{tan} , where it is understood that the tangent component of magnetization is with respect to the local coordinate system of the bound current element. As a consequence of this local coordinate system, as in (3.115), the solution of the entire system is comprised of the single pole solution alternating in sign every pole. However, in the point-matching MoM formulations used herein, the unknown quantity is \mathbf{M}_{xy} - the x - and y - component of magnetization - where the x - and y - components are with respect to the global coordinate system. Hence, we do not expect the \mathbf{M}_{xy} solution to exhibit the same direct periodicity as the \mathbf{M}_{tan} solu-

tion, but we *can* expect the \mathbf{M}_{xy} solution of the adjacent pole to be related through a series of rotation operations, that is we expect that

$$\mathbf{M}_{xy} = \begin{bmatrix} \{\mathbf{M}_{xy}\}_1 \\ \{\mathbf{M}_{xy}\}_2 \\ \vdots \\ \{\mathbf{M}_{xy}\}_{P-1} \\ \{\mathbf{M}_{xy}\}_P \end{bmatrix} = \underbrace{\begin{bmatrix} [\mathbf{R}]_1 & & & \mathbf{0} \\ & [\mathbf{R}]_2 & & \\ & & \ddots & \\ \mathbf{0} & & & [\mathbf{R}]_P \end{bmatrix}}_{\mathbf{R}} \underbrace{\begin{bmatrix} \{\mathbf{M}_{xy}\}_1 \\ -\{\mathbf{M}_{xy}\}_1 \\ \vdots \\ \{\mathbf{M}_{xy}\}_1 \\ -\{\mathbf{M}_{xy}\}_1 \end{bmatrix}}_{\mathbf{M}_{xy,\text{periodic}}} = \mathbf{R}\mathbf{M}_{xy,\text{periodic}} \quad (3.117)$$

In (3.117), each of the submatrices $[\mathbf{R}]_1$ - $[\mathbf{R}]_P$ within \mathbf{R} are themselves block-diagonal matrices, the diagonal blocks of which are rotation matrices:

$$[\mathbf{R}]_i = \begin{bmatrix} \begin{bmatrix} \cos(\theta_i) & -\sin(\theta_i) \\ \sin(\theta_i) & \cos(\theta_i) \end{bmatrix} & & & \mathbf{0} \\ & \begin{bmatrix} \cos(\theta_i) & -\sin(\theta_i) \\ \sin(\theta_i) & \cos(\theta_i) \end{bmatrix} & & \\ & & \ddots & \\ \mathbf{0} & & & \begin{bmatrix} \cos(\theta_i) & -\sin(\theta_i) \\ \sin(\theta_i) & \cos(\theta_i) \end{bmatrix} \end{bmatrix} \quad (3.118)$$

for $i = 1 \dots P$ and $\theta_i = \frac{2\pi(i-1)}{P}$. In a similar fashion to \mathbf{M}_{xy} , the total magnetic field in the 1^{st} pole may be related to the field in the remaining poles of the machine by

$$\mathbf{B}_{xy,\text{tot}} = \mathbf{R} \begin{bmatrix} \{\mathbf{B}_{xy,\text{tot}}\}_1 \\ -\{\mathbf{B}_{xy,\text{tot}}\}_1 \\ \vdots \\ \{\mathbf{B}_{xy,\text{tot}}\}_1 \\ -\{\mathbf{B}_{xy,\text{tot}}\}_1 \end{bmatrix} = \mathbf{R}\mathbf{B}_{xy,\text{tot},\text{periodic}} \quad (3.119)$$

The equation system (2.6) in the point matching formulation may be expressed in a simplified way as

$$\mathbf{B}_{xy,\text{tot}} = \mathbf{f}_{B_{\text{tot}}M} \mathbf{M}_{xy} = \mathbf{f}_{BM} \mathbf{M}_{xy} + \mathbf{B}_{xy,\text{source}} \quad (3.120)$$

where $\mathbf{B}_{xy,\text{source}}$ represents the magnetic field contribution of any sources present, i.e. free current sources, PM sources, or a combination of both. Substituting (3.117) and (3.119) into (3.120), we have that

$$\mathbf{R} \mathbf{B}_{xy,\text{tot,alt}} = \mathbf{f}_{B_{\text{tot}}M} \mathbf{R} \mathbf{M}_{xy,\text{periodic}} = \mathbf{f}_{BM} \mathbf{R} \mathbf{M}_{xy,\text{periodic}} + \mathbf{B}_{xy,\text{source}} \quad (3.121)$$

Multiplying all sides by \mathbf{R}^{-1} on the left,

$$\mathbf{B}_{xy,\text{tot,periodic}} = \mathbf{R}^{-1} \mathbf{f}_{B_{\text{tot}}M} \mathbf{R} \mathbf{M}_{xy,\text{periodic}} = \mathbf{R}^{-1} (\mathbf{f}_{BM} \mathbf{R} \mathbf{M}_{xy,\text{periodic}} + \mathbf{B}_{xy,\text{source}}) \quad (3.122)$$

Rearranging (3.122) yields the equation system

$$\mathbf{R}^{-1} (\mathbf{f}_{B_{\text{tot}}M} - \mathbf{f}_{BM}) \mathbf{R} \mathbf{M}_{xy,\text{periodic}} = \mathbf{R}^{-1} \mathbf{B}_{xy,\text{source}} \quad (3.123)$$

Further note that as is typically the case, the magnetic fields due to the sources will be periodic with respect to rotation, that is to say the magnetic field source $\mathbf{B}_{xy,\text{source}}$, similar to (3.119), may be written as

$$\mathbf{B}_{xy,\text{source}} = \mathbf{R} \begin{bmatrix} \{\mathbf{B}_{xy,\text{source}}\}_1 \\ -\{\mathbf{B}_{xy,\text{source}}\}_1 \\ \vdots \\ \{\mathbf{B}_{xy,\text{source}}\}_1 \\ -\{\mathbf{B}_{xy,\text{source}}\}_1 \end{bmatrix} = \mathbf{R} \mathbf{B}_{xy,\text{source,periodic}} \quad (3.124)$$

Substituting (3.124) into (3.123) yields

$$\mathbf{R}^{-1} (\mathbf{f}_{B_{\text{tot}}M} - \mathbf{f}_{BM}) \mathbf{R} \mathbf{M}_{xy,\text{periodic}} = \mathbf{B}_{xy,\text{source,periodic}} \quad (3.125)$$

Note that the resultant system matrix $\mathbf{R}^{-1} (\mathbf{f}_{B_{\text{tot}}M} - \mathbf{f}_{BM}) \mathbf{R}$ is block-circulant. Although not shown explicitly herein, it has been verified numerically that this is the

case, and indeed we can expect the matrix to be block circulant as this structure is required to map the alternating input $\mathbf{M}_{xy,\text{periodic}}$ to an alternating output $\mathbf{B}_{xy,\text{periodic}}$. Hence (3.125) has the proper structure that we may now exploit the periodicity, solving this system using a similar procedure as the previous subsection. Letting $\mathbf{A} = \mathbf{R}^{-1}(\mathbf{f}_{B_{\text{tot}M}} - \mathbf{f}_{BM})\mathbf{R}$ for the remainder of this analysis, in order to utilize the DBOR reduction procedure described in the prior section, it is required to compute only one block-row of \mathbf{A} . It is shown in the following expansion that this may be accomplished by computing only one block-row of the matrix $\mathbf{f} = \mathbf{f}_{B_{\text{tot}M}} - \mathbf{f}_{BM}$, hence retaining the computational benefits of the DBOR reduction procedure. First, since it is straightforward to show that

$$\mathbf{R}^{-1} = \begin{bmatrix} [\mathbf{R}]_1^{-1} & & & \mathbf{0} \\ & [\mathbf{R}]_2^{-1} & & \\ & & \ddots & \\ \mathbf{0} & & & [\mathbf{R}]_P^{-1} \end{bmatrix}, \quad (3.126)$$

then expanding \mathbf{A} yields

$$\mathbf{A} = \begin{bmatrix} [\mathbf{R}]_1^{-1} & & & \mathbf{0} \\ & [\mathbf{R}]_2^{-1} & & \\ & & \ddots & \\ \mathbf{0} & & & [\mathbf{R}]_P^{-1} \end{bmatrix} \begin{bmatrix} [\mathbf{f}]_{11} & [\mathbf{f}]_{12} & \dots & [\mathbf{f}]_{1P} \\ [\mathbf{f}]_{21} & [\mathbf{f}]_{22} & \dots & [\mathbf{f}]_{2P} \\ \vdots & \vdots & \ddots & \vdots \\ [\mathbf{f}]_{P1} & [\mathbf{f}]_{P2} & \dots & [\mathbf{f}]_{PP} \end{bmatrix} \begin{bmatrix} [\mathbf{R}]_1 & & & \mathbf{0} \\ & [\mathbf{R}]_2 & & \\ & & \ddots & \\ \mathbf{0} & & & [\mathbf{R}]_P \end{bmatrix}. \quad (3.127)$$

In performing the multiplication of the two matrices on the right, the submatrices $[\mathbf{R}]_1$ - $[\mathbf{R}]_P$ act to scale the columns of \mathbf{f} , yielding

$$\mathbf{A} = \begin{bmatrix} [\mathbf{R}]_1^{-1} & & & \mathbf{0} \\ & [\mathbf{R}]_2^{-1} & & \\ & & \ddots & \\ \mathbf{0} & & & [\mathbf{R}]_P^{-1} \end{bmatrix} \left[\begin{pmatrix} [\mathbf{f}]_{11} \\ [\mathbf{f}]_{21} \\ \vdots \\ [\mathbf{f}]_{P1} \end{pmatrix} [\mathbf{R}]_1, \begin{pmatrix} [\mathbf{f}]_{12} \\ [\mathbf{f}]_{22} \\ \vdots \\ [\mathbf{f}]_{P2} \end{pmatrix} [\mathbf{R}]_2, \dots, \begin{pmatrix} [\mathbf{f}]_{1P} \\ [\mathbf{f}]_{2P} \\ \vdots \\ [\mathbf{f}]_{PP} \end{pmatrix} [\mathbf{R}]_P \right]. \quad (3.128)$$

Expanding further, the submatrices $[\mathbf{R}]_1^{-1}$ - $[\mathbf{R}]_P^{-1}$ act to scale the rows of $\mathbf{f}\mathbf{R}$, yielding

$$\mathbf{A} = \left[\begin{pmatrix} [\mathbf{R}]_1^{-1}[\mathbf{f}]_{11} \\ [\mathbf{R}]_2^{-1}[\mathbf{f}]_{21} \\ \vdots \\ [\mathbf{R}]_P^{-1}[\mathbf{f}]_{P1} \end{pmatrix} [\mathbf{R}]_1, \begin{pmatrix} [\mathbf{R}]_1^{-1}[\mathbf{f}]_{12} \\ [\mathbf{R}]_2^{-1}[\mathbf{f}]_{22} \\ \vdots \\ [\mathbf{R}]_P^{-1}[\mathbf{f}]_{P2} \end{pmatrix} [\mathbf{R}]_2, \dots, \begin{pmatrix} [\mathbf{R}]_1^{-1}[\mathbf{f}]_{1P} \\ [\mathbf{R}]_2^{-1}[\mathbf{f}]_{2P} \\ \vdots \\ [\mathbf{R}]_P^{-1}[\mathbf{f}]_{PP} \end{pmatrix} [\mathbf{R}]_P, \right] \quad (3.129)$$

Viewing (3.129), it is apparent that the first block-row of \mathbf{A} depends only on the first block-row of \mathbf{f} . We have the block-diagonal structure of \mathbf{R} and \mathbf{R}^{-1} to thank for this. Furthermore, since $[\mathbf{R}]_1 = \mathbf{I}$, then $[\mathbf{R}]_1^{-1} = \mathbf{I}$ and the first block-row of (3.129) becomes

$$\begin{aligned} \begin{bmatrix} [\mathbf{A}]_1 & [\mathbf{A}]_2 & \dots & [\mathbf{A}]_P \end{bmatrix} &= \begin{bmatrix} [\mathbf{f}]_{11} & [\mathbf{f}]_{12} & \dots & [\mathbf{f}]_{1P} \end{bmatrix} \mathbf{R} \\ &= \begin{bmatrix} [\mathbf{f}]_{11}[\mathbf{R}]_1 & [\mathbf{f}]_{12}[\mathbf{R}]_2 & \dots & [\mathbf{f}]_{1P}[\mathbf{R}]_P \end{bmatrix}. \end{aligned} \quad (3.130)$$

Hence, the DBOR reduction procedure in the prior section involving the periodic summation may be used provided that $[\mathbf{A}]_1$ - $[\mathbf{A}]_P$ are given by (3.130) and where, since $[\mathbf{R}]_1 = \mathbf{I}$, then $\{\mathbf{b}\}_1 = \{\mathbf{B}_{xy,\text{source},\text{periodic}}\}_1 = [\mathbf{R}]_1\{\mathbf{B}_{xy,\text{source}}\}_1 = \{\mathbf{B}_{xy,\text{source}}\}_1$. Again using “20/20 hindsight,” the result (3.130) should match our intuition - with a change of variables now having periodic structure, the rotation information is embedded into the new system matrix, or equivalently, it becomes block circulant.

3.6.3 DBOR Reduction for Nonlinear Point Matching Formulations

Utilizing the DBOR reduction process to solve a nonlinear equation system such as the nonlinear point matching MoM formulation in Section 2.3 is now a straightforward extension of the prior derivation. The nonlinear equation system (2.30) is rewritten as

$$\mathbf{f}_{B_{tot}M}(\mathbf{M}_{xy}) = \mathbf{f}_{BM}\mathbf{M}_{xy} + \mathbf{B}_{xy,\text{source}} \quad (3.131)$$

where $\mathbf{B}_{xy,\text{source}}$ may represent known source terms due to free or bound current, such as $\mathbf{f}_{BI_f}I_f$ and/or $\mathbf{f}_{BI_{PM}}I_{PM}$ for example. Because the unknown vector \mathbf{M}_{xy} may not

be factored from the left-hand side of (3.131) as in (3.125), then from (3.131) we may rewrite (3.122) as

$$\begin{aligned}
\mathbf{B}_{xy,\text{tot},\text{periodic}} &= \mathbf{R}^{-1} \mathbf{f}_{B_{\text{tot}}M}(\mathbf{M}_{xy}) = \mathbf{R}^{-1} (\mathbf{f}_{BM} \mathbf{R} \mathbf{M}_{xy,\text{periodic}} + \mathbf{R} \mathbf{B}_{xy,\text{source},\text{periodic}}) \\
&= \mathbf{R}^{-1} \mathbf{f}_{BM} \mathbf{R} \mathbf{M}_{xy,\text{periodic}} + \mathbf{B}_{xy,\text{source},\text{periodic}} \\
&= \mathbf{A} \mathbf{M}_{xy,\text{periodic}} + \mathbf{B}_{xy,\text{source},\text{periodic}}
\end{aligned} \tag{3.132}$$

where since the matrix \mathbf{A} is block-circulant, then invoking similar arguments to the prior derivations, \mathbf{A} is computed using (3.130) with $\mathbf{f} = \mathbf{f}_{BM}$ and it is only necessary to solve for one block-row of (3.132). Hence, the nonlinear residual for block-row 1 of the system may be written as

$$\{\mathbf{g}(\{\mathbf{M}_{xy}\}_1)\}_1 = [\tilde{\mathbf{A}}]_{P/2+1} \{\mathbf{M}_{xy}\}_1 + \{\mathbf{B}_{xy,\text{source}}\}_1 - \{\mathbf{f}_{B_{\text{tot}}M}(\{\mathbf{M}_{xy}\}_1)\}_1 \tag{3.133}$$

where from the DBOR reduction procedure,

$$[\tilde{\mathbf{A}}]_{P/2+1} = [\mathbf{A}]_1 - [\mathbf{A}]_2 + \cdots + [\mathbf{A}]_{P-1} - [\mathbf{A}]_P. \tag{3.134}$$

The solution to the nonlinear equation system (3.133) may be found by utilizing the N-R procedure in Section 2.3 to find $\{\mathbf{M}_{xy}\}_1^*$ – the magnetization unknown of block-row 1 that achieves a residual that is below the desired tolerance. Therein, the analytical expressions in Section 2.3 used to populate the associated Jacobian matrix are modified as follows. The Jacobian matrix entries are found by differentiating (3.133) with respect to the unknown $\{\mathbf{M}_{xy}\}_1$:

$$\frac{\partial}{\partial \mathbf{x}} \{\mathbf{g}(\mathbf{x})\}_1 = \frac{\partial}{\partial \{\mathbf{M}_{xy}\}_1} \{\mathbf{g}(\{\mathbf{M}_{xy}\}_1)\}_1 = [\tilde{\mathbf{A}}]_{P/2+1} - \frac{\partial}{\partial \{\mathbf{M}_{xy}\}_1} \{\mathbf{f}_{B_{\text{tot}}M}(\{\mathbf{M}_{xy}\}_1)\}_1 \tag{3.135}$$

It should be noted that since $[\tilde{\mathbf{A}}]_{P/2+1}$ is a constant matrix, only the partial derivative terms of (3.135) are updated on every iteration. Conveniently, these partial derivative terms correspond to updating only the main, sub- and super- diagonal elements of

the Jacobian matrix, for which the expressions in Section 2.3 are used. Finally, the solution of the entire system is given by

$$\mathbf{M}_{xy}^* = \mathbf{R} \begin{bmatrix} \{\mathbf{M}_{xy}\}_1^* \\ -\{\mathbf{M}_{xy}\}_1^* \\ \vdots \\ \{\mathbf{M}_{xy}\}_1^* \\ -\{\mathbf{M}_{xy}\}_1^* \end{bmatrix}. \quad (3.136)$$

4. DESIGN OF PERMANENT MAGNET SYNCHRONOUS MACHINES

A goal of the research herein is to evaluate the performance of MoM within the population-based design (PBD) of electric machinery. As an example, the multi-objective design of a PMSM is considered. Herein, parameters describing the machine geometry, winding function and material properties are all used as genes in a GA.

A prime motivation behind exploring MoM-based electromechanical analysis is its potential usefulness in population-based design. In the last two decades, computing power has improved dramatically, enabling the large-scale problem of finding optimal designs of electric machinery in which potentially millions of designs are evaluated in order to identify the tradeoff among the competing design objectives. Analytical models are commonly used to evaluate design fitness within PBD routines. The analytical models often take a great deal of time and effort to initially derive but the benefits are then reaped within the PBD routine due to their extremely rapid evaluation. However, the topology is essentially fixed because of the assumptions imposed. Thus a major advantage inherent in numerical models such as MoM or FEA is their generality, despite the larger computational expense. This chapter explores the use of MoM to perform the magnetostatic analysis inside a PBD routine. In particular, the simplified design study of a PMSM based on the procedure set forth in Chapter 9 in [40] is repeated. Results such as accuracy and computation time are discussed.

4.1 Description of Design Problem

Herein, the simplified design study of a PMSM based on the procedure set forth in Chapter 9 in [40] is repeated. The problem setup, including design parameter ranges

and encoding types as well as design constraints and specifications, is unchanged from [40], although these quantities are all repeated herein for convenience in the tables that follow. Different from [40], the magnetic field analysis herein is performed using the MoM. The complete details and explanations of the models needed to perform the volume/mass calculations and inductance/winding voltage will not be repeated herein, the interested reader is referred to [40].

An electromagnetic field analysis is the basis for much of the design calculation in the optimization. The field analysis is conducted at several rotor positions which evenly span a slot pitch. Using the computed flux densities at said rotor positions, flux density waveforms are constructed which correspond to one electrical cycle. Peak flux density, PM demagnetization and torque constraints are evaluated for each design. With the flux density waveforms, the core loss in the teeth and backiron is computed. First, the machine geometry description is discussed, where the variables defining it are introduced.

It is assumed that the machine is being operated in a manner in which the stator currents can be controlled by a 3-phase inverter, provided there is sufficient dc-link voltage. The specifications for the design are listed in table 4.1.

The variables describing the machine geometry constitute most of the degrees of freedom within the design. Listed in Table 4.2 are parameter names of the degrees of freedom, descriptions and the ranges allowed in the GA along with encoding type of each variable (integer, linear and logarithmic). The parameters relate to the SPM geometry as shown in Fig. 4.1 (figure not shown to the scale of parameters in Table 4.2).

Design Constraints

During fitness evaluation, candidate designs are checked against constraints to ensure the designs are viable. The order in which the constraints are checked is such that the most time-consuming design analyses are saved for the latest part of the

Table 4.1.: Design Specifications

Parameter	Value	Description
v_{dc}	400 V	dc-link voltage
T_e^*	20 N · m	Commanded torque
ω_{rm}^*	5000 rpm	Commanded rotor speed
n_{spp}	2	Number slots/pole/phase
k_m	0.75	Demagnetization factor
k_{pf}	0.5	packing factor
l_{eo}	1 cm	length of end winding offset
r_{rs}	2 cm	shaft radius
v_{fs}	2 V	Forward switch drop of semiconductors
J	3	Number of discrete rotor positions evaluated
$\phi_{ss,1}$	π/S_s rad	location of stator slot 1
M_{mxa}	10 kg	Maximum allowed mass
P_{mxa}	1 kW	Maximum allowed loss
α_{tar}	10	Maximum tooth aspect ratio
α_{so}	1.5	Slot opening factor

Table 4.2.: Degrees of freedom in design

	Description	Encoding	Min	Max
s_t	Stator steel type	int	1	4
r_t	Rotor steel type	int	1	4
c_t	Conductor type	int	1	2
m_t	Magnet type	int	1	7
P_p	Pole pairs	lin	4	6
d_i	Depth of inert region (m)	lin	0	10^{-1}
d_{rb}	Depth of rotor backiron (m)	lin	10^{-3}	$5 \cdot 10^{-2}$
d_m	Depth of magnet (m)	log	10^{-3}	$5 \cdot 10^{-2}$
g	Air gap (m)	lin	$5 \cdot 10^{-4}$	$5 \cdot 10^{-2}$
d_{tb}	Depth of tooth base (m)	log	10^{-3}	$5 \cdot 10^{-2}$
α_t	Tooth fraction	lin	$5 \cdot 10^{-2}$	$95 \cdot 10^{-2}$
d_{sb}	Depth of stator backiron (m)	log	10^{-3}	$5 \cdot 10^{-2}$
α_{PM}	Magnet Fraction	lin	$5 \cdot 10^{-2}$	$95 \cdot 10^{-2}$
l	Machine length (m)	log	10^{-2}	$5 \cdot 10^{-1}$
N_{s1}^*	Peak fundamental conductor density (cond/rad)	log	10^1	10^3
α_3^*	Coefficient of third harmonic conductor density	lin	10^{-1}	$7 \cdot 10^{-1}$
I_{qs}^{r*}	Q-axis current (A)	log	10^{-1}	50
I_{ds}^{r*}	D-axis current (A)	lin	-50	0

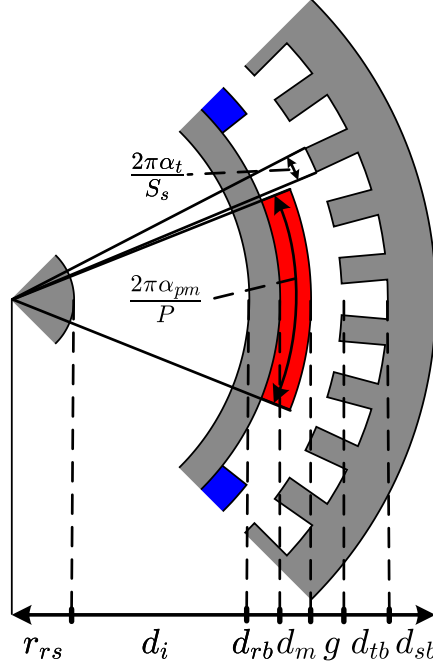


Fig. 4.1.: Machine parameter definitions.

fitness evaluation, so that computationally expensive analyses are not performed if the design isn't viable. The constraints are listed in Table 4.3. They are numbered so that they correspond to the order in which they are applied. Constraint c_1 concerns the limitation of the ratio of tooth width to tooth length. Constraint c_2 ensures that the conductor diameter does not exceed the slot opening, so that the conductor may be radially inserted into the slot during construction. A simple alternative to using a thermal model to limit the maximum temperature in the machine is to constrain the current density in the stator, accomplished using constraint c_3 . Constraint c_4 prevents excessively massive machines from being considered, while constraint c_{17} prevents excessively lossy machines from being considered. Together, these two constraints frame the window of the Pareto-optimal front. Constraint c_5 determines whether the

Table 4.3.: Design Constraints

Constraint	Description
$c_1 = \text{lte}(d_{st}, \alpha_{tar} w_{tb})$	Tooth aspect ratio
$c_2 = \text{lte}(d_c \alpha_{so}, w_{so})$	Conductor size less than slot opening
$c_3 = \text{lte}(I_s / a_c, J_{lim})$	Current density
$c_4 = \text{lte}(M, M_{mxa})$	Mass of machine
$c_5 = \text{lte}(v_{ll,pk}, v_{dc} - 2v_{fs})$	Line-line voltage
$c_6 = \text{lte}(\ \mathbf{B}_{t1cnc}\ _{\max}, B_{s,lim})$	Magnetic field stator tooth 1
$c_7 = \text{lte}(\ \mathbf{B}_{b1cnc}\ _{\max}, B_{s,lim})$	Magnetic field stator yoke 1
$c_8 = \text{lte}(B_{rbtnc,mx}, B_{r,lim})$	Tangential magnetic field rotor backiron
$c_9 = \text{lte}(B_{rbrnc,mx}, B_{r,lim})$	Radial magnetic field rotor backiron
$c_{10} = \text{gte}(H_{mnn}, H_{lim})$	Auxiliary field in PM
$c_{11} = \text{lte}(\ \mathbf{B}_{t1c}\ _{\max}, B_{s,lim})$	Magnetic field stator tooth 1
$c_{12} = \text{lte}(\ \mathbf{B}_{b1c}\ _{\max}, B_{s,lim})$	Magnetic field stator yoke 1
$c_{13} = \text{lte}(B_{rbt,mx}, B_{s,lim})$	Tangential magnetic field rotor backiron
$c_{14} = \text{lte}(B_{rbr,mx}, B_{r,lim})$	Radial magnetic field rotor backiron
$c_{15} = \text{gte}(H_{mn}, H_{lim})$	Auxiliary field in PM
$c_{16} = \text{gte}(T_{ec}, T_e^*)$	Electromagnetic torque
$c_{17} = \text{lte}(P_l, P_{lmax})$	Power loss

GA-selected Q- and D-axis stator currents can be achieved without low-frequency harmonics using the specified dc-link voltage, where

$$V_{qs}^r = r_s I_{qs}^r + \omega_r (L_d I_{ds}^r + \lambda_m^r) \quad (4.1)$$

$$V_{ds}^r = r_s I_{ds}^r - \omega_r L_q I_{qs}^r \quad (4.2)$$

$$v_{ll,pk} = \sqrt{3} \sqrt{V_{qs}^r{}^2 + V_{ds}^r{}^2} \quad (4.3)$$

Following completion of the magnetic field analysis, the flux density in critical locations of the machine is known. Constraints c_6 - c_{15} concern the magnetic field limits in these locations. During the fitness evaluation, the magnetic field analysis is conducted first using zero stator current (only PM excitation), following which constraints c_6 - c_{10} are checked. If these constraints are met, the magnetic field analysis is conducted again using the stator currents selected by the GA. Subsequently constraints c_{11} - c_{15} are checked. Finally, with the torque and magnetic field computed during the second magnetic field analysis, the corrected torque may be computed according to (4.4) and the losses may be evaluated using (4.10) - (4.9). Subsequently, constraints c_{16} and c_{17} may be evaluated.

$$T_{ec} = \begin{cases} T_e, & \omega_{rm} = 0 \\ T_e - \frac{P_c}{\omega_{rm}}, & \omega_{rm} \neq 0 \end{cases} \quad (4.4)$$

where T_{ec} represents the corrected torque, which is the computed electromagnetic torque adjusted by the amount P_c/ω_{rm} and P_c is the core loss. The core loss P_c is determined using the combined loss model of the Modified Steinmetz Equation (MSE) in conjunction with the eddy current loss. Hysteresis power loss density is given by

$$p_h = k_h \left(\frac{f_{eq}}{f_b} \right)^{\alpha-1} \left(\frac{\Delta B}{2B_b} \right)^{\beta} \frac{f}{f_b} \quad (4.5)$$

where $\Delta B = 2 \max(B)$, $f_b = 1$, $B_b = 1$ and the integral

$$f_{eq} = \frac{2}{\Delta B^2 \pi^2} \int_0^T \left(\frac{dB}{dt} \right)^2 dt \quad (4.6)$$

is evaluated numerically using the respective dB/dt waveforms which are outputs of the magnetic field analysis. Using a similar numerical integration, the eddy current loss density is determined from the flux density waveforms using

$$p_e = k_e f \int_0^T \left(\frac{dB}{dt} \right)^2 dt \quad (4.7)$$

Using (4.5) and (4.6), the hysteresis loss density is computed in one stator tooth and backiron yoke, denoted respectively by p_{ht} and p_{hb} . Using (4.7), the eddy current loss

density is computed in one stator tooth and backiron yoke, denoted respectively by p_{et} and p_{eb} . The total core loss in the teeth and backiron of the stator is given by

$$P_c = ((p_{ht} + p_{et})v_t + (p_{hb} + p_{eb})v_b) S_s \quad (4.8)$$

where v_t and v_b represent the volume of one stator tooth and one backiron yoke, respectively. The total power loss is then given by

$$P_l = P_r + P_s + P_c \quad (4.9)$$

where the stator winding resistive loss is given by

$$P_r = 3r_s I_s^2 \quad (4.10)$$

and the semiconductor loss of the inverter is given by

$$P_s = \frac{6\sqrt{2}}{\pi} v_{fs} I_s. \quad (4.11)$$

The mass of the machine is computed using analytical formulae [40]. The power loss is computed using (4.5)-(4.11). Finally, the design fitness is determined by

$$\mathbf{f} = \begin{cases} \epsilon[1 \quad 1]^T \left(\frac{C_s - N_c}{N_c} \right) & C_s < C_I \\ \left[\frac{1}{M} \quad \frac{1}{P_l} \right]^T & C_s = N_c \end{cases} \quad (4.12)$$

4.2 Observation Locations for Machine Design

In the linear Galerkin MoM formulation, the bound current sources \mathbf{I}_b at the material boundaries are solved. Subsequently the total magnetic field \mathbf{B}_{tot} is evaluated using the matrix-vector product $\mathbf{B}_{tot} = \mathbf{f}_{B_{tot}M} \mathbf{M}_{tan}$. Recall that \mathbf{B}_{tot} is the magnetic field tangent to the respective edge elements. As a post-processing step, the magnetic field anywhere else may subsequently be computed. This includes the magnetic field as a vector with x - and y - components, or the field normal to a surface. The locations at which the magnetic field is desired are referred to herein as observation locations.

Since all sources are known following the solution of the equation system, any further equation system solution is not required. However, an additional set of influence

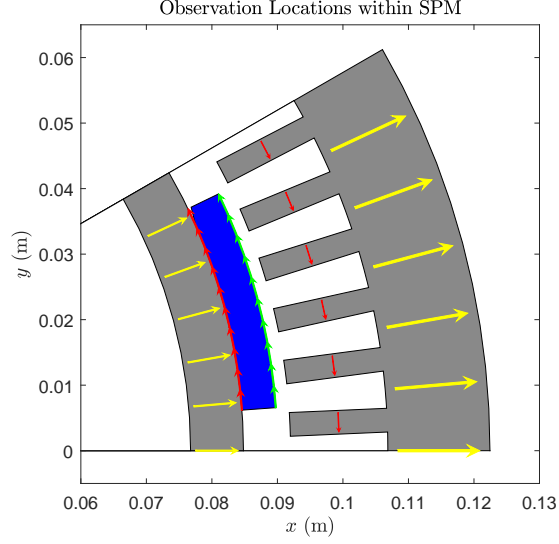


Fig. 4.2.: Magnetic field observation locations within machine cross section.

matrices must be populated, and subsequently a matrix-vector product is evaluated which yields the magnetic field at the observation locations:

$$B_{obs} = \mathbf{f}_{B_{obs}M} \mathbf{M} + \mathbf{f}_{B_{obs}I_f} \mathbf{I}_f + \mathbf{f}_{B_{obs}I_{PM}} \mathbf{I}_{PM} \quad (4.13)$$

In order to adhere to optimization constraints, in particular the magnetic field limits, a convenient set of observation locations must be selected. The locations within the machine which best serve as the observation locations are described herein.

Observation sheets are placed across the stator teeth and yoke cross sections in one pole. Subsequently, the closed form expression (3.31) for the average normal flux density is used to populate the matrices in (4.13). Following evaluation of (4.13), the elements of B_{obs} corresponding to these sheets correspond to \mathbf{B}_{t1} and \mathbf{B}_{b1} . Hence constraints c_6 , c_7 may be evaluated in the case of an unexcited stator winding. In the case of nonzero stator excitation, constraints c_{11} and c_{12} may be evaluated. Referring to Figure 4.2, the tooth observation locations correspond to the red arrows in the stator teeth and the yoke observation locations correspond to the yellow arrows in the stator backiron.

Observation sheets are placed in the rotor backiron, oriented so that the sheets traverse the rotor backiron radially. Using these, (3.31) is used to populate the matrices in (4.13). Following evaluation of (4.13), the elements of B_{obs} corresponding to these sheets correspond to B_{rbt} , hence constraints c_8 and c_{13} may be evaluated. Referring to Figure 4.2, the rotor tangential field observation locations correspond to the yellow arrows in the rotor backiron.

The line elements making up the mesh of the underside of the PM may be used without creating new observation elements. However, the expression (3.31) must still be used to populate the matrices in (4.13). Following evaluation of (4.13), the elements of B_{obs} corresponding to these elements correspond to B_{rbr} , hence constraints c_9 and c_{14} may be evaluated. Referring to Figure 4.2, the rotor radial field observation locations correspond to the red arrows at the underside of the PM.

The line elements making up the outside surface of the PM mesh may be used without creating new observation elements. the expression (3.31) must still be used to populate the matrices in (4.13). Following evaluation of (4.13), the elements of B_{obs} corresponding to these elements correspond to B_{PM} . Subsequently, $H_{PM} = \frac{1}{\mu_0\mu_{rPM}}(B_{PM} - B_r)$. Hence constraints c_{10} and c_{15} may be evaluated. Referring to Figure 4.2, the PM demagnetization field observation locations correspond to the green arrows at the outer surface of the PM.

4.3 Optimization Results

The linear Galerkin formulation detailed in Section 2.2.2 was utilized within a population-based design study performed in MATLAB using GOSET [41]. The DBOR solver was utilized for the magnetic field analysis. Each machine was evaluated at 4 rotor positions, over which the mean torque was evaluated. The Pareto-Optimal front of the design study is shown in Figure 4.3. The run utilized a population size of 500 individuals over 500 generations. The computation time required to complete the design study was 11.4 hours on a simulation workstation with an Intel Xeon

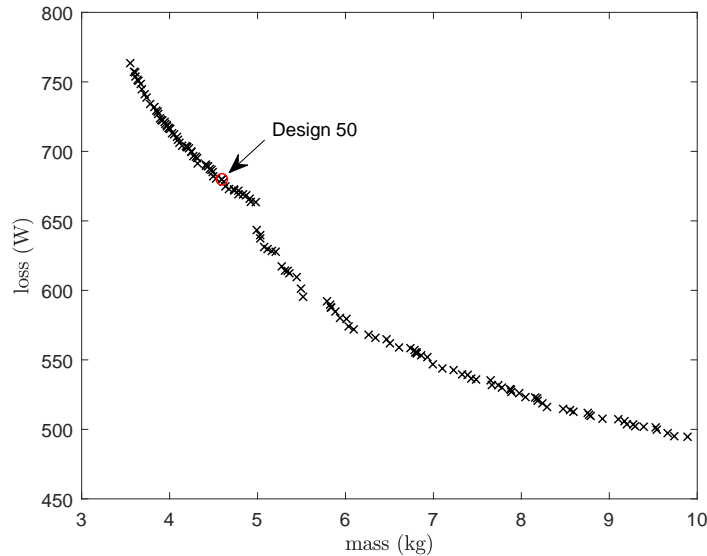


Fig. 4.3.: Pareto-optimal front of Design Study 1.

E5-2687W v2 3.4 GHz processor and 32 GB RAM. The optimization was performed using the option of parallel processing within MATLAB/GOSET, which used 8 physical cores/16 logical ones.

A machine on the Pareto front, Design 50, was selected for evaluation of the the MoM accuracy. Its cross section is shown in Figure 4.4. The geometry and operating point parameters are listed in Table 4.4 and conductor density in Table 4.5. A comparison of the computed flux density in the tooth and back-iron with that obtained using FEA is shown in Figure 4.6. The FEA was performed using the commercial package ANSYS Electronics Desktop, which required more than 10,000 unknowns per pole on average, whereas the nonlinear Point Matching MoM required 828 unknowns per pole and the Linear Galerkin MoM required only 190 unknowns per pole. An approximate FEA unknown count is given since the geometry is re-meshed at each rotor position. To obtain Figure 4.6, the spatial average of the component normal to the respective cross sections were calculated for zero stator current. The FEA model used for comparison utilized an energy-based mesh refinement, set to converge within 0.01%. Within the plot, both the linear Galerkin and nonlinear point

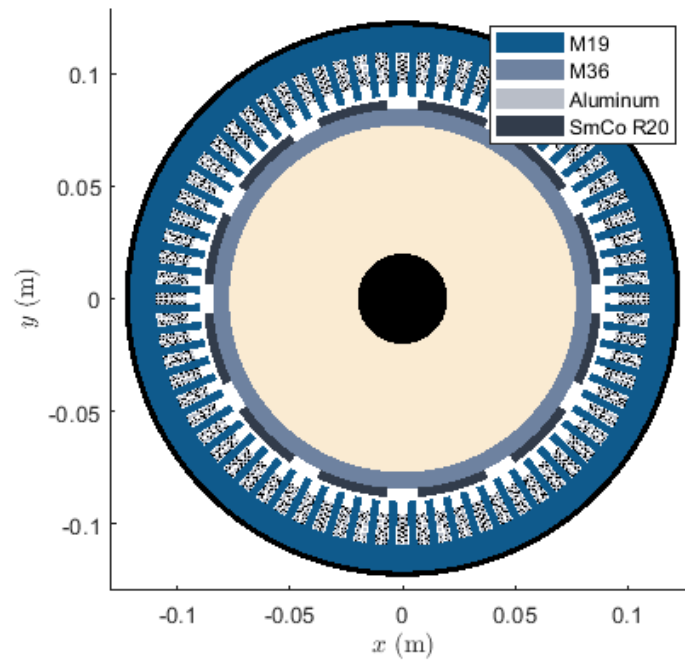


Fig. 4.4.: Cross section of Design 50.

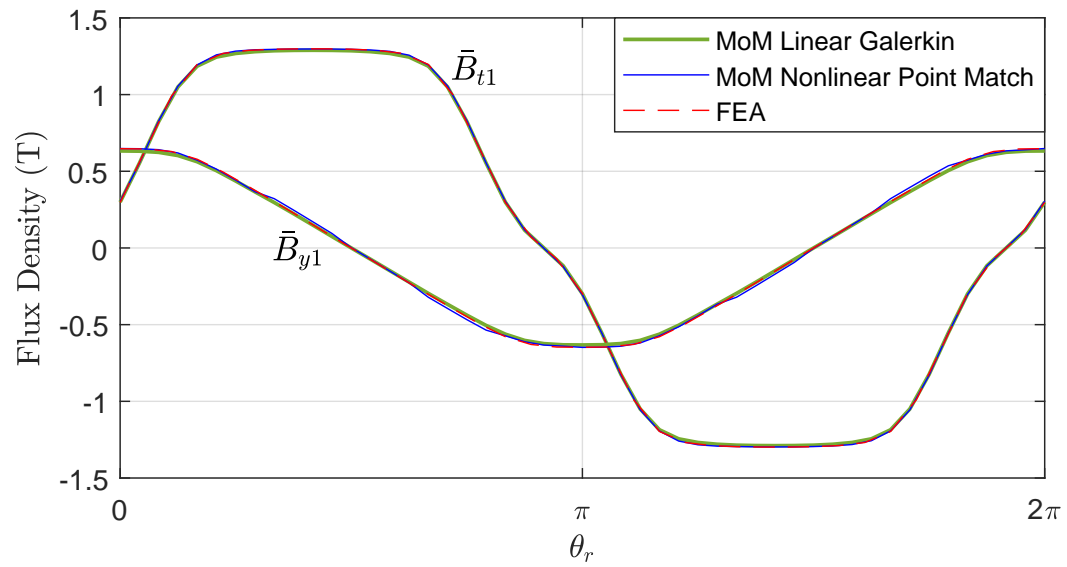


Fig. 4.5.: Flux density waveforms in teeth and backiron, zero stator current - PM flux only.

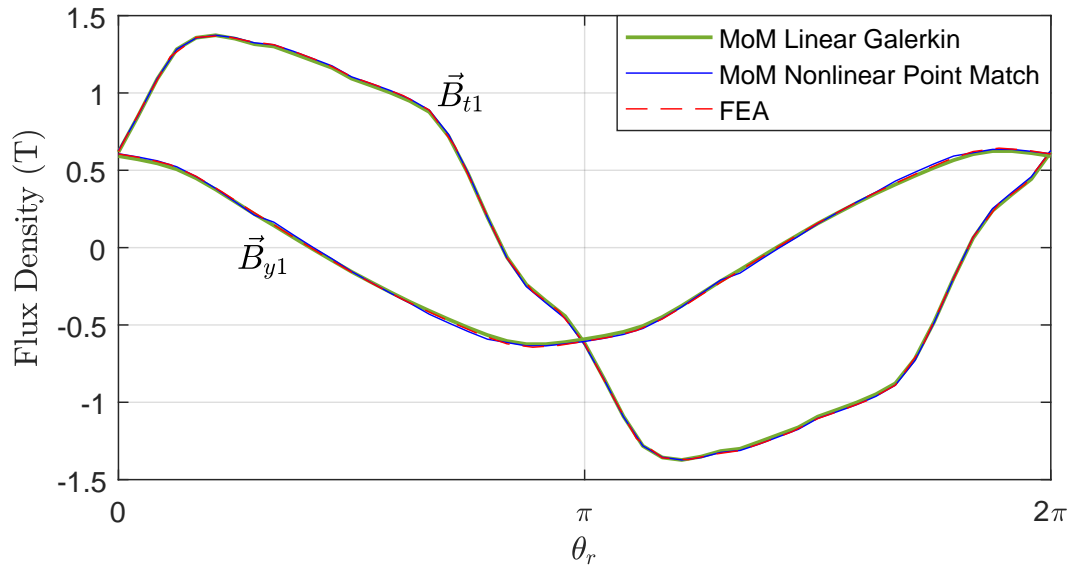


Fig. 4.6.: Flux density waveforms in teeth and backiron, rated stator current.

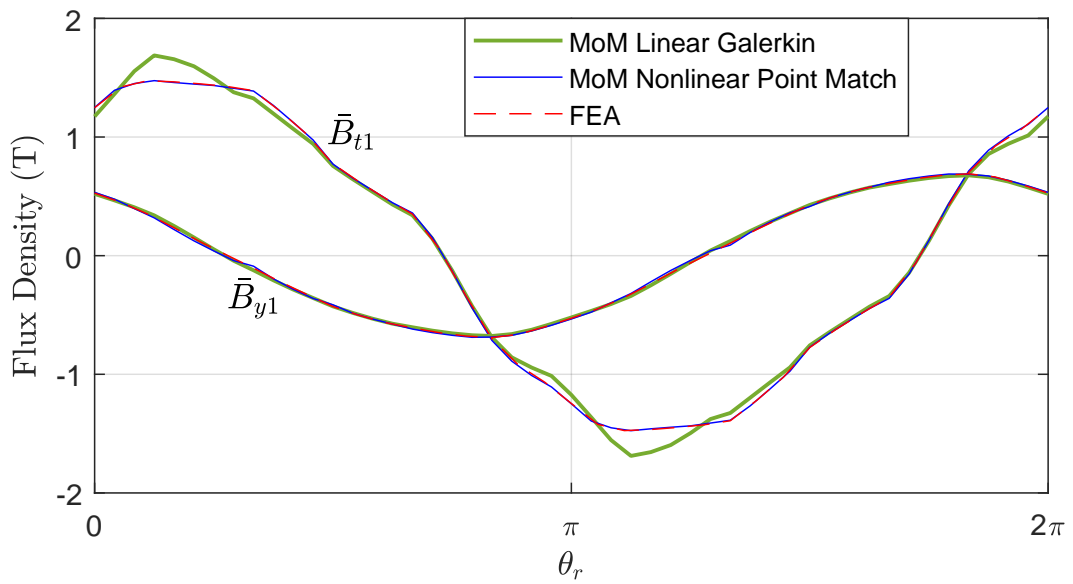


Fig. 4.7.: Flux density waveforms in teeth and backiron, saturating conditions.

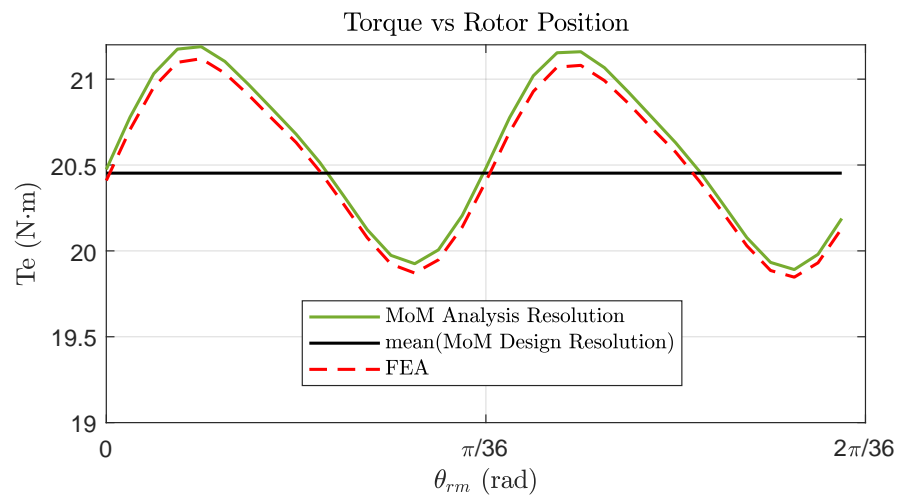


Fig. 4.8.: Torque waveform over two slot pitches in Design 50.

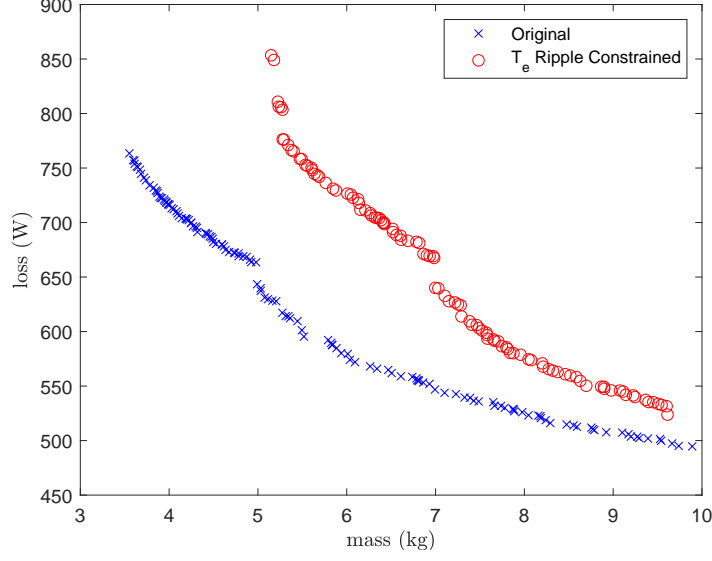


Fig. 4.9.: Comparison of Pareto-optimal Fronts, Torque Ripple Constrained.

matching MoM formulations are compared with an FEA model. The comparison was repeated for the condition of rated stator excitation where and are shown in Figure 4.6. Therein, it can be observed that the waveforms closely match that of the FEA. To view the accuracy of the nonlinear MoM, the stator excitation is set to 275% of rated and the model comparison is again repeated and is shown in Fig. 4.7. As shown, the nonlinear MoM formulation agrees well with the FEA model, whereas the linear MoM formulation exhibits inaccuracies as the iron saturates.

The torque computed using the Linear Galerkin MoM formulation is shown in Figure 4.8, wherein the designations “Analysis Resolution” and “Design Resolution” indicate respective mesh resolutions of 760 and 190 elements per pole. Furthermore, the “Analysis Resolution” waveform was computed across 32 rotor positions spanning two slot pitches, whereas the “Design Resolution” torque was computed across 8 rotor positions spanning two slot pitches and subsequently averaged. Also shown for comparison is the torque waveform obtained from a nonlinear FEA. The FEA again required more than 10,000 elements per pole on average when an adaptive meshing procedure was set to converge on torque to within 0.1%. The MoM “Analysis Res-

Table 4.4.: Design 50 Parameters

Description	Symbol	Value
Phases	N_{phase}	3
Poles	P	12
Slots	S_s	72
Shaft radius	r_{rs}	20 mm
Depth of inert region	d_i	56.750 mm
Depth of inner backiron	r_{rb}	8.069 mm
Depth of magnet	d_m	5.181 mm
Airgap	g	2.000 mm
Depth of tooth base	d_{tb}	14.856 mm
Depth of stator backiron	d_{sb}	15.581 mm
Length of machine	l	27.05 mm
Relative permeability of stator iron	μ_{rs}	32.566×10^3 H/m
Relative permeability of rotor iron	μ_{rr}	27.403×10^3 H/m
Relative permeability of magnet	μ_{rm}	1.02 H/m
Remanent flux density of magnet	B_r	0.9 T
Tooth fraction	α_t	0.4512
PM fraction	α_{PM}	0.721
Q -axis current	I_{qs}^r	32.403 A
D -axis current	I_{ds}^r	-8.566 A

olution” and FEA torque waveforms are in reasonable agreement with one another. Visually inspecting the “Design Resolution” average torque, it is apparent that the “Design Resolution” is sufficient to represent the average of the two higher-resolution waveforms. Hence, one is reassured that the Linear Galerkin formulation is of sufficient fidelity to predict the average torque in the design fitness evaluation.

Table 4.5.: Design 50 Conductor Density

Winding	Conductor Density (1 pole)					
N_{as}	0	0	6	11	6	0
N_{bs}	-6	-11	-6	0	0	0
N_{cs}	6	0	0	0	-6	-11

A second study was performed in which a torque ripple constraint was applied. After the second magnetic analysis, if the average torque passed constraint c_{16} a third magnetic analysis was performed using a higher mesh resolution, as justified in Figure 4.8. In particular, the number of rotor positions per slot pitch was doubled to 8, and the number of elements per pole was increased to 468. Subsequently, the pk-pk torque ripple was constrained to be less than 1% of the average. A comparison between the Pareto-optimal fronts of the original and torque-constrained optimizations are shown in Figure 4.9. As shown, the torque-ripple constrained designs incur a mass penalty that is quite significant. The mass penalty is roughly a factor of 1.4. The increased torque waveform resolution comes at a cost of increased CPU time; the study required 40.1 hours to finish.

It is noted that a comparison was made between a PBD run using the DBOR solver and one which computed the entire system matrix. The computation times for the entire system and DBOR are respectively 76.9 h and 10.7 h for a Population \times Generation size of 500×500 . This corresponds to a computation time improvement of a factor of roughly 7.

An evaluation of the CPU time was performed on a design chosen at random in the design process. The breakdown of the tasks involved in the solution is shown in Table 4.6. One can observe that the primary bottleneck in the MoM solution procedure is the population of the dense system matrix. Indeed, the procedure of creating

Table 4.6.: CPU Time Breakdown of MoM Field Analysis

Task	CPU Time (%)
Meshing	6.57
Matrix Assembly	60.36
Solve	1.84
Observation	21.73
Torque Calculation	9.49
Total	1.025132 s

observation locations and observing the fields there, another Matrix Assembly-heavy task, is the second most time-consuming component.

4.4 Time Comparison with FEA-based model

In this section, the computational performance of MoM is considered relative to FEA. FEA-based field predictions presented in previous sections were generated using the commercial FEA package ANSYS Electronics Desktop [42]. However, comparing the computational performance of the MATLAB-based MoM implementation with a commercial FEA package is not very meaningful for several reasons. Chief among them, the commercial package is compiled into machine code for rapid execution, and it has been optimized by teams of engineers over several decades. In contrast, the MoM toolbox is written in MATLAB, an interpreted language, by a single author without many years to optimize it. In addition to the underlying field analysis, the commercial FEA package has a computational burden that includes, for example, the graphical user interface and geometry interaction with the user. Further muddying the comparison is the possible use of advanced programming techniques such as parallelization within the commercial package. For these reasons, the FEA utilized in

this section, like the MoM toolbox, is a custom implementation written in MATLAB - a step toward the goal of a meaningful comparison. The basis for the code is the course notes from ECE 625 taught at Purdue University [43].

It is common for FEA and MoM (or, more generally, differential equation- and integral equation-based numerical methods) to be compared on the basis of computational complexities associated with each essential step. In such a comparison, it is well-known that in the FEM, the meshing and matrix assembly steps respectively scale in proportion to $\mathcal{O}(N^2)$ and $\mathcal{O}(N)$. It is also well-known that in the MoM the mesh and matrix assembly steps respectively scale in proportion to $\mathcal{O}(N)$ and $\mathcal{O}(N^2)$.

The computational cost of the solution of the $N \times N$ linear system of equations for each FEA and the MoM depends heavily on the specific algorithm. Direct solution algorithms applied to the FEM can achieve computationally efficient solutions provided that node re-orderings take place so that the stiffness matrix has a band-like structure similar to the 2D Finite Difference method which is able to be solved in $\mathcal{O}(N)$ operations [44]. Iterative solution algorithms, such as the conjugate gradient method [45] applied to the FEM can achieve computational complexities of $\mathcal{O}(N^{1.5})$ and multi-resolution type solutions may achieve $\mathcal{O}(N)$ complexity [46]. Direct methods for the solution of dense matrices, such as those encountered in integral equation numerical methods, are typically unable to escape the $\mathcal{O}(N^3)$ computational cost, and therefore most dense matrix solutions utilize iterative methods. Some iterative methods, such as the Fast Multipole Method [47], are able to achieve $\mathcal{O}(N \log N)$ computational cost but must be tailored to a specific problem. While MATLAB is capable of detecting general sparse matrices and employing some appropriate algorithms to solve them, it is unable to apply the specialized solvers required for the efficient solution of integral equation methods.

While, as previously discussed, the MoM certainly requires fewer elements, it is the sparse or full nature of the respective matrices and in turn the associated linear system solve algorithms that drive the computational complexity differences. Therefore it is

perhaps more meaningful to consider a specific example machine and mesh it with an appropriate number of elements for either FEA or MoM.

Similar to the MoM-based design evaluation, in the FEA-based design evaluation the problem is meshed once, then the fields are solved at 4 rotor positions which evenly span one slot pitch. More specifically, the rotor and stator are meshed separately using the freely-available Triangle utility [48]. Stiffness matrices are formed for the stator and rotor meshes, which are subsequently adjoined to form a global stiffness matrix. The adjoining takes place within the matrix rows/columns corresponding to a compatible set of nodes in the airgap. As the rotor angle is advanced, this stator/rotor node connection is shifted. Note that in the FEM, the nodes of the airgap interface between stator and rotor dictate the discrete values that the rotor angle can take. In other words, if a different rotation angle value is desired, then the airgap (or possibly the entire domain) must be re-meshed. In contrast, no such airgap mesh exists in the MoM and the rotor can be rotated by any desired angle, provided that the influence matrix has been updated to reflect the new position of the rotor elements.

Whereas the boundary conditions are automatically satisfied in the MoM formulation utilized herein, FEA requires the deliberate application of boundary conditions to the system matrix and input vector in order to form a matrix equation with a unique solution. Similar to the MoM design evaluation, the FEA code meshes and computes the field distribution of a single pole of the machine. However, simply truncating the domain in which the field is solved will yield incorrect results. The correct field distribution is only achieved through the application of additional boundary conditions on the edges of the truncated domains. Specifically, the condition $A_z(\phi = 0) = -A_z(\phi = \frac{2\pi}{P})$ is enforced in the stator domain, and similarly the condition $A_z(\phi = \theta_{rm}) = -A_z(\phi = \theta_{rm} + \frac{2\pi}{P})$ is enforced in the rotor domain. These boundary conditions are called “anti-periodic” since they force the field solution to repeat itself every pole, alternating in sign. Finally, the Dirichlet boundary condition $A_z = 0$ is applied at the outer domain boundary.

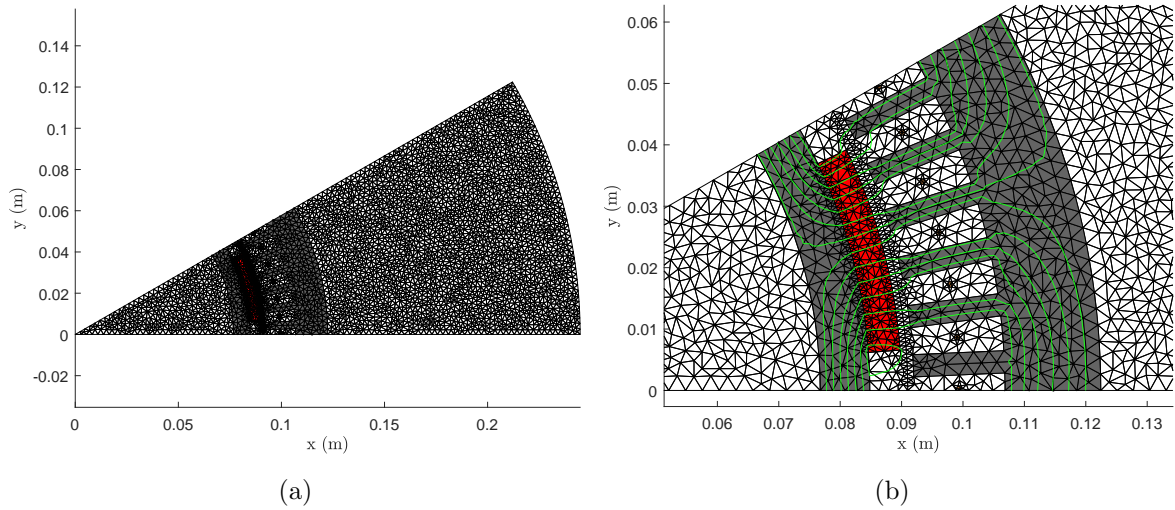


Fig. 4.10.: MATLAB FEA of SPM machine: mesh (a) and zoomed mesh, with flux lines (b).

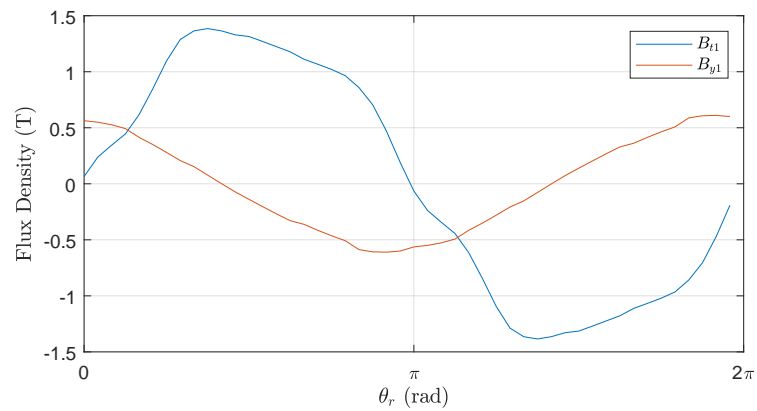


Fig. 4.11.: MATLAB FEA: Tooth and Yoke flux density waveforms.

Shown in Fig. 4.10a is the mesh of the problem region in the MATLAB-based FEA. The outer radius of the problem region was selected to be a multiple of twice the outer radius of the machine. The mesh resolution impacts the problem size and hence the computation time, and must not be selected arbitrarily. To best compare with the MoM design evaluation, the mesh resolution ought to yield a solution that is balanced between accuracy and computational labor. The procedure used herein for

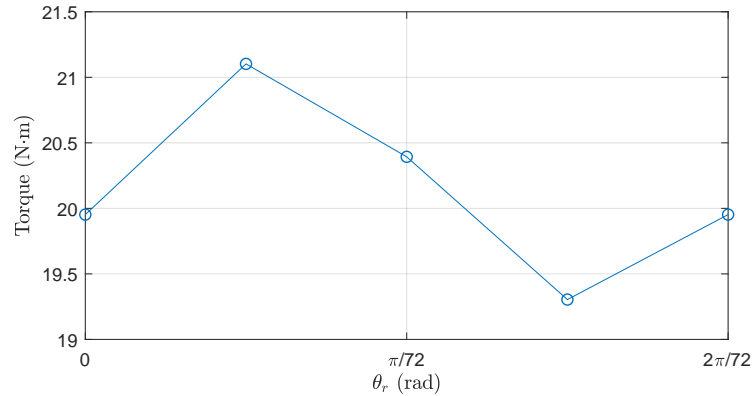


Fig. 4.12.: MATLAB FEA: Torque waveforms.

selecting the mesh resolution was as follows. As a strong basis for an accurate torque prediction, a high mesh density was first enforced within the airgap region, as shown in 4.10b in addition to the flux lines of the $\theta_{rm} = 0$ solution superimposed; this was accomplished by specifying a reasonably high node density on the rotor and stator teeth surfaces and airgap mid-lines. Subsequently, an area constraint was further placed on all triangles and the area was reduced until the average torque prediction was within 2% of the “converged” average torque predicted by the commercial FEA package. The mesh resolution utilized herein for the comparison study yielded a system with 4151 unknown node potentials.

Shown in Fig. 4.12 is the torque vs rotor position predicted by the MATLAB-based FEA (points 1-4 were computed and point 1 is repeated after these points for waveform visual continuity). Shown in Fig. 4.11 is the flux density waveforms predicted by the MATLAB-based FEA. These predictions are in good agreement with predictions of the MoM and the commercial FEA package reported in the prior sections.

The computation time breakdown of the MATLAB-based FEA is reported in Table 4.7, it is apparent that the MoM and FEA computation times are of similar magnitude. Note that the computation time dedicated to the application of boundary

Table 4.7.: CPU Time Breakdown of MATLAB-based FEA

Task	CPU Time (%)
Meshing	15.59
Matrix Assembly	32.61
Solve	2.01
Observation	44.20
Torque Calculation	5.6
Total	2.686 s

conditions to the system matrix and right-hand side is included within the Matrix Assembly portion.

In the case of FEA, the observation component of computation time consists of a routine wherein the list of triangles is searched to identify the triangles that encircle specific points at which one wishes to observe the magnetic fields. These points are triangles in the six stator teeth and six stator yokes. Subsequent to the identification of indices, the magnetic field inside these specific triangles is computed from the magnetic vector potential, i.e. $B = \nabla \times A$. Shown in Fig. 4.11 are the observed flux density waveforms in the stator teeth and yokes which were reconstructed in a similar fashion to the MoM design evaluation. The waveforms are in good agreement with the commercial FEA and MoM waveforms shown in Fig. 4.6.

A slight issue in the comparison is the fact that the meshing utility, Triangle, is a compiled program. The meshing process takes as inputs a list of unique node locations and a list of node pairs that define the boundaries of each domain. The MATLAB code which produces these lists is a modified form of the MoM meshing routine. Hence, the meshing time required in FEA can be no less than the MoM meshing time, and were the meshing utility written in MATLAB, one can expect the FEA meshing time to be longer than reported in table 4.7. Writing code that implements

surface meshing is a manageable task for a computer programmer. However a surface meshing routine such as Triangle is more specialized and is written by experts in the field of meshing. Hence, this discussion highlights the fact that there is a greater ease in meshing a geometry for MoM-based analysis than FEA.

Based on the comparison presented in this section, the MoM and FEA appear to be close in overall computation time. However, the backslash operator, “\” or “ml-divide”, is used within MATLAB herein to solve both systems. MATLAB is capable of detecting the sparseness of the FEA stiffness matrix applying a suitable computationally efficient solver. In contrast, the full MoM system matrix cannot escape the $\mathcal{O}(N^3)$ complexity without the use of specialized solvers. With this difference in mind, if an integral equation fast solver were to be used, such as the Fast Multipole Method [47], the possibility of further reducing the MoM computation time may be open.

5. HYBRID NONLINEAR MODEL FOR V-SHAPE INTERIOR PMSM

The nonlinear MoM formulation in Section 2.3 was first derived by Howard [4] to account for bound currents that reside *within the volume* of nonlinear materials. Therein, volume meshing of the magnetic material becomes necessary, increasing the element count of the mesh and consequently the computational effort of the MoM. In addition, the equation system becomes nonlinear, requiring an iterative solution. In an attempt to reduce the computational effort, herein a focus is to develop a hybrid method in which surface and volume meshing are combined. The concept of hybridization has been considered in [4]. Therein, linear and nonlinear elements co-occupy the same volume and the associated bound currents are in superposition. Herein, a primary difference is that the surface and volume elements do not act in superposition. Rather, magnetic material regions are partitioned into linear and nonlinear sub-regions and subsequently solved simultaneously.

To demonstrate the approach, a V-shaped Interior PM (IPM) is utilized. The machine features regions of significant local saturation within the so-called PM “bridges” in the rotor. Thus, a hybrid model which selectively applies volume meshing only at the locations that are saturated is an interesting prospect for this machine.

Prior to implementing the hybrid model, the machine is analyzed using a linear Galerkin formulation. This formulation is first used to show that a nonlinear MoM is indeed necessary and to foreshadow the difficulty of accurate torque predictions of the IPM. The mathematical structure of the hybrid model is then considered. This includes modifications to the N-R algorithm in Section 2.3 that are required for the hybrid model to converge within relatively few iterations. Subsequently the hybrid model of the IPM is used to examine its feasibility for PBD purposes. In doing so, several alternative combinations of linear and nonlinear elements are applied. The

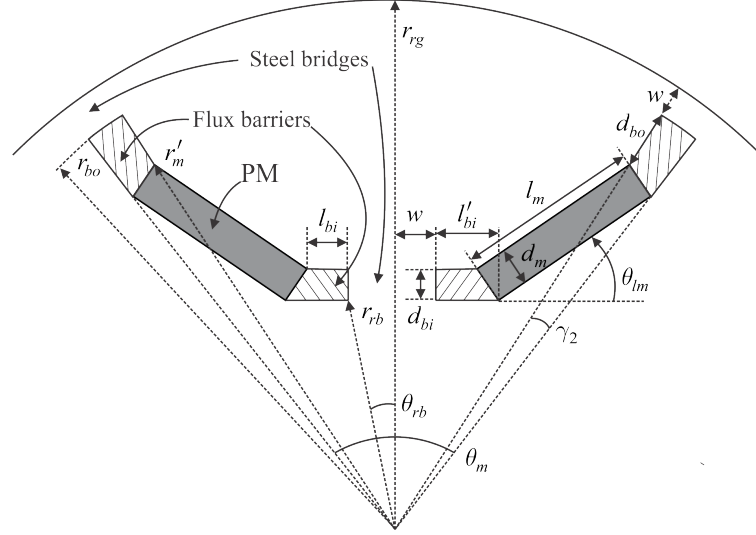


Fig. 5.1.: Diagram of rotor geometry in IPM machine.

accuracy and computational performance are compared in order to determine whether hybrid models show promise.

5.1 Motivating Nonlinear Analysis

A cross section of the IPM rotor is shown in Fig. 5.1 (reprinted with permission [49]). The IPM machine is a topology that is challenging to analyze because the so-called “bridges” of the rotor steel are heavily saturated at all times where the rotor steel presents a “short circuit” path to the PM flux. As a consequence of this saturation, the flux distribution in the airgap due to the PM is heavily dependent upon the nonlinear operating point of the rotor bridges, and thus a proper analysis of IPM machines must take bridge saturation into account.

As a first step sanity check, the MoM was used to analyze the IPM topology in the magnetically linear case utilizing the Galerkin formulation in Chapter 2 and the accompanying DBOR reduction in Chapter 3. To establish a linear model, the relative permeability in all steel elements was set to a constant 32,565.75 for M19 steel acting in the linear region. The stator excitation was set to rated, wherein $I_{qs}^r = 10.57$ A,

and $I_{ds}^r = -8.68$ A. The MoM mesh, shown in Fig. 5.3a required 8,418 elements per pole in order to reach reasonable agreement with the FEA-predicted torque. The FEA was set to adaptively refine its mesh until the change in torque was less than .01%. The MoM mesh was manually refined wherein the rotor outer surface and tooth tip surfaces were the main targets of the refinement, since one might expect that the proximity of these geometric members will impact the torque value. The flux density vs rotor position in tooth 1 and yoke 1, respectively, is shown in Fig. 5.3a and 5.3b for both the MoM and FEA. The normal and tangential components of flux density in the airgap are shown in Figs. 5.4a and 5.4b, respectively, for both MoM and FEA. The torque vs rotor position is shown in Fig. 5.5. Inspecting visually, the agreement among the flux density waveforms is respectable, yet there is noticeable disagreement in the predicted torque. This is interesting since both the MoM and FEA meshes for this study are considered to be of rather fine resolution. The torque mismatch is corroborated by examining the convergence of the respective torque calculations as their meshes are refined, as shown in Figure 5.6. The MoM torque was computed at $\theta_{rm} = 0.0654$ rad (the location of greatest mismatch) as the mesh was indiscriminately refined on all surfaces. One may notice that even with MoM element counts which are fairly high (1,000-5,000 elements per pole) there is extreme mismatch in the torque calculation, roughly by an order of magnitude. At very high element counts, although the MoM torque appears to not yet be converged, the storage requirement of the system matrix, even when utilizing the DBOR reduction, exceeded the available memory of 32 GB and computation times were reaching as high as 30 minutes per mesh resolution.

The mismatch in the torque waveform (Fig. 5.5) is unexpected since a good torque waveform agreement with FEA was observed with the SPM machine. The low value of average torque obtained is the result of the short circuiting of the PM flux. Without saturation of the flux bridge, there is very little flux from the permanent magnet crossing the airgap. Indeed, it will be shown in the next sections that nonlinear

models are required in order to obtain the expected average torque under rated stator current, which is approximately 33 Nm.

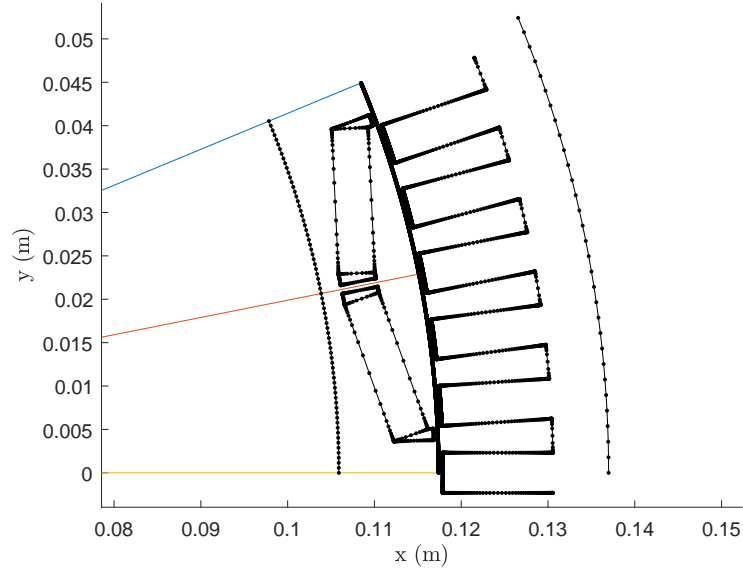


Fig. 5.2.: Linear MoM model of IPM machine: Single pole mesh of IPM machine; 8414 elements per pole.

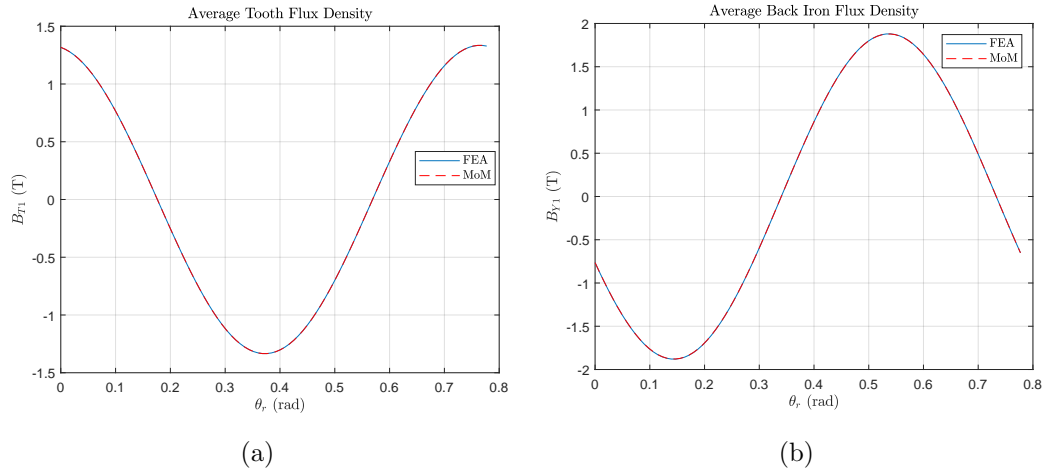


Fig. 5.3.: Linear MoM model of IPM machine: Flux density vs rotor position comparison in (a) tooth 1 and (b) yoke 1.

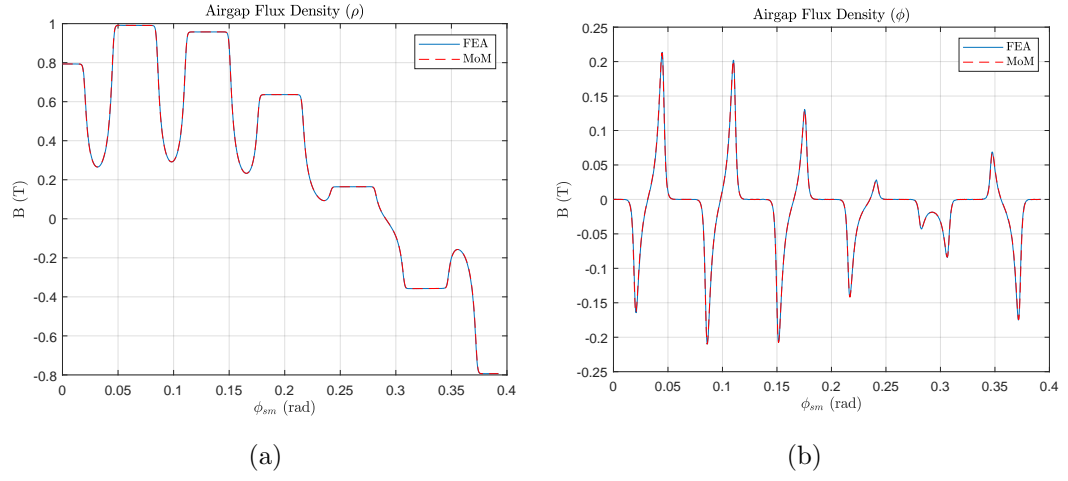


Fig. 5.4.: Linear MoM model of IPM machine: Airgap flux density comparison at $\theta_{rm} = 0$ of (a) ρ component and (b) ϕ component.

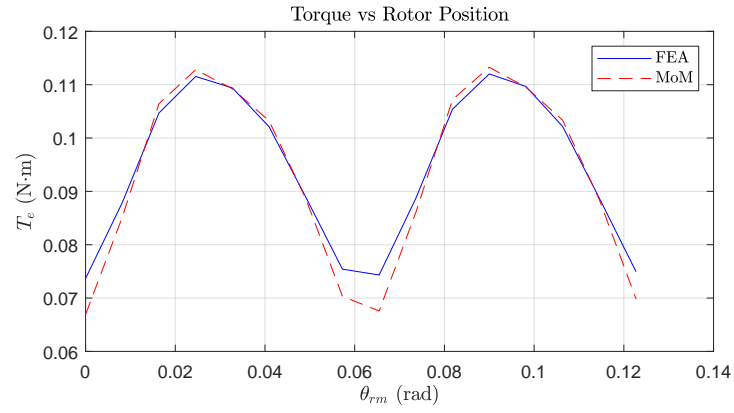


Fig. 5.5.: Linear MoM model of IPM machine: Torque vs rotor position.

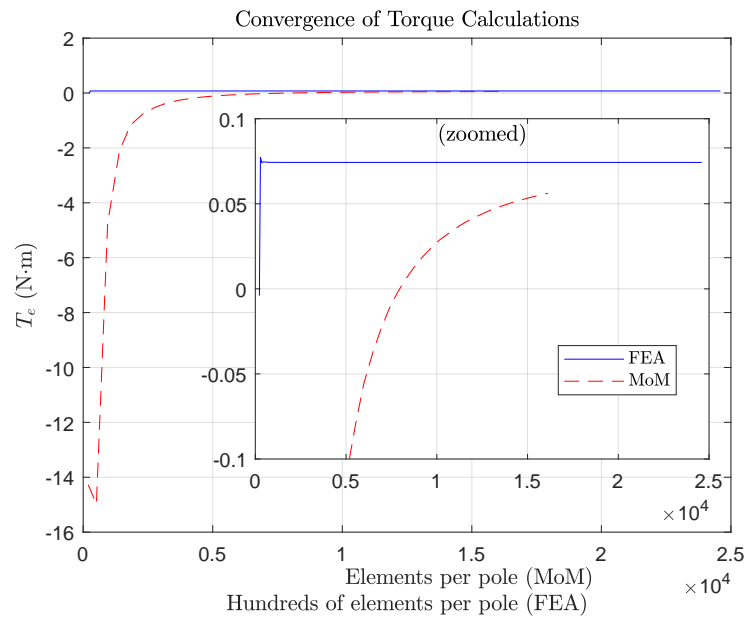


Fig. 5.6.: Linear MoM model of IPM machine: Convergence of torque calculations at $\theta_{rm} = 0.0654$ rad.

5.2 Hybrid Method Description

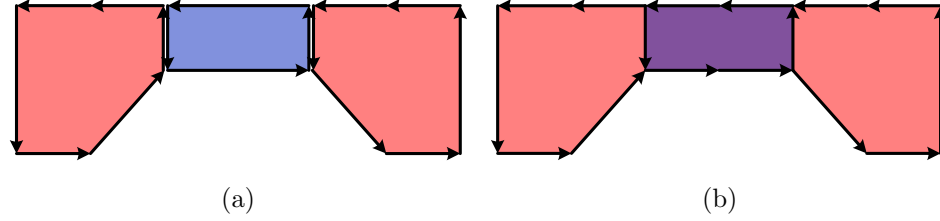


Fig. 5.7.: Hybrid MoM mesh: linear/nonlinear elements occupying separate domains (a) and in superposition(b).

5.2.1 Mesh and Nonlinear Characteristic

The hybrid model utilized in this research is one in which the linear and nonlinear elements occupy separate spatial domains. This is illustrated in Fig. 5.7a wherein a single nonlinear element (blue region) has been placed at a flux bottleneck adjacent to, but distinct from, the material meshed with linear elements (red regions on either side of the bottleneck). The separation of the domains is apparent due to the redundant boundary mesh vectors at the ports of the flux bottleneck and is exaggerated in the figure with a small separation (small white region) to further emphasize the separation. One drawback of the separate-domains formulation is that it requires the modification of an existing linear Galerkin mesh to de-enclose a region in which a nonlinear region is to be introduced and subsequently meshed.

In [4] a hybrid model was proposed in which linear and nonlinear elements co-occupy a single domain such that their respective bound currents are in superposition within the magnetic material. This is illustrated in Fig. 5.7b wherein the demagnetizing material (blue region) is superimposed upon the linear material (single red region now including the bottleneck and adjacent ports) to form the region with superimposed bound currents (purple region). The superposition hybrid formulation is

attractive since any pre-existing linear Galerkin mesh may be utilized and a selective volume mesh of the local saturation regions may be superimposed upon it where saturation is expected. Hence no modification of the linear Galerkin mesh, or a computer program to generate one, is required. This choice of model affects the material nonlinear characteristic that must be used. Specifically, the volume-meshed elements must act to de-magnetize only when flux densities near saturation. In attempting to implement this method, it was observed that such a nonlinear characteristic causes poor convergence of nonlinear equation solvers, hence the separate-domains hybrid method was chosen over it.

5.2.2 Matrix Equation

To form the hybrid model, the linear and nonlinear MoM formulations are combined. From the linear equation system (2.6) and the nonlinear residual form (2.30), the residual of the hybrid system is

$$\begin{bmatrix} \mathbf{g}_L(\mathbf{x}) \\ \mathbf{g}_{NL}(\mathbf{x}) \end{bmatrix} = \begin{bmatrix} \mathbf{f}_{B_L M_L} & \mathbf{f}_{B_L M_{NL}} \\ \mathbf{f}_{B_{NL} M_L} & \mathbf{f}_{NL M_{NL}} \end{bmatrix} \mathbf{x} + \begin{bmatrix} \mathbf{B}_{\text{source},L} \\ \mathbf{B}_{\text{source},NL} \end{bmatrix} - \begin{bmatrix} \mathbf{f}_{B_{\text{tot}} M_L} \mathbf{M}_L \\ \mathbf{f}_{B_{\text{tot}}}(\mathbf{M}_{NL}) \end{bmatrix} \quad (5.1)$$

where the unknown vector

$$\mathbf{x} = \begin{bmatrix} \mathbf{M}_L \\ \mathbf{M}_{NL} \end{bmatrix} \quad (5.2)$$

now contains both the linear and nonlinear material magnetization vectors and the source magnetic field contributions to the linear and nonlinear elements due to known free and bound current sources are given by

$$\begin{bmatrix} \mathbf{B}_{\text{source},L} \\ \mathbf{B}_{\text{source},NL} \end{bmatrix} = \begin{bmatrix} \mathbf{f}_{B_L I_f} \\ \mathbf{f}_{B_{NL} I_f} \end{bmatrix} \mathbf{I}_f + \begin{bmatrix} \mathbf{f}_{B_L I_{PM}} \\ \mathbf{f}_{B_{NL} I_{PM}} \end{bmatrix} \mathbf{I}_{PM} \quad (5.3)$$

The Galerkin formulation is used for the linear material equations and the point-matching formulation is used for the nonlinear materials equations. Hence, the unknown vector \mathbf{M}_L is the tangent component of magnetization and the unknown vector

\mathbf{M}_{NL} is the x - and y - component of magnetization, although, for sake of clarity, this information is not contained within the subscripts.

Application of the DBOR reduction to the hybrid system is accomplished by applying DBOR reductions to the linear and nonlinear portions of the hybrid tableau using the respective procedures in Sections 3.6.1 and 3.6.3. It is desired to reduce the linear and nonlinear components of (5.1) to one block-row each. Applying the DBOR reductions yields

$$\begin{bmatrix} \{\mathbf{g}_L(\mathbf{x})\}_1 \\ \{\mathbf{g}_{NL}(\mathbf{x})\}_1 \end{bmatrix} = \begin{bmatrix} [\tilde{\mathbf{A}}_{L,L}]_{P/2+1} & [\tilde{\mathbf{A}}_{L,NL}]_{P/2+1} \\ [\tilde{\mathbf{A}}_{NL,L}]_{P/2+1} & [\tilde{\mathbf{A}}_{NL,NL}]_{P/2+1} \end{bmatrix} \mathbf{x} + \begin{bmatrix} \{\mathbf{B}_{\text{source},L}\}_1 \\ \{\mathbf{B}_{\text{source},NL}\}_1 \end{bmatrix} - \begin{bmatrix} [\mathbf{f}_{B_{\text{tot}}M_L}]_1 \{\mathbf{M}_L\}_1 \\ \mathbf{f}_{B_{\text{tot}}}(\{\mathbf{M}_{NL}\}_1) \end{bmatrix} \quad (5.4)$$

where due to the DBOR reduction process, each of the four matrices within the system matrix tableau are given by

$$\begin{aligned} [\tilde{\mathbf{A}}_{L,L}]_{P/2+1} &= [\mathbf{A}_{L,L}]_1 - [\mathbf{A}_{L,L}]_2 + \cdots + [\mathbf{A}_{L,L}]_{P-1} - [\mathbf{A}_{L,L}]_P \\ [\tilde{\mathbf{A}}_{L,NL}]_{P/2+1} &= [\mathbf{A}_{L,NL}]_1 - [\mathbf{A}_{L,NL}]_2 + \cdots + [\mathbf{A}_{L,NL}]_{P-1} - [\mathbf{A}_{L,NL}]_P \\ [\tilde{\mathbf{A}}_{NL,L}]_{P/2+1} &= [\mathbf{A}_{NL,L}]_1 - [\mathbf{A}_{NL,L}]_2 + \cdots + [\mathbf{A}_{NL,L}]_{P-1} - [\mathbf{A}_{NL,L}]_P \\ [\tilde{\mathbf{A}}_{NL,NL}]_{P/2+1} &= [\mathbf{A}_{NL,NL}]_1 - [\mathbf{A}_{NL,NL}]_2 + \cdots + [\mathbf{A}_{NL,NL}]_{P-1} - [\mathbf{A}_{NL,NL}]_P \end{aligned} \quad (5.5)$$

where each of which are comprised, respectively, of the blocks within block-row 1 of the matrices

$$\begin{aligned} \mathbf{A}_{L,L} &= \mathbf{f}_{B_L M_L} \\ \mathbf{A}_{L,NL} &= \mathbf{R}^{-1} \mathbf{f}_{B_L M_{NL}} \mathbf{R} \\ \mathbf{A}_{NL,L} &= \mathbf{f}_{B_{NL} M_L} \\ \mathbf{A}_{NL,NL} &= \mathbf{R}^{-1} \mathbf{f}_{B_{NL} M_{NL}} \mathbf{R}. \end{aligned} \quad (5.6)$$

The relationship (3.130) is used to form the first block-row of each $\mathbf{A}_{L,NL}$ and $\mathbf{A}_{NL,NL}$.

5.2.3 Modified Newton-Raphson Algorithm

The Newton-Raphson (N-R) method is a popular choice for solving systems of nonlinear equations due to its quadratic convergence property. This quality is enjoyed

provided the initial guess is in the vicinity of the solution. Otherwise, taking the “full” Newton step

$$\mathbf{x}_{\text{full}}^{k+1} = \mathbf{x}^k - \mathbf{J}^{-1} \mathbf{g}(\mathbf{x}^k) \quad (5.7)$$

at each iteration may cause failure of convergence. A common means to prevent such a failure is to relax, or dampen, the Newton step by using a weighted sum of the old iterate (index k) and full Newton step (index $k + 1$):

$$\begin{aligned} \mathbf{x}_{\text{relaxed}}^{k+1} &= \alpha \mathbf{x}_{\text{full}}^{k+1} + (1 - \alpha) \mathbf{x}^k \\ &= \mathbf{x}^k - \alpha \mathbf{J}^{-1} \mathbf{g}(\mathbf{x}^k) \end{aligned} \quad (5.8)$$

where $\alpha \in (0, 1]$ is termed the “relaxation factor.”

In applying the N-R process of Section 2.3, it was observed that the solution trajectory would often venture into regions with extremely high magnetic fields – in excess of 1×10^4 T – and subsequently many iterations (hundreds) were required to attain convergence, with some trajectories failing to converge. A relatively straightforward method of overcoming this was found by detecting any large change in flux density. Specifically, the change in flux density is monitored between each iteration by computing

$$\Delta B^{k+1} = \mathbf{f}_{B_{\text{tot}}}(\mathbf{M}_{\text{NL}}^{k+1}) - \mathbf{f}_{B_{\text{tot}}}(\mathbf{M}_{\text{NL}}^k) \quad (5.9)$$

When a large change in magnetic field is observed, the progress made by the prior full Newton step is adjusted along its original direction:

$$\begin{aligned} \mathbf{x}_{\text{relaxed}}^k &= \alpha \mathbf{x}^k + (1 - \alpha) \mathbf{x}^{k-1} \\ \mathbf{x}^k &= \mathbf{x}_{\text{relaxed}}^k \end{aligned} \quad (5.10)$$

using a small value for α - a process known as back-tracking [50]. It was found that a back-tracking step with $\alpha = 0.05$ tends to correct the solution trajectory in the vast majority of cases encountered. This modified N-R process may be viewed as a binary variant of the globally convergent N-R method [50]. A flowchart of the N-R process is depicted in Fig. 5.8. In this research, the linear solution of the hybrid model was used as an initial guess, however the respective relative permeabilities

used in the $\mathbf{f}_{B_{\text{tot}}M}$ diagonal entries are computed using functions [26] which depend on flux density, wherein the flux density is set to a value on the saturation knee of the material.

5.3 Comparison of Hybrid Models

In this section, four hybrid models are used to compute the relevant information needed for a fitness evaluation in a PBD design run; this information includes torque vs rotor position, and flux densities vs rotor position in one stator tooth and backiron segment over the angular span of two slot pitches. The core loss is predicted using the flux density waveforms as was done in the design study in Chapter 4. The models are compared in terms of their accuracy in torque and loss predictions and in terms of their computation time components. The particular machine design studied is “IPM Design 284” operating under condition “OP 1” from [49]. For convenience, the geometry and operating condition parameters for this machine/study are listed in Table 5.1.

All four hybrid models in the comparison utilize the separate-domains hybrid method for their mesh and nonlinear material characteristic and all models use the modified N-R algorithm of Section 5.2.3 to solve the nonlinear matrix equation. The magnetic material properties/nonlinear characteristics were taken from the Power Magnetic Material Toolbox [26] for the respective materials in Table 5.1. The four hybrid models differ in the degree to which they are volume meshed, ranging from a full volume mesh of all steel to only the rotor bridges having a volume mesh. The hybrid models are used to compute flux density and the torque waveforms. Each model utilizes both a low resolution (LR) and high resolution (HR) mesh to examine the effect of element count on accuracy. A comparison table is provided following the waveform comparisons of each hybrid model. The table is used to report the computation time breakdown of each hybrid model and resolution as well as the linear and nonlinear element counts, maximum iterations required and error in average torque

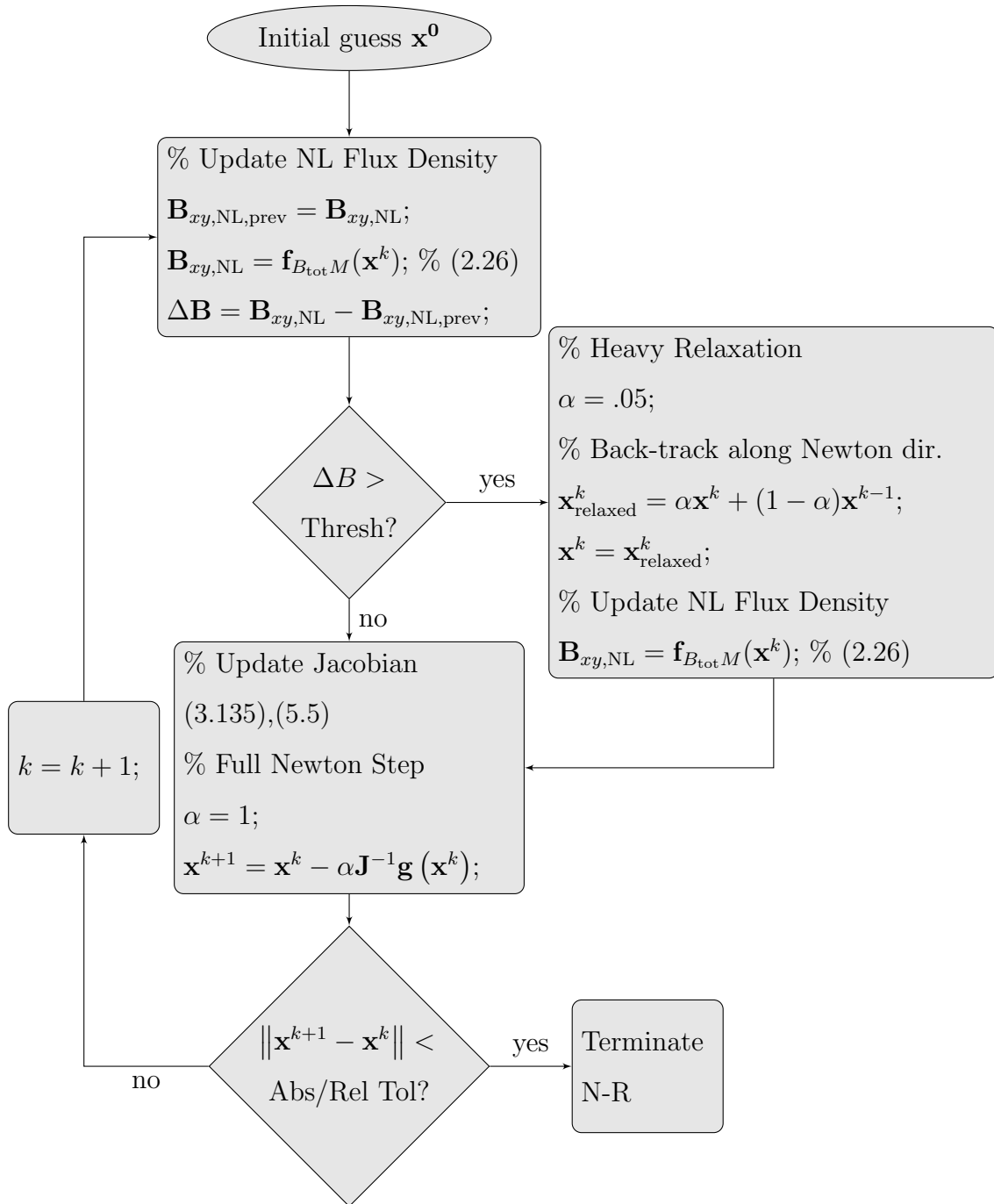


Fig. 5.8.: Flow chart for selective relax N-R process.

and loss. FEA-based predictions of the same quantities for the same machine/conditions are used as the basis of the comparisons.

A final note is made on the error calculation of flux density waveforms. In the MSE loss calculation, the derivatives of flux density waveforms are established via numerical differentiation and are subsequently squared. This process leads to a nonlinear mapping of the error in the waveforms to the error in the loss prediction. Instead of percent error in calculated loss, the error in the flux density waveforms is established using a Mean Relative Error:

$$MRE_{B_{T1}} = \frac{1}{N} \sum_{i=1}^N \frac{|\mathbf{B}_{T1,MoM}(i) - \mathbf{B}_{T1,FEA}(i)|}{\max(\mathbf{B}_{T1,FEA})} \quad (5.11)$$

$$MRE_{B_{Y1}} = \frac{1}{N} \sum_{i=1}^N \frac{|\mathbf{B}_{Y1,MoM}(i) - \mathbf{B}_{Y1,FEA}(i)|}{\max(\mathbf{B}_{Y1,FEA})} \quad (5.12)$$

where instead of using the denominator $|\mathbf{B}_{FEA}(i)|$, as is standard, we use the maximum of the “reference” waveform as the denominator to avoid introducing artificial error near zero crossings. The quantity $MRE_B = \frac{100}{2}(MRE_{B_{T1}} + MRE_{B_{Y1}})$ is reported as a percentage in the following comparison tables.

5.3.1 All Steel Nonlinear: Model A

In this hybrid method, the stator and rotor steel are fully volume meshed with triangles using the PDE Toolbox [51]. The linear PM material is meshed with a logarithmically-spaced surface mesh. Results predicted using both low and (relatively) high mesh resolution MoM hybrid methods are compared with similar results predicted by FEA. The LR and HR meshes are shown in Figs. 5.9a and 5.9b. A closer view of the rotor bridge mesh for the LR and HR cases is shown in Figs. 5.10a and 5.10b. The predicted flux density waveforms in a stator tooth over rotor positions spanning two poles for the LR and HR cases is shown in Figs. 5.11a and 5.11b. Surprisingly, the LR case is visually determined to be in better agreement with FEA than the HR case. The predicted flux density waveforms in a stator backiron yoke

Table 5.1.: Comparison Conditions “OP 1” and Parameters for “Design 284” [49]

Parameter	Value	Unit	Description
I_{qs}^r	10.75	A	Q-axis stator current
I_{ds}^r	−8.68	A	D-axis stator current
	M19		Stator Steel Type
	M19		Rotor Steel Type
	Ferrite AC-12		Permanent Magnet Type
P	16		Pole count
N_{as}	[0 4 13 13 4 0]		a -phase conductor density (1 pole)
ω_{rm}	104.72	rad/s	rotor speed, mechanical
S_s	96		Number of stator slots
l	34.2	mm	Machine length
l'_{bi}	1.3	mm	Length of flux barrier
r_{rs}	20.0	mm	Rotor shaft radius
r_{ri}	105.9	mm	Radius to inner rotor backiron
r_{rb}	108.3	mm	Radius to inside corner of inner flux barrier
r_{bo}	116.9	mm	Radius to underside of outer bridge
w_{bo}	0.5	mm	Width of outer bridge
g	0.5	mm	Airgap
r_{st}	117.9	mm	Radius to stator tooth tips
r_{sb}	130.59	mm	Radius to stator backiron
r_{ss}	136.99	mm	Outer radius of machine
α_{tt}	0.6		Tooth fraction
α_{pm}	0.8357		PM fraction
α_{dm}	0.2502		Depth of PM fraction
θ_{lm}	0.1495	rad	PM angle of inclination

over rotor positions spanning two poles for the LR and HR cases is shown in Figs. 5.12a and 5.12b. Respectable agreement is attained in both. The torque waveforms predicted over rotor positions spanning two slots for the LR and HR cases is shown in Figs. 5.13a and 5.13b. The torque waveform visually differs from FEA, yet in the average sense both the LR and HR cases appear to agree well with FEA. This is somewhat expected considering the discussion of the linear IPM model in Section 5.1. The computational performance is listed in Table 5.2. Notable is the accuracy in average torque in both LR and HR cases, although the computation times are both relatively high.

As the mesh is refined, it is expected that FEA and MoM will improve their agreement with one another. The flux density waveform B_{T1} of the HR case stands out as there are two regions of obvious disagreement, going against expectations. The reason for this disagreement is not yet known, except to say that further mesh refinements did not improve the agreement and the disagreement became stationary. It is currently thought that using a volume integral to establish the influence between edge and polygon elements may be a possible remedy.

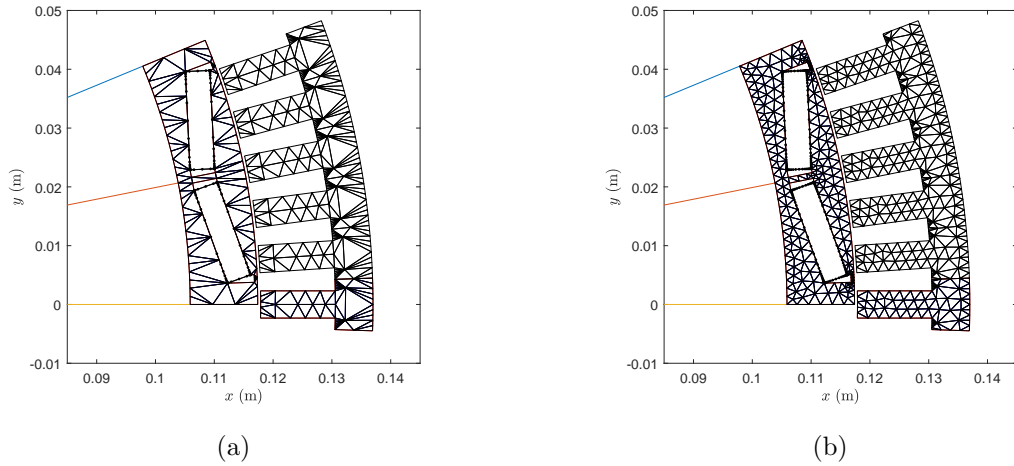


Fig. 5.9.: Hybrid MoM model of IPM machine: low (a) and high (b) mesh resolution cases - all steel nonlinear NL.

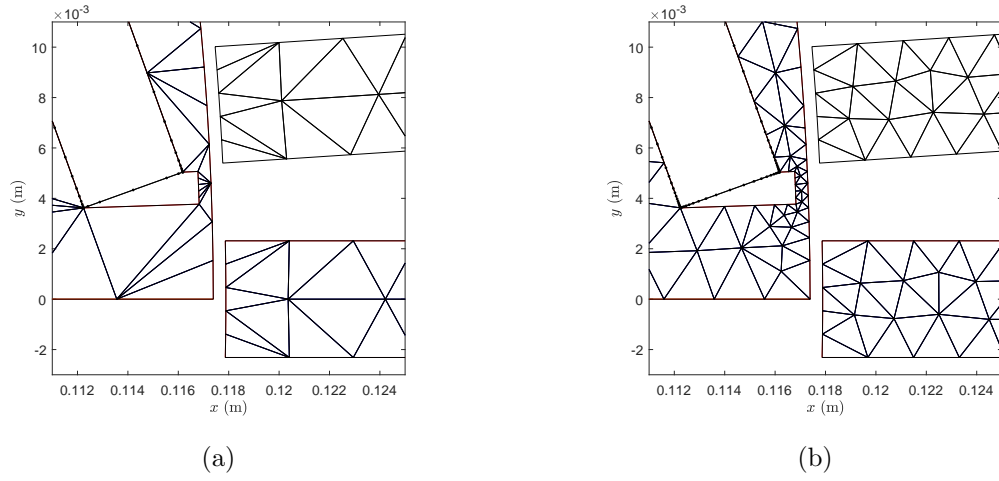


Fig. 5.10.: Hybrid MoM model of IPM machine: low (a) and high (b) mesh resolution cases - all steel nonlinear (zoomed view of bridge/teeth).

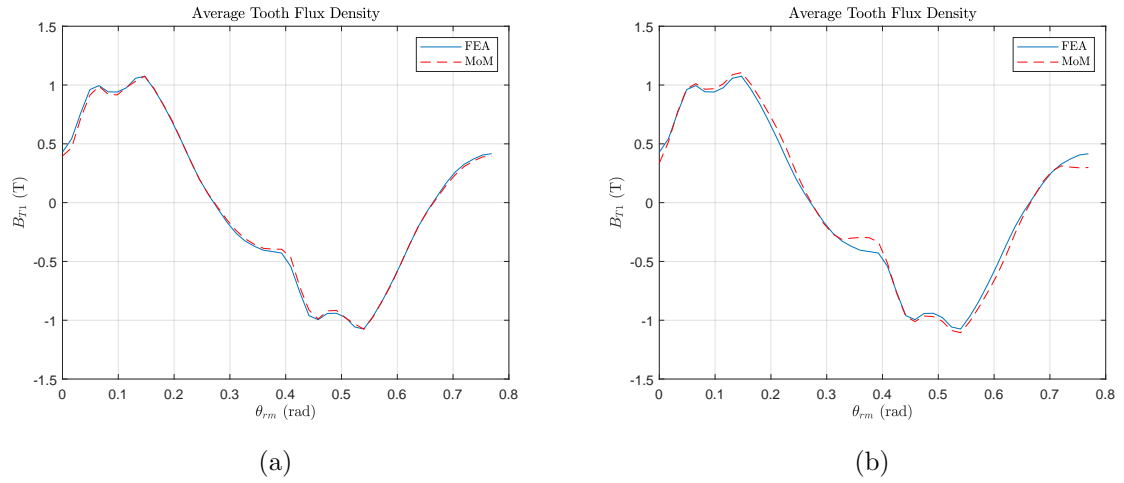


Fig. 5.11.: Hybrid MoM model of IPM machine: Magnetic field vs rotor position in stator tooth 1 in low (a) and high (b) mesh resolution cases - all steel nonlinear.

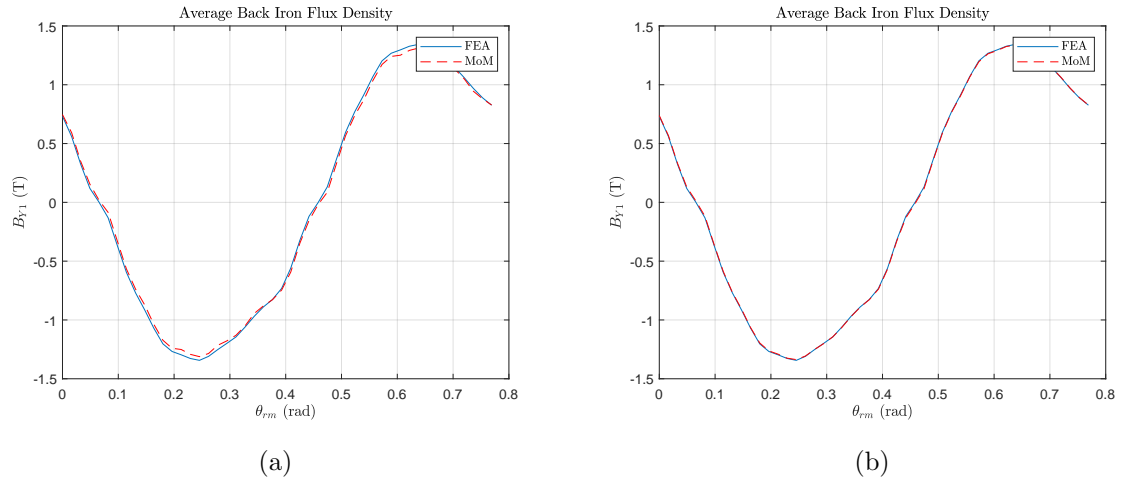


Fig. 5.12.: Hybrid MoM model of IPM machine: Magnetic field vs rotor position in stator yoke 1 in low (a) and high (b) mesh resolution cases - all steel nonlinear.

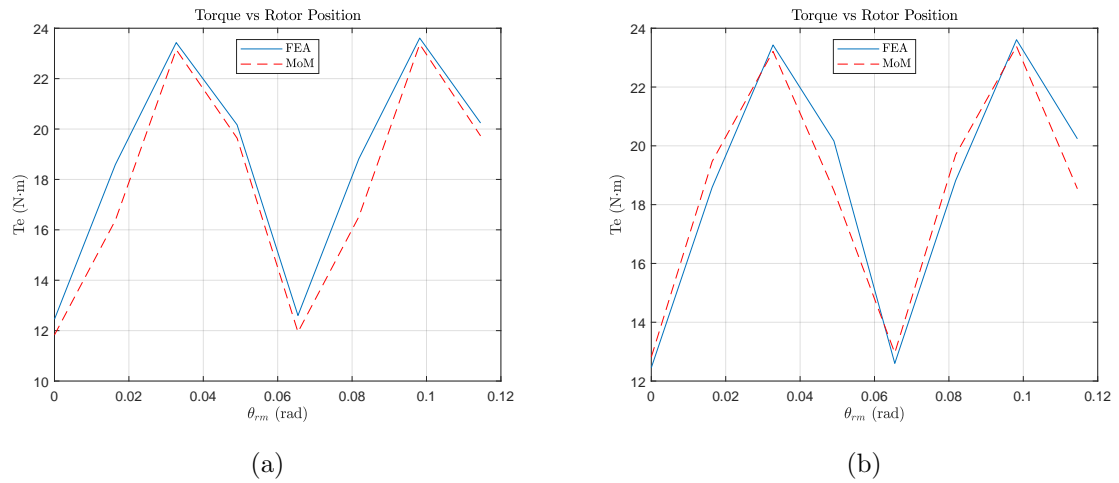


Fig. 5.13.: Hybrid MoM model of IPM machine: Torque vs rotor position in stator tooth 1 in low (a) and high (b) mesh resolution cases - all steel nonlinear.

Table 5.2.: Computational Performance Comparison - All Steel Nonlinear

	Low Resolution	High Resolution	
Metric	Value	Value	Unit
Mesh	0.95	.66	s
Matrix population	23.47	213.26	s
Solve	5.78	29.34	s
Observation	21.55	45.97	s
Torque	6.53	28.88	s
Total CPU Time	58.29	318.11	s
Max NL Iterations	17	23	
Error Avg. Torque	4.90	0.904	%
MRE_B	1.85	2.22	%
Elements/pole	104(L)+422(NL)	240(L)+952(NL)	

5.3.2 Nonlinear Rotor Bridges and Full Stator: Model B

In this hybrid method, the stator and rotor bridges are volume meshed using 4-sided polygons, which was manually programmed in order to have control over local mesh density. The linear PM material is meshed with a logarithmically-spaced surface mesh. Results predicted using a low and (relatively) high mesh resolution MoM hybrid method are compared with similar results predicted by FEA. The LR and HR meshes are shown in Figs. 5.14a and 5.14b. A closer view of the rotor bridge mesh of the LR and HR cases is shown in Figs. 5.15a and 5.15b. The predicted flux density waveforms in a stator tooth over rotor positions spanning two poles for the LR and HR cases is shown in Figs. 5.16a and 5.16b. Neither waveform matches FEA well, although the HR case achieves an improvement. The predicted flux density waveforms in a stator backiron yoke over rotor positions spanning two poles for the LR and HR cases is shown in Figs. 5.17a and 5.17b. Again neither waveform matches FEA well, although the resolution mesh achieves an improvement. The torque waveforms predicted over rotor positions spanning two slots for the LR and HR cases is shown in Figs. 5.18a and 5.18b. The torque waveforms have similarly poor agreement and additionally visually disagree in the average torque. The computational performance is listed in Table 5.3. Notable is the low computation time of the LR method and low nonlinear iterations of both LR and HR cases. Also notable is the poor performance in every other metric.

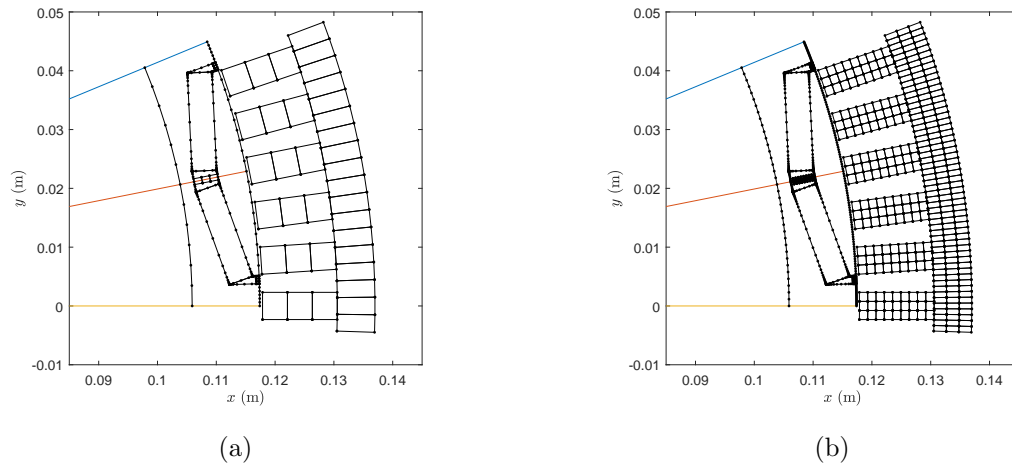


Fig. 5.14.: Hybrid MoM model of IPM machine: low (a) and high (b) mesh resolution cases - rotor bridges and stator NL.

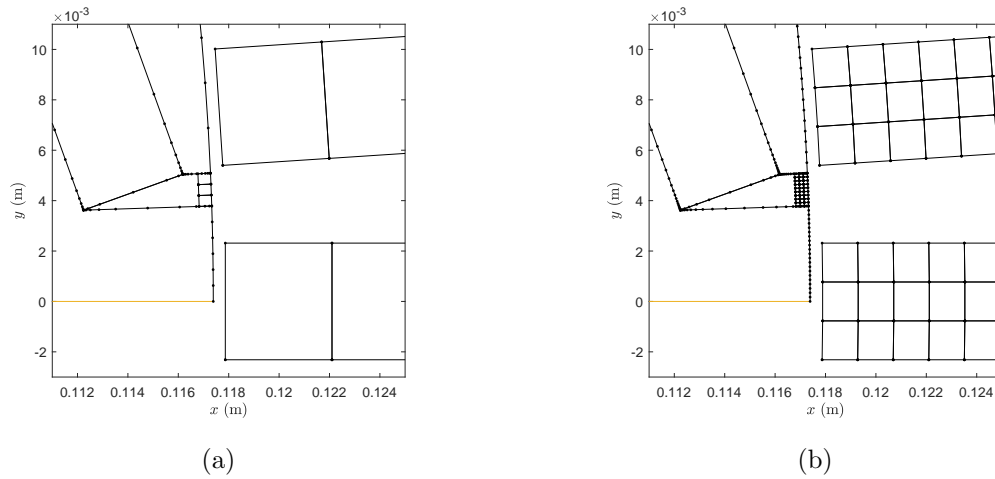


Fig. 5.15.: Hybrid MoM model of IPM machine: low (a) and high (b) mesh resolution cases - rotor bridges and stator NL (zoomed view of bridge/teeth).

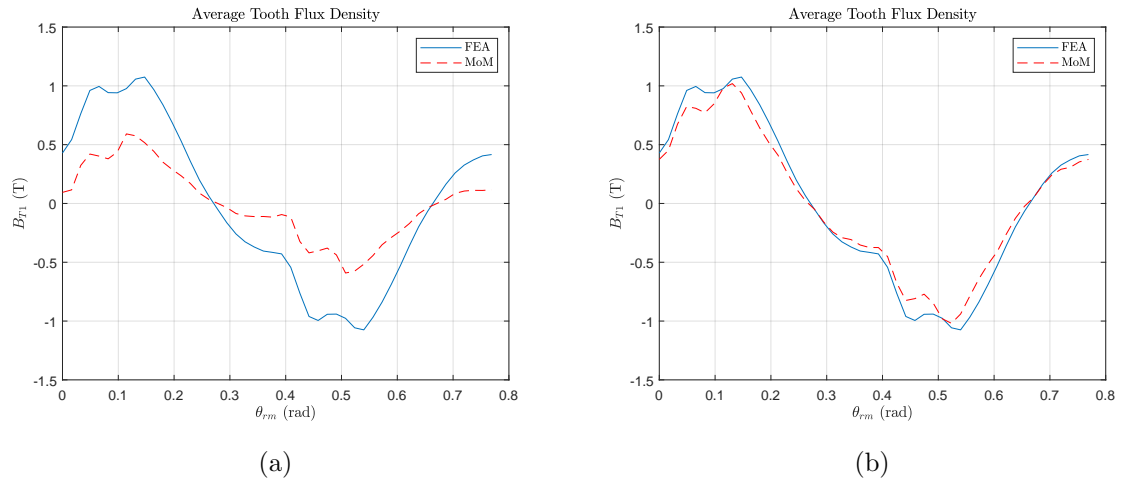


Fig. 5.16.: Hybrid MoM model of IPM machine: Magnetic field vs rotor position in stator tooth 1 in low (a) and high (b) mesh resolution cases - rotor bridges and stator NL.

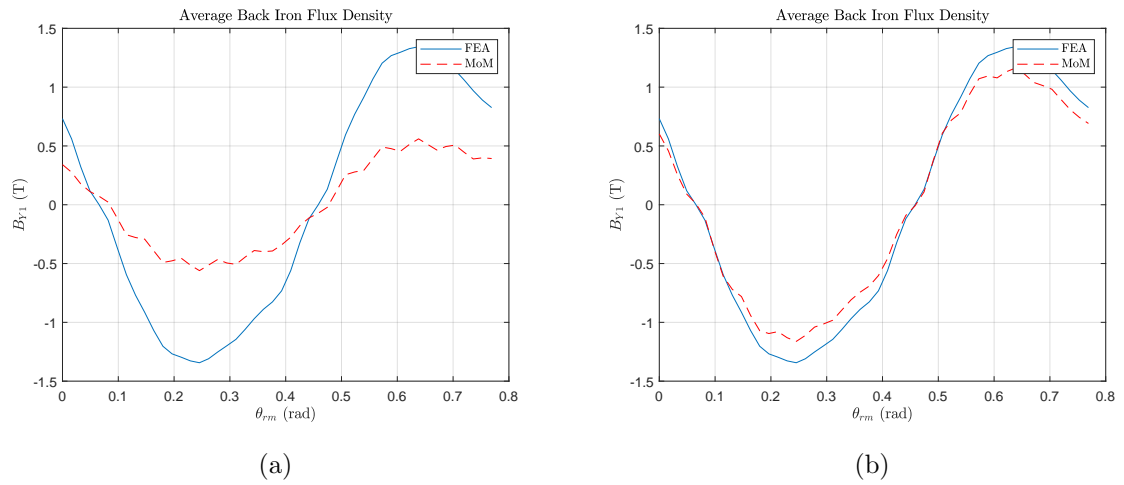


Fig. 5.17.: Hybrid MoM model of IPM machine: Magnetic field vs rotor position in stator yoke 1 in low (a) and high (b) mesh resolution cases - rotor bridges and stator NL.

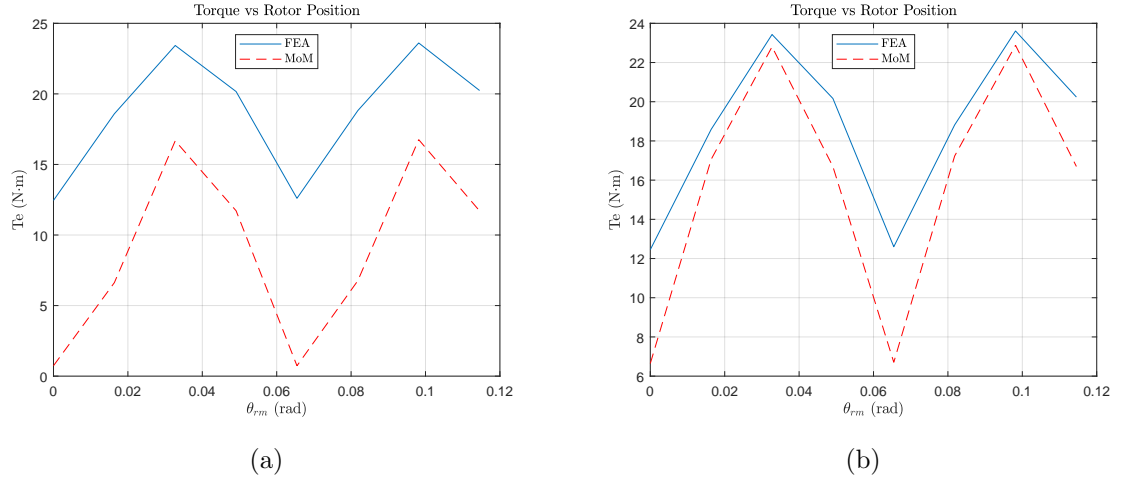


Fig. 5.18.: Hybrid MoM model of IPM machine: Torque vs rotor position in stator tooth 1 in low (a) and high (b) mesh resolution cases - rotor bridges and stator NL.

Table 5.3.: Computational Performance Comparison - Rotor Bridges and Stator Non-linear

	Low Resolution	High Resolution	
Metric	Value	Value	Unit
Mesh	0.31	0.45	s
Matrix population	2.78	44.44	s
Solve	2.38	4.36	s
Observation	5.88	31.00	s
Torque	1.25	15.68	s
Total CPU Time	12.6	95.93	s
Max NL Iterations	12	13	
Error Avg. Torque	52.16	15.47	%
MRE_B	35.33	8.65	%
Elements/pole	208(L)+45(NL)	494(L)+405(NL)	

5.3.3 Nonlinear Rotor Bridges and Stator Teeth: Model C

In this hybrid method, the stator (teeth only) and rotor bridges are volume meshed using 4-sided polygons, which was manually programmed in order to have control over local mesh density. The linear PM material is meshed with a logarithmically-spaced surface mesh. Results predicted using a low and (relatively) high mesh resolution MoM hybrid method are compared with similar results predicted by FEA. The LR and HR meshes are shown in Figs. 5.19a and 5.19b. A closer view of the rotor bridge mesh of the LR and HR cases is shown in Figs. 5.20a and 5.20b. The predicted flux density waveforms in a stator tooth over rotor positions spanning two poles for the LR and HR cases is shown in Figs. 5.21a and 5.21b. The agreement is reasonable in both cases with a slight improvement achieved in the HR case. The predicted flux density waveforms in a stator backiron yoke over rotor positions spanning two poles for the LR and HR cases is shown in Figs. 5.22a and 5.22b. It is visually examined that the LR waveform has higher harmonic content than FEA and the HR case improves on this to attain a reasonable agreement. The torque waveforms predicted over rotor positions spanning two slots for the LR and HR cases is shown in Figs. 5.23a and 5.23b. The torque waveforms have agreeable average values and visually have disagreement in the peak-peak torque. The computational performance is listed in Table 5.4. Notable is the low computation time of the LR method, low nonlinear iterations of both LR and HR cases and good average torque agreement.

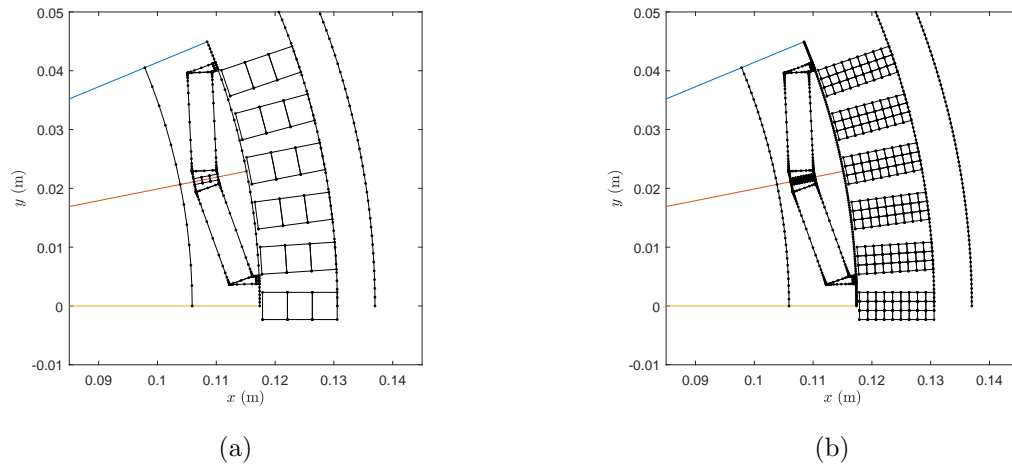


Fig. 5.19.: Hybrid MoM model of IPM machine: low (a) and high (b) mesh resolution cases - only rotor bridges and stator teeth NL.

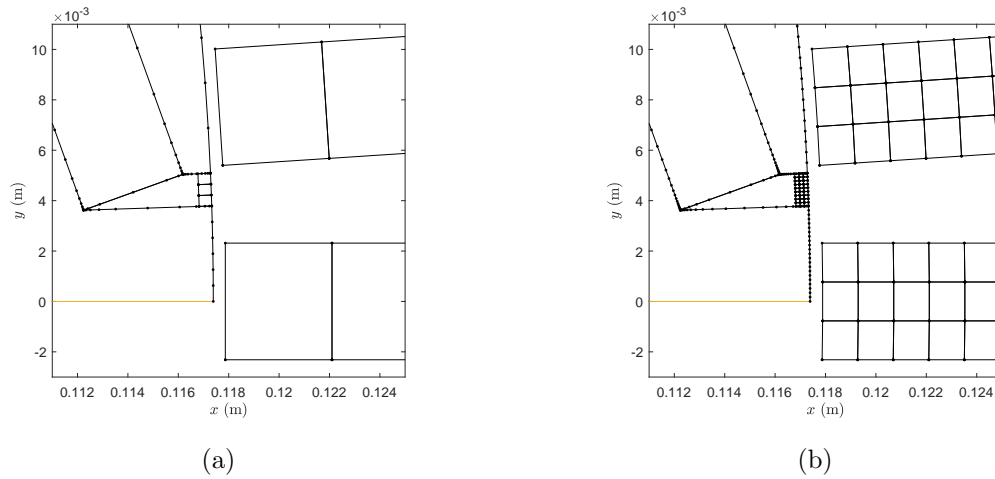


Fig. 5.20.: Hybrid MoM model of IPM machine: low (a) and high (b) mesh resolution cases - only rotor bridges and stator teeth NL (zoomed view of bridge/teeth).

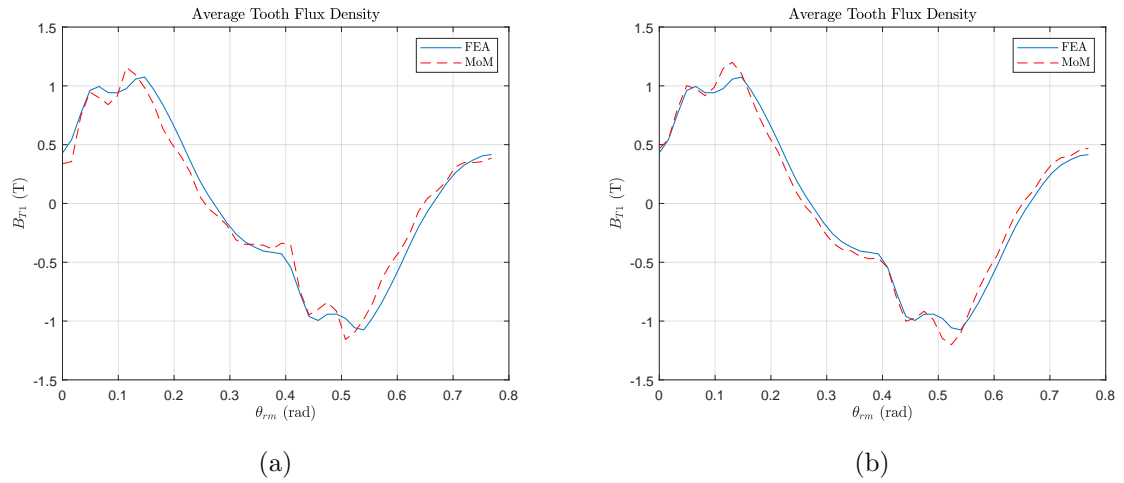


Fig. 5.21.: Hybrid MoM model of IPM machine: Magnetic field vs rotor position in stator tooth 1 in low (a) and high (b) mesh resolution cases - only rotor bridges and stator teeth NL.

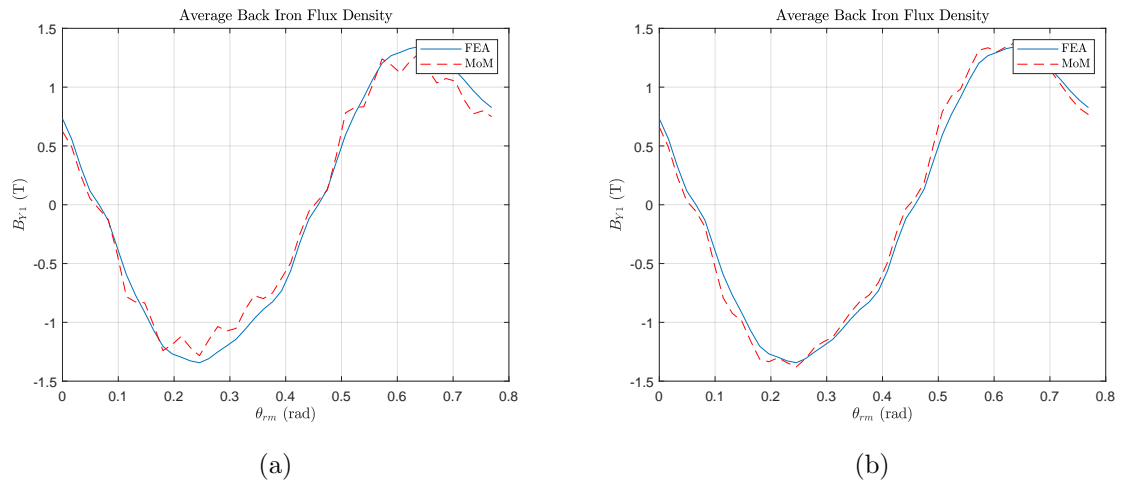


Fig. 5.22.: Hybrid MoM model of IPM machine: Magnetic field vs rotor position in stator yoke 1 in low (a) and high (b) mesh resolution cases - only rotor bridges and stator teeth NL.

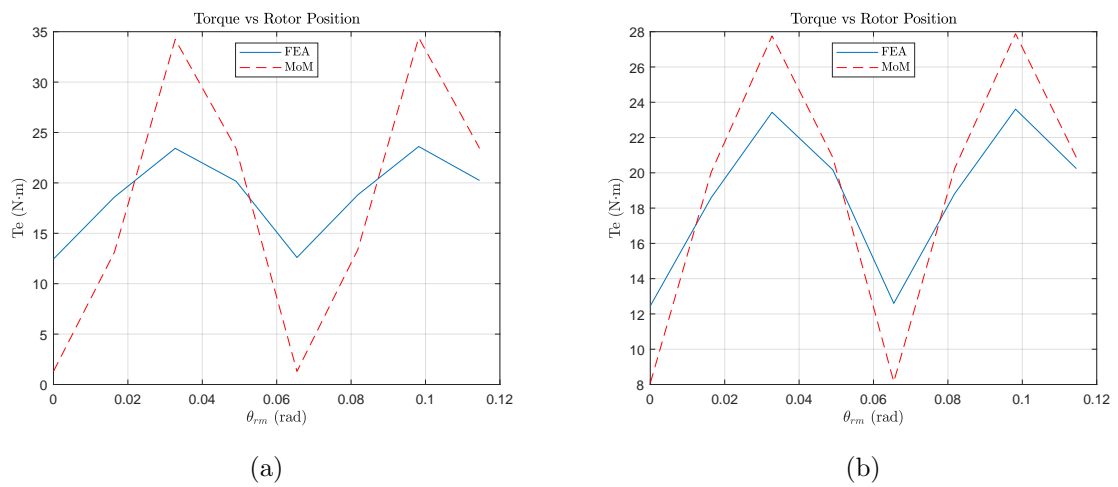


Fig. 5.23.: Hybrid MoM model of IPM machine: Torque vs rotor position in stator tooth 1 in low (a) and high (b) mesh resolution cases - only rotor bridges and stator teeth NL.

Table 5.4.: Computational Performance Comparison - Rotor Bridges and Stator Teeth
Nonlinear

	Low Resolution	High Resolution	
Metric	Value	Value	Unit
Mesh	0.20	0.26	s
Matrix population	3.45	26.83	s
Solve	2.81	3.81	s
Observation	5.95	24.03	s
Torque	1.11	13.04	s
Total CPU Time	13.52	67.97	s
Max NL Iterations	14	10	
Error Avg. Torque	3.54	2.65	%
MRE_B	7.71	5.69	%
Elements/pole	280(L)+27(NL)	638(L)+243(NL)	

5.3.4 Nonlinear Rotor Bridges Only: Model D

In this section, the most bare bones hybrid model is examined. In this hybrid method, the stator (teeth only) and rotor bridges are volume meshed using 4-sided polygons, which was manually programmed in order to have control over local mesh density. The linear PM material is meshed with a logarithmically-spaced surface mesh. Results predicted using a low and (relatively) high mesh resolution MoM hybrid method are compared with similar results predicted by FEA. The LR and HR meshes are shown in Figs. 5.24a and 5.24b. A closer view of the rotor bridge mesh of the LR and HR cases is shown in Figs. 5.25a and 5.25b. The predicted flux density waveforms in a stator tooth over rotor positions spanning two poles for the LR and HR cases is shown in Figs. 5.26a and 5.26b. The agreement is reasonable in both cases with a slight improvement achieved in the HR case. Both waveforms overestimate the flux density. The predicted flux density waveforms in a stator backiron yoke over rotor positions spanning two poles for the LR and HR cases is shown in Figs. 5.27a and 5.27b. Again the waveforms overpredict the flux density. The torque waveforms predicted over rotor positions spanning two slots for the LR and HR cases is shown in Figs. 5.28a and 5.28b. The torque waveforms have agreeable average values and visually have disagreement in the peak-peak torque. The computational performance is listed in Table 5.5. Notable is the low computation time of the LR method, low nonlinear iterations of both LR and HR cases and good average torque agreement.

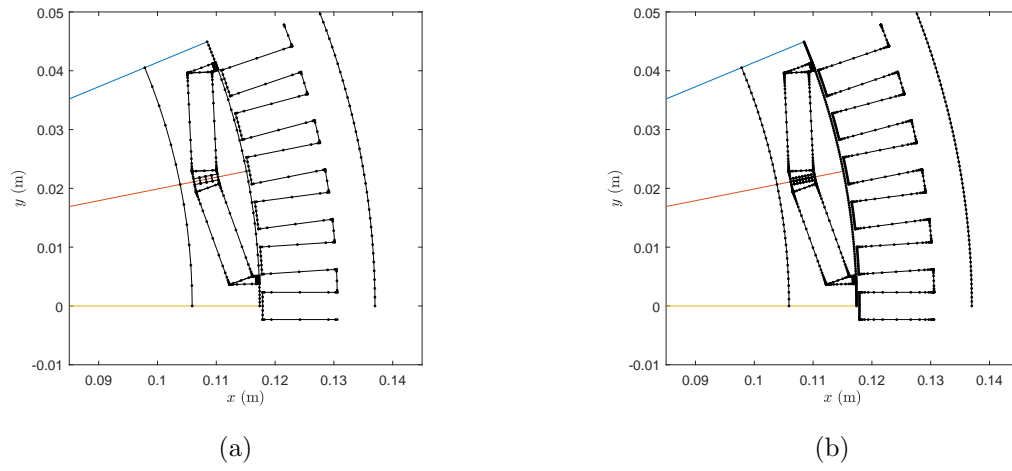


Fig. 5.24.: Hybrid MoM model of IPM machine: low (a) and high (b) mesh resolution cases - only rotor bridges NL.

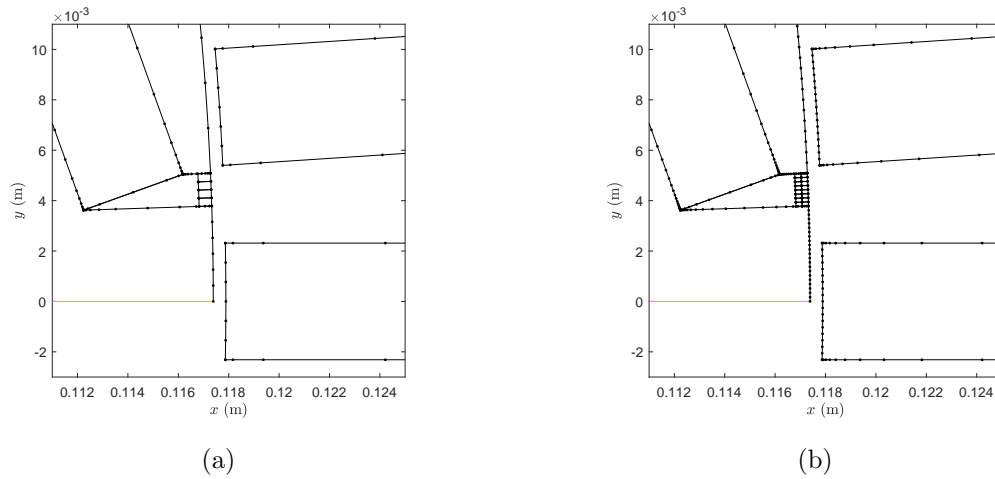


Fig. 5.25.: Hybrid MoM model of IPM machine: low (a) and high (b) mesh resolution cases - only rotor bridges NL (zoomed view of bridge/teeth).

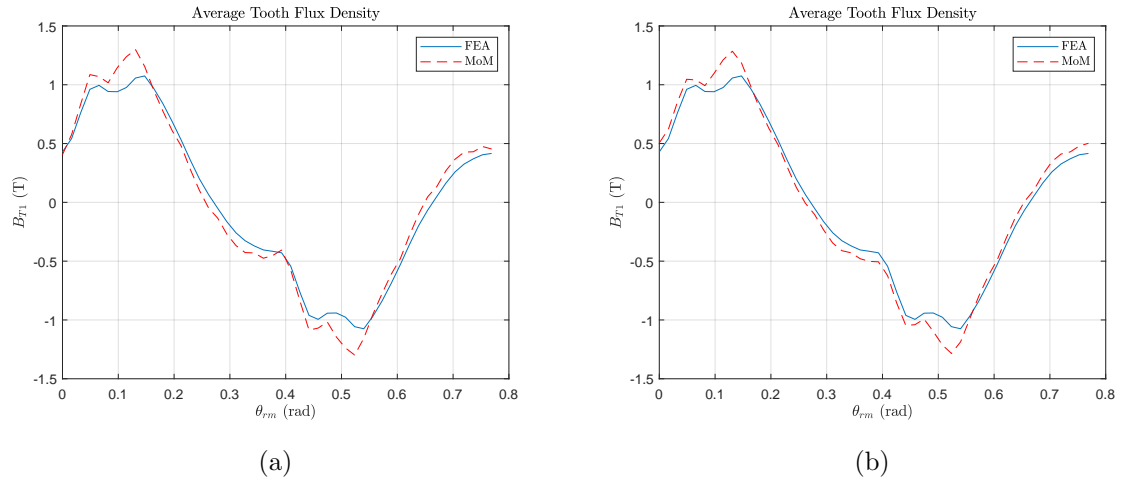


Fig. 5.26.: Hybrid MoM model of IPM machine: Magnetic field vs rotor position in stator tooth 1 in low (a) and high (b) mesh resolution cases - only rotor bridges NL.

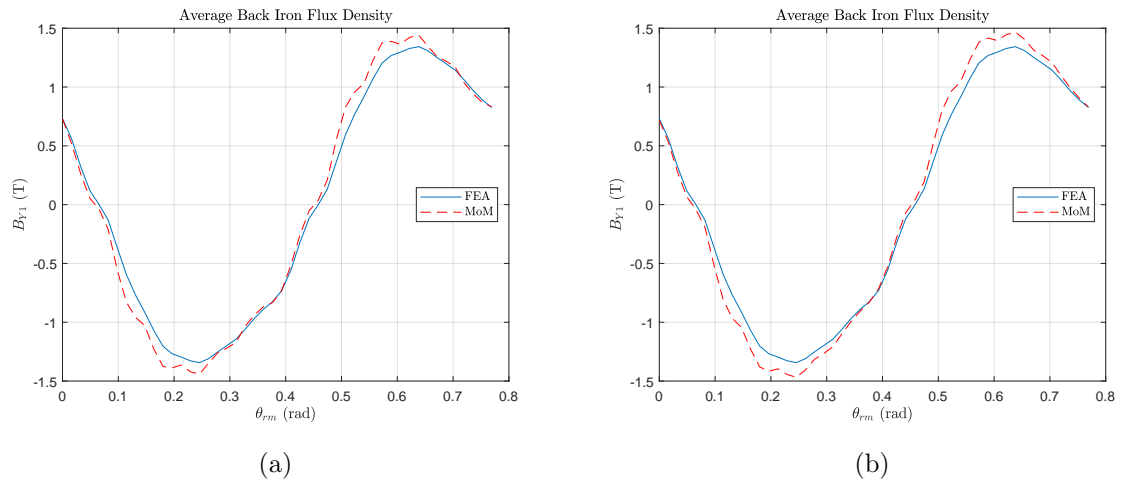


Fig. 5.27.: Hybrid MoM model of IPM machine: Magnetic field vs rotor position in stator yoke 1 in low (a) and high (b) mesh resolution cases - only rotor bridges NL.

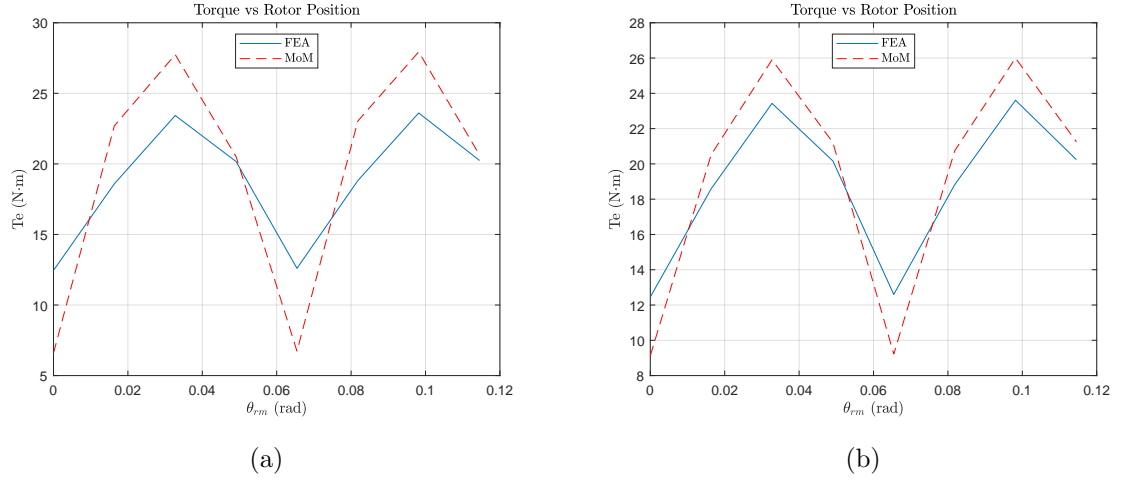


Fig. 5.28.: Hybrid MoM model of IPM machine: Torque vs rotor position in stator tooth 1 in low (a) and high (b) mesh resolution cases - only rotor bridges NL.

Table 5.5.: Computational Performance Comparison - Only Rotor Bridges Nonlinear

	Low Resolution	High Resolution	
Metric	Value	Value	Unit
Mesh	0.46	0.34	s
Matrix population	4.54	22.77	s
Solve	2.44	3.38	s
Observation	6.61	18.23	s
Torque	1.40	6.98	s
Total CPU Time	15.45	51.73	s
Max NL Iterations	11	12	
Error Avg. Torque	3.98	2.71	%
MRE_B	7.32	7.27	%
Elements/pole	388(L)+12(NL)	998(L)+48(NL)	

5.4 Comparing Computation with FEA

Similar to section 4.4, a direct computational comparison with a MATLAB-based FEA of the IPM machine is presented in this section. Herein the differences are highlighted, but the reader is referred to Section 4.4 for more complete details. The FEA is evaluated at 8 rotor positions which evenly span two slot pitches. The FEA solution employs the Newton-Raphson method to solve the nonlinear equation system [43]. The mesh refinement procedure was equivalent to that used in Section 4.4. The mesh is shown in Fig. 5.29 with flux lines of the $\theta_{rm} = 0$ solution superimposed. The corresponding global stiffness matrix involves 15,105 unknown potentials.

The computation time breakdown of the MATLAB-based FEA design evaluation is shown in Table 5.6. Note that within the Newton-Raphson solve, the stiffness matrix is updated every iteration; the solve time reported in Table 5.6 represents only the linear equation system solve time within each nonlinear iteration and the matrix assembly time represents initial assembly and all updates that occur to the stiffness matrix within nonlinear iterations, including the enforcement of boundary conditions.

The flux density waveforms in the stator teeth and backiron are shown in Figs. 5.31a and 5.31b. The Torque waveform is shown in Fig. 5.30 (points 1-8 were computed and point 1 is repeated after these points for waveform visual continuity). These waveforms are in strong agreement with those reported in the prior sections by both MoM and the commercial FEA package.

5.5 Discussion

Based on the results comparison of the four hybrid models, there are two models which may be suitable for a PBD application, namely Models C and D. Reasonably low computation time and average torque agreement render the models promising.

Although the computation times reported for all hybrid models are at least an order of magnitude larger than those reported for SPM Design 50 in Chapter 4, it

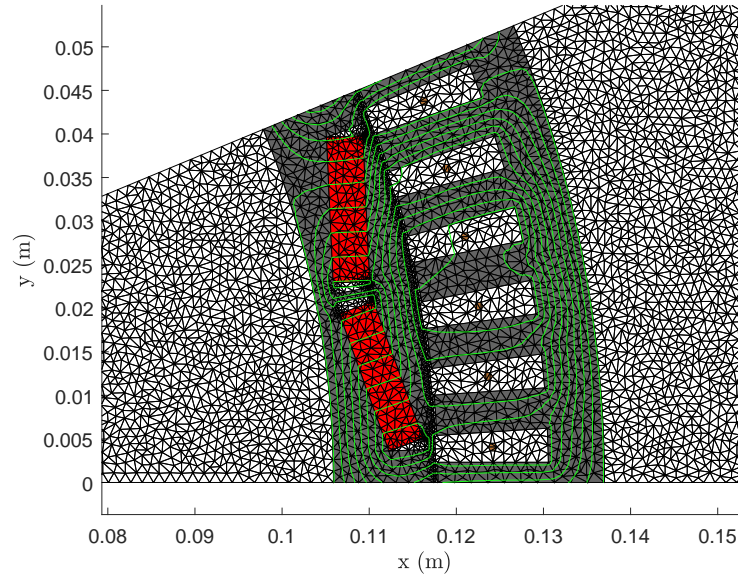


Fig. 5.29.: MATLAB FEA of IPM machine: zoomed in mesh with flux lines.

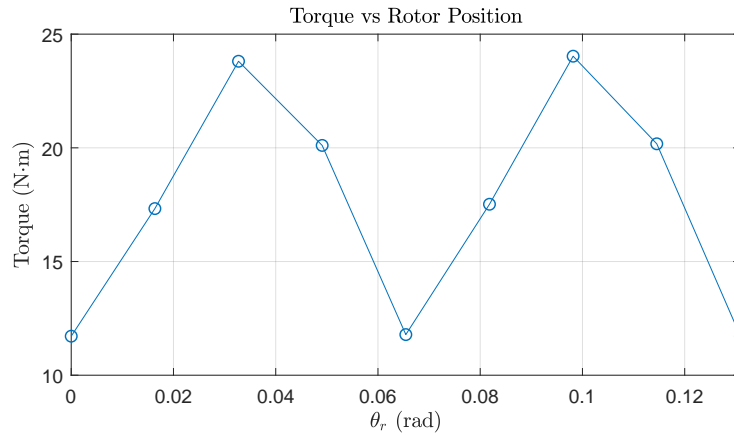


Fig. 5.30.: MATLAB FEA of IPM: Torque waveforms.

is not necessarily fair to directly compare the computational performance of these two machines. Aside from the impacts that volume meshing and nonlinear equation solving have on computational performance, several other factors are at play. Since the pole count is higher in IPM Design 284, more blocks are present in block-row 1 of the DBOR reduction, hence increasing the total element count and computational expense. Further impacting hybrid method computational performance is the fact

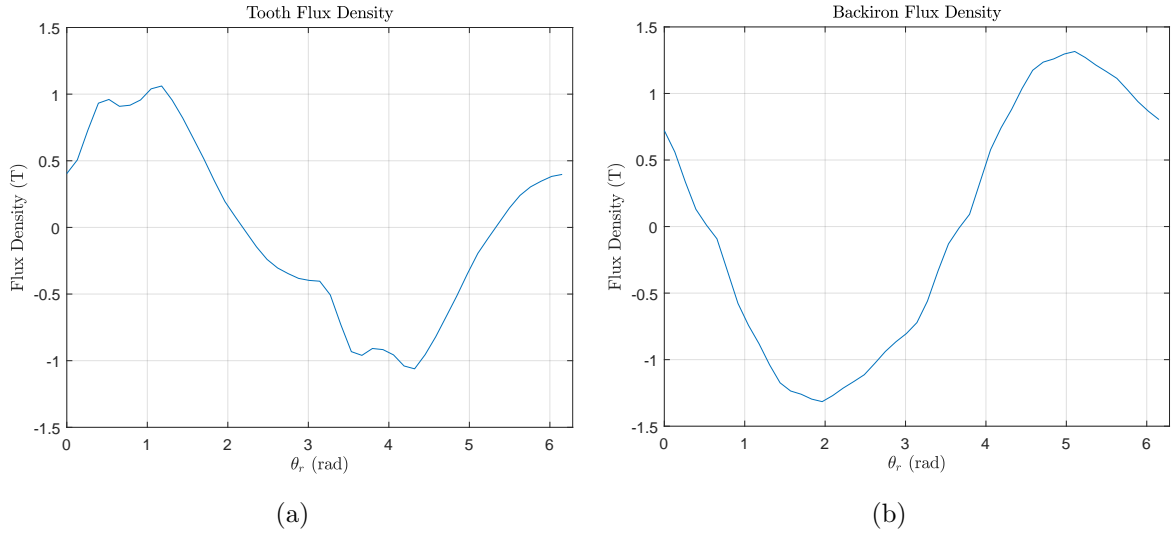


Fig. 5.31.: MATLAB FEA of IPM machine: flux waveform density in teeth (a) and backiron (b).

Table 5.6.: CPU Time Breakdown of MATLAB-based FEA of IPM Machine

Task	CPU Time (%)
Meshing	0.46
Matrix Assembly	95.25
Solve	2.65
Observation	1.024
Torque Calculation	0.62
Total	220.907 s
Max NL Iterations	13

that the IPM has more boundaries requiring a mesh than the SPM which impacts the per-pole element count. Any mesh elements on a redundant boundary may not be eliminated in the nonlinear case, as was done in Chapter 3.

6. SUMMARY AND CONCLUSIONS

This research focused on the use of the MoM in the design and analysis of electric machinery. Several extensions to the MoM formulations described in [4] were derived herein. These include the contribution of closed-form magnetic field integral expressions supplementing those derived in [4], closed-form torque integral expressions, the calculation of distributed winding inductance and a method that exploits the geometric periodicity inherent in electric machines. The formulations and extensions were utilized within the magnetic field analysis of a PBD routine to determine the Pareto-optimal mass/loss front for surface mount PMSMs. The computational performance of the PMSM design study led to the conclusion that the linear Galerkin MoM is a useful magnetic field analysis tool for PBD purposes. Finally, the linear Galerkin and nonlinear point-matching formulations were combined into a hybrid method which was used to model an IPM machine in order to examine the hybrid formulation for use within PBD.

6.1 Suggested Future Work

The suggested future research following this dissertation is centered around the theme of further reduction of the computational expense of each magnetostatic solution to increase the attractiveness of employing the MoM within PBD optimization. This goal may be approached along several fronts. The importance of algebraic simplification to attain compact closed-form integral solutions was stressed in [4] and was carried forward in this research. Aside from simplifying the underlying mathematical expressions, there is almost always room for improvement in the computer code that implements the expressions. The MATLAB code for the MoM toolbox described herein was written with efficiency in mind, taking advantage of vectorization

to the extent possible. However, moving the core matrix population functions to C MATLAB Executable (MEX) functions will retain the unimpeded rapid development granted by interpreted languages such as MATLAB while also benefiting from the reduction of computational effort provided by a compiled language such as C.

An MoM formulation utilizing higher order basis/testing functions in the influence matrices, such as linear or quadratic functions, typically leads to a given accuracy with fewer unknowns than the formulation utilizing pulse/delta bases used herein. The closed-form expressions recently developed in [16] may be useful toward this goal. Utilizing the higher order formulations would also entail the derivation of compatible force, torque and inductance expressions. In this research, the DBOR reduction eliminated the need to compute the entire influence matrix by the exploitation of geometric periodicity and its corresponding equation system structure. Exploring the exploitation of any remaining geometric periodicity, such as among the stator teeth, is of interest to further reduce the number of influence matrix elements explicitly computed during the matrix assembly stage.

A modified Newton-Raphson-based algorithm was developed in this research which solved the hybrid formulation nonlinear equation system in relatively few iterations. More advanced algorithms may lead to a further reduction in the iteration counts required for convergence. Perhaps avoidance of iteration altogether is possible. One such non-iterative nonlinear solution method is the Holomorphic Embedded Load Flow Method (HELM) [52]. It is interesting to consider the use of such a non-iterative method, or the principles on which it is based, outside the context of the load flow problem, and used to solve nonlinear MoM problems.

Finally, it is recognized that many so-called “fast algorithms” have been developed to solve the matrix equations in integral-equation-based numerical methods. Some, such as the Fast Multipole Method (FMM), are based on the principle that the field contributions of a group of far-field sources in close proximity to one another may be lumped together into a single influence matrix element, introducing sparsity into the influence matrix. In fact, it is claimed that the FMM [47] transforms the

storage requirements from $\mathcal{O}(N^2)$ to $\mathcal{O}(N)$. Since the effect of grouping sources is only approximately true, the sparsity comes at the cost of introduced error. Yet the error may be controlled by the degree to which sources are grouped and the distance to the influenced element. Since the components of electric machine geometries are interacting at relatively close distances compared to radiation and scattering problems, it would be interesting to explore the tradeoff between increased sparsity and introduced error. Since it was found in this research that the matrix population time is the largest component of computational effort, it is hoped that employing the FMM will significantly reduce the total computational effort.

REFERENCES

REFERENCES

- [1] R. F. Harrington, *Field Computation by Moment Methods*. Wiley-IEEE Press, 1993.
- [2] J. M. Jin, *Theory and Computation of Electromagnetic Fields*. Wiley-IEEE Press, 2015.
- [3] W. Chew, E. Michielssen, J. M. Song, and J. M. Jin, Eds., *Fast and Efficient Algorithms in Computational Electromagnetics*. Norwood, MA, USA: Artech House, Inc., 2001.
- [4] R. A. Howard, "Derivation, application, and evaluation of the method of moments to solve two-dimensional magnetostatic problems," Ph.D. dissertation, Purdue University, West Lafayette, IN, 2013.
- [5] R. Harrington, "Origin and development of the method of moments for field computation," *IEEE Antennas and Propagation Magazine*, vol. 32, no. 3, pp. 31–35, June 1990.
- [6] A. Ruehli, G. Antonini, and L. Jiang, *Circuit Oriented Electromagnetic Modeling Using the PEEC Techniques*. IEEE, 2017. [Online]. Available: <https://ieeexplore.ieee.org/document/7953970>
- [7] M. Newman, C. Trowbridge, and L. Turner, "Gfun: an interactive program as an aid to magnet design." 1972.
- [8] P. Elleaume, O. Chubar, and J. Chavanne, "Computing 3d magnetic fields from insertion devices," in *Proceedings of the 1997 Particle Accelerator Conference (Cat. No.97CH36167)*, vol. 3, May 1997, pp. 3509–3511 vol.3.
- [9] O. Chubar, P. Elleaume, and J. Chavanne, "A three-dimensional magnetostatics computer code for insertion devices," *Journal of Synchrotron Radiation*, vol. 5, no. 3, pp. 481–484, May 1998. [Online]. Available: <https://doi.org/10.1107/S0909049597013502>
- [10] O. Chadebec, J. . Coulomb, and F. Janet, "A review of magnetostatic moment method," *IEEE Transactions on Magnetics*, vol. 42, no. 4, pp. 515–520, April 2006.
- [11] M. Andriollo, G. Martinelli and A. Morini, and A. Tortella, "Application of the surfacecurrent method to the analysis of saturated electromagnetic devices," *COMPEL - The international journal for computation and mathematics in electrical and electronic engineering*, vol. 23, no. 1, pp. 328–347, 2004.
- [12] O. Kukrer and H. B. Ertan, "An integral equation approach to the computation of nonlinear fields in electrical machines," *IEEE Transactions on Magnetics*, vol. 24, no. 4, pp. 2118–2124, July 1988.

- [13] M. Aliahmadi, H. Tahanian, M. Moallem, and R. Nasiri-Zarandi, "On the use of boundary element method for the study of low frequency electromagnetic devices," in *2018 International Symposium on Power Electronics, Electrical Drives, Automation and Motion (SPEEDAM)*, June 2018, pp. 1113–1118.
- [14] T. C. O'Connell, "An investigation of boundary-based field analysis methods for electric machines: The schwarz-christoffel and boundary element methods," Ph.D. dissertation, University of Illinois, Urbana-Champaign, IL, 2008.
- [15] W. C. Gibson, *The Method of Moments in Electromagnetics*. CRC Press, 2015.
- [16] A. D. Brovont, "A galerkin boundary element method for two-dimensional non-linear magnetostatics," Ph.D. dissertation, Purdue University, West Lafayette, IN, 2016.
- [17] C. W. Trowbridge, "On the shoulders of giants," in *COMPUMAG 2013, 19th International Conference on the Computation of Electromagnetic Fields*, June 2013.
- [18] A. D. Brovont, "Exploring the boundary element method for optimization-based machine design," in *2017 IEEE International Electric Machines and Drives Conference (IEMDC)*, May 2017, pp. 1–7.
- [19] Y. Li, S. Ravi, and D. C. Aliprantis, "Tooth shape optimization of switched reluctance motors for improved torque profiles," in *2015 IEEE International Electric Machines Drives Conference (IEMDC)*, May 2015, pp. 569–575.
- [20] G. Y. Sizov, D. M. Ionel, and N. A. O. Demerdash, "Modeling and parametric design of permanent-magnet ac machines using computationally efficient finite-element analysis," *IEEE Transactions on Industrial Electronics*, vol. 59, no. 6, pp. 2403–2413, June 2012.
- [21] S. J. Salon, *Finite Element Analysis of Electrical Machines*. Springer US, 1995.
- [22] Y. Wang, D. M. Ionel, M. Jiang, and S. J. Stretz, "Establishing the relative merits of synchronous reluctance and pm-assisted technology through systematic design optimization," *IEEE Transactions on Industry Applications*, vol. 52, no. 4, pp. 2971–2978, July 2016.
- [23] D. J. Griffiths, *Introduction to Electrodynamics*, 4th ed. Pearson, 2013.
- [24] A. Zangwill, *Modern Electrodynamics*. Cambridge University Press, 2013.
- [25] R. Howard, A. Brovont, and S. Pekarek, "Analytical evaluation of 2-d flux integral for magnetostatic galerkin method of moments," *IEEE Transactions on Magnetics*, vol. 52, pp. 1–8, April 2016.
- [26] S. D. Sudhoff, "Power magnetic material toolbox," February 2010. [Online]. Available: https://engineering.purdue.edu/ECE/Research/Areas/PEDS/power_magnetic_material_toolbox/
- [27] C. L. Holloway, E. F. Kuester, A. E. Ruehli, and G. Antonini, "Partial and internal inductance: Two of clayton r. pauls many passions," *IEEE Transactions on Electromagnetic Compatibility*, vol. 55, no. 4, pp. 600–613, Aug 2013.

- [28] R. Howard and S. Pekarek, "Two-dimensional galerkin magnetostatic method of moments," *IEEE Transactions on Magnetics*, vol. 53, no. 12, pp. 1–6, Dec 2017.
- [29] A. J. Mardsen, J. E.; Tromba, *Vector Calculus*, 5th ed. W. H. Freeman and Company, 2003.
- [30] T. J. E. Hendershot, J. R.; Miller, *Design of Brushless Permanent-Magnet Machines*. Motor Design Books LLC, 2010.
- [31] "Product: Ac/dc module," <https://www.comsol.com/acdc-module>, accessed: 2019-10-21.
- [32] P. Krause, O. Wasynczuk, S. D. Sudhoff, and S. Pekarek, *Permanent-Magnet ac Machine*. IEEE, 2013, pp. 121–141. [Online]. Available: <https://ieeexplore.ieee.org/document/6739377>
- [33] C. R. Paul, *Loop Inductance vs. Partial Inductance*. IEEE, 2010.
- [34] J. Grainger and W. Stevenson, *Power system analysis*, ser. McGraw-Hill series in electrical and computer engineering: Power and energy. McGraw-Hill, 1994. [Online]. Available: <https://books.google.com/books?id=NBloAQAAMAAJ>
- [35] H. T. Anastassiou, J. L. Volakis, and D. S. Filipovic, "Integral equation modeling of cylindrically periodic scatterers in the interior of a cylindrical waveguide," *IEEE Transactions on Microwave Theory and Techniques*, vol. 46, no. 11, pp. 1713–1720, Nov 1998.
- [36] M. A. Carr, J. L. Volakis, and D. C. Ross, "Acceleration of moment method solutions for discrete bodies of revolution in free space," in *IEEE Antennas and Propagation Society International Symposium. Transmitting Waves of Progress to the Next Millennium. 2000 Digest. Held in conjunction with: USNC/URSI National Radio Science Meeting (C)*, vol. 4, July 2000, pp. 2286–2289 vol.4.
- [37] M. A. Carr, J. L. Volakis, and D. Ross, "Acceleration of free-space discrete body of revolution codes by exploiting circulant submatrices," *IEEE Transactions on Antennas and Propagation*, vol. 50, no. 9, pp. 1319–1322, Sep. 2002.
- [38] K. D. Czuprynski, "Parallel boundary element solutions of block circulant linear systems for acoustic radiation problems with rotationally symmetric boundary surfaces," Master's thesis, Pennsylvania State University, 2012.
- [39] G. Strang, *Computational Science and Engineering*. Wellesley-Cambridge Press, 2007.
- [40] S. D. Sudhoff, *Power Magnetic Devices*. Wiley-IEEE Press, 2014.
- [41] —, "Genetic optimization system engineering tool," January 2014. [Online]. Available: <https://engineering.purdue.edu/ECE/Research/Areas/PEDS/GOSET2p6.zip/>
- [42] *ANSYS Electronics Desktop (v. 19.0)*. ANSYS Inc., Accessed: 14-July-2020. [Online]. Available: <https://www.ansys.com/products/electronics/ansys-electronics-desktop>
- [43] *ECE 62500: Analysis of Electromechanical Systems II*. Purdue University, West Lafayette, IN, Taken: Spring 2016.

- [44] O. Axelsson and V. A. Barker, *Finite Element Solution of Boundary Value Problems*. Society for Industrial and Applied Mathematics, 2001. [Online]. Available: <https://epubs.siam.org/doi/abs/10.1137/1.9780898719253>
- [45] M. R. Hestenes and E. Stiefel, “Methods of conjugate gradients for solving linear systems,” *Journal of research of the National Bureau of Standards*, vol. 49, pp. 409–436, 1952.
- [46] Weng Cho Chew, Jian-Ming Jin, Cai-Cheng Lu, E. Michielssen, and J. M. Song, “Fast solution methods in electromagnetics,” *IEEE Transactions on Antennas and Propagation*, vol. 45, no. 3, pp. 533–543, 1997.
- [47] L. Greengard and V. Rokhlin, “A fast algorithm for particle simulations,” *Journal of Computational Physics*, vol. 135, no. 2, pp. 280–292, 1997.
- [48] J. R. Shewchuk, *Triangle: A Two-Dimensional Quality Mesh Generator and Delaunay Triangulator.*, Accessed: 15-July-2020. [Online]. Available: <https://www.cs.cmu.edu/~quake/triangle.html>
- [49] R. Lin, “A design paradigm for v-shape interior permanent-magnet machines using multi-objective optimization,” Ph.D. dissertation, Purdue University, West Lafayette, IN, 2017.
- [50] W. H. Press, S. A. Teukolsky, W. T. Vetterling, and B. P. Flannery, *Numerical Recipes 3rd Edition: The Art of Scientific Computing*, 3rd ed. USA: Cambridge University Press, 2007.
- [51] “Partial differential equation toolbox,” <https://www.mathworks.com/products/pde.html>, accessed: 2020-02-16.
- [52] A. Trias, “The holomorphic embedding load flow method,” in *2012 IEEE Power and Energy Society General Meeting*, July 2012, pp. 1–8.

APPENDICES

A. ANALYTICAL EVALUATION OF TORQUE INTEGRAL

The force on an observation element was shown in Section 2.4 to be derived from the Lorentz force and is expressed

$$F(\vec{p}) = \vec{I}(\vec{p}) \times \vec{B}(\vec{p}) \quad (\text{A.1})$$

The force is integrated to obtain the total force on element \mathbf{l}_2 :

$$F_{\mathbf{l}_2} = \int_{\mathbf{l}_2} \left(\frac{I_{\mathbf{l}_2}}{l_2} \hat{z} \right) \times \vec{B}_s(\vec{p}) dp \quad (\text{A.2})$$

In Section 2.4, it was shown that in order to compute the torque contribution of one edge element, one may assume that the force is concentrated at the midpoint of the element, and then compute the cross product $\vec{\tau} = \vec{r} \times \vec{F}$, where \vec{r} is the vector from the origin to the observation element midpoint. In the approach detailed herein, the torque at point \vec{p} in element \mathbf{l}_2 is integrated along \mathbf{l}_2 . Hence no assumption is made about the concentration of the force at the element's midpoint. The integral of the torque is expressed as

$$\vec{T}(\vec{p}) = \vec{p} \times \left(\vec{I}(\vec{p}) \times \vec{B}(\vec{p}) \right) \quad (\text{A.3})$$

$$\vec{T}_{\mathbf{l}_2} = \int_{\mathbf{l}_2} \vec{p} \times \left(\frac{I_{\mathbf{l}_2}}{l_2} \hat{z} \right) \times \vec{B}_s(\vec{p}) dp \quad (\text{A.4})$$

where again the magnetic field at point \vec{p} is related through rotation by

$$\vec{B}_s(\vec{p}) = \begin{bmatrix} B_{x,s}(\vec{p}) \\ B_{y,s}(\vec{p}) \end{bmatrix} = \begin{bmatrix} \cos \phi_1 & -\sin \phi_1 \\ \sin \phi_1 & \cos \phi_1 \end{bmatrix} \begin{bmatrix} B'_{x,s}(\vec{r}') \\ B'_{y,s}(\vec{r}') \end{bmatrix} \quad (\text{A.5})$$

The integration is performed using a parameterization of the vector \vec{p} by the variable t , then the integral becomes

$$\vec{T}_{\mathbf{l}_2} = \frac{I_{\mathbf{l}_2}}{l_2} \int_0^1 \vec{p}(t) \times \hat{z} \times \vec{B}_s(\vec{p}(t)) \left\| \frac{d}{dt} \vec{p}(t) \right\| dt \quad (\text{A.6})$$

Cancelling terms and expanding yields

$$\begin{aligned}\vec{T}_{l_2} &= I_{l_2} \int_0^1 \langle p_x(t), p_y(t), 0 \rangle \times \langle 0, 0, 1 \rangle \times \langle B_{x,s}(\vec{p}(t)), B_{y,s}(\vec{p}(t)), 0 \rangle dt \\ &= I_{l_2} \hat{z} \int_0^1 p_x(t) B_{x,s}(\vec{p}(t)) + p_y(t) B_{y,s}(\vec{p}(t)) dt\end{aligned}\quad (\text{A.7})$$

Substituting the components of (A.5) into (A.7),

$$T_{l_2} = I_{l_2} \int_0^1 \left(\begin{aligned} &p_x(t) \left(\cos \phi_1 B'_{x,s}(\vec{r}'(t)) - \sin \phi_1 B'_{y,s}(\vec{r}'(t)) \right) \\ &+ p_y(t) \left(\sin \phi_1 B'_{x,s}(\vec{r}'(t)) + \cos \phi_1 B'_{y,s}(\vec{r}'(t)) \right) \end{aligned} \right) dt \quad (\text{A.8})$$

Substituting expressions for the components of $\vec{p}(t)$ from (3.19), the integral may be expanded as

$$T_{l_2} = I_{l_2} \left(\begin{aligned} &(x_c \cos \phi_1 + y_c \sin \phi_1) \int_0^1 B'_{x,s}(\vec{r}'(t)) dt \\ &+ (-x_c \sin \phi_1 + y_c \cos \phi_1) \int_0^1 B'_{y,s}(\vec{r}'(t)) dt \\ &+ ((x_d - x_c) \cos \phi_1 + (y_d - y_c) \sin \phi_1) \int_0^1 t B'_{x,s}(\vec{r}'(t)) dt \\ &+ (-(x_d - x_c) \sin \phi_1 + (y_d - y_c) \cos \phi_1) \int_0^1 t B'_{y,s}(\vec{r}'(t)) dt \end{aligned} \right) \quad (\text{A.9})$$

The first two integrals in (A.9) are given in Ch. 3 by (3.10) and (3.11) respectively. The remainder of this appendix will be devoted to obtaining closed form expressions for the evaluation of the latter two integrals. The resultant combined analytical expression for T_{l_2} will then be simplified to obtain a final expression amenable to rapid computer evaluation.

A.1 Third Integral Term

Substituting the expression (3.5) for the magnetic field x' component, the 3^{rd} integral in (A.9) may be expressed as

$$\begin{aligned}T_{int3} &= \int_0^1 t B'_{x,s}(\vec{r}'(t)) dt \\ &= -\frac{\mu_0 I_{l_1}}{2\pi l_1} \int_0^1 \left[t \tan^{-1} \left(\frac{l_1 - r'_x(t)}{r'_y(t)} \right) - t \tan^{-1} \left(\frac{-r'_x(t)}{r'_y(t)} \right) \right] dt\end{aligned}\quad (\text{A.10})$$

Substituting (3.3) and (3.4) for r'_x and r'_y , respectively and simplifying, the integral (A.10) can be expressed as

$$T_{int3} = -\frac{\mu_0 I_{l_1}}{2\pi l_1} \left(\int_0^1 t \tan^{-1} \left(\frac{a_1 t + b_1 + l_1}{c_1 t + d_1} \right) dt - \int_0^1 t \tan^{-1} \left(\frac{a_1 t + b_1}{c_1 t + d_1} \right) dt \right) \quad (\text{A.11})$$

where the following substitutions have been made:

$$\begin{aligned} a_1 &= -\cos \phi_1 (x_d - x_c) - \sin \phi_1 (y_d - y_c) \\ b_1 &= -\cos \phi_1 (x_c - x_a) - \sin \phi_1 (y_c - y_a) \\ c_1 &= -\sin \phi_1 (x_d - x_c) + \cos \phi_1 (y_d - y_c) \\ d_1 &= -\sin \phi_1 (x_c - x_a) + \cos \phi_1 (y_c - y_a) \end{aligned} \quad (\text{A.12})$$

A closed form solution to the integrals appearing in (A.11) is [16]

$$\begin{aligned} & \int_0^1 x \tan^{-1} \left(\frac{ax + b}{cx + d} \right) dx \\ &= \frac{1}{2} \left(\begin{aligned} & \tan^{-1} \left(\frac{a+b}{c+d} \right) - \frac{ad-bc}{a^2+c^2} \\ & + \frac{(ab+cd)(ad-bc)}{(a^2+c^2)^2} \ln \left(\frac{(a+b)^2+(c+d)^2}{b^2+d^2} \right) \\ & - \frac{(ab+cd)^2-(ad-bc)^2}{(a^2+c^2)^2} \text{atan2}(ad-bc, ab+cd+b^2+d^2) \end{aligned} \right) \end{aligned} \quad (\text{A.13})$$

By observing Fig.3.1a it is apparent that

$$\begin{aligned} x_d - x_c &= l_2 \cos(\phi_2) \\ y_d - y_c &= l_2 \sin(\phi_2) \end{aligned} \quad (\text{A.14})$$

Hence, with (A.14) and the angle difference formulae:

$$\begin{aligned} \sin(\alpha + \beta) &= \sin(\alpha) \cos(\beta) + \cos(\alpha) \sin(\beta) \\ \cos(\alpha + \beta) &= \cos(\alpha) \cos(\beta) - \sin(\alpha) \sin(\beta) \\ \sin(\alpha - \beta) &= \sin(\alpha) \cos(\beta) - \cos(\alpha) \sin(\beta) \\ \cos(\alpha - \beta) &= \cos(\alpha) \cos(\beta) + \sin(\alpha) \sin(\beta) \end{aligned} \quad (\text{A.15})$$

substitutions (A.12) may be simplified to

$$\begin{aligned}
a_1 &= -l_2 \cos(\phi_2 - \phi_1) \\
b_1 &= -l_3 \cos(\phi_3 - \phi_1) \\
c_1 &= l_2 \sin(\phi_2 - \phi_1) \\
d_1 &= l_3 \sin(\phi_3 - \phi_1)
\end{aligned} \tag{A.16}$$

Utilizing (A.13), (A.11) may be expanded as

$$\begin{aligned}
T_{int3} = & \\
& - \frac{\mu_0 I l_1}{4\pi l_1} \left(\begin{aligned} & \tan^{-1} \left(\frac{a_1 + b_1 + l_1}{c_1 + d_1} \right) - \frac{a_1 d_1 - (b_1 + l_1) c_1}{a_1^2 + c_1^2} \\ & + \frac{(a_1(b_1 + l_1) + c_1 d_1)(a_1 d_1 - (b_1 + l_1) c_1)}{(a_1^2 + c_1^2)^2} \ln \left(\frac{(a_1 + (b_1 + l_1))^2 + (c_1 + d_1)^2}{(b_1 + l_1)^2 + d_1^2} \right) \\ & - \frac{(a_1(b_1 + l_1) + c_1 d_1)^2 - (a_1 d_1 - (b_1 + l_1) c_1)^2}{(a_1^2 + c_1^2)^2} \end{aligned} \right) \\
& + \frac{\mu_0 I l_1}{4\pi l_1} \left(\begin{aligned} & \tan^{-1} \left(\frac{a_1 + b_1}{c_1 + d_1} \right) - \frac{a_1 d_1 - b_1 c_1}{a_1^2 + c_1^2} \\ & + \frac{(a_1 b_1 + c_1 d_1)(a_1 d_1 - b_1 c_1)}{(a_1^2 + c_1^2)^2} \ln \left(\frac{(a_1 + b_1)^2 + (c_1 + d_1)^2}{b_1^2 + d_1^2} \right) \\ & - \frac{(a_1 b_1 + c_1 d_1)^2 - (a_1 d_1 - b_1 c_1)^2}{(a_1^2 + c_1^2)^2} \end{aligned} \right) \\
& \cdot \text{atan2}(a_1 d_1 - (b_1 + l_1) c_1, a_1(b_1 + l_1) + c_1 d_1 + (b_1 + l_1)^2 + d_1^2) \\
& \cdot \text{atan2}(a_1 d_1 - b_1 c_1, a_1 b_1 + c_1 d_1 + b_1^2 + d_1^2)
\end{aligned} \tag{A.17}$$

The expressions appearing inside (A.17) are simplified in the following development, making use of the law of cosines, the angle difference formulae (A.15) and the following identities derived in [4]:

$$l_\alpha \cos(\phi_\alpha - \phi_\zeta) + l_\beta \cos(\phi_\beta - \phi_\zeta) + l_\gamma \cos(\phi_\gamma - \phi_\zeta) = 0 \tag{A.18}$$

$$l_\alpha \sin(\phi_\alpha - \phi_\zeta) + l_\beta \sin(\phi_\beta - \phi_\zeta) + l_\gamma \sin(\phi_\gamma - \phi_\zeta) = 0 \tag{A.19}$$

where the selection of vectors \mathbf{l}_α , \mathbf{l}_β and \mathbf{l}_γ is restricted such that their sum is zero, i.e.

$$\mathbf{l}_\alpha + \mathbf{l}_\beta + \mathbf{l}_\gamma = 0, \tag{A.20}$$

and no restriction is placed on the common vector \mathbf{l}_ζ and its angle ϕ_ζ with the x -axis.

Substituting expressions in (A.16), utilizing the angle difference formulae (A.15) and the vector identities (A.18), the expressions appearing in (A.17) may be simplified as follows, in the order in which they appear:

$$\begin{aligned}
\frac{a_1 + b_1 + l_1}{c_1 + d_1} &= \frac{-l_2 \cos(\phi_2 - \phi_1) - l_3 \cos(\phi_3 - \phi_1) + l_1}{l_2 \sin(\phi_2 - \phi_1) + l_3 \sin(\phi_3 - \phi_1)} \\
&= \frac{-l_5 \cos(\phi_5 - \phi_1) + l_1 \cos(\phi_1 - \phi_1)}{l_2 \sin(\phi_2 - \phi_1) + l_3 \sin(\phi_3 - \phi_1)} \\
&= \frac{-l_6 \cos(\phi_6 - \phi_1)}{l_5 \sin(\phi_5 - \phi_1) - l_1 \sin(\phi_1 - \phi_1)} \\
&= -\frac{l_6 \cos(\phi_6 - \phi_1)}{l_6 \sin(\phi_6 - \phi_1)} \\
&= -\frac{\cos(\phi_6 - \phi_1)}{\sin(\phi_6 - \phi_1)}
\end{aligned} \tag{A.21}$$

$$\begin{aligned}
-\frac{a_1 d_1 - (b_1 + l_1) c_1}{a_1^2 + c_1^2} &= -\frac{\begin{pmatrix} -l_2 l_3 \cos(\phi_2 - \phi_1) \sin(\phi_3 - \phi_1) \\ -(-l_3 \cos(\phi_3 - \phi_1) + l_1) l_2 \sin(\phi_2 - \phi_1) \end{pmatrix}}{l_2^2 (\cos^2(\phi_2 - \phi_1) + \sin^2(\phi_2 - \phi_1))} \\
&= -\frac{\begin{pmatrix} -l_2 l_3 \cos(\phi_2 - \phi_1) \sin(\phi_3 - \phi_1) \\ +l_2 l_3 \sin(\phi_2 - \phi_1) \cos(\phi_3 - \phi_1) \\ -l_1 l_2 \sin(\phi_2 - \phi_1) \end{pmatrix}}{l_2^2} \\
&= \frac{l_3 \sin(\phi_3 - \phi_2) - l_1 \sin(\phi_1 - \phi_2)}{l_2} \\
&= \frac{l_4}{l_2} \sin(\phi_4 - \phi_2)
\end{aligned} \tag{A.22}$$

$$\begin{aligned}
& \frac{(a_1(b_1 + l_1) + c_1 d_1)(a_1 d_1 - (b_1 + l_1)c_1)}{(a_1^2 + c_1^2)^2} \\
&= \frac{(a_1 b_1 + a_1 l_1 + c_1 d_1)(a_1 d_1 - b_1 c_1 - l_1 c_1)}{(a_1^2 + c_1^2)^2} \\
&= \frac{\begin{pmatrix} -l_1 l_2 \cos(\phi_2 - \phi_1) \\ +l_2 l_3 \cos(\phi_2 - \phi_1) \cos(\phi_3 - \phi_1) \\ +l_2 l_3 \sin(\phi_2 - \phi_1) \sin(\phi_3 - \phi_1) \end{pmatrix} \begin{pmatrix} -l_1 l_2 \sin(\phi_2 - \phi_1) \\ -l_2 l_3 \cos(\phi_2 - \phi_1) \sin(\phi_3 - \phi_1) \\ +l_2 l_3 \cos(\phi_3 - \phi_1) \sin(\phi_2 - \phi_1) \end{pmatrix}}{(l_2^2 \cos^2(\phi_2 - \phi_1) + l_2^2 \sin^2(\phi_2 - \phi_1))^2} \quad (\text{A.23}) \\
&= \frac{\begin{pmatrix} -l_1 \cos(\phi_1 - \phi_2) \\ +l_3 \cos(\phi_3 - \phi_2) \end{pmatrix} \begin{pmatrix} l_1 \sin(\phi_1 - \phi_2) \\ -l_3 \sin(\phi_3 - \phi_2) \end{pmatrix}}{l_2^2} \\
&= -\frac{l_4^2}{l_2^2} \cos(\phi_4 - \phi_2) \sin(\phi_4 - \phi_2)
\end{aligned}$$

$$\begin{aligned}
& \frac{(a_1 + b_1 + l_1)^2 + (c_1 + d_1)^2}{(b_1 + l_1)^2 + d_1^2} \\
& \frac{\left(\begin{array}{c} a_1^2 + b_1^2 + c_1^2 + d_1^2 + l_1^2 \\ +2a_1b_1 + 2b_1l_1 + 2a_1l_1 + 2c_1d_1 \end{array} \right)}{b_1^2 + d_1^2 + l_1^2 + 2b_1l_1} \\
& = \frac{\left(\begin{array}{c} l_2^2 \cos^2(\phi_2 - \phi_1) + l_2^2 \sin^2(\phi_2 - \phi_1) + l_3^2 \cos^2(\phi_3 - \phi_1) \\ + l_3^2 \sin^2(\phi_3 - \phi_1) + l_1^2 + 2l_2l_3 \cos(\phi_2 - \phi_1) \cos(\phi_3 - \phi_1) \\ - 2l_1l_3 \cos(\phi_3 - \phi_1) - 2l_1l_2 \cos(\phi_2 - \phi_1) + 2l_2l_3 \sin(\phi_2 - \phi_1) \sin(\phi_3 - \phi_1) \end{array} \right)}{l_3^2 \cos^2(\phi_3 - \phi_1) + l_3^2 \sin^2(\phi_3 - \phi_1) + l_1^2 - 2l_1l_3 \cos(\phi_3 - \phi_1)} \\
& = \frac{\left(\begin{array}{c} l_1^2 + l_2^2 + l_3^2 + 2l_2l_3 \cos(\phi_2 - \phi_3) \\ - 2l_1l_3 \cos(\phi_3 - \phi_1) - 2l_1l_2 \cos(\phi_2 - \phi_1) \end{array} \right)}{l_1^2 + l_3^2 - 2l_1l_3 \cos(\phi_3 - \phi_1)} \\
& = \frac{\left(\begin{array}{c} l_1^2 + l_2^2 + l_3^2 + 2l_2l_4 \cos(\phi_4 - \phi_2) \\ - 2l_1l_3 \cos(\phi_3 - \phi_1) \end{array} \right)}{l_4^2} \\
& = \frac{l_4^2 + l_2^2 + 2l_2l_4 \cos(\phi_4 - \phi_2)}{l_4^2} \\
& = \frac{l_4^2 + l_2^2 - 2l_2l_4 \cos(\pi - (\phi_4 - \phi_2))}{l_4^2} \\
& = \frac{l_6^2}{l_4^2}
\end{aligned}$$

(A.24)

$$\begin{aligned}
& - \frac{(a_1(b_1 + l_1) + c_1 d_1)^2 - (a_1 d_1 - (b_1 + l_1) c_1)^2}{(a_1^2 + c_1^2)^2} \\
& = - \frac{\begin{pmatrix} -l_1 l_2 \cos(\phi_2 - \phi_1) \\ l_2 l_3 \cos(\phi_2 - \phi_1) \cos(\phi_3 - \phi_1) \\ + l_2 l_3 \sin(\phi_2 - \phi_1) \sin(\phi_3 - \phi_1) \end{pmatrix}^2 - \begin{pmatrix} -l_1 l_2 \sin(\phi_2 - \phi_1) \\ -l_2 l_3 \cos(\phi_2 - \phi_1) \sin(\phi_3 - \phi_1) \\ + l_3 l_2 \cos(\phi_3 - \phi_1) \sin(\phi_2 - \phi_1) \end{pmatrix}^2}{(l_2^2 \cos^2(\phi_2 - \phi_1) + l_2^2 \sin^2(\phi_2 - \phi_1))^2} \\
& = - \frac{l_2^2 \begin{pmatrix} -l_1 \cos(\phi_2 - \phi_1) \\ + l_3 \cos(\phi_2 - \phi_3) \end{pmatrix}^2 - l_2^2 \begin{pmatrix} -l_1 \sin(\phi_2 - \phi_1) \\ + l_3 \sin(\phi_2 - \phi_3) \end{pmatrix}^2}{(l_2^2)^2} \\
& = - \frac{(l_4 \cos(\phi_4 - \phi_2))^2 - (-l_4 \sin(\phi_4 - \phi_2))^2}{l_2^2} \\
& = - \frac{l_4^2}{l_2^2} \cos(2(\phi_4 - \phi_2))
\end{aligned} \tag{A.25}$$

$$\begin{aligned}
a_1 d_1 - (b_1 + l_1) c_1 &= \begin{pmatrix} -l_1 l_2 \sin(\phi_2 - \phi_1) \\ -l_2 l_3 \cos(\phi_2 - \phi_1) \sin(\phi_3 - \phi_1) \\ + l_3 l_2 \cos(\phi_3 - \phi_1) \sin(\phi_2 - \phi_1) \end{pmatrix} \\
&= l_2 (l_1 \sin(\phi_1 - \phi_2) - l_3 \sin(\phi_3 - \phi_2)) \\
&= -l_2 l_4 \sin(\phi_4 - \phi_2)
\end{aligned} \tag{A.26}$$

$$\begin{aligned}
& a_1(b_1 + l_1) + c_1 d_1 + (b_1 + l_1)^2 + d_1^2 \\
&= a_1 b_1 + a_1 l_1 + c_1 d_1 + b_1^2 + l_1^2 + 2b_1 l_1 + d_1^2 \\
&= \begin{pmatrix} l_2 l_3 \cos(\phi_2 - \phi_1) \cos(\phi_3 - \phi_1) - l_1 l_2 \cos(\phi_2 - \phi_1) \\ + l_2 l_3 \sin(\phi_2 - \phi_1) \sin(\phi_3 - \phi_1) + l_3^2 \cos^2(\phi_3 - \phi_1) \\ + l_1^2 - 2l_3 l_1 \cos(\phi_3 - \phi_1) + l_3^2 \sin^2(\phi_3 - \phi_1) \end{pmatrix} \\
&= \begin{pmatrix} l_2(l_3 \cos(\phi_2 - \phi_3) - l_1 \cos(\phi_2 - \phi_1)) \\ + l_3^2 + l_1^2 - 2l_3 l_1 \cos(\phi_3 - \phi_1) \end{pmatrix} \\
&= l_2 l_4 \cos(\phi_4 - \phi_2) + l_4^2 \\
&= l_4(l_2 \cos(\phi_4 - \phi_2) + l_4 \cos(\phi_4 - \phi_4)) \\
&= l_4 l_6 \cos(\phi_6 - \phi_4)
\end{aligned} \tag{A.27}$$

$$\begin{aligned}
\frac{a_1 + b_1}{c_1 + d_1} &= \frac{-l_2 \cos(\phi_2 - \phi_1) - l_3 \cos(\phi_3 - \phi_1)}{l_2 \sin(\phi_2 - \phi_1) + l_3 \sin(\phi_3 - \phi_1)} \\
&= \frac{-l_5 \cos(\phi_5 - \phi_1)}{l_5 \sin(\phi_5 - \phi_1)} \\
&= -\frac{\cos(\phi_5 - \phi_1)}{\sin(\phi_5 - \phi_1)}
\end{aligned} \tag{A.28}$$

$$\begin{aligned}
-\frac{a_1 d_1 - b_1 c_1}{a_1^2 + c_1^2} &= -\frac{-l_2 l_3 \cos(\phi_2 - \phi_1) \sin(\phi_3 - \phi_1) + l_2 l_3 \cos(\phi_3 - \phi_1) \sin(\phi_2 - \phi_1)}{l_2^2 \cos^2(\phi_2 - \phi_1) + l_2^2 \sin^2(\phi_2 - \phi_1)} \\
&= -\frac{l_2 l_3 \sin(\phi_2 - \phi_3)}{l_2^2} \\
&= -\frac{l_3}{l_2} \sin(\phi_2 - \phi_3)
\end{aligned} \tag{A.29}$$

$$\begin{aligned}
& \frac{(a_1 b_1 + c_1 d_1)(a_1 d_1 - b_1 c_1)}{(a_1^2 + c_1^2)^2} \\
&= \frac{\begin{pmatrix} l_2 l_3 \cos(\phi_2 - \phi_1) \cos(\phi_3 - \phi_1) \\ + l_2 l_3 \sin(\phi_2 - \phi_1) \sin(\phi_3 - \phi_1) \end{pmatrix} \begin{pmatrix} -l_2 l_3 \cos(\phi_2 - \phi_1) \sin(\phi_3 - \phi_1) \\ + l_2 l_3 \cos(\phi_2 - \phi_1) \sin(\phi_3 - \phi_1) \end{pmatrix}}{(l_2^2 \cos^2(\phi_2 - \phi_1) + l_2^2 \sin^2(\phi_2 - \phi_1))^2} \\
&= \frac{l_3^2}{l_2^2} \cos(\phi_2 - \phi_3) \sin(\phi_2 - \phi_3)
\end{aligned} \tag{A.30}$$

$$\begin{aligned}
& \frac{(a_1 + b_1)^2 + (c_1 + d_1)^2}{b_1^2 + d_1^2} \\
&= \frac{a_1^2 + b_1^2 + c_1^2 + d_1^2 + 2a_1b_1 + 2c_1d_1}{b_1^2 + d_1^2} \\
&= \frac{\left(l_2^2 \cos^2(\phi_2 - \phi_1) + l_3^2 \cos^2(\phi_3 - \phi_1) + l_2^2 \sin^2(\phi_2 - \phi_1) + l_3^2 \sin^2(\phi_3 - \phi_1) \right. \\
&\quad \left. + 2l_2l_3 \cos(\phi_2 - \phi_1) \cos(\phi_3 - \phi_1) + 2l_2l_3 \sin(\phi_2 - \phi_1) \sin(\phi_3 - \phi_1) \right)}{l_3^2 \cos^2(\phi_3 - \phi_1) + l_3^2 \sin^2(\phi_3 - \phi_1)} \\
&= \frac{l_2^2 + l_3^2 + 2l_2l_3 \cos(\phi_2 - \phi_3)}{l_3^2} \\
&= \frac{l_2^2 + l_3^2 - 2l_2l_3 \cos(\pi - (\phi_2 - \phi_3))}{l_3^2} \\
&= \frac{l_5^2}{l_3^2}
\end{aligned} \tag{A.31}$$

$$\begin{aligned}
& - \frac{(a_1b_1 + c_1d_1)^2 - (a_1d_1 - b_1c_1)^2}{a_1^2 + c_1^2} \\
&= - \frac{\left(l_2l_3 \cos(\phi_2 - \phi_1) \cos(\phi_3 - \phi_1) \right)^2 - \left(-l_2l_3 \cos(\phi_2 - \phi_1) \sin(\phi_3 - \phi_1) \right)^2}{(l_2^2 \cos^2(\phi_2 - \phi_1) + l_2^2 \sin^2(\phi_2 - \phi_1))^2} \\
&= - \frac{l_2^2 l_3^2 (\cos^2(\phi_2 - \phi_3) - \sin^2(\phi_2 - \phi_3))}{(l_2^2)^2} \\
&= - \frac{l_3^2}{l_2^2} \cos(2(\phi_2 - \phi_3))
\end{aligned} \tag{A.32}$$

$$\begin{aligned}
a_1d_1 - b_1c_1 &= -l_2l_3 \cos(\phi_2 - \phi_1) \sin(\phi_3 - \phi_1) + l_2l_3 \cos(\phi_3 - \phi_1) \sin(\phi_2 - \phi_1) \\
&= l_2l_3 \sin(\phi_2 - \phi_3)
\end{aligned} \tag{A.33}$$

$$\begin{aligned}
a_1 b_1 + c_1 d_1 + b_1^2 + d_1^2 &= \begin{pmatrix} l_2 l_3 \cos(\phi_2 - \phi_1) \cos(\phi_3 - \phi_1) \\ + l_2 l_3 \sin(\phi_2 - \phi_1) \sin(\phi_3 - \phi_1) \\ + l_3^2 \cos^2(\phi_3 - \phi_1) + l_3^2 \sin^2(\phi_3 - \phi_1) \end{pmatrix} \\
&= l_2 l_3 \cos(\phi_2 - \phi_3) + l_3^2 \\
&= l_3 (l_2 \cos(\phi_2 - \phi_3) + l_3 \cos(\phi_3 - \phi_3)) \\
&= l_3 l_5 \cos(\phi_5 - \phi_3)
\end{aligned} \tag{A.34}$$

Substituting (A.21)-(A.34) into (A.17),

$$\begin{aligned}
T_{int3} &= \\
\frac{\mu_0 I_{l_1}}{4\pi l_1} &\left(\begin{aligned} & -\text{atan} \left(-\frac{\cos(\phi_6 - \phi_1)}{\sin(\phi_6 - \phi_1)} \right) - \frac{l_4}{l_2} \sin(\phi_4 - \phi_2) \\ & + \frac{l_4^2}{l_2^2} \cos(\phi_4 - \phi_2) \sin(\phi_4 - \phi_2) \ln \left(\frac{l_6^2}{l_4^2} \right) \\ & + \frac{l_4^2}{l_2^2} \cos(2(\phi_4 - \phi_2)) \text{atan2}(-l_2 l_4 \sin(\phi_4 - \phi_2), l_4 l_6 \cos(\phi_6 - \phi_4)) \\ & \text{atan} \left(-\frac{\cos(\phi_5 - \phi_1)}{\sin(\phi_5 - \phi_1)} \right) + \frac{l_3}{l_2} \sin(\phi_3 - \phi_2) \\ & - \frac{l_3^2}{l_2^2} \cos(\phi_3 - \phi_2) \sin(\phi_3 - \phi_2) \ln \left(\frac{l_5^2}{l_3^2} \right) \\ & - \frac{l_3^2}{l_2^2} \cos(2(\phi_2 - \phi_3)) \text{atan2}(l_2 l_3 \sin(\phi_2 - \phi_3), l_3 l_5 \cos(\phi_5 - \phi_3)) \end{aligned} \right)
\end{aligned} \tag{A.35}$$

The 1st argument in each respective atan2 function in (A.35) may be manipulated using (A.18) as

$$\begin{aligned}
-l_2 l_4 \sin(\phi_4 - \phi_2) &= l_2 l_4 \sin(\phi_2 - \phi_4) \\
&= l_4 (l_2 \sin(\phi_2 - \phi_4) + l_4 \underbrace{\sin(\phi_4 - \phi_4)}_0) \\
&= l_4 l_6 \sin(\phi_6 - \phi_4)
\end{aligned} \tag{A.36}$$

$$\begin{aligned}
l_2 l_3 \sin(\phi_2 - \phi_3) &= l_3 (l_2 \sin(\phi_2 - \phi_3) + \underbrace{l_3 \sin(\phi_3 - \phi_3)}_0) \\
&= l_3 l_5 \sin(\phi_5 - \phi_3)
\end{aligned} \tag{A.37}$$

A difference of 2-quadrant arctangent functions may be converted to the 4-quadrant arctangent function [4]. Specifically, since

$$\begin{aligned}
\text{atan}\left(\frac{\cos(\phi_\alpha - \phi_\zeta)}{\sin(\phi_\alpha - \phi_\zeta)}\right) &= \text{atan}(\cot(\phi_\alpha - \phi_\zeta)) \\
&= \text{atan}(\tan(\frac{\pi}{2} - (\phi_\alpha - \phi_\zeta))) \\
&= \frac{\pi}{2} - (\phi_\alpha - \phi_\zeta)
\end{aligned} \tag{A.38}$$

then,

$$\begin{aligned}
&\text{atan}\left(\frac{\cos(\phi_\alpha - \phi_\zeta)}{\sin(\phi_\alpha - \phi_\zeta)}\right) - \text{atan}\left(\frac{\cos(\phi_\beta - \phi_\zeta)}{\sin(\phi_\beta - \phi_\zeta)}\right) \\
&= \frac{\pi}{2} - (\phi_\alpha - \phi_\zeta) - \frac{\pi}{2} + (\phi_\beta - \phi_\zeta) \\
&= \phi_\beta - \phi_\alpha.
\end{aligned} \tag{A.39}$$

The resultant angle $\phi_\beta - \phi_\alpha$ was found to range from $-\pi$ to π [4] which matches the use case of the 4-quadrant arctangent function atan2 , hence

$$\begin{aligned}
\phi_\beta - \phi_\alpha &= \text{atan2}(\sin(\phi_\beta - \phi_\alpha), \cos(\phi_\beta - \phi_\alpha)) \\
&= \text{atan2}(\mathbf{l}_\alpha \times_2 \mathbf{l}_\beta, \mathbf{l}_\alpha \cdot \mathbf{l}_\beta)
\end{aligned} \tag{A.40}$$

where it is readily shown that

$$\mathbf{l}_\alpha \times_2 \mathbf{l}_\beta = \sin(\phi_\beta - \phi_\alpha) \tag{A.41}$$

$$\mathbf{l}_\alpha \cdot \mathbf{l}_\beta = \cos(\phi_\beta - \phi_\alpha). \tag{A.42}$$

Utilizing (A.36)-(A.41), invoking the exponent property of logarithms, reordering terms for favorable sign flips and factoring l_2^2 from the denominator, T_{int3} may now be written as

$$T_{int3} = \quad (A.43)$$

$$- \frac{\mu_0 I_{l_1}}{4\pi l_1 l_2^2} \begin{pmatrix} l_2^2 \text{atan2}(\mathbf{l}_5 \times_2 \mathbf{l}_6, \mathbf{l}_5 \cdot \mathbf{l}_6) \\ -l_4^2 \cos(2(\phi_4 - \phi_2)) \text{atan2}(\mathbf{l}_4 \times_2 \mathbf{l}_6, \mathbf{l}_4 \cdot \mathbf{l}_6) \\ -l_3^2 \cos(2(\phi_2 - \phi_3)) \text{atan2}(\mathbf{l}_5 \times_2 \mathbf{l}_3, \mathbf{l}_5 \cdot \mathbf{l}_3) \\ -2l_4^2 \cos(\phi_4 - \phi_2) \sin(\phi_4 - \phi_2) \ln\left(\frac{l_6}{l_4}\right) \\ +2l_3^2 \cos(\phi_3 - \phi_2) \sin(\phi_3 - \phi_2) \ln\left(\frac{l_3}{l_5}\right) \\ -l_3 l_2 \sin(\phi_3 - \phi_2) + l_4 l_2 \sin(\phi_4 - \phi_2) \end{pmatrix} \quad (A.44)$$

A.2 Fourth Integral Term

Substituting the expression (3.6) for the magnetic field y' component, the 4th integral term in (A.9) may be expressed as

$$\begin{aligned} T_{int4} &= \int_0^1 t B'_{y,s}(\mathbf{r}'(t)) dt \\ &= -\frac{\mu_0 I_{l_1}}{4\pi l_1} \int_0^1 t \ln \left(\frac{(l_1 - r'_x)^2 - r_y'^2}{r_x'^2 + r_y'^2} \right) dt \\ &= -\frac{\mu_0 I_{l_1}}{4\pi l_1} \int_0^1 \left(t \ln \left((l_1 - r'_x)^2 - r_y'^2 \right) - t \ln \left(r_x'^2 + r_y'^2 \right) \right) dt \end{aligned} \quad (A.45)$$

Substituting (3.3)-(3.4) for r'_x and r'_y , respectively and simplifying, the integral (A.45) can be expressed as

$$T_{int4} = -\frac{\mu_0 I_{l_1}}{4\pi l_1} \left(\int_0^1 t \ln(a_2 t^2 + b_2 t + c_2) dt - \int_0^1 t \ln(a_3 t^2 + b_3 t + c_3) dt \right) \quad (A.46)$$

where, utilizing (A.16), the following additional substitutions have been made:

$$\begin{aligned}
a_2 &= a_1^2 + c_1^2 \\
&= l_2^2 \\
b_2 &= 2a_1(b_1 + l_1) + 2c_1d_1 \\
&= 2l_2l_4 \cos(\phi_4 - \phi_2) \\
c_2 &= d_1^2 + (b_1 + l_1)^2 \\
&= l_4^2 \\
a_3 &= a_2 \\
&= l_2^2 \\
b_3 &= 2a_1b_1 + 2c_1d_1 \\
&= 2l_2l_3 \cos(\phi_3 - \phi_2) \\
c_3 &= b_1^2 + d_1^2 \\
&= l_3^2
\end{aligned} \tag{A.47}$$

A closed form solution to the integrals appearing in (A.46) is [16]

$$\begin{aligned}
&\int_0^1 x \ln(ax^2 + bx + c) dx \\
&= \left(\begin{aligned} &\frac{2a^2 - b^2 + 2ac}{4a^2} \ln(a + b + c) + \frac{b^2 - 2ac}{4a^2} \ln(c) \\ &- \frac{b\sqrt{4ac - b^2}}{2a^2} \operatorname{atan2}\left(\sqrt{4ac - b^2}, 2c + b\right) + \frac{b}{2a} - \frac{1}{2} \end{aligned} \right)
\end{aligned} \tag{A.48}$$

Utilizing (A.48), (A.46) may be expanded as

$$\begin{aligned}
T_{int4} &= -\frac{\mu_0 I_{l_1}}{4\pi l_1} \left(\begin{aligned} &\frac{2a_2^2 - b_2^2 + 2a_2c_2}{4a_2^2} \ln(a_2 + b_2 + c_2) + \frac{b_2^2 - 2a_2c_2}{4a_2^2} \ln(c_2) \\ &- \frac{b_2\sqrt{4a_2c_2 - b_2^2}}{2a_2^2} \operatorname{atan2}\left(\sqrt{4a_2c_2 - b_2^2}, 2c_2 + b_2\right) + \frac{b_2}{2a_2} - \frac{1}{2} \end{aligned} \right) \\
&+ \frac{\mu_0 I_{l_1}}{4\pi l_1} \left(\begin{aligned} &\frac{2a_3^2 - b_3^2 + 2a_3c_3}{4a_3^2} \ln(a_3 + b_3 + c_3) + \frac{b_3^2 - 2a_3c_3}{4a_3^2} \ln(c_3) \\ &- \frac{b_3\sqrt{4a_3c_3 - b_3^2}}{2a_3^2} \operatorname{atan2}\left(\sqrt{4a_3c_3 - b_3^2}, 2c_3 + b_3\right) + \frac{b_3}{2a_3} - \frac{1}{2} \end{aligned} \right)
\end{aligned} \tag{A.49}$$

The expressions appearing inside (A.49) are simplified in the remainder of this section, making use of the law of cosines, the angle difference formulae (A.15), and the identities (A.18) and substitutions (A.16). In the order in which they appear:

$$\begin{aligned}
& \frac{2a_2^2 - b_2^2 + 2a_2c_2}{4a_2^2} \\
&= \frac{2l_2^4 - 4l_2^2l_4^2 \cos^2(\phi_4 - \phi_2) + 2l_2^2l_4^2}{4l_2^4} \\
&= \frac{l_2^2 - l_4^2 \cos(2(\phi_4 - \phi_2))}{2l_2^2}
\end{aligned} \tag{A.50}$$

$$\begin{aligned}
a_2 + b_2 + c_2 &= l_2^2 + 2l_2l_4 \cos(\phi_4 - \phi_2) + l_4^2 \\
&= l_2^2 + l_4^2 - 2l_2l_4 \cos(\pi - (\phi_4 - \phi_2)) \\
&= l_6^2
\end{aligned} \tag{A.51}$$

$$\begin{aligned}
\frac{b_2^2 - 2a_2c_2}{4a_2^2} &= \frac{4l_2^2l_4^2 \cos^2(\phi_4 - \phi_2) - 2l_2^2l_4^2}{4l_2^4} \\
&= \frac{l_4^2(-1 + 2 \cos^2(\phi_4 - \phi_2))}{2l_2^2} \\
&= \frac{l_4^2}{2l_2^2} \cos(2(\phi_4 - \phi_2))
\end{aligned} \tag{A.52}$$

$$\begin{aligned}
& - \frac{b_2 \sqrt{4a_2c_2 - b_2^2}}{2a_2^2} \\
&= - \frac{2l_2l_4 \cos(\phi_4 - \phi_2) \sqrt{4l_2^2l_4^2 - 4l_2^2l_4^2 \cos^2(\phi_4 - \phi_2)}}{2l_2^4} \\
&= - \frac{2l_2l_4 \cos(\phi_4 - \phi_2) \sqrt{4l_2^2l_4^2 \sin^2(\phi_4 - \phi_2)}}{2l_2^4} \\
&= - \frac{4l_2^2l_4^2 \cos(\phi_4 - \phi_2) \sin(\phi_4 - \phi_2)}{2l_2^4} \\
&= - \frac{l_4^2}{l_2^2} \sin(2(\phi_4 - \phi_2))
\end{aligned} \tag{A.53}$$

$$\begin{aligned}
\sqrt{4a_2c_2 - b_2^2} &= \sqrt{4l_2^2l_4^2 - 4l_2^2l_4^2 \cos^2(\phi_4 - \phi_2)} \\
&= 2l_2l_4 \sin(\phi_4 - \phi_2)
\end{aligned} \tag{A.54}$$

$$\begin{aligned}
2c_2 + b_2 &= 2l_4^2 + 2l_2l_4 \cos(\phi_4 - \phi_2) \\
&= 2l_4(l_4 \cos(\phi_4 - \phi_4) + l_4 \cos(\phi_4 - \phi_2)) \\
&= 2l_4l_6 \cos(\phi_6 - \phi_4)
\end{aligned} \tag{A.55}$$

$$\begin{aligned}
\frac{b_2}{2a_2} - \frac{1}{2} &= \frac{2l_2l_4 \cos(\phi_4 - \phi_2)}{2l_2^2} - \frac{1}{2} \\
&= \frac{l_4}{l_2} \cos(\phi_4 - \phi_2) - \frac{1}{2}
\end{aligned} \tag{A.56}$$

$$\begin{aligned}
&\frac{2a_3^2 - b_3^2 + 2a_3c_3}{4a_3^2} \\
&= \frac{2l_2^4 - 4l_2^2l_3^2 \cos^2(\phi_3 - \phi_2) + 2l_2^2l_3^2}{4l_2^4} \\
&= \frac{l_2^2 + l_3^2(1 - 2\cos^2(\phi_3 - \phi_2))}{2l_2^2} \\
&= \frac{l_2^2 - l_3^2 \cos(2(\phi_3 - \phi_2))}{2l_2^2}
\end{aligned} \tag{A.57}$$

$$\begin{aligned}
a_3 + b_3 + c_3 &= l_2^2 + l_3^2 + 2l_2l_3 \cos(\phi_3 - \phi_2) \\
&= l_2^2 + l_3^2 - 2l_2l_3 \cos(\pi - (\phi_3 - \phi_2)) \\
&= l_5^2
\end{aligned} \tag{A.58}$$

$$\begin{aligned}
\frac{b_3^2 - 2a_3c_3}{4a_3^2} &= \frac{4l_2^2l_3^2 \cos^2(\phi_3 - \phi_2) - 2l_2^2l_3^2}{4l_2^4} \\
&= \frac{l_3^2}{2l_2^2}(-1 + \cos^2(\phi_3 - \phi_2)) \\
&= \frac{l_3^2}{2l_2^2} \cos(2(\phi_3 - \phi_2))
\end{aligned} \tag{A.59}$$

$$\begin{aligned}
&-\frac{b_3 \sqrt{4a_3c_3 - b_3^2}}{2a_3^2} \\
&= -\frac{2l_2l_3 \cos(\phi_3 - \phi_2) \sqrt{4l_2^2l_3^2 - 4l_2^2l_3^2 \cos^2(\phi_3 - \phi_2)}}{2l_2^4} \\
&= -2\frac{l_3^2}{l_2^2} \cos(\phi_3 - \phi_2) \sin(\phi_3 - \phi_2) \\
&= -\frac{l_3^2}{l_2^2} \sin(2(\phi_3 - \phi_2))
\end{aligned} \tag{A.60}$$

$$\begin{aligned}
\sqrt{4a_3c_3 - b_3^2} &= \sqrt{4l_2^2l_3^2 - 4l_2^2l_3^2 \cos^2(\phi_3 - \phi_2)} \\
&= 2l_2l_3 \sin(\phi_3 - \phi_2)
\end{aligned} \tag{A.61}$$

$$\begin{aligned}
2c_3 + b_3 &= 2l_3^2 + 2l_2l_3 \cos(\phi_3 - \phi_2) \\
&= 2l_3(l_3 \cos(\phi_3 - \phi_3) + l_2 \cos(\phi_2 - \phi_3)) \\
&= 2l_3l_5 \cos(\phi_5 - \phi_3)
\end{aligned} \tag{A.62}$$

$$\begin{aligned}
\frac{b_3}{2a_3} - \frac{1}{2} &= \frac{2l_2l_3 \cos(\phi_3 - \phi_2)}{2l_2^2} - \frac{1}{2} \\
&= \frac{l_3}{l_2} \cos(\phi_3 - \phi_2) - \frac{1}{2}
\end{aligned} \tag{A.63}$$

Substituting (A.50)-(A.63) into (A.49),

$$T_{int4} = -\frac{\mu_0 I_{l_1}}{4\pi l_1} \left(\begin{aligned} &\frac{l_2^2 - l_4^2 \cos(2(\phi_4 - \phi_2))}{2l_2^2} \ln(l_6^2) + \frac{l_4^2}{2l_2^2} \cos(2(\phi_4 - \phi_2)) \ln(l_4^2) \\ &- \frac{l_4^2}{l_2^2} \sin(2(\phi_4 - \phi_2)) \operatorname{atan2}(2l_2l_4 \sin(\phi_4 - \phi_2), 2l_4l_6 \cos(\phi_6 - \phi_4)) \\ &\quad + \frac{l_4}{l_2} \cos(\phi_4 - \phi_2) - \frac{1}{2} \\ &- \frac{l_2^2 - l_3^2 \cos(2(\phi_3 - \phi_2))}{2l_2^2} \ln(l_5^2) - \frac{l_3^2}{2l_2^2} \cos(2(\phi_3 - \phi_2)) \ln(l_3^2) \\ &+ \frac{l_3^2}{l_2^2} \sin(2(\phi_3 - \phi_2)) \operatorname{atan2}(2l_2l_3 \sin(\phi_3 - \phi_2), 2l_3l_5 \cos(\phi_5 - \phi_3)) \\ &\quad - \frac{l_3}{l_2} \cos(\phi_3 - \phi_2) + \frac{1}{2} \end{aligned} \right) \tag{A.64}$$

Splitting logarithm coefficients and combining like terms,

$$T_{int4} = -\frac{\mu_0 I_{l_1}}{4\pi l_1} \left(\begin{aligned} &- \frac{l_4^2}{l_2^2} \sin(2(\phi_4 - \phi_2)) \operatorname{atan2}(2l_2l_4 \sin(\phi_4 - \phi_2), 2l_4l_6 \cos(\phi_6 - \phi_4)) \\ &+ \frac{l_3^2}{l_2^2} \sin(2(\phi_3 - \phi_2)) \operatorname{atan2}(2l_2l_3 \sin(\phi_3 - \phi_2), 2l_3l_5 \cos(\phi_5 - \phi_3)) \\ &\quad + \frac{1}{2} (\ln(l_6^2) - \ln(l_5^2)) \\ &\quad + \frac{l_4^2}{2l_2^2} \cos(2(\phi_4 - \phi_2)) (\ln(l_4^2) - \ln(l_6^2)) \\ &\quad + \frac{l_3^2}{2l_2^2} \cos(2(\phi_3 - \phi_2)) (\ln(l_5^2) - \ln(l_3^2)) \\ &\quad + \frac{l_4}{l_2} \cos(\phi_4 - \phi_2) - \frac{l_3}{l_2} \cos(\phi_3 - \phi_2) \end{aligned} \right) \tag{A.65}$$

Utilizing (A.36)-(A.37) for the arguments of atan2 functions, combining difference of logarithm terms, invoking the exponent property of logarithms, utilizing (A.41), rearranging terms to obtain favorable sign flips and factoring l_2^2 from the denominator, (A.65) may be rewritten as

$$T_{int4} = -\frac{\mu_0 I_{l_1}}{4\pi l_1 l_2^2} \left(\begin{array}{l} l_4^2 \sin(2(\phi_4 - \phi_2)) \text{atan2}(\mathbf{l}_4 \times_2 \mathbf{l}_6, \mathbf{l}_4 \cdot \mathbf{l}_6) \\ + l_3^2 \sin(2(\phi_3 - \phi_2)) \text{atan2}(\mathbf{l}_5 \times_2 \mathbf{l}_3, \mathbf{l}_5 \cdot \mathbf{l}_3) \\ + l_2^2 \ln\left(\frac{l_6}{l_5}\right) \\ - l_4^2 \cos(2(\phi_4 - \phi_2)) \ln\left(\frac{l_6}{l_4}\right) \\ - l_3^2 \cos(2(\phi_3 - \phi_2)) \ln\left(\frac{l_3}{l_5}\right) \\ - l_3 l_2 \cos(\phi_3 - \phi_2) + l_4 l_2 \cos(\phi_4 - \phi_2) \end{array} \right) \quad (\text{A.66})$$

A.3 Combining Integral Terms

Substituting (A.14) into the coefficients of the integrals appearing in (A.9) and using angle difference formulae, (A.9) may be rewritten as

$$T_{l_2} = I_{l_2} \left(\begin{array}{l} (x_c \cos \phi_1 + y_c \sin \phi_1) \int_0^1 B'_{x,s}(\vec{r}'(t)) dt \\ + (-x_c \sin \phi_1 + y_c \cos \phi_1) \int_0^1 B'_{y,s}(\vec{r}'(t)) dt \\ + l_2 \cos(\phi_2 - \phi_1) \int_0^1 t B'_{x,s}(\vec{r}'(t)) dt \\ + l_2 \sin(\phi_2 - \phi_1) \int_0^1 t B'_{y,s}(\vec{r}'(t)) dt \end{array} \right) \quad (\text{A.67})$$

Substituting expressions (3.10), (3.11) with expanded coefficients using relationships for \cdot and \times_2 in (A.41) and substituting (A.43) and (A.66), (A.67) may be written as

$$\begin{aligned}
T_{l_2} = & \frac{-\mu_0 I_{l_1} I_{l_2}}{4\pi l_1 l_2^2} \left(\begin{aligned} & 2 \begin{pmatrix} x_c \cos \phi_1 \\ +y_c \sin \phi_1 \end{pmatrix} \begin{pmatrix} l_2^2 \cos(\phi_2 - \phi_2) \text{atan2}(\mathbf{l}_5 \times_2 \mathbf{l}_6, \mathbf{l}_5 \cdot \mathbf{l}_6) \\ +l_4 l_2 \cos(\phi_4 - \phi_2) \text{atan2}(\mathbf{l}_4 \times_2 \mathbf{l}_6, \mathbf{l}_4 \cdot \mathbf{l}_6) \\ +l_3 l_2 \cos(\phi_3 - \phi_2) \text{atan2}(\mathbf{l}_5 \times_2 \mathbf{l}_3, \mathbf{l}_5 \cdot \mathbf{l}_3) \\ -l_2 l_4 \sin(\phi_2 - \phi_4) \ln \left(\frac{l_6}{l_4} \right) \\ -l_2 l_3 \sin(\phi_2 - \phi_3) \ln \left(\frac{l_3}{l_5} \right) \end{pmatrix} \\ & +2 \begin{pmatrix} -x_c \sin \phi_1 \\ +y_c \cos \phi_1 \end{pmatrix} \begin{pmatrix} l_2 l_4 \sin(\phi_2 - \phi_4) \text{atan2}(\mathbf{l}_4 \times_2 \mathbf{l}_6, \mathbf{l}_4 \cdot \mathbf{l}_6) \\ +l_2 l_3 \sin(\phi_2 - \phi_3) \text{atan2}(\mathbf{l}_5 \times_2 \mathbf{l}_3, \mathbf{l}_5 \cdot \mathbf{l}_3) \\ +l_2^2 \ln \left(\frac{l_6}{l_5} \right) \\ +l_2 l_4 \cos(\phi_2 - \phi_4) \ln \left(\frac{l_6}{l_4} \right) \\ +l_2 l_3 \cos(\phi_2 - \phi_3) \ln \left(\frac{l_3}{l_5} \right) \end{pmatrix} \\ & +l_2 \cos(\phi_2 - \phi_1) \begin{pmatrix} l_2^2 \text{atan2}(\mathbf{l}_5 \times_2 \mathbf{l}_6, \mathbf{l}_5 \cdot \mathbf{l}_6) \\ -l_4^2 \cos(2(\phi_4 - \phi_2)) \text{atan2}(\mathbf{l}_4 \times_2 \mathbf{l}_6, \mathbf{l}_4 \cdot \mathbf{l}_6) \\ -l_3^2 \cos(2(\phi_2 - \phi_3)) \text{atan2}(\mathbf{l}_5 \times_2 \mathbf{l}_3, \mathbf{l}_5 \cdot \mathbf{l}_3) \\ -2l_4^2 \cos(\phi_4 - \phi_2) \sin(\phi_4 - \phi_2) \ln \left(\frac{l_6}{l_4} \right) \\ +2l_3^2 \cos(\phi_3 - \phi_2) \sin(\phi_3 - \phi_2) \ln \left(\frac{l_3}{l_5} \right) \\ -l_3 l_2 \sin(\phi_3 - \phi_2) + l_4 l_2 \sin(\phi_4 - \phi_2) \end{pmatrix} \\ & +l_2 \sin(\phi_2 - \phi_1) \begin{pmatrix} l_4^2 \sin(2(\phi_4 - \phi_2)) \text{atan2}(\mathbf{l}_4 \times_2 \mathbf{l}_6, \mathbf{l}_4 \cdot \mathbf{l}_6) \\ +l_3^2 \sin(2(\phi_3 - \phi_2)) \text{atan2}(\mathbf{l}_5 \times_2 \mathbf{l}_3, \mathbf{l}_5 \cdot \mathbf{l}_3) \\ +l_2^2 \ln \left(\frac{l_6}{l_5} \right) \\ -l_4^2 \cos(2(\phi_4 - \phi_2)) \ln \left(\frac{l_6}{l_4} \right) \\ -l_3^2 \cos(2(\phi_3 - \phi_2)) \ln \left(\frac{l_3}{l_5} \right) \\ -l_3 l_2 \cos(\phi_3 - \phi_2) + l_4 l_2 \cos(\phi_4 - \phi_2) \end{pmatrix} \end{aligned} \right) \quad (\text{A.68})
\end{aligned}$$

Observing (A.68), it is apparent that the final expression for T_{l_2} will be of the form

$$T_{l_2} = C \begin{pmatrix} C_{\text{atan56}} \text{atan2}(\mathbf{l}_5 \times_2 \mathbf{l}_6, \mathbf{l}_5 \cdot \mathbf{l}_6) \\ + C_{\text{atan46}} \text{atan2}(\mathbf{l}_4 \times_2 \mathbf{l}_6, \mathbf{l}_4 \cdot \mathbf{l}_6) \\ + C_{\text{atan53}} \text{atan2}(\mathbf{l}_5 \times_2 \mathbf{l}_3, \mathbf{l}_5 \cdot \mathbf{l}_3) \\ + C_{\ln56} \ln\left(\frac{l_6}{l_5}\right) \\ + C_{\ln46} \ln\left(\frac{l_6}{l_4}\right) \\ + C_{\ln53} \ln\left(\frac{l_3}{l_5}\right) \\ + K \end{pmatrix} \quad (\text{A.69})$$

Collecting terms in (A.68), simplified expressions for the coefficients C , $C_{\text{atan56}} - C_{\ln53}$ and constant K follow.

$$\begin{aligned} C_{\text{atan56}} &= l_2^3 \cos(\phi_2 - \phi_1) + 2l_2^2 (x_c \cos \phi_1 + y_c \sin \phi_1) \\ &= l_2 l_2^2 \frac{\mathbf{l}_1 \cdot \mathbf{l}_2}{l_1 l_2} + 2\mathbf{l}_2 \cdot \mathbf{l}_2 (x_c \cos \phi_1 + y_c \sin \phi_1) \\ &= \frac{1}{l_1} ((\mathbf{l}_2 \cdot \mathbf{l}_2)(\mathbf{l}_1 \cdot \mathbf{l}_2) + 2l_1(\mathbf{l}_2 \cdot \mathbf{l}_2) (x_c \cos \phi_1 + y_c \sin \phi_1)) \end{aligned} \quad (\text{A.70})$$

The term $1/l_1$ will be factored out from all coefficients $C_{\text{atan56}} - C_{\ln53}$ into the coefficient C , therefore

$$C_{\text{atan56}} = (\mathbf{l}_2 \cdot \mathbf{l}_2)(\mathbf{l}_1 \cdot \mathbf{l}_2) + 2l_1(\mathbf{l}_2 \cdot \mathbf{l}_2) (x_c \cos \phi_1 + y_c \sin \phi_1) \quad (\text{A.71})$$

Collecting terms in (A.68),

$$C_{\text{atan46}} = \begin{pmatrix} 2l_4 l_2 (x_c \cos \phi_1 + y_c \sin \phi_1) \cos(\phi_4 - \phi_2) \\ + 2l_2 l_4 (-x_c \sin \phi_1 + y_c \cos \phi_1) \sin(\phi_2 - \phi_4) \\ - l_2 l_4^2 \cos(\phi_2 - \phi_1) \cos(2(\phi_4 - \phi_2)) \\ + l_2 l_4^2 \sin(\phi_2 - \phi_1) \sin(2(\phi_4 - \phi_2)) \end{pmatrix} \quad (\text{A.72})$$

The last two terms in (A.72) may be simplified further as

$$\begin{aligned}
& \begin{pmatrix} -l_2 l_4^2 \cos(\phi_2 - \phi_1)(2 \cos^2(\phi_4 - \phi_2) - 1) \\ +l_2 l_4^2 \sin(\phi_2 - \phi_1) 2 \sin(\phi_4 - \phi_2) \cos(\phi_4 - \phi_2) \end{pmatrix} \\
= & \begin{pmatrix} -2l_2 l_4^2 \cos(\phi_4 - \phi_2) (\cos(\phi_1 - \phi_2) \cos(\phi_4 - \phi_2) + \sin(\phi_1 - \phi_2) \sin(\phi_4 - \phi_2)) \\ +l_2 l_4^2 \cos(\phi_2 - \phi_1) \end{pmatrix} \\
= & \begin{pmatrix} -2l_2 l_4^2 \cos(\phi_4 - \phi_2) \cos(\phi_4 - \phi_1) \\ +l_2 l_4^2 \cos(\phi_2 - \phi_1) \end{pmatrix} \\
= & \begin{pmatrix} -l_2 l_4^2 \cos(\phi_4 - \phi_2) \cos(\phi_4 - \phi_1) \\ -l_2 l_4^2 \cos(\phi_4 - \phi_2) \cos(\phi_4 - \phi_1) \\ +l_2 l_4^2 \cos(\phi_2 - \phi_1) \end{pmatrix} \\
= & \begin{pmatrix} -l_2 l_4^2 \cos(\phi_4 - \phi_2) \cos(\phi_4 - \phi_1) \\ -l_2 l_4^2 (\cos(\phi_2 - \phi_1) - \sin(\phi_2 - \phi_4) \sin(\phi_1 - \phi_4)) \\ +l_2 l_4^2 \cos(\phi_2 - \phi_1) \end{pmatrix} \\
= & \begin{pmatrix} -l_2 l_4^2 \cos(\phi_4 - \phi_2) \cos(\phi_4 - \phi_1) \\ +l_2 l_4^2 \sin(\phi_2 - \phi_4) \sin(\phi_1 - \phi_4) \end{pmatrix} \\
& \tag{A.73}
\end{aligned}$$

Utilizing (A.41), C_{atan46} may be expressed as

$$C_{\text{atan46}} = \frac{1}{l_1} \begin{pmatrix} 2l_1 \mathbf{l}_4 \cdot \mathbf{l}_2 (x_c \cos \phi_1 + y_c \sin \phi_1) \\ +2l_1 \mathbf{l}_4 \times_2 \mathbf{l}_2 (-x_c \sin \phi_1 + y_c \cos \phi_1) \\ -(\mathbf{l}_4 \cdot \mathbf{l}_2)(\mathbf{l}_4 \cdot \mathbf{l}_1) \\ +(\mathbf{l}_4 \times_2 \mathbf{l}_2)(\mathbf{l}_4 \times_2 \mathbf{l}_1) \end{pmatrix} \tag{A.74}$$

Finally, factoring the $1/l_1$ term into C :

$$C_{\text{atan46}} = \begin{pmatrix} 2l_1 \mathbf{l}_4 \cdot \mathbf{l}_2 (x_c \cos \phi_1 + y_c \sin \phi_1) \\ +2l_1 \mathbf{l}_4 \times_2 \mathbf{l}_2 (-x_c \sin \phi_1 + y_c \cos \phi_1) \\ -(\mathbf{l}_4 \cdot \mathbf{l}_2)(\mathbf{l}_4 \cdot \mathbf{l}_1) \\ +(\mathbf{l}_4 \times_2 \mathbf{l}_2)(\mathbf{l}_4 \times_2 \mathbf{l}_1) \end{pmatrix} \quad (\text{A.75})$$

A similar procedure yields a similar expression for C_{atan53} , this may be arrived at simply by exchanging subscripts '4' for '3' in (A.75):

$$C_{\text{atan53}} = \begin{pmatrix} 2l_1 \mathbf{l}_3 \cdot \mathbf{l}_2 (x_c \cos \phi_1 + y_c \sin \phi_1) \\ +2l_1 \mathbf{l}_3 \times_2 \mathbf{l}_2 (-x_c \sin \phi_1 + y_c \cos \phi_1) \\ -(\mathbf{l}_3 \cdot \mathbf{l}_2)(\mathbf{l}_3 \cdot \mathbf{l}_1) \\ +(\mathbf{l}_3 \times_2 \mathbf{l}_2)(\mathbf{l}_3 \times_2 \mathbf{l}_1) \end{pmatrix} \quad (\text{A.76})$$

Collecting terms in (A.68),

$$\begin{aligned} C_{\text{ln56}} &= \begin{pmatrix} 2(x_c \cos \phi_1 + y_c \sin \phi_1)(0) \\ +2(-x_c \sin \phi_1 + y_c \cos \phi_1)(l_2^2) \\ +l_2 \cos(\phi_2 - \phi_1)(0) \\ +l_2 \sin(\phi_2 - \phi_1)(l_2^2) \end{pmatrix} \\ &= \frac{1}{l_1} \begin{pmatrix} 2l_1 \mathbf{l}_2 \cdot \mathbf{l}_2 (-x_c \sin \phi_1 + y_c \cos \phi_1) \\ +(\mathbf{l}_2 \cdot \mathbf{l}_2)(\mathbf{l}_1 \times_2 \mathbf{l}_2) \end{pmatrix} \end{aligned} \quad (\text{A.77})$$

Finally, factoring the $1/l_1$ term into C :

$$C_{\text{ln56}} = \begin{pmatrix} 2l_1 \mathbf{l}_2 \cdot \mathbf{l}_2 (-x_c \sin \phi_1 + y_c \cos \phi_1) \\ +(\mathbf{l}_2 \cdot \mathbf{l}_2)(\mathbf{l}_1 \times_2 \mathbf{l}_2) \end{pmatrix} \quad (\text{A.78})$$

Collecting terms in (A.68),

$$C_{\ln 46} = \begin{pmatrix} 2(x_c \cos \phi_1 + y_c \sin \phi_1)(-l_2 l_4 \sin(\phi_2 - \phi_4)) \\ +2(-x_c \sin \phi_1 + y_c \cos \phi_1)(l_2 l_4 \cos(\phi_2 - \phi_4)) \\ +l_2 \cos(\phi_2 - \phi_1)(-2l_4^2 \cos(\phi_4 - \phi_2) \sin(\phi_4 - \phi_2)) \\ +l_2 \sin(\phi_2 - \phi_1)(-l_4^2 \cos(2(\phi_4 - \phi_2))) \end{pmatrix} \quad (\text{A.79})$$

The last two terms in (A.79) may be simplified as

$$\begin{aligned} & \begin{pmatrix} +l_2 \cos(\phi_2 - \phi_1)(-2l_4^2 \cos(\phi_4 - \phi_2) \sin(\phi_4 - \phi_2)) \\ +l_2 \sin(\phi_2 - \phi_1)(-l_4^2 \cos(2(\phi_4 - \phi_2))) \end{pmatrix} \\ &= \begin{pmatrix} -2l_2 l_4^2 \cos(\phi_2 - \phi_1) \cos(\phi_4 - \phi_2) \sin(\phi_4 - \phi_2) \\ -l_2 l_4^2 \sin(\phi_2 - \phi_1)(2 \cos^2(\phi_4 - \phi_2) - 1) \end{pmatrix} \\ &= \begin{pmatrix} -2l_2 l_4^2 \cos(\phi_4 - \phi_2)(\cos(\phi_1 - \phi_2) \sin(\phi_4 - \phi_2) - \cos(\phi_4 - \phi_2) \sin(\phi_1 - \phi_2)) \\ +l_2 l_4^2 \sin(\phi_2 - \phi_1) \end{pmatrix} \\ &= \begin{pmatrix} -2l_2 l_4^2 \cos(\phi_4 - \phi_2) \sin(\phi_4 - \phi_1) \\ +l_2 l_4^2 \sin(\phi_2 - \phi_1) \end{pmatrix} \\ &= \begin{pmatrix} -l_2 l_4^2 \cos(\phi_4 - \phi_2) \sin(\phi_4 - \phi_1) \\ -l_2 l_4^2 \cos(\phi_4 - \phi_2) \sin(\phi_4 - \phi_1) \\ +l_2 l_4^2 \sin(\phi_2 - \phi_1) \end{pmatrix} \\ &= \begin{pmatrix} -l_2 l_4^2 \cos(\phi_4 - \phi_2) \sin(\phi_4 - \phi_1) \\ -l_2 l_4^2 (\sin(\phi_2 - \phi_1) - \sin(\phi_2 - \phi_4) \cos(\phi_1 - \phi_4)) \\ +l_2 l_4^2 \sin(\phi_2 - \phi_1) \end{pmatrix} \\ &= \begin{pmatrix} -l_2 l_4^2 \cos(\phi_4 - \phi_2) \sin(\phi_4 - \phi_1) \\ +l_2 l_4^2 (\sin(\phi_2 - \phi_4) \cos(\phi_1 - \phi_4)) \end{pmatrix} \\ &= \frac{1}{l_1} ((\mathbf{l}_1 \cdot \mathbf{l}_4)(\mathbf{l}_4 \times_2 \mathbf{l}_2) + (\mathbf{l}_2 \cdot \mathbf{l}_4)(\mathbf{l}_4 \times_2 \mathbf{l}_1)) \end{aligned} \quad (\text{A.80})$$

Finally, factoring the $1/l_1$ term into C :

$$C_{\ln 46} = \begin{pmatrix} 2l_1 \mathbf{l}_2 \times_2 \mathbf{l}_4 (x_c \cos \phi_1 + y_c \sin \phi_1) \\ 2l_1 \mathbf{l}_2 \cdot \mathbf{l}_4 (-x_c \sin \phi_1 + y_c \cos \phi_1) \\ (\mathbf{l}_1 \cdot \mathbf{l}_4)(\mathbf{l}_4 \times_2 \mathbf{l}_2) + (\mathbf{l}_2 \cdot \mathbf{l}_4)(\mathbf{l}_4 \times_2 \mathbf{l}_1) \end{pmatrix} \quad (\text{A.81})$$

A similar procedure yields a similar expression for $C_{\ln 53}$, this may be derived simply by exchanging subscripts '4' for '3' in (A.81):

$$C_{\ln 53} = \begin{pmatrix} 2l_1 \mathbf{l}_2 \times_2 \mathbf{l}_3 (x_c \cos \phi_1 + y_c \sin \phi_1) \\ 2l_1 \mathbf{l}_2 \cdot \mathbf{l}_3 (-x_c \sin \phi_1 + y_c \cos \phi_1) \\ (\mathbf{l}_1 \cdot \mathbf{l}_3)(\mathbf{l}_3 \times_2 \mathbf{l}_2) + (\mathbf{l}_2 \cdot \mathbf{l}_3)(\mathbf{l}_3 \times_2 \mathbf{l}_1) \end{pmatrix} \quad (\text{A.82})$$

$$\begin{aligned} K &= \begin{pmatrix} l_2 \cos(\phi_2 - \phi_1)(-l_3 l_2 \sin(\phi_3 - \phi_2) + l_4 l_2 \sin(\phi_4 - \phi_2)) \\ +l_2 \sin(\phi_2 - \phi_1)(-l_3 l_2 \cos(\phi_3 - \phi_2) + l_4 l_2 \cos(\phi_4 - \phi_2)) \end{pmatrix} \\ &= \begin{pmatrix} l_2 \cos(\phi_2 - \phi_1)(-l_2 l_1 \sin(\phi_1 - \phi_2)) \\ +l_2 \sin(\phi_2 - \phi_1)(-l_2 l_1 \cos(\phi_1 - \phi_2)) \end{pmatrix} \\ &= 0 \end{aligned} \quad (\text{A.83})$$

Since we have factored l_1 from the denominator in all coefficients,

$$C = \frac{-\mu_0 I_1 I_2}{4\pi l_1^2 l_2^2} \quad (\text{A.84})$$

Substituting the previously derived coefficients of all terms, the torque may be written as

$$T_{\mathbf{l}_2} = \frac{-\mu_0 I_{\mathbf{l}_1} I_{\mathbf{l}_2}}{4\pi l_1^2 l_2^2} \left(\begin{aligned} & \left(\begin{aligned} & 2l_1(\mathbf{l}_2 \cdot \mathbf{l}_2)(x_c \cos \phi_1 + y_c \sin \phi_1) \\ & + (\mathbf{l}_2 \cdot \mathbf{l}_2)(\mathbf{l}_1 \cdot \mathbf{l}_2) \end{aligned} \right) \text{atan2}(\mathbf{l}_5 \times_2 \mathbf{l}_6, \mathbf{l}_5 \cdot \mathbf{l}_6) \\ & + \left(\begin{aligned} & 2l_1 \mathbf{l}_4 \cdot \mathbf{l}_2 (x_c \cos \phi_1 + y_c \sin \phi_1) \\ & + 2l_1 \mathbf{l}_4 \times_2 \mathbf{l}_2 (-x_c \sin \phi_1 + y_c \cos \phi_1) \\ & - (\mathbf{l}_4 \cdot \mathbf{l}_2)(\mathbf{l}_4 \cdot \mathbf{l}_1) \\ & + (\mathbf{l}_4 \times_2 \mathbf{l}_2)(\mathbf{l}_4 \times_2 \mathbf{l}_1) \end{aligned} \right) \text{atan2}(\mathbf{l}_4 \times_2 \mathbf{l}_6, \mathbf{l}_4 \cdot \mathbf{l}_6) \\ & + \left(\begin{aligned} & 2l_1 \mathbf{l}_3 \cdot \mathbf{l}_2 (x_c \cos \phi_1 + y_c \sin \phi_1) \\ & + 2l_1 \mathbf{l}_3 \times_2 \mathbf{l}_2 (-x_c \sin \phi_1 + y_c \cos \phi_1) \\ & - (\mathbf{l}_3 \cdot \mathbf{l}_2)(\mathbf{l}_3 \cdot \mathbf{l}_1) \\ & + (\mathbf{l}_3 \times_2 \mathbf{l}_2)(\mathbf{l}_3 \times_2 \mathbf{l}_1) \end{aligned} \right) \text{atan2}(\mathbf{l}_5 \times_2 \mathbf{l}_3, \mathbf{l}_5 \cdot \mathbf{l}_3) \\ & + \left(\begin{aligned} & 2l_1 \mathbf{l}_2 \cdot \mathbf{l}_2 (-x_c \sin \phi_1 + y_c \cos \phi_1) \\ & + (\mathbf{l}_2 \cdot \mathbf{l}_2)(\mathbf{l}_1 \times_2 \mathbf{l}_2) \end{aligned} \right) \ln \left(\frac{l_6}{l_5} \right) \\ & + \left(\begin{aligned} & 2l_1 \mathbf{l}_2 \times_2 \mathbf{l}_4 (x_c \cos \phi_1 + y_c \sin \phi_1) \\ & 2l_1 \mathbf{l}_2 \cdot \mathbf{l}_4 (-x_c \sin \phi_1 + y_c \cos \phi_1) \\ & (\mathbf{l}_1 \cdot \mathbf{l}_4)(\mathbf{l}_4 \times_2 \mathbf{l}_2) + (\mathbf{l}_2 \cdot \mathbf{l}_4)(\mathbf{l}_4 \times_2 \mathbf{l}_1) \end{aligned} \right) \ln \left(\frac{l_6}{l_4} \right) \\ & + \left(\begin{aligned} & 2l_1 \mathbf{l}_2 \times_2 \mathbf{l}_3 (x_c \cos \phi_1 + y_c \sin \phi_1) \\ & 2l_1 \mathbf{l}_2 \cdot \mathbf{l}_3 (-x_c \sin \phi_1 + y_c \cos \phi_1) \\ & (\mathbf{l}_1 \cdot \mathbf{l}_3)(\mathbf{l}_3 \times_2 \mathbf{l}_2) + (\mathbf{l}_2 \cdot \mathbf{l}_3)(\mathbf{l}_3 \times_2 \mathbf{l}_1) \end{aligned} \right) \ln \left(\frac{l_3}{l_5} \right) \end{aligned} \right) \quad (\text{A.85})$$

The atan2 and ln coefficients may be further simplified to more closely resemble the Lorentz force formulas. Defining $\mathbf{l}_c = \langle x_c, y_c \rangle$ and since $\mathbf{l}_1 = \langle l_1 \cos \phi_1, l_1 \sin \phi_1 \rangle = \langle$

$l_{1x}, l_{1y} >$, the l_1 term may be absorbed and the coefficient C_{atan56} may be rewritten as

$$\begin{aligned} C_{\text{atan56}} &= (\mathbf{l}_2 \cdot \mathbf{l}_2)(\mathbf{l}_1 \cdot \mathbf{l}_2 + 2\mathbf{l}_c \cdot \mathbf{l}_1) \\ &= (\mathbf{l}_2 \cdot \mathbf{l}_2)(\mathbf{l}_1 \cdot (\underbrace{\mathbf{l}_2 + \mathbf{l}_c}_{\mathbf{l}_d} + \mathbf{l}_c)) \end{aligned} \quad (\text{A.86})$$

By (3.29) and (3.30), this may be expanded as

$$C_{\text{atan56}} = l_2^2 l_1 l_d \cos(\phi_2 - \phi_2) \cos(\phi_1 - \phi_d) + l_2^2 l_1 l_c \cos(\phi_2 - \phi_2) \cos(\phi_1 - \phi_c) \quad (\text{A.87})$$

The coefficient is unchanged by adding the term $0 = l_2^2 l_1 l_d \sin(\phi_2 - \phi_2) \sin(\phi_1 - \phi_d) + l_2^2 l_1 l_c \sin(\phi_2 - \phi_2) \sin(\phi_1 - \phi_c)$, and by doing so the coefficient may be cast into the form

$$\begin{aligned} C_{\text{atan56}} &= l_2^2 l_1 l_d \cos(\phi_2 - \phi_2) \cos(\phi_1 - \phi_d) + l_2^2 l_1 l_c \cos(\phi_2 - \phi_2) \cos(\phi_1 - \phi_c) \\ &\quad l_2^2 l_1 l_d \sin(\phi_2 - \phi_2) \sin(\phi_1 - \phi_d) + l_2^2 l_1 l_c \sin(\phi_2 - \phi_2) \sin(\phi_1 - \phi_c) \\ &= l_1 l_2 l_2 l_c \cos(\phi_1 + \phi_2 - \phi_2 - \phi_c) \\ &\quad + l_1 l_2 l_2 l_d \cos(\phi_1 + \phi_2 - \phi_2 - \phi_d) \end{aligned} \quad (\text{A.88})$$

The expression involves a difference in angles $\phi_2 - \phi_2$: although zero, it is convenient to write in this form since the remaining coefficients are of similar form, as will be shown.

The coefficient C_{atan46} may be written as

$$\begin{aligned} C_{\text{atan46}} &= \begin{pmatrix} (\mathbf{l}_4 \cdot \mathbf{l}_2) (2\mathbf{l}_1 \cdot \mathbf{l}_c - \mathbf{l}_1 \cdot \mathbf{l}_4) \\ + (\mathbf{l}_4 \times_2 \mathbf{l}_2) (2\mathbf{l}_1 \times_2 \mathbf{l}_c - \mathbf{l}_1 \times_2 \mathbf{l}_4) \end{pmatrix} \\ &= \begin{pmatrix} (\mathbf{l}_4 \cdot \mathbf{l}_2) (\mathbf{l}_1 \cdot (\mathbf{l}_c + \mathbf{l}_c - \mathbf{l}_4)) \\ + (\mathbf{l}_4 \times_2 \mathbf{l}_2) (\mathbf{l}_1 \times_2 (\mathbf{l}_c + \underbrace{\mathbf{l}_c - \mathbf{l}_4}_{\mathbf{l}_b})) \end{pmatrix} \end{aligned} \quad (\text{A.89})$$

By (3.29) and (3.30), this may be expanded as

$$\begin{aligned} C_{\text{atan46}} &= l_4 l_2 l_1 l_c \cos(\phi_4 - \phi_2) \cos(\phi_1 - \phi_c) + l_4 l_2 l_1 l_b \cos(\phi_4 - \phi_2) \cos(\phi_1 - \phi_b) \\ &\quad + l_4 l_2 l_1 l_c \sin(\phi_4 - \phi_2) \sin(\phi_1 - \phi_c) + l_4 l_2 l_1 l_b \sin(\phi_4 - \phi_2) \sin(\phi_1 - \phi_b) \end{aligned} \quad (\text{A.90})$$

By the angle difference formulae, this may be written compactly as

$$\begin{aligned} C_{\text{atan46}} = & l_1 l_2 l_4 l_c \cos(\phi_1 + \phi_2 - \phi_4 - \phi_c) \\ & + l_1 l_2 l_4 l_b \cos(\phi_1 + \phi_2 - \phi_4 - \phi_b) \end{aligned} \quad (\text{A.91})$$

A similar simplification process may be applied to C_{atan53} by exchanging subscripts ‘4’ for ‘3’ and ‘b’ for ‘a’. The coefficient C_{ln56} may be written as

$$\begin{aligned} C_{\text{ln56}} = & (\mathbf{l}_2 \cdot \mathbf{l}_2)(2\mathbf{l}_1 \times_2 \mathbf{l}_c + \mathbf{l}_1 \times_2 \mathbf{l}_2) \\ = & (\mathbf{l}_2 \cdot \mathbf{l}_2)(\mathbf{l}_1 \times_2 (\mathbf{l}_c + \underbrace{\mathbf{l}_c + \mathbf{l}_2}_{\mathbf{l}_d})) \end{aligned} \quad (\text{A.92})$$

C_{ln56} may be expanded as

$$C_{\text{ln56}} = -l_2 l_2 l_1 l_c \cos(\phi_2 - \phi_2) \sin(\phi_c - \phi_1) - l_2 l_2 l_1 l_d \cos(\phi_2 - \phi_2) \sin(\phi_d - \phi_1) \quad (\text{A.93})$$

Adding the term $0 = -l_2 l_2 l_1 l_c \sin(\phi_4 - \phi_2) \cos(\phi_1 - \phi_c) - l_2 l_2 l_1 l_b \sin(\phi_2 - \phi_2) \cos(\phi_1 - \phi_d)$ leaves the coefficient unchanged, yielding

$$\begin{aligned} C_{\text{ln56}} = & -l_2 l_2 l_1 l_c \cos(\phi_2 - \phi_2) \sin(\phi_1 - \phi_c) - l_2 l_2 l_1 l_d \cos(\phi_2 - \phi_2) \sin(\phi_1 - \phi_d) \\ & - l_2 l_2 l_1 l_c \sin(\phi_4 - \phi_2) \cos(\phi_1 - \phi_c) - l_2 l_2 l_1 l_b \sin(\phi_2 - \phi_2) \cos(\phi_1 - \phi_d) \\ = & -l_1 l_2 l_2 l_c \sin(\phi_1 + \phi_2 - \phi_2 - \phi_c) \\ & - l_1 l_2 l_2 l_d \sin(\phi_1 + \phi_2 - \phi_2 - \phi_d) \end{aligned} \quad (\text{A.94})$$

The coefficient C_{ln46} may be written as

$$\begin{aligned} C_{\text{ln46}} = & (\mathbf{l}_2 \times_2 \mathbf{l}_4)(2\mathbf{l}_1 \cdot \mathbf{l}_c - \mathbf{l}_1 \cdot \mathbf{l}_4) \\ & + (\mathbf{l}_2 \cdot \mathbf{l}_4)(2\mathbf{l}_1 \times_2 \mathbf{l}_c - \mathbf{l}_1 \times_2 \mathbf{l}_4) \\ = & (\mathbf{l}_2 \times_2 \mathbf{l}_4)(\mathbf{l}_1 \cdot (\mathbf{l}_c + \mathbf{l}_c - \mathbf{l}_4)) \\ & + (\mathbf{l}_2 \cdot \mathbf{l}_4)(\mathbf{l}_1 \times_2 (\mathbf{l}_c + \underbrace{\mathbf{l}_c - \mathbf{l}_4}_{\mathbf{l}_b})) \end{aligned} \quad (\text{A.95})$$

By (3.29) and (3.30), this may be expanded as

$$\begin{aligned} C_{\text{ln46}} = & -l_2 l_4 l_1 l_c \sin(\phi_2 - \phi_4) \cos(\phi_1 - \phi_c) - l_2 l_4 l_1 l_b \sin(\phi_2 - \phi_4) \cos(\phi_1 - \phi_b) \\ & - l_4 l_2 l_1 l_c \cos(\phi_2 - \phi_4) \sin(\phi_1 - \phi_c) - l_4 l_2 l_1 l_b \cos(\phi_2 - \phi_4) \sin(\phi_1 - \phi_b) \end{aligned} \quad (\text{A.96})$$

By the angle difference formulae, this may be written compactly as

$$\begin{aligned}
 C_{\ln 46} = & -l_1 l_2 l_4 l_c \sin(\phi_1 + \phi_2 - \phi_4 - \phi_c) \\
 & -l_1 l_2 l_4 l_b \sin(\phi_1 + \phi_2 - \phi_4 - \phi_b)
 \end{aligned} \tag{A.97}$$

A similar simplification process may be applied to $C_{\ln 53}$ by exchanging subscripts ‘4’ for ‘3’ and ‘b’ for ‘a’. Substituting these coefficients yields the following final form for the torque expression:

$$T_{l_2} = -\frac{\mu_0 I_1 I_2}{4\pi l_1^2 l_2^2} \left(\begin{aligned} & \left(\begin{aligned} & l_1 l_2 l_2 l_c \cos(\phi_1 + \phi_2 - \phi_2 - \phi_c) \\ & + l_1 l_2 l_2 l_d \cos(\phi_1 + \phi_2 - \phi_2 - \phi_d) \end{aligned} \right) \text{atan2} \left(\begin{aligned} & \mathbf{l}_5 \times_2 \mathbf{l}_6, \\ & \mathbf{l}_5 \cdot \mathbf{l}_6 \end{aligned} \right) \\ & + \left(\begin{aligned} & l_1 l_2 l_3 l_c \cos(\phi_1 + \phi_2 - \phi_3 - \phi_c) \\ & + l_1 l_2 l_3 l_a \cos(\phi_1 + \phi_2 - \phi_3 - \phi_a) \end{aligned} \right) \text{atan2} \left(\begin{aligned} & \mathbf{l}_5 \times_2 \mathbf{l}_3, \\ & \mathbf{l}_5 \cdot \mathbf{l}_3 \end{aligned} \right) \\ & + \left(\begin{aligned} & l_1 l_2 l_4 l_c \cos(\phi_1 + \phi_2 - \phi_4 - \phi_c) \\ & + l_1 l_2 l_4 l_b \cos(\phi_1 + \phi_2 - \phi_4 - \phi_b) \end{aligned} \right) \text{atan2} \left(\begin{aligned} & \mathbf{l}_4 \times_2 \mathbf{l}_6, \\ & \mathbf{l}_4 \cdot \mathbf{l}_6 \end{aligned} \right) \\ & - \left(\begin{aligned} & l_1 l_2 l_2 l_c \sin(\phi_1 + \phi_2 - \phi_2 - \phi_c) \\ & + l_1 l_2 l_2 l_d \sin(\phi_1 + \phi_2 - \phi_2 - \phi_d) \end{aligned} \right) \log \left(\frac{l_6}{l_5} \right) \\ & - \left(\begin{aligned} & l_1 l_2 l_3 l_c \sin(\phi_1 + \phi_2 - \phi_3 - \phi_c) \\ & + l_1 l_2 l_3 l_a \sin(\phi_1 + \phi_2 - \phi_3 - \phi_a) \end{aligned} \right) \log \left(\frac{l_3}{l_5} \right) \\ & - \left(\begin{aligned} & l_1 l_2 l_4 l_c \sin(\phi_1 + \phi_2 - \phi_4 - \phi_c) \\ & + l_1 l_2 l_4 l_b \sin(\phi_1 + \phi_2 - \phi_4 - \phi_b) \end{aligned} \right) \log \left(\frac{l_6}{l_4} \right) \end{aligned} \right) \tag{A.98}$$

B. MESH GENERATION

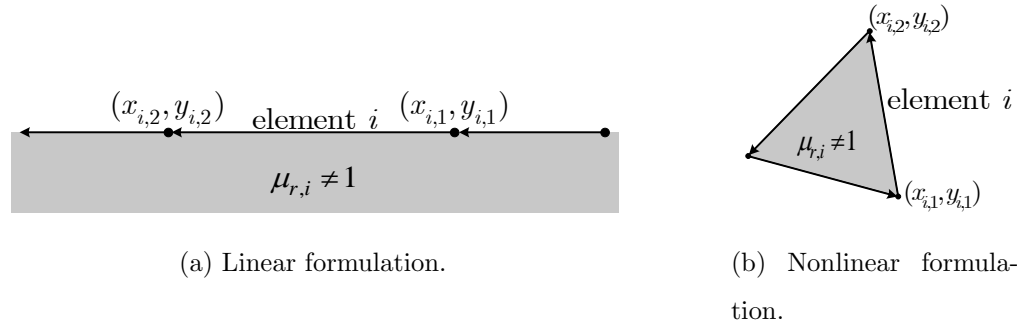


Fig. B.1.: Mesh element orientation.

In a meshing procedure, the collection of nodes and lines are created which discretely approximate the geometry of the device under study. In this research, the geometry of electric machines is defined in terms of lines and arc segments.

In order to mesh a line in the linear Galerkin formulation, a MATLAB function was written which takes as its primary arguments 1) the points defining the line, 2) the number of nodes to divide the line into and 3) a flag to select logarithmically- or linearly-spaced nodes. This option may be used to select the node spacing such that the points meshing the distance from the line midpoint to the one end point are related logarithmically and the points from midpoint to the opposite end point mirror them. An example of each type of node spacing is shown in Figure B.2, where the concentration of nodes is greatest near the outside corners, achieved using logarithmic spacing, whereas since the inside edge has rounded corners, linearly-spaced nodes suffice. Using the logarithmically-spaced node option, the bound current distribution is allowed to change more abruptly near corners in the geometry. In order to mesh an arc segment in the linear Galerkin formulation, a MATLAB function was written which takes as its primary arguments 1) the arc center point, 2) the arc radius, 3)

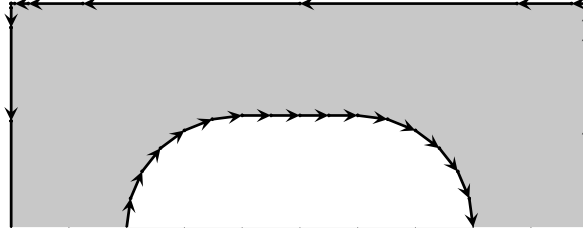


Fig. B.2.: Example of linearly- and logarithmically- spaced nodes.

two angles which define the beginning and end of the arc segment and 4) a flag to select logarithmically- or linearly-spaced nodes.

In the linear Galerkin formulation, the points defining edge element i , $p_{i,1} = (x_{i,1}, y_{i,1})$ and $p_{i,2} = (x_{i,2}, y_{i,2})$, must be such that as one traverses along the material boundary in the direction of the vector $\vec{a}_i = \vec{p}_{i,2} - \vec{p}_{i,1}$ while the magnetizeable material is on the left, as depicted in Figure B.1a.

In the case of the nonlinear point matching formulation, the nodes defining each line must be such that the vectors formed circulate around the polygon in a counter clockwise fashion, as shown in Figure B.1b. Although shown with triangles, the nonlinear mesh can consist of any combinations of polygons, which can be convenient as a tool for designing machines using pre-meshed geometries. The use of triangles is common due to widely available meshing tools for FEA. The triangular volume meshes were formed in this research using the Partial Differential Equation Toolbox available from Mathworks [51].

VITA

VITA

Daniel Horvath received the BSEE and BSCompE degrees in 2014 and the MSEE degree in 2016 from Purdue University in West Lafayette, Indiana. His research interests include computational electromagnetics, design, analysis and prototyping of electric machinery and power electronics as well as embedded programming of control systems.